Università degli studi di Padova
Università degli studi di Napoli Federico II

Centro Ricerche Fusione – Consorzio RFX

Joint Doctoral Programme in Fusion Science and Engineering
XXXVI Cycle

Turbulence induced particle and heat load on the first wall in different confinement regimes

Coordinator:
Prof. Gianmaria De Tommasi

Supervisor:
Dr. Nicola Vianello

Co-supervisor:
Prof. Piero Martin

Doctoral dissertation of:
Adriano Stagni

Padova, January 10, 2024

“One can always do better. You are never finished.
You are never ready. You are never certain.
If you think you are, you are in the wrong field.”

— Bruce Scott

Alla mia famiglia, alla mia compagna,
E ai miei nonni, ovunque voi siate.

CONTENTS

DISCLAIMER

Adriano Stagni
Turbulence induced particle and heat load on the first wall in different confinement regimes
Joint Doctoral Programme in Fusion Science and Engineering

This doctoral research project has been carried out at Centro Ricerche Fusione - Consorzio RFX (Università degli Studi di Padova, 35127 Padova, Italy) jointly with Università degli Studi di Napoli Federico II. The results presented in this manuscript have been obtained in collaboration with Swiss Plasma Center (École Polytechnique Fédérale de Lausanne, 1015 Lausanne, Switzerland). This work has been carried out within the framework of the EUROfusion Consortium, partially funded by the European Union via the Euratom Research and Training Programme (Grant Agreement No 101052200 — EUROfusion). The Swiss contribution to this work has been funded by the Swiss State Secretariat for Education, Research and Innovation (SERI). Views and opinions expressed are however those of the author only and do not necessarily reflect those of the European Union, the European Commission or SERI. Neither the European Union nor the European Commission nor SERI can be held responsible for them. This work was supported in part by the Swiss National Science Foundation, and in part by the US Department of Energy under award No. DE-SC0010529.

Centro Ricerche Fusione - Consorzio RFX: www.igi.cnr.it
Università degli Studi di Padova: www.unipd.it
Università degli Studi di Napoli Federico II: www.unina.it
Swiss Plasma Center - EPFL: spc.epfl.ch
EUROfusion Consortium: www.euro-fusion.org
Swiss National Science Foundation: www.snsf.ch
US Department of Energy: www.energy.gov

LIST OF FIGURES

List of Tables

ABSTRACT

THE turbulent dynamics taking place in the edge and scrape-off layer regions of tokamak devices determines the level of particle and heat fluxes impinging on plasma-facing components, both at the divertor targets and at the first wall. The purpose of the present doctoral thesis work is to contribute to the everlasting gap in the knowledge of the highly non-linear SOL turbulent nature, understanding the correlations between the main machine input parameters and the fundamental properties of the SOL profiles and fluctuations. Two extensive datasets have been acquired on the TCV tokamak, covering a great portion of the machine operational space by varying either the gas fuelling rate from different locations in the vessel or the plasma shaping, at constant plasma current, toroidal field and heating scheme. The transport level and the characteristics of the SOL profiles have been correlated with the α_t turbulence control parameter defined in [Eich *et al* 2020 *Nucl. Fusion* **60** 056016], acting as a proxy for the relative level of resistive ballooning transport against drift wave turbulence. Analysis of the plasma discharges within the gas fuelling scan database has revealed a transition from a type-I ELMy regime to the Quasi-continuous exhaust (QCE) scenario, respectively at low and high divertor dissipation or, equivalently, neutral pressure. Correspondingly, a continuous broadening of both the divertor heat flux and near SOL upstream density profiles have been registered, together with the progressive formation of a density shoulder in the far SOL. These changes have been correlated to an enhancement of the radial filamentary transport level, with blobs becoming bigger and travelling radially faster towards the first wall. The detected filaments have been found to belong mainly to the resistive X-point and resistive ballooning propagation regimes and, as such, they are likely to be disconnected from the target plates, reaching at most only partially into the divertor chamber. In the shaping scan database, the changes in edge safety factor induced by a scan in upper triangularity δ_{up} determine a modification of the α_t parameter towards higher values and thus a more resistive ballooning unstable edge-SOL plasma. Once again, a transition from type-I ELMs to QCE takes place from low to high shaping, the divertor heat load and the near SOL density profile broaden, and a density shoulder forms in the far SOL. These behaviours have been correlated to an enhanced filamentary activity near the first wall, with the average value and standard deviation and the frequency of fast filamentary fluctuation measurements increasing at high plasma shaping. Finally, the work addresses also some indirect effects of δ_{up} on setting the parameters defining α_t, in particular midplane neutral pressure measurements indicate that indirect effects of the shaping on local ionization sources do not play a significant role in setting the far SOL density profile. On the other hand, a significant increase of the total radiated power is observed at high δ_{up}, originating from a higher level of carbon impurity intake from the first wall tiles due to the changes in magnetic topology from low to high shaping.

SOMMARIO

La dinamica turbolenta avente luogo nelle regioni di bordo e scrape-off layer di reattori tokamak determina i flussi di particelle e calore impattanti sui componenti a contatto con il plasma, con una maggiore attenzione rivolta ai target del divertore ed alla prima parete. Lo scopo del presente lavoro di tesi di dottorato è quello di contribuire all'eterna lacuna nella conoscenza della natura turbolenta e altamente non lineare del SOL, comprendendo le correlazioni tra i principali parametri ingegneristici di macchina e le proprietà fondamentali dei profili e delle fluttuazioni nel SOL. Sono stati acquisiti due ampi database sperimentali sul tokamak TCV, in maniera tale da coprire una porzione significativa dello spazio dei parametri della macchina, variando alternativamente la velocità di gas puffing da diversi punti del vessel o la forma del plasma, tenendo costanti la corrente di plasma, il campo toroidale e lo schema di riscaldamento. Le caratteristiche del trasporto e dei profili nel SOL sono state correlate con il cosiddetto parametro di controllo della turbolenza α_t definito in [Eich *et al* 2020 *Nucl. Fusion* **60** 056016], il quale quantifica il livello di turbolenza di tipo resistive ballooning relativamente al trasporto tramite onde di deriva. L'analisi delle scariche di plasma con shaping costante e velocità di gas puffing variabile ha rivelato una transizione di regime da ELM di tipo I ben definiti al cosiddetto regime di Quasi-continuous exhaust (QCE), rispettivamente a bassa ed alta dissipazione nel divertore o, equivalentemente, pressione dei neutri. A questo cambiamento segue un allargamento continuo tanto del profilo di carico termico sul target del divertore, quanto del profilo di densità in prossimità della separatrice attorno al piano mediano, oltre alla formazione progressiva di una spalla di densità nel SOL lontano. Questi cambiamenti sono stati correlati con un aumento del livello di trasporto filamentare in direzione radiale, con filamenti progressivamente più grandi e veloci. I filamenti rilevati appartengono principalmente ai regimi resistive X-point e resistive ballooning, il che costituisce un'indicazione della loro disconnessione dai target e la loro estensione al più parziale all'interno della regione del divertore. All'interno del database con shaping variabile, un cambiamento del fattore di sicurezza al bordo indotto da un diverso valore della triangolarità superiore δ_{up} provoca un aumento di α_t e quindi una maggiore instabilità del plasma di bordo e SOL verso modi resistive ballooning. Si osserva nuovamente una transizione da ELM di tipo I al regime QCE, accompagnata da un allargamento dei profili di carico termico e densità nel SOL vicino e dalla formazione di una spalla di densità nel SOL lontano. Questo comportamento è correlato ad un aumento dell'attività filamentare in prossimità della prima parete attorno al piano mediano, dal momento che misure veloci di fluttuazione acquisiscono un valor medio e una deviazione standard più alti in corrispondenza di un alto shaping. Infine, il lavoro si focalizza sugli effetti indiretti di una variazione di δ_{up} sui parametri che entrano nella definizione di α_t. In particolare, alcune misure di pressione dei neutri attorno al piano mediano suggeriscono che lo shaping non gioca un ruolo dominante nel determinare le sorgenti locali di ionizzazione nel far SOL, le quali contribuiscono localmente alla forma del profilo di densità. D'altro canto, la modifica della topologia magnetica conseguente ad un aumento dello shaping è correlata ad un aumento significativo della potenza irradiata dal core, a causa di un maggior numero di impurità di carbonio estratte dalla prima parete.

PREFACE

THE energy supply for the basic needs of human and social life is one of the most crucial issues to face in the coming decades. In front of the foreseen rise in energy demand, due to the improvements in the quality of life in advanced countries as well as the industrial and economic development of emerging nations, the need for a sustainable, clean, CO_2-free energy mix is nowadays as pressing as it has ever been. Nuclear energy represents a viable option due to its remarkably high energy density, sustainability, reliability and safety, while being one of the sources with the lowest carbon footprint. In this framework, significant progress has been made in research towards the exploitation of controlled thermonuclear fusion, aiming to the generation of electric energy from the fusion of deuterium and tritium nuclei. The requirement of confining a hot plasma for a sufficiently long time, so that enough reactions can take place for the system to be self-heated by the fusion products, represents as of now the main obstacle in achieving net energy gain from the reaction itself.

Within the currently investigated approaches, magnetic confinement is certainly the most advanced scheme towards commercial exploitation of fusion energy. One of the main unsolved challenges in magnetic confinement fusion research is that linked to the proper handling of the particle and power exhaust in the boundary region of plasmas in diverted magnetic configurations. In particular, the divertor targets experience the strongest interaction with the exhausted plasma, especially within operating scenarios performing at a reactor-relevant level like H-mode. It is foreseen that the material limits of the target, in particular the maximum peak heat load of 10 MW/m^2, will be exceeded in reactor-sized devices both during steady-state H-mode phases and during the fast type-I ELM transients. A solution to this problem may be operating the device in high density conditions, which facilitates access to divertor detachment and favours operation in the Quasi-continuous exhaust (QCE) regime, where the stationary peak heat loads are strongly mitigated and the large infrequent ELMs are replaced by a continuous ejection of small bursts into the boundary region, called scrape-off layer (SOL). A proper understanding of the SOL dynamics is crucial for safe high density H-mode tokamak operation, yet the fusion research community is still far from achieving a full comprehension of the transport phenomena in the scrape-off layer due to it being strongly anomalous and non-linear in nature. The main motivation behind this doctoral dissertation thesis is to help filling in the gap in the knowledge of the relationship between the main input operating conditions and the fundamental characterizing properties of the SOL plasma profiles and turbulent fluctuations behaviour.

To this aim, two extensive experimental datasets have been acquired on the TCV tokamak, covering a large part of the operational space in terms of both separatrix density and edge safety factor. The first database consists of a set of high density, highly shaped H-mode discharges in a baffled TCV vessel configuration, with the aim of assessing the effects of increasing divertor neutral pressure on the properties of inter-ELM profiles and transport. The transition towards a more dissipative divertor state, achieved by a scan in the gas puffing rate, is accompanied by an increase of the separatrix density and a change in the operating regime from type-I ELMs to QCE. The level of transport and the SOL profile features have been correlated with the α_t turbulence control parameter introduced in [Eich *et al* 2020 *Nucl. Fusion* **60** 056016], which quantifies the strength of resistive ballooning turbulence with respect to drift wave transport. Analysis of these pulses has revealed a general broadening of the upstream SOL profiles at increasing α_t, in terms of a continuously increasing divertor heat load fall-off length and near SOL density *e*-folding length. In the far SOL a density shoulder is seen to progressively form and increase in amplitude. These modifications are accompanied by the enhancement of the turbulent transport level, with larger filamentary coherent structures being expelled from the edge region, travelling radially faster towards the first wall. The detected filaments have been found to be pertaining to the resistive X-point and resistve ballooning regimes of propagation, thus they are presumed to be mostly disconnected from the divertor target. While the observed divertor broadening is beneficial for the survival and preservation of the target materials, the density shoulder formation and associated increase in filamentary activity may pose some risk for the safety of the first wall plasma-facing components around the midplane towards excessive heat load or erosion processes.

The second dataset is composed of TCV plasma discharges in which the upper triangularity has been varied, while keeping all the other engineering inputs constant. The shaping scan comprises plasmas with values of δ_{up} ranging between 0 and 0.6, excluding negative values. This scan results in a variation of the edge safety factor, thus a shift of the α_t parameter towards higher values, indicating a larger level of interchange turbulence at high shaping. Once again, a transition takes place from well-defined type-I ELMs at low shaping to fully established QCE at high shaping. As for the fuelling scan experiment, the divertor heat load broadening, the flattening of the density gradient near the separatrix and the formation of a density shoulder in the far SOL are all recovered when moving from low to high δ_{up}. These behaviours have been related to a more intense filamentary activity in the proximity of the first wall, as measured by wall-mounted Langmuir probes as well as the Thermal Helium Beam diagnostic. In particular, the average and standard deviation of the fast fluctuation measurements from the two diagnostics shift towards larger values, with filaments being generated and expelled more frequently from the separatrix towards the first wall at high plasma shaping. Indirect effects of the upper triangularity on other quantities influencing α_t, like the level of recycling at the main chamber walls, the neutral particles population density and the total impurity content were studied by means of discharges at the extreme δ_{up} values, with otherwise the same input quantities. It is shown that the midplane neutral pressure does not change greatly during the H-mode phase of the discharges, suggesting that indirect effects of the shaping on neutral particle ionization sources should indeed play a marginal role. Instead, an increase of the total core radiated power is observed at high δ_{up} owing to a higher level of carbon impurity intake from the first wall, likely associated to both the enhanced fluctuation level, a smaller outer gap and the change in magnetic topology towards a close-to-double-null geometry at high plasma shaping.

1

INTRODUCTION

THIS introductive chapter will address the energy supply issue and present nuclear fusion power as a possible solution. In section 1.1 an overview of the main fusion reactions is given, along with the main parameters for their characterization. Section 1.2 introduces magnetic confinement fusion and makes a description of the tokamak device. In section 1.3 the plasma boundary region is outlined and the particle and energy exhaust problem is introduced. Section 1.4 discusses the steady-state and transient exhaust control issues encountered in the H-mode confinement regime, together with an alternative regime as a possible solution. As a last point, section 1.5 contains the scope and the main goals of the present doctoral project, as well as an outline of this manuscript.

1.1 CONTROLLED THERMONUCLEAR FUSION

Energy, in its every form, is a critical resource needed in all human activities, from the food sector to industrial production. On this regard, providing a safe, clean and reliable energy supply for this and the next centuries is one of the most outstanding open points currently undergoing intense research effort. While on the one hand the energy demand will inevitably grow in the next years, due to both an increase in world population and further economic advancements of developing countries, on the other hand the increasingly pressing need to tackle climate change issues pushes more and more towards the full exploitation of carbon-free energy sources. According to the 2021 International Energy Outlook report by the U.S. Energy Information Administration [1], the overall world energy consumption will rise by approximately $\sim 50\%$ by the year 2050 with respect to

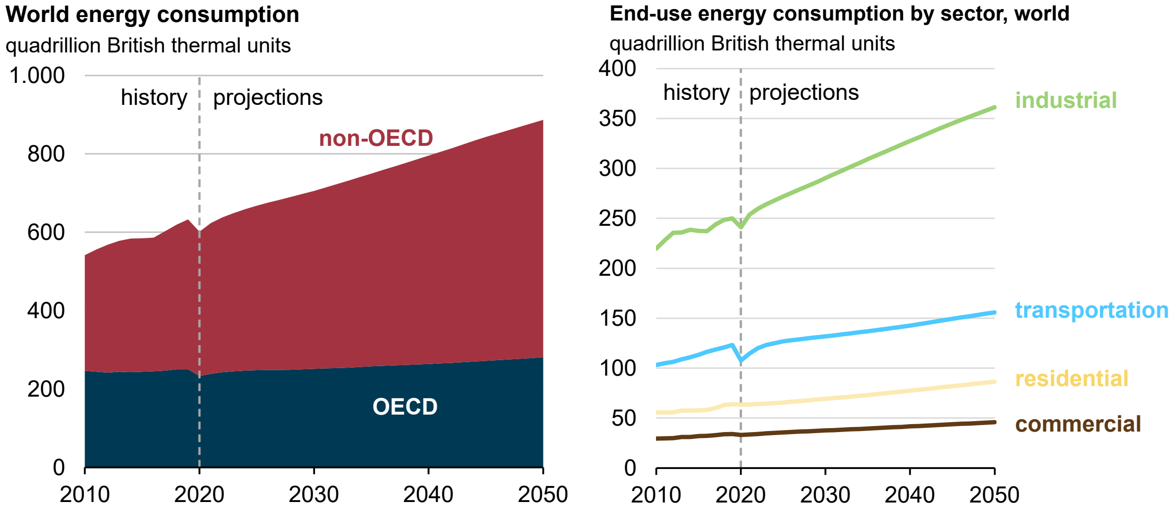

Figure 1.1: Left: historical and foreseen world energy consumption, in quadrillion Btu, for OECD and non-OECD countries from 2010 to 2050. Right: world energy consumption by sector. Adapted from [1].

2020. As shown in figure 1.1, the largest share of this increase pertains to nations which are not part of OECD (*Organization for Economic Co-operation and Development*) and is foreseen to be determined mainly by the expansion of industrial activities.

While most developed countries are starting to shift the majority of their energy production towards renewable sources, these cannot be fully suited to deliver a reliable base-load power with minimal greenhouse gas emission, due to their intrinsic dependence on weather patterns. Among the available energy production methods, nuclear power will inevitably have to be considered of utmost relevance for this century's energy transition due to having one of the lowest carbon footprints among all energy sources while providing a safe and reliable power output. Moreover, the extremely high energy density of nuclear fuels leads to a power output per single reaction millions of times higher than fossil sources, ensuring that a much lower mass of waste products is produced.

The countries that have developed a domestic nuclear energy program rely so far only on nuclear fission power plants. In the core of these facilities a *nuclear fission* reaction takes place, in which a heavy nuclide such as $^{235}_{92}$U or $^{239}_{94}$Pu is split into two lighter elements after absorbing a neutron. The opposite process is *nuclear fusion*, in which two light elements collide and merge, forming a heavier nuclide. Both processes can be visualized in figure 1.2, showing the binding energy per nucleon as a function of the nuclide mass number. Nuclides with $A \sim 60$ have the highest binding energy per nucleon, thus they are the most stable ones. Given that a higher nuclear binding energy is associated to an overall lower nuclide mass with respect to that of its single nucleons combined, by the well-known Einstein energy-mass relation $\Delta E = \Delta mc^2$, a net release of energy can be obtained

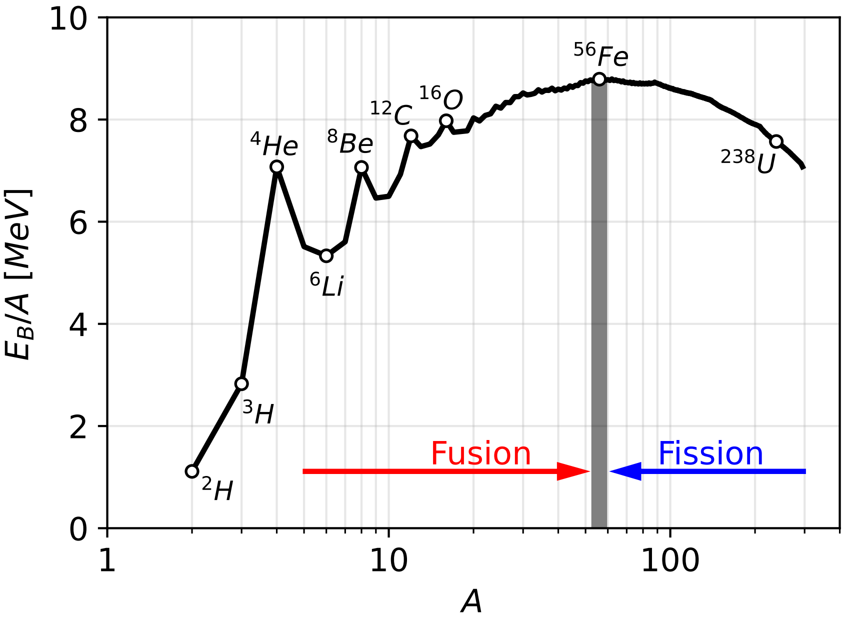

Figure 1.2: Binding energy per nucleon E_B/A as a function of the nuclide mass number A. The plotted curve represents the nuclides having the highest E_B/A at a given value of A. Data source: NNDC NuDat3 database [2].

by transmuting a nuclide from either end of the curve towards its maximum. For fission reactions the difference in E_B/A is fairly small ($\lesssim 1$ MeV), however the large number of nucleons involved in the process ensures an average energy yield of $\sim$ 200 MeV per single reaction. Much fewer nucleons are involved instead in fusion processes, however the typical reaction releases between $\sim$ 3 and $\sim$ 20 MeV. Considering that some of the highest yields are associated to reactions involving isotopes of hydrogen (see section 1.1.1), fusion reactions can potentially release even more energy than fission per unit of mass.

One of the most prominent physical challenges to solve in order to achieve net power from fusion reactions is the electrostatic potential barrier between the two interacting positively charged particles, which must be overcome for the nuclei to fuse. For this purpose, kinetic energies of the order of $\sim$ 10 keV or more must be provided to the particles in the form of thermal energy, corresponding to temperatures of $\sim 10^8$ °C. At this temperature values the atoms cannot hold on to their less bound electrons and get ionized, forming a *plasma* [3]. The process of generating energy from fusion reactions in a hot plasma is known as *thermonuclear fusion* and has been firstly exploited in the second half of the 20th century for military purposes, becoming in the meantime the subject of one of the currently most intense research endeavours for civil applications. The outstanding issues in confining a plasma at these temperature values are ultimately the bottleneck preventing, as of now, the exploitation of nuclear fusion reactions as a commercially viable source of energy.

I.I.I FUSION REACTIONS

In the universe, fusion reactions ordinarily take place inside the core of stars with mass similar to or lower than that of the Sun through the so-called *proton-proton chain*, resulting in the transmutation of four protons and two electrons into an alpha particle (i.e. a ${}^4_2\mathrm{He}$ nuclide). The 26.7 MeV mass defect of this process is the highest among all fusion reactions and is released in the form of light and kinetic energy of the products. Nevertheless, given the long characteristic times associated to it, this reaction requires stellar-like masses and timescales to proceed, making it unfeasible for reproduction on Earth.

A few candidate processes for laboratory exploitation still rely on hydrogen isotopes, like deuterium (D) and tritium (T). Some of these are

$$\mathrm{D} + \mathrm{D} \rightarrow \begin{cases} {}^3_2\mathrm{He} + \mathrm{n} + 3.27\,\mathrm{MeV} & \sim 50\% \\ \mathrm{T} + \mathrm{p} + 4.03\,\mathrm{MeV} & \sim 50\% \end{cases},$$

$$\mathrm{D} + {}^3_2\mathrm{He} \rightarrow {}^4_2\mathrm{He} + \mathrm{p} + 18.3\,\mathrm{MeV},$$

$$\mathrm{D} + \mathrm{T} \rightarrow {}^4_2\mathrm{He} + \mathrm{n} + 17.6\,\mathrm{MeV}.$$

For a generic nuclear fusion process with monoenergetic species, the volumetric reaction rate R_{AB} depends on the particle densities of the interacting populations n_A and n_B, their relative velocity $v = \|\mathbf{v}_A - \mathbf{v}_B\|$ and the fusion reaction cross-section σ_{AB} through the equation $R_{AB} = n_A n_B \sigma_{AB} v$. Since the particles in a plasma are not monoenergetic, this relation must be generalized to yield

$$R_{AB} = n_A n_B \langle \sigma v \rangle_{AB}. \tag{1.1}$$

The quantity $\langle \sigma v \rangle_{AB}$ is called fusion reactivity, with the average calculated over a given velocity distribution function. At thermodynamic equilibrium the relative velocities of the particles are distributed according to a Maxwell-Boltzmann function and the reactivity is given by

$$\langle \sigma v \rangle = \frac{4}{\sqrt{2\pi\mu T^3}} \int_0^\infty \sigma(E_{CM}) E_{CM} \exp\left(-\frac{E_{CM}}{T}\right) dE_{CM} \tag{1.2}$$

with μ the reduced mass of the colliding particles, E_{CM} their relative kinetic energy in the center-of-mass reference frame and T the temperature of the system in eV. The cross sections and the

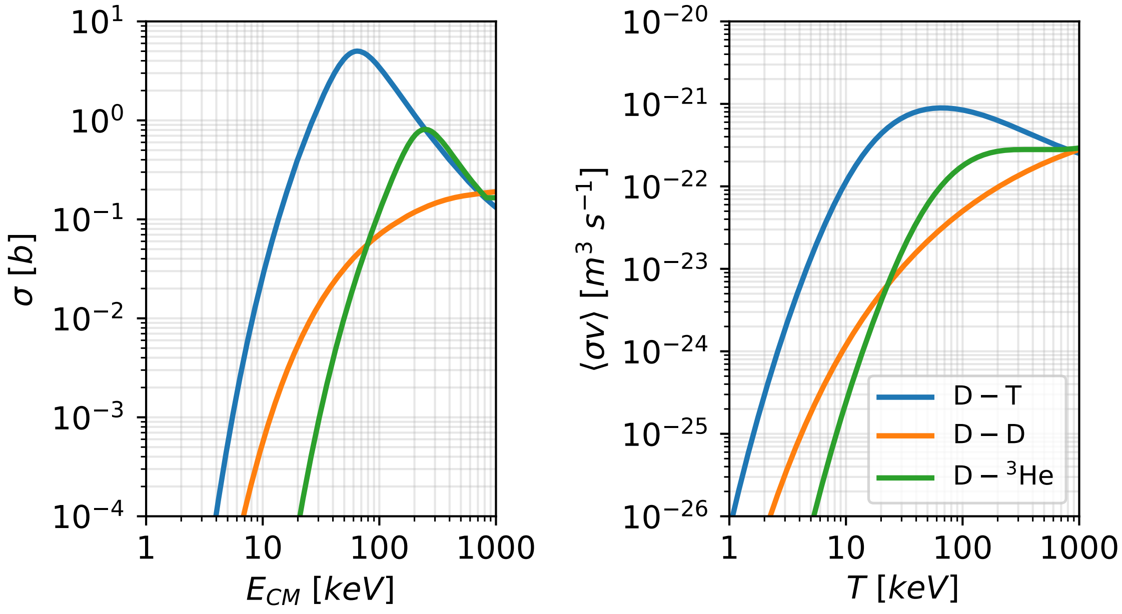

Figure 1.3: Left: cross sections of the D − T, D − D and D − $^{3}_{2}$He reactions, with the abscissa being the relative kinetic energy of the interacting particles in the center-of-mass reference frame. The cross sections are measured in *barns* (b), where $1\ \mathrm{b} = 10^{-28}\ \mathrm{m}^2$. Right: fusion reactivities of the same reactions as a function of temperature. Data source: ENDF/B-VIII.0 database [4, 5].

reactivities for each of these reactions are represented in figure 1.3. The D − T process is characterised by the maximum reactivity at a temperature of $T \sim 50$ keV, which is also the lowest value at which the maximum occurs for the three reactions. For this reason, the D − T reaction is currently taken under consideration for commercial exploitation.

While deuterium is widely available in every hydrogen-containing chemical species, making it possible to be extracted from Earth's waters, tritium management is more challenging. Since it is a radioactive isotope of hydrogen with a half-life of ∼ 12 years, it occurs only in trace concentration in nature because of the interaction of cosmic rays with the uppermost parts of the atmosphere. It is produced artificially in pressurized water fission reactors via interaction of thermal and fast neutrons with the moderator and absorber materials, but again the yield is too low for powering a fusion power station. Breeding tritium from lithium can be a possible solution, exploiting the two reactions

$$^{6}_{3}\mathrm{Li} + \mathrm{n} \rightarrow {}^{4}_{2}\mathrm{He} + \mathrm{T} + 4.80\,\mathrm{MeV}$$

$$^{7}_{3}\mathrm{Li} + \mathrm{n} \rightarrow {}^{4}_{2}\mathrm{He} + \mathrm{T} + \mathrm{n} - 2.50\,\mathrm{MeV}$$

where the first one is exothermic and the second one is endothermic. Given the abundance of both deuterium and lithium within Earth's crust, the D – T reaction could potentially provide a virtually limitless energy source for the next centuries.

1.1.2 POWER BALANCE IN A FUSION REACTOR

In order for a fusion reaction to be self-sustained and thus viable in a power station, the generated thermonuclear fusion power must balance at all times the energy loss terms. At steady state, the energy balance in a hot D – T plasma with additional external heating mechanisms reads

$$S_{heat} + S_{\alpha} = S_B + S_{th}. \tag{1.3}$$

S_{heat} denotes the thermal power injected into the plasma by means of auxiliary heating systems. The S_{α} term represents the volumetric power deposited by the generated alpha particles into the plasma. It must be kept in mind that not all energy generated by the D – T reactions is converted to plasma heating: part of this energy goes to fast neutrons, which are electrically neutral and therefore escape from the confined plasma without interacting with it. From momentum balance it follows that, out of the $E_{DT} = 17.6$ MeV reaction yield, only $E_{\alpha} = 3.5$ MeV is carried by the alphas. The volumetric alpha heating term, assuming equal deuterium and tritium particle densities $n_D = n_T = n/2$, is therefore given by

$$S_{\alpha} = \frac{1}{4} n^2 \langle \sigma v \rangle E_{\alpha}. \tag{1.4}$$

The S_B term represents the energy emitted by radiative processes taking place in a hot plasma. These include the line radiation associated to transitions of excited neutral or partially ionized impurities towards their ground state, as well as the cyclotron radiation due to particle motion in a magnetic field which, in the case of a magnetic confinement fusion device (see section 1.2), is however reabsorbed by the plasma. However, usually the dominating contribution is represented by *bremsstrahlung* radiation due to electron-ion Coulomb collisions. It can be shown that

$$S_B = c_B Z_{eff} n_e^2 T_e^{1/2} \tag{1.5}$$

with $c_B = 3.34 \cdot 10^{-21}$ m^3 s^{-1} keV$^{1/2}$ a numerical constant. The presence of multiple ion species with which the electrons collide is taken care of in equation 1.5 by the effective ion charge, defined exploiting the plasma charge quasi-neutrality as

$$Z_{eff} = \frac{\sum_j Z_j^2 n_j}{n_e} \tag{1.6}$$

where the sum is performed over all ion species. Physically, its role is to reduce a multi-component plasma with various atomic numbers Z_j down to a single-species system in which the ions have an equivalent atomic number Z_{eff}.

The term S_{th} embodies the thermal losses of a plasma, due to the conductive and convective transport of particles and energy associated with the coherent and thermal motions of the particles at various temporal and spatial scales. By defining the average plasma pressure as $p = nT$, the thermal loss power density can be written as

$$S_{th} = \frac{3p}{\tau_E} \tag{1.7}$$

where τ_E is a phenomenological timescale known as *energy confinement time*. In practice, τ_E is currently one of the most difficult quantities to predict in thermonuclear plasma physics research. It is often determined via empirical scalings, regressed over extensive datasets obtained over the timespan of various decades on a multitude of research devices.

Ideally, in a fusion power plant the alpha heating is able to balance all the loss terms without any external sources. A first working condition for a thermonuclear plasma at steady state is that the fusion power must be able to replenish at least the radiative losses, i.e. $S_\alpha = S_B$. This condition, called *ideal ignition*, is translated directly onto a lower operational limit on the plasma temperature in a fusion reactor, which for a 50-50 $\mathrm{D-T}$ mixture with no impurities is ~ 4.3 keV. The point at which instead the full power balance is satisfied, including also thermal losses, is called *ignition*. Considering flat density and temperature profiles, or taking into account only their average value, the ignition condition is given by the so-called *Lawson criterion* [6]

$$nT\tau_E \geq \frac{12\, T^2}{\langle\sigma v\rangle E_\alpha - 4c_B Z_{eff} T^{1/2}}. \tag{1.8}$$

where the quantity $nT\tau_E$ is often called *triple product*. The ignition threshold for the other reactions listed in section 1.1.1 can be derived in a similar fashion, keeping in mind that the deposited fusion power for the $\mathrm{D-D}$ reaction presents a factor $1/2$ instead of $1/4$ to avoid double counting reactions. Figure 1.4 shows the ignition threshold for all considered reactions, together with their ideal ignition limit. All the curves are characterised by a temperature at which the threshold triple product is minimum, and thus ignition is the easiest to attain. The $\mathrm{D-T}$ process is seen once again to be the most advantageous, being characterised by the lowest triple product threshold. Assuming parabolic profiles, the Lawson criterion for the peak density and temperature values around the minimum triple product is

$$nT\tau_E \gtrsim 5 \cdot 10^{21}\mathrm{m}^{-3}\,\mathrm{s\,keV}, \tag{1.9}$$

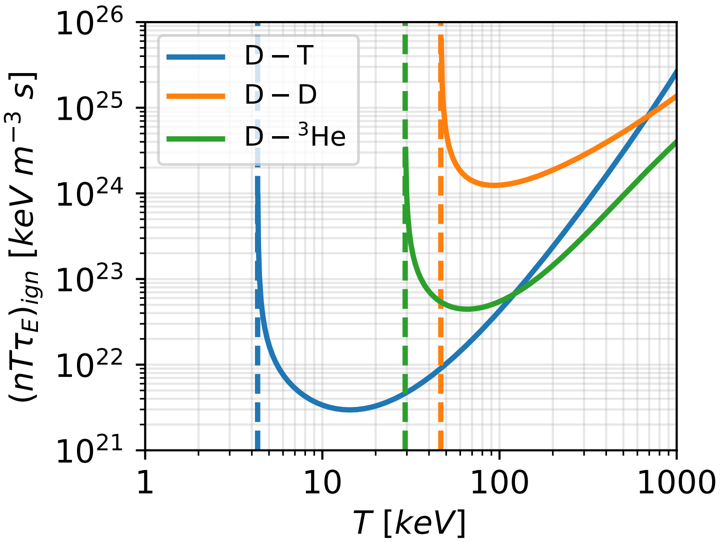

Figure 1.4: Triple product at ignition threshold for the D − T, D − D and D − $^3_2$He reactions, as a function of the temperature of the system, assuming equal particle densities for the two reacting species. The vertical dashed lines indicate the ideal ignition operational limit for each reaction.

achievable with $T \sim 14$ keV, $n \sim 10^{20}$ m^{-3} and $\tau_E \sim 3.5$ s. No device so far has been able to reach neither the required plasma temperature nor the ignition threshold, even if progressive but significant improvements have been made in the last decades.

In presence of applied external heating, a figure of merit for the performance of the device is the ratio between the produced fusion power and the supplied energy

$$Q = \frac{S_{fus}}{S_{heat}} \tag{1.10}$$

where S_{fus} includes also the energy to fast neutrons, which is assumed to be fully recovered in a reactor. From the engineering point of view, in a fusion power station equation 1.10 must be modified in order to account for the net input and output electric energy, yielding

$$Q_{eng} = \frac{P_{el,out} - P_{el,in}}{P_{el,in}}. \tag{1.11}$$

The Q parameter is more related to physics considerations, with $Q = 1$ when the fusion power breaks even with the externally provided heating and $Q = \infty$ when ignition is achieved with no external sources. The record for the highest steady state fusion power achieved in a single experiment currently belongs to the *Joint European Torus* (JET), with $\sim$ 11 MW obtained for 5 s and $Q \sim 0.35$

[7]. Most recently, break-even has been achieved and surpassed at the *National Ignition Facility* (NIF) in the U.S. with $\sim$ 3.15 MJ of energy released by the reaction out of $\sim$ 2.05 MJ delivered to the fuel, corresponding to $Q \sim 1.54$ [8]. The Q_{eng} parameter instead takes into account the numerous efficiency factors arising both when delivering the external heating to the plasma and when converting the extracted thermal energy into electrical energy through a proper thermodynamic cycle. For the technology to be economically viable, a minimum $Q_{eng} = 10$ is required for a fusion power plant.

1.2 MAGNETIC CONFINEMENT FUSION

From the physical point of view, the Lawson criterion establishes the minimum number of reactions needed so that a positive power balance can be reached in a fusion plasma. However, the combination of choices that can be made to achieve the threshold triple product remains a free parameter, so that for instance the required energy confinement time τ_E is known only once the average plasma pressure $p = nT$ is given. Different combinations of parameters correspond to different methods of plasma confinement, with the same objective of realising enough fusion reactions. Being gravitational confinement clearly unfeasible on Earth, the two currently most investigated laboratory approaches are magnetic and inertial confinement fusion.

Within the *inertial confinement fusion* (ICF) approach [9, 10] no confinement is attempted at all on the plasma. Instead, a sub-mm spherical pellet of $\mathrm{D-T}$ mixture at the triple point of hydrogen is adiabatically compressed by a collection of high-intensity laser pulses with an isotropic power deposition profile. Ignition is reached once the fuel mixture in the pellet centre is compressed at such a point as to reach thermonuclear conditions. In this situation, the energy confinement time is limited within a few ns only by the inertia of the hot $\mathrm{D-T}$ mixture, so that for a temperature $T \sim 14$ keV the central density and pressure reach extreme values at, respectively, $n \sim 10^{29}\ \mathrm{m}^{-3}$ and $p \sim 8$ Gbar. This scheme is adopted especially in research facilities in the U.S., where laboratories such as the NIF are located.

The *magnetic confinement fusion* (MCF) approach is currently the most scientifically advanced and exploited confinement scheme in Europe, with the energy confinement time $\tau_E \sim 1$ s and the plasma pressure $p \sim 8$ bar. In order to contain the plasma within a fixed volume, keeping it far from direct contact with any material surface, a proper combination of externally imposed magnetic fields is used. Being electrically charged, the plasma particles are subject to the Lorentz force $\mathbf{F} = q\mathbf{v} \times \mathbf{B}$ acting perpendicular to their motion direction. Under the influence of this force, the charged particles motion parallel to the magnetic field is unaffected whereas the perpendicular component of their orbit follows a uniform circular motion, called *gyromotion*, with radius and angular frequency

$$\rho_L = \frac{mv_\perp}{|q|\,B}, \qquad \Omega_c = \frac{|q|\,B}{m} \tag{1.12}$$

where the velocity $v_\perp$ is of the order of the particles' thermal velocity. The quantities ρ_L and Ω_c are known, respectively, as *Larmor radius* and *cyclotron frequency*.

On small enough time scales the instantaneous motion of plasma particles in an external magnetic field is effectively constrained along the direction perpendicular to **B**, within a maximum displacement of the order of the Larmor radius. Conversely, it can be shown that on time scales much longer than Ω_c^{-1} the gyromotion averages out, leaving only the particles' *guiding centre* moving at constant parallel velocity or, in presence of an electric field **E**, with a parallel acceleration proportional to $E_\parallel$. The remaining leading-order contribution to the perpendicular component of the guiding centre orbit is given by a charge-independent term called $\mathbf{E} \times \mathbf{B}$ drift:

$$\mathbf{v}_E = \frac{\mathbf{E} \times \mathbf{B}}{B^2}. \tag{1.13}$$

The trajectory along the parallel direction is still left unconstrained, meaning that in a cylindrical geometry with axially-directed parallel magnetic field lines most particles would be lost at either end of the plasma column. A solution to this issue is to bend the field lines in a toroidal configuration, so that the whole system is confined inside a torus-like volume where the toroidal magnetic field is generated by a set of so-called *toroidal field coils*. While it solves the end losses issue, this solution implies different challenges to be addressed. Indeed, from Ampère's law $\nabla \times \mathbf{B} = \mu_0 \mathbf{j}$ it follows that the toroidal field magnitude is inversely proportional to the radial distance from the torus central axis and that the field lines are curved around the toroidal direction. At first order in the gyromotion a further perpendicular drift arises, called *magnetic drift*

$$\mathbf{v}_{magn} = \frac{m}{q}\left(\frac{v_\perp^2}{2} + v_\parallel^2\right)\frac{\mathbf{B} \times \nabla B}{B^2} \tag{1.14}$$

due to both the radial gradient of the toroidal field magnitude and the field line curvature. Notably, this drift is charge-dependent and gives rise to a vertical charge separation between the electrons and ions, therefore to an electric field. This is accompanied by an outwards radial $\mathbf{E} \times \mathbf{B}$ drift, which would effectively prevent confinement along the radial direction with only a toroidal field component. A further magnetic field component must be thus added along the *poloidal direction*, binormal to both the toroidal field and the radial directions, so that the resulting field lines wind around the torus surface in a helical fashion. The resulting alternating vertical motion pattern of the charged particles compensates for the macroscopic ∇B drift effects. The full derivation of particle drifts in an external electromagnetic field is summarized in appendix A.

1.2.1 The tokamak device

Depending on how the poloidal field component is generated, different magnetic confinement schemes have been devised, with the most important ones having a toroidal field magnitude several times higher than the poloidal field magnitude. In the case of a *stellarator*, both components of the magnetic configuration are generated by means of properly shaped magnetic field coils. An example of such a configuration is represented by the *Wendelstein 7-X* device in Greifswald, Germany, which has recently achieved promising results in high-performance plasma scenarios [11].

The configuration considered in this work is the *tomakak* [12], schematized in figure 1.5. Contrary to the stellarator, in this device only the toroidal field is generated by means of properly designed toroidal field coils, whereas the poloidal component is generated by a large *plasma current* flowing in the toroidal direction. The plasma current, in turn, is driven by a central solenoid acting as the primary circuit of a transformer, where the secondary circuit is instead represented by the conductive plasma itself. The time variation of the current in the central solenoid is translated into a voltage drop along the toroidal direction due to the Faraday-Neumann-Lenz law.

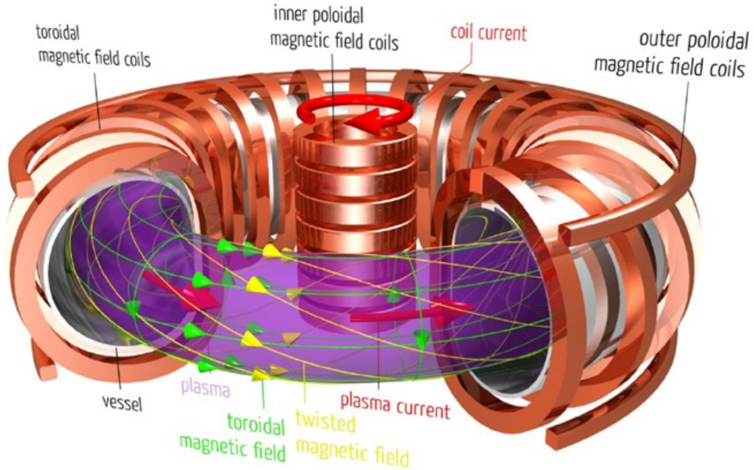

Figure 1.5: Schematic representation of the tokamak configuration. The toroidal and poloidal field coils, including the central solenoid, are shown in copper colour. The big red arrows at the centre of the plasma column (in purple) symbolizes the plasma current induced by the central solenoid. The toroidal and total magnetic fields are represented, respectively, by means of green and yellow field lines.

On top of the field generated by the plasma current, additional poloidal field coils are often used to stabilize and shape the plasma column within the tokamak chamber. The resulting magnetic configuration is axisymmetric, meaning that it is invariant with respect to a rotation around the toroidal direction.

The tokamak configuration remains the most scientifically exploited and advanced magnetic confinement fusion device to date, with a great number of both current and next generation fusion facilities being based on this scheme. Among the latter it is worth mentioning ITER (*International Thermonuclear Experimental Reactor*) [13], with the purpose of demonstrating net thermal energy gain from the $D-T$ reaction in a MCF device, and DEMO [14], aiming to prove fusion power feasibility for electric energy production. Given the necessity of maintaining an induced plasma current, however, the operation of a tokamak is intrinsically pulsed. The duration of a tokamak plasma discharge is constrained by either the physical limits of the toroidal field coils, or the maximum current that can be provided to the central solenoid by the power supplies. A typical discharge duration is of the order of several seconds, in contrast with the $\sim$ 1000 seconds requirement for ITER and the continuous operation constraint for DEMO and any other fusion power plant. Stellarators are not affected by this issue since no magnetic field component is of inductive nature, nevertheless their engineering complexity is far greater than that of tokamaks due to the particular shape of the field coils. Part of the current research efforts are pushing towards a steady-state tokamak scenario.

1.2.2 AXISYMMETRIC TOKAMAK EQUILIBRIA

The main operational parameters of a tokamak arise from the knowledge of the topology of the magnetic field lines, i.e. their spatial distribution and arrangement inside the torus chamber. The requirement for a static equilibrium is translated into a force balance between the magnetic force density and the kinetic pressure gradient through the *ideal magnetohydrodynamic* (MHD) equilibrium equation

$$\nabla p = \mathbf{j} \times \mathbf{B} \tag{1.15}$$

where p and $\mathbf{j}$ are, respectively, the pressure and current density distributions in the plasma volume. It results from this equation that $\mathbf{B} \cdot \nabla p = 0$, i.e. the magnetic field lines lie on nested magnetic surfaces identified with the contour surfaces of the pressure profile. Exploiting Gauss' law $\nabla \cdot \mathbf{B} = 0$ and the axial symmetry of the magnetic field one can write also $\mathbf{B} \cdot \nabla \psi = 0$, having introduced the poloidal flux function ψ representing the poloidal magnetic flux lying within a given magnetic surface. The resulting full expression for the equilibrium magnetic field is

$$\mathbf{B} = \frac{1}{R} \nabla \psi \times \mathbf{e}_\phi + B_\phi (R) \, \mathbf{e}_\phi \tag{1.16}$$

where the right-handed cylindrical coordinate system (R, ϕ, Z) is used as illustrated in figure 1.6, with R and Z respectively the major radius and elevation coordinates, and ϕ the toroidal angle. By

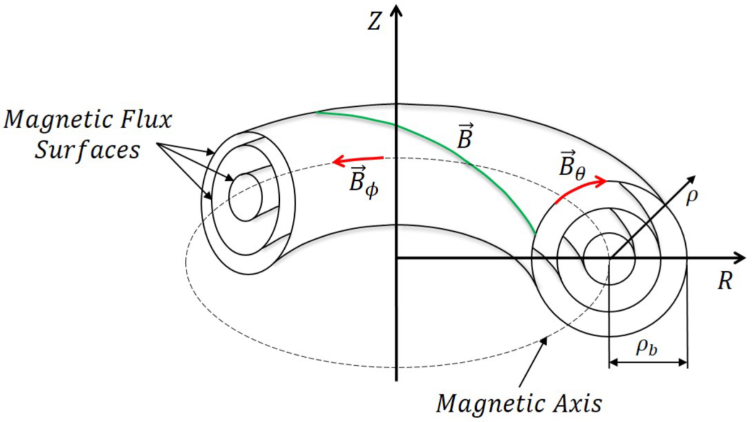

Figure 1.6: Nested magnetic flux surfaces in a tokamak configuration, together with the associated cylindrical coordinate system. Reproduced from [17].

manipulating equation 1.15 together with Gauss' and Ampère's laws an equation for the poloidal flux function can be derived

$$R\frac{\partial}{\partial R}\left(\frac{1}{R}\frac{\partial\psi}{\partial R}\right)+\frac{\partial^2\psi}{\partial Z^2}=-\mu_0 R^2\frac{dp}{d\psi}-F\frac{dF}{d\psi} \tag{1.17}$$

called Grad-Shafranov equation [15, 16]. The functions $p = p\left(\psi\right)$ and $F = F(\psi) = RB_\phi$ effectively act as degrees of freedom, having to be specified beforehand in order to solve the equation.

1.2.3 Main tokamak operational parameters and limits

Several quantities can be defined starting from the knowledge of the poloidal flux function ψ, some of which are greatly relevant for the operation of a tokamak and the stability of the underlying magnetic equilibrium. In the first place, the differential advancement of a given field line along the toroidal direction ϕ with respect to the corresponding one along the poloidal direction θ is described by the *safety factor* q. In the infinite aspect ratio limit, that is $a/R_0 \ll 1$ with a and R_0 respectively the tokamak minor and major radii, one has

$$q\left(r\right)=\frac{rB_\phi\left(r\right)}{RB_\theta\left(r\right)}. \tag{1.18}$$

The safety factor plays a crucial role in the stability of the magnetic equilibrium. Indeed, some disruptive *current-driven* MHD instabilities take place when the safety factor at the minor radius is $q\left(a\right) \leq 2$ [18, 19], therefore setting an upper boundary on the maximum tolerable plasma current at fixed toroidal field and machine size.

A further important operational quantity is the normalized pressure or so-called *beta parameter* $\beta = 2\mu_0 p/B^2$, quantifying the performance of the magnetic field in confining a plasma with a given pressure profile. This parameter is also relevant in assessing the plasma stability towards major *pressure-driven* modes (caused by the coupling between a strong pressure gradient and magnetic field line curvature) or mixed current-pressure driven modes. In particular, a stability limit holds on the so-called *normalized beta* or *Troyon factor* [20]

$$\beta_N = \beta\,[\%]\,\frac{a\,[\mathrm{m}]\,B_\phi\,[\mathrm{T}]}{I_p\,[\mathrm{MA}]}. \tag{1.19}$$

In most current devices β_N values higher than ~ 3.5 cannot be obtained, with very few exceptions.

Finally, an operational boundary is imposed on the maximum averaged plasma density, above which a tokamak discharge cannot be sustained anymore without loss of confinement or even a disruption. This *density limit* has been first quantified by an empirical scaling law found by Greenwald et al [21]:

$$n_{GW}\left[10^{20}\,\mathrm{m}^{-3}\right] = \frac{I_p\,[\mathrm{MA}]}{\pi\,(a\,[m])^2}. \tag{1.20}$$

The physical origin of this limit is not yet fully understood. One of the most credited explanations suggests it is triggered by an excessive cooling of the plasma near the tokamak boundary at very high density, leading to enhanced radiation in this region and ultimately to a collapse of the discharge. An extensive list of the currently available theory-based scaling laws for the density limit, also expanding on other dependencies not reported in equation 1.20, is given in [22] and references therein.

1.3 THE POWER EXHAUST PROBLEM

At steady state the total input power in a tokamak must be entirely lost to the machine boundary. As a consequence, the plasma-facing components (PFCs) and the first wall may be subject to quite harsh interactions with the hot plasma itself, sometimes leading to unbearable power loads on the materials. For future fusion devices, a widely accepted upper boundary on the maximum heat flux to actively cooled PCFs and wall in stationary conditions is ~ 10 MW/m^2 [23]. Above this limit the PFCs material may start to be excessively eroded or melted, or even undergo recrystallization in case of tungsten components. To this day, the *power exhaust* issue remains one of the most challenging unsolved points of magnetic confinement fusion research, involving multiple aspects from plasma physics to materials science.

The most widely adopted heat exhaust solution in current and future fusion facilities is the *divertor*. This solution is realized by flowing a current in an external poloidal field coil with the same sign as

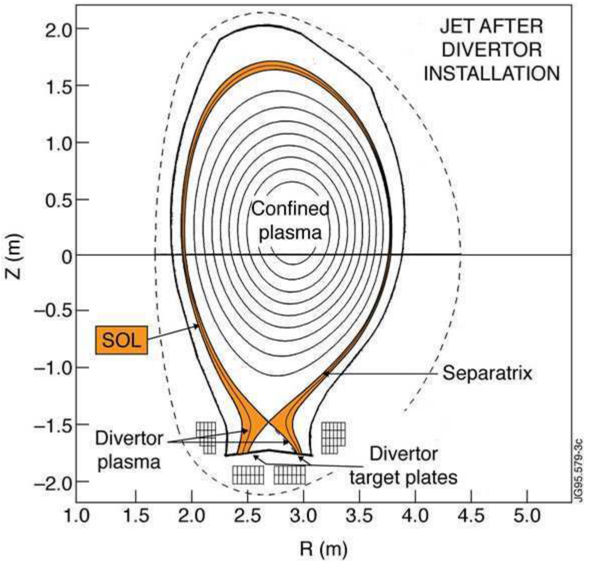

Figure 1.7: Poloidal cross section of a diverted magnetic configuration in the JET tokamak. Adapted from [24].

the plasma current, so that a poloidal magnetic field null arises inside the torus chamber. This null is called *X-point* and the flux label associated to it represents a radial coordinate separating closed magnetic surfaces, inside which the plasma is confined, from open field lines directed towards dedicated target plates. The flux surface on which the X-point is located is called *last closed flux surface* (LCFS) or *separatrix*. The divertor targets have to be designed specifically to withstand high heat fluxes and particle sputtering, and have to be placed at a safe distance from the confined plasma so that the latter is not polluted by the eroded impurities. An example of diverted magnetic configuration is shown for a JET plasma discharge in figure 1.7. The region indicated in orange, constituted by all and only the magnetic field lines laying on open flux surfaces, is called *scrape-off layer* (SOL). The physics taking place in the scrape-off layer ultimately sets not only the boundary conditions for the main confined plasma, but also the particle and heat loads impinging onto the divertor plates and first wall components. For this reason, the dynamics taking place in the scrape-off layer is one of the most investigated sectors of plasma physics.

1.4 The high confinement mode

Another major point to be addressed when operating a tokamak device, and one very closely related to that of SOL and boundary physics, is the issue of plasma confinement. Indeed, according to equation 1.8 a high energy confinement time τ_E is desirable in order to reach ignition, but unfortunately as of today no solid theoretical ground exists to estimate its value, due to the high complexity of the phenomena underlying thermal losses.

In past experiments on the ASDEX device it has been found that, by providing external heating above a certain threshold, the plasma confinement abruptly improves and an *edge transport barrier* is formed [25]. A region arises in the vicinity of the separatrix, called *pedestal*, in which the density, temperature and pressure profiles are characterized by a strong radial gradient. This operating scenario is generally called high confinement mode or *H-mode*, to be distinguished from the *L-mode* regime of operation in which the confinement is worse and no edge transport barrier is present. It is experimentally estimated that the energy confinement time in H-mode is higher than in L-mode by a factor ~ 2, making for this reason the former as the reference operating scenario for ITER [27] and future fusion devices. The power threshold for the L-H transition is typically given by empirical scalings, such as the Martin scaling [28], in terms of the power crossing the separatrix P_{sep}

$$P_{sep} > P_{LH}\,[\mathrm{MW}] = 2.15 \cdot \left(n_e\left[10^{20}\mathrm{m}^{-3}\right]\right)^{0.78} \times \left(B_\phi\,[T]\right)^{0.77}\left(a\,[m]\right)^{0.98}\left(R_0\,[m]\right)^{1.0}. \quad (1.21)$$

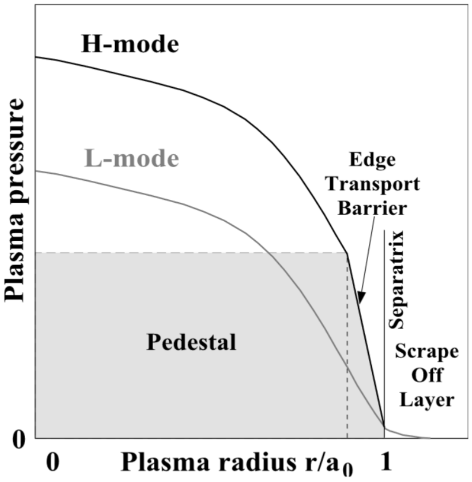

Figure 1.8: Typical L- and H-mode pressure profiles, plotted against the normalized plasma radius. Reproduced from [26].

The degree of confinement for a given plasma discharge is usually benchmarked against the energy confinement time in H-mode conditions with the same engineering inputs, with τ_E estimated via a given scaling law. One of the most famous power law regressions for the H-mode τ_E is the IPB98(y,2) empirical scaling [27]

$$\tau_E^{IPB98(y,2)}\,[\mathrm{s}] = 0.0562 \cdot \left(I_p\,[\mathrm{MA}]\right)^{0.93}\left(B_\phi\,[\mathrm{T}]\right)^{0.15}\left(P_{sep}\,[\mathrm{MW}]\right)^{-0.69} \times \left(n_e\left[10^{19}\mathrm{m}^{-3}\right]\right)^{0.41}\left(m_i\,[\mathrm{a.m.u.}]\right)^{0.19}\left(R_0\,[\mathrm{m}]\right)^{1.97}\varepsilon^{0.58}\kappa^{0.78} \quad (1.22)$$

with m_i the effective ion mass, $\varepsilon = a/R_0$ the tokamak inverse aspect ratio and κ the plasma elongation (see section 2.1). Based on equation 1.22, the ratio $H_{98(y,2)} = \tau_E^{exp}/\tau_E^{IPB98(y,2)}$ can be defined measuring the confinement degree of a plasma with given operational parameters. Ideally one should have $H_{98(y,2)} = 1$ or higher, with a value of ~ 0.8 usually identified as a lower boundary for proper reactor operation.

The physics of the edge transport barrier formation in H-mode is not fully understood yet, even if it is clear that the scrape-off layer plays a dominant role in this. Currently, one of the most credited explanations for it relies on the role of the edge radial electric field profile E_r. At high input power a pronounced E_r well arises in the vicinity of the separatrix, so that the radial shear of the corresponding poloidal $\mathbf{E} \times \mathbf{B}$ drift velocity field acts to suppress turbulent structures that are ultimately believed to be the cause of enhanced transport and poor confinement in L-mode [29].

1.4.1 STATIONARY H-MODE DIVERTOR HEAT LOAD

While good confinement is indeed desirable for a reactor in order to maximize the fusion power production, stationary H-mode operation implies a series of challenges on the power exhaust side. Indeed, in H-mode the scrape-off layer becomes narrower, due to the inhibition of turbulent transport across the separatrix. Consequently, at steady-state the same SOL input power P_{sep} must be exhausted on a smaller surface area than in L-mode, implying higher heat loads onto the divertor plates. With typical radial SOL extension values of $\sim 2 - 8$ mm around the outer midplane, it is foreseen that the 10 MW/m^2 material limit constraint will be most likely overcome within the foreseen operating scenarios for next generation MCF devices. The situation is even worse when considering low density, low collisionality H-mode scenarios, for which the scrape-off layer is foreseen to be even narrower than anticipated [30]. The full description of the SOL dynamics and main models is demanded to chapter 2.

This implicates the necessity of adopting a dissipative divertor solution where the peak heat flux profiles are mitigated by radiating away most of the power entering the SOL. This solution provides the further benefit of a considerable reduction of the plasma temperature in front of the divertor plates, with $T_e \leq 5eV$ strictly required to keep target erosion under control. This condition, known as *divertor detachment*, must be satisfied at least partially for safe ITER operation [31]. For DEMO-like parameters [32], it is foreseen that at least $\sim 95\%$ of the power crossing the separatrix must be dissipated by volumetric radiation, without significant loss of core plasma performance.

1.4.2 EDGE LOCALIZED MODES

On top of its steady-state power exhaust issues, the H-mode suffers from heavy transient particle and heat loads on the divertor plates and first wall owing to periodic relaxations of the pressure profile. These outbursts, known as *edge localized modes* (ELMs), originate as large current and pressure-driven MHD instabilities arising near the edge due to the local strong pressure gradient and associated high current density [33]. The typical evolution of the pressure profile during an ELM is visualized in figure 1.9. Each ELM is associated to a collapse of both the pedestal top pressure and gradient, with the ejection of part of the total stored particles and energy from the confined region to the scrape-off layer, ultimately ending onto the divertor plates and first wall components. Subsequently, the pedestal gradient starts rising again, the pressure and current profiles gradually reform until the next ELM is triggered.

An H-mode plasma can be characterized by different kinds of ELMs, in fact a full classification is quite difficult since there exists a multitude of possible behaviours [33, 35] appearing under quite diverse operating conditions. The most impactful ones for power exhaust issues are the type-I ELMs, occurring well above the L-H threshold, while their frequency increases with the input power. They are best described by the ideal coupled peeling-ballooning MHD model [36, 37] and appear as well defined and distinct sharp bursts in the D_α signal. They are associated with the largest energy loss relative to the total plasma energy content, up to $\Delta W_{ELM}/W_{tot} \sim 15-20\%$. As such, they can impose transient energy fluxes to the divertor targets of the order of several GW/m^2 in future big devices [38]. In ITER, which is foreseen to operate in a standard type-I ELMy H-mode scenario, events of this kind must be at least mitigated whereas they have to be avoided at all costs in a full-scale reactor.

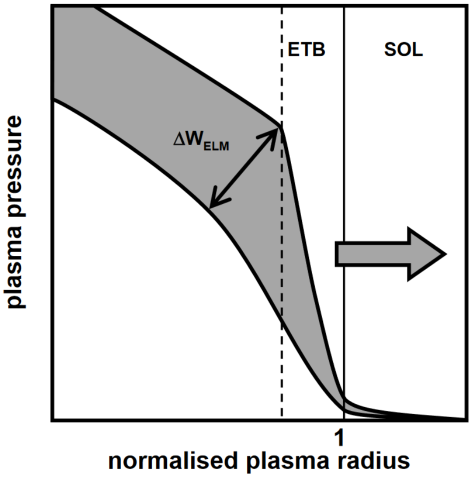

Figure 1.9: Pre-ELM and post-ELM edge plasma pressure profile, plotted against a normalized radius. The pre-ELM pedestal top position and the separatrix are indicated by, respectively, dashed and solid lines. Reproduced from [34].

Type-II ELMs represent another relevant category. They are observed in several devices [39, 40, 41, 42] at high edge density and high plasma triangularity. Their behaviour is independent of the heating power and they occur much more frequently and with much smaller energy losses ($\sim 1-5\%$) than type-I ELMs, appearing in the D_α signal as a large-amplitude noise, thus they are also denoted as *grassy* ELMs. Finally, type-III ELMs are smaller than type-I ELMs, occurring much closer to the L-H threshold, however their frequency decreases with the input power. Their generation mechanism is not yet clarified, even if so far ideal MHD has been ruled out as the base explanatory model.

1.4.3 THE QUASI-CONTINUOUS EXHAUST REGIME

Among the aforementioned ELM regimes, significant research efforts are being currently put forward in developing knowledge on the type-II ELMy H-mode. Thanks to the required high edge density, this scenario is promising for the purpose of optimizing the core reaction rate while, at the same time, radiating away a significant part of the power flowing into the scrape-off layer [43]. On top of this, in such a regime long stationary phases can take place in which no type-I ELMs are triggered, being instead replaced by high frequency, small amplitude incoherent bursts of particle and energy being ejected into the scrape-off layer. Because of this latter feature this regime has recently taken on the name of *Quasi-continuous exhaust* (QCE) H-mode [44].

A comparison between the two different ELMing behaviours can be visualized in figure 1.10. Recent studies carried out at the ASDEX-Upgrade and TCV devices [44, 45, 46] have highlighted a significant broadening of the scrape-off layer power channel, with a strong increase of λ_q, when moving from a type-I ELM to a QCE regime via an increase of the gas puffing and resulting high separatrix density, resulting from enhanced perpendicular transport upstream. The role of the safety factor in establishing the QCE scenario has been highlighted as well, both via a variation of the central toroidal magnetic field on ASDEX-Upgrade [47] and a variation of the plasma triangularity on TCV [48]. QCE therefore seems a good option to relieve the divertor heat load, nonetheless without significant loss of main plasma confinement. A pedestal structure is indeed retained in both the temperature and density profiles, with the $H_{98(y,2)}$ factor being ~ 1 most of the time.

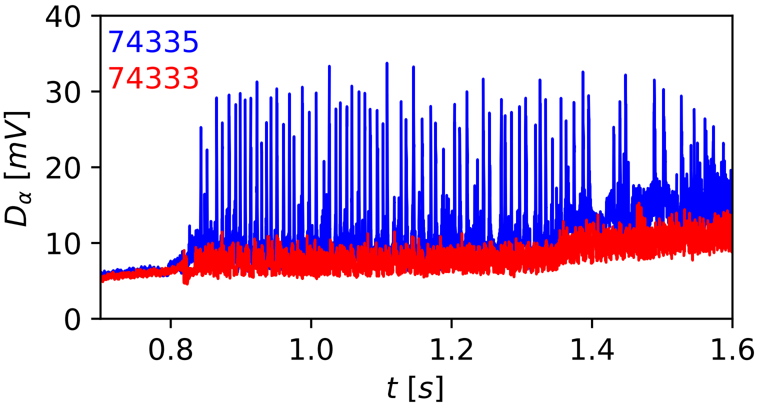

Figure 1.10: Divertor line of sight photodiode D_α time traces for two TCV shots, one with type-I ELMs (74335, blue) and one with type-II ELMs/QCE (74333, red).

On the other hand, the increased cross-field upstream particle transport taking place in QCE leads to a significant modification of the SOL density profiles, in the form of an increase in the near SOL density decay length λ_n. In addition, a further flattening of the profile is observed in the far SOL, taking the name of *density shoulder*. This feature is not exclusive to QCE: it has been experimentally observed in a multitude of regimes, spanning both L-mode [49, 50, 51, 52, 53, 54, 55] and H-mode [56, 57, 44, 58] scenarios, as well as being widely explored from the numerical point of view (see e.g. [59, 60, 61] for L-mode cases). One of the most credited explanations for the density shoulder formation is based on the interplay between turbulent filamentary structures upstream and high divertor and midplane neutral pressure. More specifically, an enhancement of the turbulent activity around the separatrix leads to a more frequent ejection of intermittent high-density fluctuations towards the far SOL. The energy associated to the enhanced radial particle and heat fluxes towards the first wall can lead to an augmented ionization of SOL neutrals, locally increasing the electron density and leading to a flattening of the density profile. In the QCE regime the presence of a density shoulder can be detrimental for the preservation of first wall PFCs around the midplane, due to the associated enhanced radial convective transport and increased particle load leading to significant erosion.

Despite previous extensive attempts, a commonly agreed description of the SOL dynamics governing the evolution of the upstream profiles and turbulence in high density H-mode regimes is still lacking. Based on the present knowledge derived from experimental AUG and TCV data (see e.g. [41, 42, 62, 63]), it is believed that the key factor responsible for the occurrence of small ELMs and turbulent transport in QCE is the development of ballooning modes near the pedestal foot. More precisely, a higher separatrix density should result in an increase in the level of transport connected with these modes. In high plasma shaping conditions, namely in a close to double null magnetic configuration, the magnetic shear at the separatrix at the outer midplane (OMP) decreases, therefore also its stabilizing effect on ballooning modes should be reduced. The described conditions result in a plasma that is only marginally stable against ballooning modes near the separatrix. The increased transport level causes the local pressure profile around the separatrix to flatten, resulting in a narrower pedestal width and the stabilisation of type-I ELMs.

1.5 SCOPE AND OUTLINE OF THIS WORK

As already extensively pointed out, high density H-mode regimes (including but not limited to QCE) represent an attractive option for ITER and DEMO-sized devices, given their particularly favourable radiative and divertor power exhaust properties. Conversely, some worries may arise with regard to the overall redistribution of particle fluxes towards the midplane portions of the first wall, potentially leading to severe levels of material sputtering and erosion. The present manuscript is devoted to further understanding the physics of the scrape-off layer and the properties of power and particle exhaust in different operating regimes, spanning both type-I ELMy and QCE H-modes. An experimental activity has been carried out on the *Tokamak à Configuration Variable* (TCV), exploiting its notorious flexibility in operating conditions and extensive edge diagnostic coverage.

As a first goal, in this work the response of the upstream SOL profiles and the behaviour of turbulent SOL fluctuations in H-mode conditions have been probed with respect to changes in separatrix density and safety factor. For this purpose two large experimental datasets have been acquired on TCV, consisting in deuterium-fuelled H-mode discharges in which either the divertor gas fuelling rate and position or the plasma upper triangularity have been varied in a wide range of values.

The main gas scan database is complemented with a small set of discharges with a different heating scheme, higher input power and lower edge density.

Secondly, a first attempt is made on TCV to put the experimental results into context within a recently proposed theoretical description of the scrape-off layer dynamics based on a fluid approach, assessing the competition between different plasma instabilities giving rise to perpendicular transport. For proper comparison, the results are benchmarked as well with respect to the currently most credited empirical scaling laws for type-I ELMy H-modes, like the multi-machine regression #14 in [30], or the reference SOL transport models in H-mode like the heuristic-drift model in [64, 65].

The outline of the thesis is as follows:

- In chapter 2 the main aspects of SOL physics are introduced, including both a brief discussion of plasma-wall interaction and an in-depth description of the fluid models used in this work. A recap on the well-known two-point model is given, providing the reference methodology to estimate the relevant separatrix operational parameters. The Drift-Alfvén turbulence model is presented, which attempts to describe the SOL plasma through dimensionless global parameters derived from separatrix quantities.

- Chapter 3 presents the TCV tokamak, with an excursion over the actuators exploited to achieve the desired operational scenarios and the edge diagnostics used to characterize the upstream and divertor profiles and fluctuations.

- In chapter 4 the main analysis methodologies used throughout this research project are detailed. These include a method for proper selection, ELM filtering and regularization of both upstream profile data and downstream divertor heat load target measurements, the framework exploited for a physically robust estimation of the separatrix position and the procedure for characterization of the turbulent structures in the scrape-off layer.

- Chapter 5 presents the experimental setup and the main results of the gas fuelling scan dataset, illustrating the modifications induced on the up- and downstream edge profiles and turbulent transport by a variation in the upstream separatrix electron density. The main correlations with the main separatrix operational parameters are also presented and evaluated.

- In chapter 6 the effects of a variation in the safety factor, induced by a scan in upper triangularity, are assessed. The changes in upstream SOL profiles in response to a modification of the upper triangularity are analyzed and compared with the results of the fuelling scan experiment analysis. The fluctuation behaviour at the first wall tiles and plasma-facing components, as well as the features of the plasma-wall interaction, are correlated with the shaping parameters.

- Finally, chapter 7 will summarize the main scientific results contained in this manuscript and propose further developments of the present study.

2

SCRAPE-OFF LAYER MODELS

In this chapter the main characteristics of the tokamak boundary region and models for the description of the scrape-off layer are presented. In the first place, in section 2.1 the main geometrical features of the scrape-off layer are addressed. In section 2.2, starting from the principal SOL conservation equations and boundary conditions, the well-known two-point model is formulated. Starting from the main conclusions of the two-point model, section 2.3 focuses on the divertor operating regimes and their differences. In section 2.4 an introduction to the main physical mechanisms responsible for perpendicular turbulent transport in the scrape-off layer is given, with particular regard to intermittent filamentary structures driving the formation of the already anticipated density shoulder. Finally, section 2.5 deals with the main model considered here for characterization of the different transport regimes experimentally seen in this work.

2.1 PLASMA BOUNDARY GEOMETRICAL DEFINITIONS

As anticipated in chapter 1, the experimental efforts presented in this work have been carried out all in diverted plasma configuration. In such a magnetic topology, the radial extent of the scrape-off layer, the shape of the plasma profiles and the interaction of the plasma with the solid wall materials all depend both on the overall magnetic field line distribution and on the balance between the different parallel and cross-field transport phenomena, as well as on the SOL source terms. In this section the main parameters defining the geometrical shape of the confined region and the topology of the SOL field lines are treated.

2.1.1 PLASMA SHAPING

In a diverted configuration, the separatrix represents the geometrical boundary between the confined region and the scrape-off layer. In most diverted tokamak plasmas the separatrix has typically a non-circular shape and presents at least some degree of asymmetry between the radial and vertical extensions. Some parameters can be defined, constituting the so-called *plasma shaping*, which greatly affect the confinement and stability of a given equilibrium. The main shaping parameters can be defined based on the radial and vertical extents of a flux tube, based on figure 2.1 [66]:

- Major radius: $R_{geo} = (R_{max} - R_{min})\,/2$,
- Minor radius: $a = (R_{max} - R_{min})\,/2$,
- Elongation: $\kappa_{geo} = (Z_{max} - Z_{min})\,/\,(R_{max} - R_{min})$,
- Upper triangularity: $\delta_{up} = \left(R_{geo} - R_{Z_{max}}\right)/a$,
- Lower triangularity: $\delta_{low} = \left(R_{geo} - R_{Z_{min}}\right)/a$.

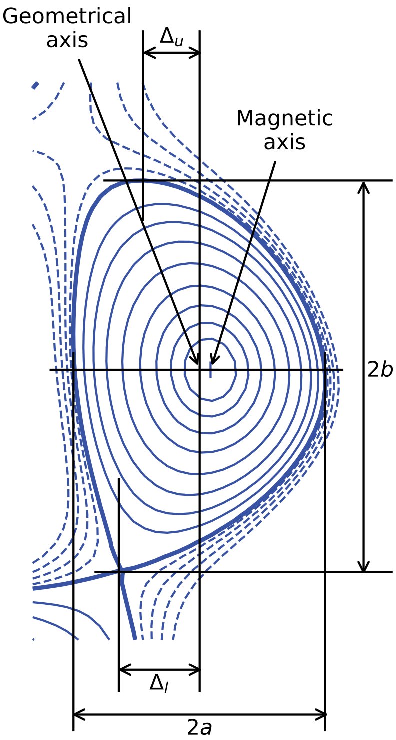

Figure 2.1: Indication of several quantities useful for plasma shaping characterization, highlighted through a TCV equilibrium.

In these equations, R_{max} and R_{min} are the outermost and innermost radii of the separatrix, whereas Z_{max} (Z_{min}) and $R_{Z_{max}}$ ($R_{Z_{min}}$) are, respectively, the vertical and radial coordinates of its uppermost (lowermost) point. An average triangularity can be defined as well, using the upper and lower values, as $\delta = (\delta_u + \delta_l)\,/2$. It is worth noting that the previous definitions are not exclusive to the separatrix and each quantity can be computed for every flux surface within the confined region.

2.1.2 SOL MAGNETIC COORDINATES

Since several equilibrium quantities are constant on a flux tube, the poloidal flux function ψ is particularly suited for defining a radial coordinate. The origin of the latter is usually identified with the *magnetic axis*, representing the value of ψ at which the flux contours degenerate into a circle running around the torus on the equatorial plane. Given ψ_0 the value of ψ at the magnetic axis, one can define the normalized poloidal flux label given by

$$\rho_\psi = \sqrt{\frac{\psi - \psi_0}{\psi_{sep} - \psi_0}}, \tag{2.1}$$

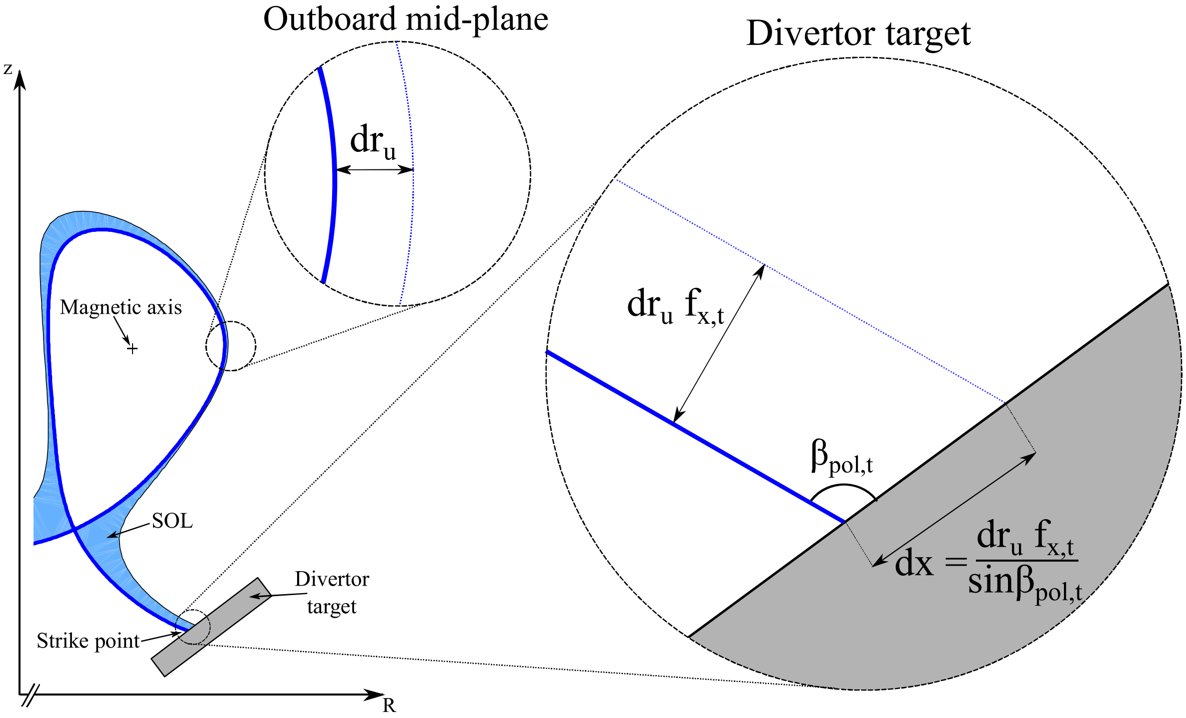

Figure 2.2: Geometrical definition of the SOL upstream radial coordinate dr_u and its relation with the downstream radial flux surface separation by means of the poloidal flux expansion. Reproduced from [67].

so that $\rho_\psi = 0$ at the magnetic axis and $\rho_\psi = 1$ at the LCFS.

Alternatively, one can assign a radial coordinate to a flux tube based on its radial distance from the separatrix. This quantity is actually not constant over a flux surface and depends in principle on the poloidal position along a field line, therefore only when the latter is fixed a proper label can be defined. Conventionally, the position of the separatrix at the outer midplane is chosen as reference, so that each flux surface can be labelled by means of the upstream radial coordinate

$$dr_u = R_u - R_{u,sep} \tag{2.2}$$

visualized in figure 2.2 and defined as the geometrical distance between the flux tube and the separatrix evaluated at the vertical height of the magnetic axis.

2.1.3 Flux expansion and field line mapping

The process of converting the upstream flux contour radial separation to an equivalent coordinate at another poloidal position is called *field line mapping* and it is quite helpful for comparing the upstream spatial distribution of any physical quantity with that at the divertor plates.

The radial distance between two neighbouring flux surfaces strongly depends on the magnitude of the poloidal magnetic field at a given position in the scrape-off layer. More in detail, it is generally maximum around the X-point where B_θ is weakest, whereas it is approximately constant in the vicinity of the outer midplane, where it depends only on the plasma current and shaping. For a given flux contour, the ratio between the radial distance evaluated at the divertor target with respect to the upstream position (see figure 2.2) is called *target poloidal flux expansion*

$$f_{\chi,t} = \frac{dr_t}{dr_u} = \frac{R_u B_{\theta,u}}{R_t B_{\theta,t}}. \tag{2.3}$$

From the geometrical point of view $f_{\chi,t}$ represents a scale factor for all characteristic SOL lengths between any physical quantity measured upstream with respect to its corresponding divertor target distribution, in the case of flux surface contours perpendicular to the divertor target. In case of non-normal incidence, the poloidal tilt angle of a field line at the target $\beta_{pol,t}$ has to be taken into account through a factor $1/\sin\beta_{pol,t}$ as in figure 2.2 to convert from upstream to divertor target coordinates.

Along the parallel direction instead, the poloidal flux expansion directly affects the path followed by plasma particles via a change in B_θ. The length of the field line connecting the outer midplane to a divertor target on a fixed scrape-off layer flux contour is called *parallel connection length* $L_\parallel$ and is given by

$$L_\parallel(\rho_\psi) = \int ds_\parallel = \int_u^t ds_\theta \frac{B_{tot}(\rho_\psi, s_\theta)}{B_\theta(\rho_\psi, s_\theta)}. \tag{2.4}$$

The connection lenght plays a largely relevant role in the SOL physical phenomena, since it sets the parallel spatial scales over which heat and particle fluxes are exhausted by convective and/or conductive transport.

Also the cross-sectional area of the flux tube spanned by the radial extent dr_u varies when moving along a field line in the poloidal direction, due to variations in the total magnetic field magnitude coupled with total magnetic flux conservation. Since $B \approx B_\phi$ at any location in the vessel, the *target total flux expansion* is

$$f_{tot,t} = \frac{dA_t}{dA_u} \approx \frac{B_{\phi,u}}{B_{\phi,t}} = \frac{R_t}{R_u} \tag{2.5}$$

with R_t and R_u the separatrix major radii at the target and upstream, respectively. This quantity scales surface areas between upstream and target, quantifying the spread in the divertor plates heat and particle footprints attributable to the magnetic topology alone.

The poloidal and total flux expansions allow to compute the relation between the heat flux hitting the target perpendicularly $q_{\perp t}$ and that flowing upstream parallel to field lines $q_{\parallel u}$. The *grazing* *angle* α at which the field lines intercept the target has to be accounted for as well, yielding

$$q_{\|u} = q_{\|t} f_{tot,t} \approx q_{\|t}\frac{R_t}{R_u} = \frac{q_{\perp t}}{\sin\alpha}\frac{R_t}{R_u} \approx q_{\perp t}\frac{R_t}{R_u}\left|\frac{B_{tot,u}}{B_{\theta,u}}\right|\frac{f_{\chi,t}}{\sin\beta_{pol,t}}. \tag{2.6}$$

The full proof for equation 2.6 can be found in reference [67].

2.1.4 Plasma wetted area

The peak heat flux impinging on a divertor plate depends not only on the total power flowing into the scrape-off layer, but also on the spatial extent of its footprint and thus on the cross-field transport phenomena taking place all along the flux tube. It can be assumed that the upstream parallel heat flux profile decays as an exponential

$$q_{\|u} = q_{\|u,0}\exp\left(-\frac{dr_u}{\lambda_{q,u}}\right) \tag{2.7}$$

where $\lambda_{q,u}$ is the upstream SOL power width. The perpendicular heat flux at the target is given by a similar expression, with the characteristic length given by $\lambda_{q,t} = \lambda_{q,u} f_{\chi,t}/\sin\beta_{pol,t}$.

By integrating the target heat flux over the whole divertor plate area one gets $P_{dep,t} = A_{wet} q_{\perp t,0}$, with $P_{dep,t}$ the power deposited onto the considered target and A_{wet} the *plasma wetted area*. Under the ansatz expressed by equation 2.7 the latter can be written as

$$A_{wet} = 2\pi R_t \lambda_{q,t} = 2\pi R_t \lambda_{q,u}\frac{f_{\chi,t}}{\sin\beta_{pol,t}} \approx 2\pi R_t \lambda_{q,u}\left|\frac{B_{\theta,u}}{B_{tot,u}}\right|\frac{1}{\sin\alpha}. \tag{2.8}$$

It can be assumed that the deposited power $P_{dep,t}$ is a fraction f_t of the total power entering the scrape-off layer P_{sep} (see [68] for a model of the divertor target power sharing). Provided that no part of this power is dissipated along the SOL field lines, the resulting peak perpendicular heat load is given by

$$q_{\perp t,0} = \frac{P_{dep,t}}{A_{wet}} = \frac{f_t P_{sep}}{2\pi R_t \lambda_{q,u}}\left|\frac{B_{tot,u}}{B_{\theta,u}}\right|\sin\alpha. \tag{2.9}$$

Equation 2.9 shows that the divertor heat load can be relieved by acting on the magnetic topology. In particular, R_t or the poloidal flux expansion can be increased, giving rise to some of the currently most investigated alternative divertor configurations such as the X-divertor or the Super-X divertor [69]. The field line grazing angle α can be changed as well by increasing the poloidal tilt angle of the target $\beta_{pol,t}$, however its value is bounded from below at $\sim 3°$ due to power load tolerance issues for the ITER divertor tile monoblock design [70].

An alternative way of mitigating the heat load would be to act on the transport phenomena in order to increase $\lambda_{q,u}$. Common values for this quantity in low density type-I ELMy H-mode regimes are $\sim 2 - 8$ mm across a multitude of tokamak devices, whereas an empirical multi-machine scaling based on the upstream poloidal field only [30]

$$\lambda_{q,u}\,[\mathrm{mm}] = (0.63 \pm 0.08) \cdot (B_{\theta,u}\,[\mathrm{T}])^{-1.19 \pm 0.08} \tag{2.10}$$

extrapolates $\lambda_{q,u} \sim 1$ mm for ITER baseline parameters [71]. These values will likely lead to intolerable stationary peak heat loads impinging onto the divertor targets, requiring that the machine is operated in a highly radiative scenario with SOL volumetric power dissipation. In addition, the QCE regime looks like a good alternative for steady-state operation as described in chapter 1.

2.2 PARALLEL TRANSPORT IN THE SCRAPE-OFF LAYER

The shapes of the SOL plasma profiles, as well as the value of the SOL power width, are the result of the competition between parallel transport from the outer midplane to the divertor targets and perpendicular transport from the confined region towards the first wall, balanced with source and sink terms in the scrape-off layer. A full understanding of these processes is still missing due to their inherent complexity and non-linearity, however by using reduced models a first level of qualitative insight can be achieved. In the following, the basic SOL description proposed in [24] is reproduced.

2.2.1 FLUID PARALLEL CONSERVATION EQUATIONS

In most cases, the SOL dynamics can be treated by means of a *fluid* model. The validity of this approach is limited to cases in which the mean free path for Coulomb collisions is much smaller than the parallel connection length. The inverse ratio of these two quantities at the outer midplane is called *collisionality*

$$\nu^* \sim 10^{-16} L_\parallel \frac{n_u}{T_u^2} Z_i, \tag{2.11}$$

being equal for ions and electrons in the case of $T_e = T_i$. In the scrape-off layer of current devices this quantity is considerably greater than 1 due to the typically low temperatures compared to the confined region, thereby justifying the adoption of a fluid approach.

In the fluid limit, a reduced one-dimensional model for the transport of particles, momentum and energy along the parallel direction can be formulated based on the Braginskii equations [72], summarized in appendix B. These are a set of 3D equations evolving the lowest order moments of the velocity distribution function. Starting from a kinetic equation, in which collisional and generation terms are included, the Braginskii equations embody the conservation laws for the plasma density (zeroth-order moment) as well as the velocity (first-order) and the kinetic energy (second-order) of both ions and electrons. The $n-$th moment conservation law contains also quantities related to the $(n+1)-$th order, so that a truncation is required to avoid working with an infinite hierarchy of equations. In the Braginskii approach, a closure for each equation is provided by means of properly calculated transport coefficients whose values are different along and across the magnetic field lines. The resulting equations are then reduced dimensionally in order to obtain a description of steady-state parallel transport along a given flux tube. In order to provide a complete SOL description, one has also to consider the interaction of plasma particles with neutrals, which can be expected to play a major role in the scrape-off layer due to the lower temperatures than in the confined region and the proximity to the plasma-facing components and gas injection location.

The first of such equations is the continuity law for the plasma density n

$$\nabla_{||}\left(nv\right) = S_p \tag{2.12}$$

with v the plasma fluid velocity and S_p the volumetric particle source/sink, resulting from cross-field particle transport as well as neutrals ionization and plasma recombination.

The plasma parallel momentum balance can be expressed by summing Newton's second law for ions and electrons, yielding

$$\nabla_{||}\left(m_i n v^2 + p_e + p_i + \pi_i\right) = S_{in} + S_{mom,p}. \tag{2.13}$$

where the electron inertia has been neglected, due to $m_e \ll m_i$. The term on the left-hand side of equation 2.13 is the parallel variation of the total plasma pressure, including a term describing the *parallel viscous drag* force π_i arising due to ion pressure anisotropy. The latter term can be expressed, under several assumptions, as

$$\pi_i = -\eta_{||}\nabla_{||}v \tag{2.14}$$

with $\eta_{||}$ the *parallel viscosity coefficient*, thus eliminating the need for another equation for the parallel transport of the ion perpendicular pressure. The most important contributions to momentum sources (i.e. forces), reported on the right-hand side of equation 2.13, include a term accounting for ion-neutral collisional momentum transfer and a net source/sink $S_{mom,p}$ associated to cross-field momentum transport and the generation or destruction of plasma particles, thus to the S_p term in the continuity equation.

Furthermore, some other contributions may still be relevant for single-species momentum balance but do not appear in equation 2.13 due to being equal and opposite for ions and electrons. The most important missing contribution is that due to parallel momentum transfer between the oppositely charged species:

$$R_{\|} = en\frac{j_{\|}}{\sigma_{\|}} - 0.71n\nabla_{\|}T_e. \tag{2.15}$$

The first term accounts for ion-electron friction, where the quantities $j_{\|} = en\left(v_i - v_e\right)$ and $\sigma_{\|} = 1.96e^2n\tau_e/m_e$ are, respectively, the parallel current density and electrical conductivity, with τ_e the average electron collision time. The second one is a thermal force stemming from unbalanced frictional momentum transfer among neighbouring electrons moving at different thermal velocity due to the presence of a temperature gradient. From the electron momentum balance, neglecting the electron inertia, the *generalized Ohm's law* can be derived as

$$E_{\|} = \frac{j_{\|}}{\sigma_{\|}} - \frac{1}{en}\nabla_{\|}p_e - \frac{0.71}{e}\nabla_{\|}T_e. \tag{2.16}$$

reflecting the parallel electric field as a product of friction, pressure and thermal forces.

Finally, the steady-state plasma total energy equation reads

$$\nabla_{\|}\left[\frac{5}{2}\Gamma_{\|e}T_e + \left(\frac{5}{2}T_i + \frac{1}{2}m_iv^2\right)\Gamma_{\|i} + q^{cond}_{\|i} + q^{cond}_{\|e} + \pi_iv\right] = S_R + S_{Ei} + S_{Ee}. \tag{2.17}$$

The terms on the left-hand side represent, respectively and in order, the electron thermal energy flux, the ion thermal and kinetic energy fluxes, the ion and electron conduction terms, the work done by the viscous drag, with $\Gamma_{\|e}$ and $\Gamma_{\|i}$ the electron and ion parallel particle fluxes. These are balanced on the right-hand side by the frictional joule heating term S_R, as well as external heat sources/sinks due to cross-field transport, ion-neutral interactions, ionization/recombination processes and volumetric radiation losses. The parallel conducted heat fluxes can be derived from kinetic theory in the Spitzer-Härm formulation [73] and are given by, respectively

$$q^{cond}_{\|e} = -\kappa_{0e}T_e^{5/2}\nabla_{\|}T_e, \quad \kappa_{0e} = \frac{30692}{Z_i\ln\Lambda} \tag{2.18}$$

$$q^{cond}_{\|i} = -\kappa_{0i}T_i^{5/2}\nabla_{\|}T_i, \quad \kappa_{0i} = \frac{1249}{Z_i^4m_i^{1/2}\ln\Lambda}, \tag{2.19}$$

where m_i is the ion mass expressed in amu and $\ln\Lambda$ is the Coulomb logarithm. For a pure deuterium plasma at typical SOL density and temperature values the parallel electron and ion heat conduction coefficients κ_{0e} and κ_{0i} are, respectively, $\sim$ 2000 and $\sim$ 60 $\mathrm{W}/\left(\mathrm{eV}^{7/2}\mathrm{m}\right)$. Given these values, at similar ion and electron temperatures the parallel ion conduction term is typically neglected in practical situations, nonetheless potentially becoming important when $T_i > T_e$ due to the 5/2 exponent in the heat conductivities.

VOLUMETRIC PARTICLE SOURCES

Each source term in equations 2.12, 2.13 and 2.17 describes, among others, a number of different processes involving the interactions between the plasma particles and the neutral atoms and molecules in the scrape-off layer. A non-exhaustive list of these processes is presented in figure 2.3 and table 2.1, whereas a more comprehensive one including a vast amount of atomic and molecular interactions can be found in [61]. Among these, the most important ones for the creation and destruction of plasma particles are ionization and recombination processes. Ionization reactions are dominant at temperatures higher than $\sim 4-5$ eV, with the ionization energy of atomic hydrogen and deuterium being 13.6 eV. Instead, in cold plasmas with lower temperatures recombination processes take over.

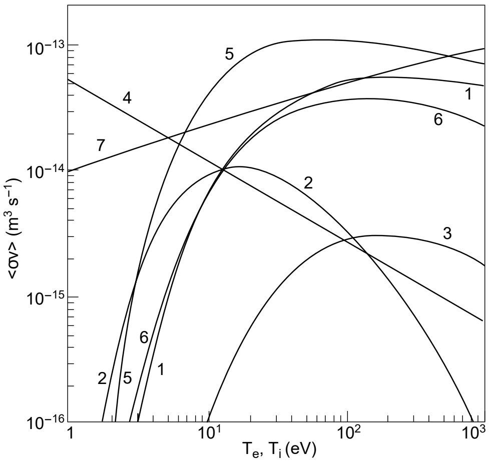

Figure 2.3: Reactivities for some key volumetric particle processes taking place in the scrape-off layer. Reproduced from [24].

#	Type	Reaction
1	EI-MI	$e^- + H_2 \rightarrow e^- + H_2^+ + e^-$
2	EI-MD	$e^- + H_2 \rightarrow e^- + H^0 + H^0$
3	EI-DI	$e^- + H_2 \rightarrow e^- + H^+ + H^0 + e^-$
4	EI-DR	$e^- + H_2^+ \rightarrow H^0 + H^0$
5	EI-DI	$e^- + H_2^+ \rightarrow e^- + H^+ + H^0$
6	EI-AI	$e^- + H^0 \rightarrow e^- + H^+ + e^-$
7	CX	$H^+ + H^0 \rightarrow H^0 + H^+$

Table 2.1: List of reactions, numbered as shown in figure 2.3. Type of reactions: electron impact (EI), molecular ionization (MI), molecular dissociation (MD), dissociative ionization (DI), dissociative recombination (DR), atomic ionization (AI), charge-exchange (CX).

The interaction between plasma particles and neutrals takes place also in the form of *charge-exchange* reactions, where a collision between a hot ion and a cold neutral causes the electrical charge to be transferred from one to the other. While on the one hand this process does not certainly lead to a change in plasma density, on the other hand it provides a strong frictional ion momentum sink and energy loss term, where the ions are effectively slowed down and the neutrals are accelerated instead.

2.2.2 Plasma interaction with a solid boundary

The transport coefficients in the Braginskii equations are derived within the fluid limit under the hypothesis that the velocity distribution function of both ions and electrons is essentially a Maxwellian with the addition of at most a small perturbation, describing a situation of local thermodynamic equilibrium [72]. This assumption is indeed valid in the bulk of the SOL plasma but fails in the proximity of a solid interface, where large perturbations to the distribution functions are introduced. Given also that a proper set of boundary conditions is needed for the equations introduced in section 2.2.1, a description of plasma-material interactions becomes crucial.

The Debye sheath

Due to the large difference in mass between electrons and ions, at similar temperature the former species will travel at a much higher thermal velocity than the latter. In the proximity of an electrically insulated, initially uncharged interface the electrons will travel much faster than the ions towards the solid boundary, accumulating a net negative charge on the exposed surface and making its electrostatic potential negative with respect to the bulk plasma potential. As a result, a new equilibrium will be reached in which negative charges are repelled from and positive ones attracted towards the wall, until an *ambipolar flow* situation is re-established in which the ion and electron particle fluxes become once again equal. The resulting potential drop between the plasma and the wall, called *floating potential*, develops over a narrow region called *plasma sheath* or *Debye sheath*, extending from the wall by a distance $\lambda_D = \sqrt{\varepsilon_0 T_e/(e^2 n)}$ called *Debye length*.

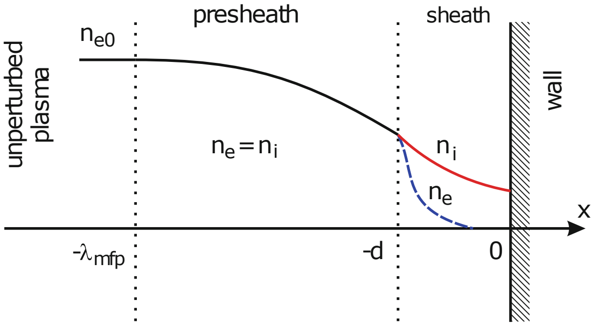

Figure 2.4: Scheme of the plasma sheath and presheath regions in the proximity of a solid boundary. Reproduced from [74].

Since plasma particles experience a negative potential in this region, a net positive charge accumulation will result which counters the surface negative charge at the interface, therefore the ion and electron densities are different and quasi-neutrality does not hold anymore in the Debye sheath. Furthermore, since the Debye length is much smaller than the collisional mean free path, the fluid approach is not adequate to characterize the properties of the sheath and a more detailed, kinetic description is needed. In particular, due to their low mass the electrons have a so-called *adiabatic* (i.e. almost instantaneous) response to spatial changes in the electrostatic potential and they can still be considered to be at local thermodynamic equilibrium, with appropriate changes due to the potential drop. The treatment for the ions is different, since they have a much larger mass than electrons. Exploiting single-particle momentum and energy balances, coupled with flow ambipolarity and Maxwell's equations for the potential drop, it can be shown that the so-called *Bohm-Chodura* criterion [75] must hold at all points within the sheath

$$v \geq c_s = \sqrt{\frac{Z_i T_e + T_i}{m_i}} \tag{2.20}$$

where c_s is the *ion sound speed* and corresponds to the progagation velocity of ion sound waves in a plasma. Upstream of the sheath entrance, the particle and momentum balances can be used to show [24] that the plasma flow must always be subsonic, i.e. $v \leq c_s$, in order to avoid introducing an unphysical singularity with infinite parallel gradients in the fields and flows anywhere but at the sheath interface with the plasma. Indeed, such a condition can be sustained solely within the sheath, being the latter intended as a very thin region where finite changes in a given quantity result in much larger gradients than in the bulk plasma, so that they can be approximated as infinite at least at the sheath boundary. Ultimately, the physical extension of the Debye sheath into the bulk plasma, of the order of λ_D, is set as the distance from the wall at which equation 2.20 is satisfied identically.

In the case of a magnetic field with oblique incidence with respect to the interface, like in most cases in a tokamak since $B_\phi \gg B_\theta$ at the first wall, further zones develop before the Debye sheath in which quasi-neutrality is not violated, but the properties of ions and electrons are nonetheless influenced by the sheath potential drop. These are the *magnetic presheath* and the *collisional presheath*, extending respectively over distances of the order of the *ion sound Larmor radius* $\rho_s = c_s/\Omega_{ci}$ and the collisional mean free path. The full picture of both presheath and sheath regions is represented in figure 2.4. Ions are first accelerated in the collisional presheath while their motion, taking place along the magnetic field lines, is still dominated by Coulomb collisions. At the magnetic presheath entrance the ion flow has become sonic and the plasma is still quasi-neutral, but the electric force takes over the Lorentz force and dominates the ion motion. Finally, in the Debye sheath quasi-neutrality is violated in order to establish flow ambipolarity towards the wall and the motion of electrons becomes as well dominated by the electric force.

Using Debye sheath theory, proper boundary conditions for the 1D parallel conservation equations of section 2.2.1 can be provided in terms of particle and heat fluxes, knowing that $v = c_s$ at the sheath entrance. In the first place, almost all ions will be accelerated towards the wall by the sheath potential drop, whereas electrons get repelled and only those travelling at sufficient velocity will manage to reach the interface. The particle fluxes for both species at the Debye sheath entrance under these conditions can be derived from kinetic theory and read

$$\Gamma^{se}_{\parallel i} \approx \frac{1}{2} n c_s, \quad \Gamma^{se}_{\parallel e} \approx \frac{1}{4} n v_{th,e} \exp\left[-\frac{e\left(\varphi_{se} - \varphi_{fl}\right)}{T_e} \right] \tag{2.21}$$

where $v_{th,e} = \sqrt{T_e/\left(2\pi m_e\right)}$ is the electron thermal velocity, φ_{se} is the electrostatic potential at the sheath entrance and φ_{fl} is the floating potential of the solid wall.

Secondly, the further requirement of ambipolar flow for an electrically insulated interface results in a net zero electrical current through the sheath, translating onto a relation for the sheath potential drop

$$\varphi_{se} - \varphi_{fl} = -0.5 \ln\left[\frac{2\pi m_e}{m_i} \left(1 + \frac{T_i}{T_e}\right) \right] \frac{T_e}{e} = \Lambda \frac{T_e}{e} \tag{2.22}$$

where $\Lambda \sim 3$ for a deuterium plasma with $T_i = T_e$. In a similar way, it can be demonstrated that a first smaller drop takes place within the presheath, of the order of $\Delta\varphi_{presheath} \approx 0.7 T_e/e$.

Finally, due to the collisionless behaviour of the plasma in the sheath, the total heat flux transported by particles across the sheath entrance is of purely convective nature and is given, using kinetic theory, by

$$q^{se}_{\parallel} = \left(\frac{5}{2} T_i + \frac{1}{2} m_i c_s^2 \right) \Gamma^{se}_{\parallel i} + \left(2T_e + e\left|\varphi_{se} - \varphi_{fl}\right| + e\left|\Delta\varphi_{presheath}\right| \right) \Gamma^{se}_{\parallel e} \tag{2.23}$$

with the second and third electron terms accounting for the net transfer of energy from the electrons to the ions, where the former are decelerated and the latter are accelerated by the presheath and sheath potential drops. Since flow ambipolarity implies $\Gamma^{se}_{\parallel i} = \Gamma^{se}_{\parallel e}$, exploiting the definition of c_s it is often convenient to rewrite equation 2.23 as

$$q^{se}_{\parallel} = \gamma T_e \Gamma^{se}_{\parallel} \tag{2.24}$$

where γ is the *total sheath heat transmission coefficient*. Typical numerical values for this parameter are $\gamma \sim 7-8$ for $T_e = T_i$, of which $5-6$ is attributable to the electrons and $2-3$ to the ions.

PLASMA-WALL PARTICLE AND POWER BALANCE

In providing a boundary condition for parallel transport, the physical role of the divertor target surface must be accounted for as well. Specifically, when an ion strikes any material surface after having crossed the Debye sheath several things can happen:

- the ion picks up an electron from the wall, gets neutralized and then sticks to the solid surface as an adsorbed neutral;

- the ion is first adsorbed as described in the first point, but is quickly released at a velocity distributed according to the wall temperature;
- the ion picks up an electron from the wall and is released into the plasma as a fast neutral without wall adsorption;
- the ion is reflected back into the plasma with a fraction of its initial energy, still retaining its charge.

In most processes the impacting ion is transformed into a neutral and is lost by the plasma, therefore the solid wall acts as an effective sink for the plasma particles. The resulting neutrals then penetrate into the plasma and have a chance to be re-ionized, usually by electron impact according (but not limited) to the ionization reactions listed in table 2.1. At steady state a situation can be reached, which takes the name of *particle recycling*, in which the neutralization of ions, with or without surface adsorption, proceeds at the same rate as the subsequent ionization of the resulting neutrals into the bulk plasma.

The fraction of neutrals that remain adsorbed at the wall are effectively removed from the particle balance, for which reason a solid surface acts not only as a plasma sink but also as a passive pumping system. This works up until the wall is saturated with neutrals, at which point the outflux of ions and the influx of released neutrals are equilibrated. In this way the plasma can effectively refuel itself with the ions lost to the wall as neutrals, provided that the latter are not removed by active pumping when released (by means of e.g. turbomolecular or cryogenic pumps) and a heating mechanism is always available to provide the necessary ionization energy for the recycled species.

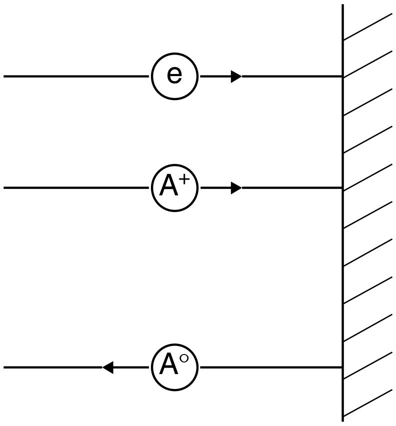

Figure 2.5: Illustration of the recycling process: ion/electron neutralization at the wall, neutral particle adsorption and subsequent release at a solid surface. Reproduced from [24].

Lastly, the ions release their kinetic energy onto the solid surface, determining a certain heat flux to be deposited on the wall. On top of this, however, the neutralization process is also accompanied by an energy release due to the fact that the picked up electrons fall from a free state to a more energetically favourable bound one. Moreover, in the case of hydrogenic species, once at the wall two neutral atoms can recombine to molecules, releasing a further energy contribution. The ionization and molecular dissociation energies, of the order of respectively $E_{iz} = 13.6$ eV and $E_{diss} = 2.38$ eV per hydrogen atom, is generally assumed to be deposited onto the solid surface, resulting in a further heat flux contribution on top of that crossing the Debye sheath in equation 2.24. The total particle heat load deposited onto the wall material is

$$q_{\perp t}^{part} = q_{\parallel}^{se} \sin\alpha + (E_{iz} + E_{diss})\Gamma_{\parallel i}^{se}. \tag{2.25}$$

Together with the radiative and fast neutrals contributions, this heat flux must be kept under control or mitigated in reactor-relevant scenarios to prevent severe damage of the divertort target material.

2.2.3 THE TWO-POINT MODEL

Using the 1D conservation laws and the boundary conditions derived in sections 2.2.1 and 2.2.2, by means of additional assumptions one can further reduce the dimensionality of the parallel transport problem. This leads to the formulation of the so-called *two-point model*, consisting of a set of simple relations linking the properties of the upstream plasma (subscript 'u' in the following) to those in the vicinity of the divertor target (subscript 't'). The main assumptions of the two-point model in its simplest form are:

- *Particle balance*: particle sources/sinks are neglected except within a thin layer in front of the divertor target, where all the recycled neutrals are assumed to be immediately re-ionized along the same field line on which they were generated. As a consequence, no parallel flow takes place along the bulk of a SOL flux tube, whereas the plasma velocity increases from zero at the ionization layer entrance up to c_s at the sheath entrance. No cross-field transport takes place either among neighbouring flux tubes.

- *Momentum balance*: ion-neutral friction, cross-field momentum transport and viscous drag forces are neglected along a flux tube, so that the total pressure (static plus dynamic) between the upstream and target regions is conserved. Assuming that, as previously anticipated, the plasma is stagnating upstream while flowing at sound speed in front of the target where $T_e = T_i$, the pressure balance reads

$$n_u T_u = 2 n_t T_t \tag{2.26}$$

- *Power balance*: since $v = 0$ within most of a flux tube, the scrape-off layer parallel heat flux is purely conducted along the connection length $L_{\parallel}$. If the power enters the flux tube at a single point at the upstream region, equation 2.18 can be readily integrated, yielding

$$T_{e,u}^{7/2} = T_{e,t}^{7/2} + \frac{7}{2}\frac{q_{\parallel} L_{\parallel}}{\kappa_{0e}}. \tag{2.27}$$

The analogous equation for the conducted ion heat flux is not considered here, due to the ion conductivity being much lower than for the electrons. Neglecting cross-field heat transport and provided that no volumetric power generation or removal takes place along the flux tube, the previous expression must be balanced with the parallel heat flux lost at the target sheath entrance

$$q_{\|t} = \gamma n_t T_t c_{s,t}. \tag{2.28}$$

Equations 2.26, 2.27 and 2.28 constitute the basis for the simplest two-point model formulation of SOL parallel transport. In the case of n_u and $q_\|$ being externally controlled variables, for $T_t \ll T_u$ the model provides a set of scaling laws for T_u, T_t, n_t and also for the target particle flux Γ_t:

$$T_u \simeq \left(\frac{7}{2}\frac{q_\| L_\|}{\kappa_{0e}}\right)^{2/7}, \tag{2.29}$$

$$T_t \propto n_u^{-2} q_\|^{10/7} L_\|^{-4/7}, \tag{2.30}$$

$$n_t \propto n_u^3 q_\|^{-8/7} L_\|^{6/7}, \tag{2.31}$$

$$\Gamma_t \propto n_u^2 q_\|^{-3/7} L_\|^{4/7}. \tag{2.32}$$

Firstly, T_u is not a function of n_u while, due to the heat conductivity being a strong function of the temperature, it is only weakly dependent on changes in $q_\|$ or $L_\|$. On the contrary, T_t scales faster than linearly with $q_\|$ while being a weak function of the connection length. Most importantly (and fortunately), T_t is a strong decreasing function of n_u, meaning that the most efficient way to cool down the plasma in front of the target is simply to increase the main plasma density. This decrease is, however, more than compensated by the cubic dependence of n_t on n_u, so that the flux of particles impinging on the target surface still increases more than linearly with the upstream density.

VOLUMETRIC LOSS FACTORS

The two-point model must be refined in the presence of volumetric processes dissipating part of the power and momentum transported into a flux tube. In particular, one can condense all the radiative and charge-exchange energy losses through a single *power loss factor* f_{power} through the expression

$$q_{\|,t} = (1 - f_{power}) q_\|. \tag{2.33}$$

Momentum losses due to ion-neutral CX friction, viscous drag forces and volume recombination are instead embodied by a momentum loss factor f_{mom} into the pressure conservation equation

$$f_{mom} n_u T_u = 2 n_t T_t. \tag{2.34}$$

Finally, part of the heat flux is still convected despite the presence of large temperature gradients. A convected power fraction f_{conv} is introduced so that $q_{\|,cond} = (1 - f_{conv})\, q_{\|}$, not including power losses assuming that they occur below the X-point. The two-point model scalings are extended as:

$$T_u \propto (1 - f_{conv})^{2/7}\,, \tag{2.35}$$

$$T_t \propto \left(1 - f_{power}\right)^2 f_{mom}^{-2} (1 - f_{conv})^{-4/7}\,, \tag{2.36}$$

$$n_t \propto f_{mom}^3 (1 - f_{conv})^{6/7} \left(1 - f_{power}\right)^2\,, \tag{2.37}$$

$$\Gamma_t \propto f_{mom}^2 (1 - f_{conv})^{4/7} \left(1 - f_{power}\right)^{-1}\,. \tag{2.38}$$

No strong dependence on f_{conv} appears in these equations. Conversely, high power losses lead to strong target temperature reduction, whereas momentum losses act as to decrease the particle flux.

2.3 DIVERTOR OPERATING REGIMES

According to the parallel transport models that have been introduced in section 2.2, one can make a distinction between different behaviours of the SOL plasma, to which different particle and heat transport mechanisms correspond. An important feature that helps in distinguishing between different SOL operating regimes is whether there actually exists a significant temperature gradient along a field line, since this defines the kind of heat transport as mostly convective or conductive.

The main parameter regulating the transition from one regime of parallel transport to the other is the main plasma density. When this quantity is low, the neutrals recycled at the target are allowed to travel large distances compared to $L_{\|}$ before getting ionized, so that the ionization region is not limited to a thin layer in front of the target but potentially reaches far into the upstream SOL plasma. This results in a large parallel flow of ions along most of the flux tube, in order to equilibrate the neutral recycling flux with the ion flux reaching the target, meaning that most of the particles and heat will be carried in the scrape-off layer by parallel convection and little to no temperature gradients arise along a field line. The heat flux that is able to reach the target is then limited only by the sheath heat transmission capabilities, i.e. by equation 2.24, hence this operating scenario is given the name of *sheath-limited regime*. In absence of a parallel temperature gradient large plasma temperatures are established in front of the target of the order of the upstream temperature ($\sim$ 100 eV or more in reactor-sized devices), albeit with a low particle flux, thus it goes without saying that this regime is not of interest in future bigger facilities due to the high risk of divertor material damage.

At higher main plasma density more particles are able to reach the targets, increasing the density locally and shortening the ionization mean free path of the recycled neutrals. As a consequence, a large temperature drop is established along a field line with most of the power being exhausted via Spitzer-Härm parallel electron heat conduction. In this situation, called *conduction-limited regime*, significantly lower temperatures can be achieved in front of the target. In accordance with the basic two-point model assumptions, the recycled neutrals are ionized within a thin layer in front of the targets, creating a local high-density region which results, by particle balance, in a positive feedback loop in which the particle flux increases and is balanced by a correspondingly higher recycling flux. This *high recycling regime* is reflected in the two-point model conclusions according to which at high density a low target temperature is counter-intuitively associated to a large increase of the parallel flux to the targets, scaling with the square of the main plasma density. Expressed in terms of upstream quantities, the transition from the sheath-limited to the conduction limited regime takes place within a narrow range of SOL collisionality values. In particular, it can be shown [24] that $\nu^* \lesssim 10$ is required for a temperature drop smaller than $\sim 67\%$ from upstream to target. On the contrary, if $\nu^* \gtrsim 15$ the target temperature already drops to less than a third of the upstream one.

In absence of volumetric losses, according to the two-point model scaling laws the particle flux at the target would continue to increase indefinitely as the main plasma density increases, due to momentum conservation along a flux tube. However, at sufficiently low target temperatures it is experimentally observed that the target density and particle flux “roll over”, meaning that they start decreasing. This situation, called *divertor detachment*, is generally identified via a simultaneous reduction of the pressure/momentum along a field line and a decrease of the particle flux hitting the targets. Also the power load onto the divertor targets is reduced, which would be greatly beneficial for the operation of future fusion devices and is therefore often included among the requirements for a detached divertor. Accounting for volumetric loss factors is a necessary step in the qualitative explanation of the transition from the conduction-limited regime to detachment. Specifically, the low target temperature required for detachment onset is firstly produced both by the increase of the upstream density and by volumetric radiative power dissipation, strongly favoured by the high ion and neutral densities. At the parallel position at which detachment starts occurring, the first physical mechanism providing a pressure drop along a field line, and thus a means for decreasing Γ_t, is represented by ion-neutral frictional momentum dissipation via charge-exchange collisions, effective for target temperature as low as $\sim$ 5 eV. Once lower T_t is reached, of the order of $\sim 1 - 2$ eV, volume recombination starts to play a role by effectively removing ions from the particle balance, further decreasing Γ_t. The resulting decrease of plasma density and particle flux makes the region in front of the targets transparent to the recycled neutrals, so that they have to travel a longer distance before being again ionized in the hot plasma. In this sense, what was once a thin surface particle sink in front of the targets becomes now a spatially extended region acting as a volumetric sink for both particles and momentum, self sustained by the neutrals recycled from the solid surface. In terms of upstream conditions, a SOL collisionality $\nu^* \gtrsim 85$ is required for full detachment onset with typical main plasma parameters in large devices [24].

2.4 MAIN ASPECTS OF PERPENDICULAR TRANSPORT

Contrary to the description of parallel flow, the question of cross-field SOL particle and energy transport is still one of the main challenges currently addressed by the scrape-off layer physics research community, since no widely accepted first-principles theoretical explanation exists at the moment. The first, most basic but comprehensive description of perpendicular transport is based on the assumption that the plasma behaves like a set of non-interacting particles occasionally undergoing binary collisions. In this case, the kinetic theory approach developed by Boltzmann can be used, which with the addition of the effect of electromagnetic fields on the motion of plasma particles, assuming a spatially uniform external magnetic field, leads to the *classical* description [76, 77]. The inclusion of magnetic field spatial non-homogeneity, much like that encountered in a tokamak where the toroidal field intensity scales with the inverse of the major radius, leads to the formulation of the *neo-classical* theory [78]. In particular, the transport rates predicted by the neo-classical approach tend to be higher by a factor q^2 than those associated to collisional effects only within a classical model.

Nonetheless, experimental measurements performed in the current devices reveal that the actual particle and energy fluxes are far greater than those predicted by the classical and neo-classical models alone, being therefore dubbed as *anomalous* [79]. The question of anomalous transport is deeply connected with turbulent phenomena taking place in the edge and scrape-off layer regions of tokamak devices. Indeed, it has been observed that a large fraction of the corresponding fluxes can be imputable to collective motions of the plasma due to the generation of density, temperature and potential fluctuations and their amplification via interaction with the background fields by means of some localized micro-instability process. The difficulty in achieving a common understanding of anomalous transport in a plasma is ultimately owed to the inherent non-linearity of turbulent phenomena, as well as to the wide range of micro-instabilities that can give rise to it.

2.4.1 RADIAL SHAPE OF SOL PLASMA PROFILES

The shapes of the plasma profiles at the outer midplane ultimately depend on the relative importance of perpendicular and parallel fluxes. More in detail, particles and energy are first radially exhausted from the confined region into the scrape-off layer by means of cross-field transport, travelling then mostly along field lines towards the divertor target surfaces which act as sink for both quantities. For the simple case of the density profile at the outer midplane, one can write a time-dependent radial continuity equation neglecting particle sources as

$$\frac{\partial n}{\partial t} = \frac{\partial}{\partial r}\left(D_n \frac{\partial n}{\partial r}\right) - \frac{n}{\tau_{\parallel}} \tag{2.39}$$

where the radial particle flux has been expressed in purely diffusive terms by using a single anomalous diffusion parameter D_n, while the parallel draining of particles has been modelled via a characteristic SOL parallel confinement time $\tau_{\parallel} = L_{\parallel}/c_s$. At steady state, assuming that the diffusion coefficient is constant across the whole SOL radius, one obtains an exponential decay for the density profile

$$n\left(r\right) = n_{sep} \exp\left(-\frac{r}{\lambda_n}\right) \tag{2.40}$$

where $\lambda_n = \sqrt{D_n \tau_{\parallel}}$ is called *density decay length*. Similarly, a continuity equation can be written for both the ion and electron temperatures, taking into account that the heat can be exhausted in the perpendicular direction both via convection and via conduction. The result is, once again, an exponential decay for the temperature profiles

$$T_{e/i} = T_{e/i,sep} \exp\left(-\frac{r}{\lambda_{T_{e/i}}}\right) \tag{2.41}$$

with $\lambda_{T_{e/i}}$ being the *temperature decay lengths*, depending on the values of anomalous thermal diffusivities $\chi_{e/i}$. The measured particle diffusion coefficients have values around $D_n \sim 0.1 - 1$ m^2/s, whereas the thermal diffusivities typically vary in the range $\chi_{e/i} \sim 1 - 10$ m^2/s. The radial shape of the upstream heat flux profile has been introduced in section 2.1.4 and is also exponential, with the heat flux width λ_q intimately linked to the parallel transport regime. In particular, in the sheath-limited regime the algebraic combination of the density and temperature profiles reported in equation 2.24 yields

$$\lambda_q = \left(\frac{1}{\lambda_n} + \frac{3}{2\lambda_T}\right)^{-1}. \tag{2.42}$$

Instead, in the conduction-limited regime the SOL power fall-off length is given by

$$\lambda_q = \frac{2}{7}\lambda_T. \tag{2.43}$$

The picture introduced here is in any case a very simplified one of pure diffusion across the entire SOL radial coordinate, where a single exponential decay stems from the assumption of radially constant particle and thermal diffusivities. In reality, things can be much more complicated than this and a radial profile for both D_n and $\chi_{e/i}$ must be considered. For instance, a number of experimental [80, 81] and numerical [82, 83] observations made on the density profile have managed to clearly resolve two different exponential decays, one limited to the region near the separatrix (i.e. *near SOL*) and the other localized well into the scrape-off layer (i.e. *far SOL*) being also larger than the former, corresponding to particle diffusivities of the order of $\sim$ 10 m^2/s. As it will be shown in section 2.4.3, such a high diffusion coefficient is linked to the radial convective propagation of intermittent turbulent structures into the far SOL. In the general picture, the SOL decay lengths are themselves increasing functions of the radial coordinate and can be expressed as

$$\lambda_n = -\left(\frac{1}{n}\frac{dn}{dr}\right)^{-1}, \quad \lambda_{T_{e/i}} = -\left(\frac{1}{T_{e/i}}\frac{dT_{e/i}}{dr}\right)^{-1}. \tag{2.44}$$

2.4.2 TURBULENT TRANSPORT DRIVING MECHANISMS

Depending on the micro-instability associated with the largest growth rates, different turbulent transport mechanisms can be responsible for the perpendicular particle and energy fluxes at various radial locations, and hence for the radial shape of the upstream SOL plasma profiles. In this section the physical mechanisms driving the development of the most relevant instabilities observed in the manuscript are considered.

MACROSCOPIC FLUID DRIFT VELOCITIES

The edge and SOL turbulence is a strongly non-linear phenomenon, in which no single instability at a fixed wavenumber $\mathbf{k}$ and angular frequency ω dominates over the others. Rather, the perturbations are characterized by a broadband spectrum of spatial and temporal scales occupying a large part of the $(\mathbf{k}, \omega)$ space [84]. In the first place, experiments points towards strong spatial anisotropy, with the fluctuations being typically much more extended along the parallel direction and localized along the cross-field one, or equivalently $k_{\|} \ll k_{\perp}$. Moreover, the observed typical fluctuation perpendicular scales are characterized by $\lambda_{\perp} \gg \rho_s$, where $\lambda_{\perp}$ is the extension (or wavelength) of the perturbation and ρ_s is the ion sound Larmor radius but also the largest characteristic length associated to the plasma particles gyromotion. Similarly, the edge fluctuations evolve over frequencies $\omega \ll c_s/\lambda_{\perp} \ll \Omega_{ci}$, or equivalently much slower timescales than the ion gyro-period. These observations indicate that the turbulent edge and SOL dynamics is dominated by low frequency fluctuations, predominantly transported along the perpendicular direction by macroscopic fluid drift velocities.

One is then allowed to exploit the so-called *drift ordering* to reduce the complexity of the problem. This consists, at leading order, in eliminating from all dynamic equations any term involving powers of the smallness parameter $\rho_s/\lambda_{\perp} \ll 1$. In this limit, the fluid momentum equation for the generic plasma species a can be written as

$$-\nabla p_a + eZ_a n_a \left(\mathbf{E} + \mathbf{v}_a \times \mathbf{B}\right) \simeq 0. \tag{2.45}$$

Taking the cross product of both sides with the magnetic field $\mathbf{B}$ one gets a zero-order approximation for the perpendicular component of the fluid velocity as $\mathbf{v}_{\perp a}^{(0)} = \mathbf{v}_E + \mathbf{v}_{*a}$. In this expression, $\mathbf{v}_E$ is the $\mathbf{E} \times \mathbf{B}$ drift already mentioned in section 1.2 for single particle motion, and here appearing as well as a major contribution to the perpendicular plasma fluid motion. On the other hand, $\mathbf{v}_{*a}$ is the so-called *diamagnetic drift* velocity for species a

$$\mathbf{v}_{*a} = \frac{1}{eZ_a n_a} \frac{\mathbf{B} \times \nabla p_a}{B^2}, \tag{2.46}$$

also being of leading order as $\mathbf{v}_E$. From a physical point of view, the diamagnetic drift can be intended as the macroscopic velocity contribution originating when the oppositely directed Larmor orbits of neighbouring particles do not completely cancel one another due to the presence of a temperature or a density gradient. In contrast to the single-particle guiding center ∇B and curvature drift motions, the diamagnetic drift is indeed a collective movement of the plasma acting also in presence of a uniform magnetic field. On the other side, much like the ∇B and curvature drifts, the diamagnetic drift velocity is charge-dependent and as such it can give rise to charge separation. The corresponding electric current generates a magnetic field that partially opposes the external one so that the plasma exhibits a diamagnetic behaviour, hence the name of this drift velocity component.

BALLOONING MODES

Some of the main modes often found in the edge of tokamaks plasmas are the so-called *ballooning modes*. Described in detail in [85], these modes are driven unstable by an appropriate coupling between the magnetic field line curvature and a pressure gradient. The source of this drive stems directly from the diamagnetic currents arising as a consequence of local density and temperature fluctuations, and hence gradients. In particular, one can easily show from the definition of $\mathbf{v}_{*a}$ that

$$\mathbf{v}_{*a} = -\frac{1}{eZ_a n} \nabla \times \left(p_a \frac{\mathbf{b}}{B} \right) + 2 \frac{T_a}{eZ_a B} \mathbf{b} \times \boldsymbol{\kappa} \tag{2.47}$$

where the unit vector $\mathbf{b} = \mathbf{B}/B$ and the magnetic curvature vector $\boldsymbol{\kappa} = (\mathbf{b} \cdot \nabla)\, \mathbf{b}$ have been introduced and the approximate relation $\nabla \times (\mathbf{b}/B) \simeq 2/B\, (\mathbf{b} \times \boldsymbol{\kappa})$ has been exploited, valid for negligible local electric current density. Since the first term on the right-hand side of equation 2.47 is solenoidal by construction, the diamagnetic particle flux stems only from the second one, therefore from field line curvature and magnetic field gradient. Furthermore, it is aligned with the direction perpendicular to both **b** and $\boldsymbol{\kappa}$, which at the outer midplane coincides with the vertical direction.

The basic picture of how the ballooning modes are destabilized by the coupling between a density gradient and magnetic curvature at the tokamak low-field side (LFS) is represented in figure 2.6. Since the diamagnetic flux shifts the electron and ion populations along opposite directions, a local charge separation arises in presence of a small density perturbation at the LFS, as shown in figure 2.6. Consequently, an electric field arises which is associated to an $\mathbf{E} \times \mathbf{B}$ drift velocity, which at the LFS amplifies the initial density perturbation and leads to an instability. At the tokamak high-field side (HFS) the background density gradient and the magnetic curvature are directed opposite to each other, so also the diamagnetic flux is reversed and the initial perturbation is effectively damped by the $\mathbf{E} \times \mathbf{B}$ drift. For this reason the tokamak low- and high-field sides are often referred to, respectively, as bad and good curvature sides. It is clear from this picture that all the particle dynamics required to destabilize the ballooning mode takes place on the poloidal plane, making this instability intrinsically 2D with no parallel structure along the magnetic field lines.

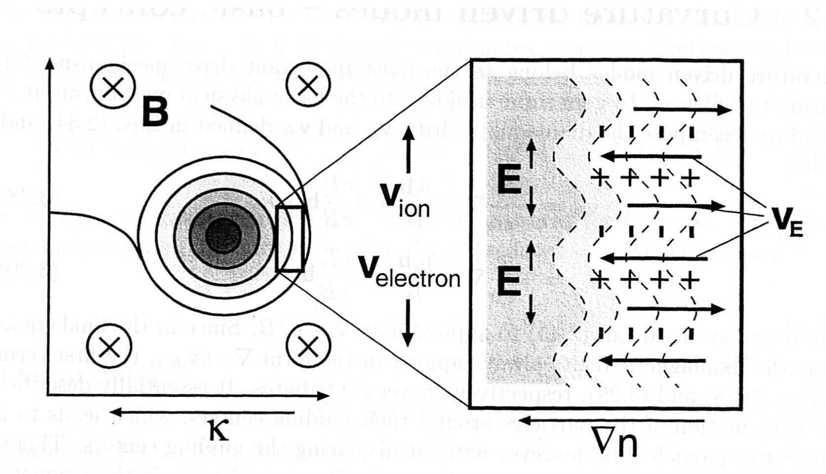

Figure 2.6: Rosenbluth-Longmire picture of the ballooning instability. Reproduced from [85].

This description is analogous to that of a neutral fluid in the presence of a density gradient counter-directed with respect to the gravitational buoyancy forces, resulting in a positional exchange of the high density and low density fluid portions. For this reason, the ballooning instability is often referred to also as *interchange instability*, where an effective gravitational force is represented in this case by the centrifugal force associated to magnetic curvature. Similarly to ballooning modes, other interchange-like modes may be driven unstable in the presence of electron or ion temperature gradients on the bad curvature side of the machine, being therefore named *electron temperature gradient* or *ion temperature gradient* modes.

From figure 2.6 another important detail emerges in that, for the ballooning mode to be destabilized, a finite phase shift must exist between potential and density fluctuations. In the figure the situation of a $\pi/2$ phase is depicted, in the presence of which the radial particle transport is maximum. To understand where this phase shift arises from, one can rewrite the generalized parallel Ohm's law (equation 2.16) in the electromagnetic limit, still neglecting electron inertia, as

$$\nabla_{\|}\varphi + \frac{\partial A_{\|}}{\partial t} + \frac{j_{\|}}{\sigma_{\|}} - \frac{1}{en}\nabla_{\|}p_e - \frac{0.71}{e}\nabla_{\|}T_e = 0 \tag{2.48}$$

where φ and $A_{\|}$ are the electric and parallel magnetic vector potential, respectively. One can then adopt a linearized approach, where each perturbation is written as $\exp i\left(\mathbf{k}\cdot\mathbf{x} - \omega t\right)$, with $\mathbf{k}$ and ω respectively the perturbation wavenumber and angular frequency. In the collisionless limit, further neglecting the parallel temperature gradient and electromagnetic fluctuations, the equation relates the density perturbation $\tilde{n}$ and the electric potential fluctuation $\tilde{\varphi}$ as

$$\frac{\tilde{n}}{n} = \frac{e\tilde{\varphi}}{T_e} \tag{2.49}$$

meaning that the parallel electron response to the potential fluctuations is adiabatic and the density and potential fluctuations are completely in phase. A finite phase shift can therefore only exist when the electron adiabaticity is broken by means of some non-ideality in the parallel electron motion. In particular, in equation 2.48 a finite parallel conductivity gives rise to the so-called *resistive ballooning mode*, usually being the most relevant ballooning mode branch for practical situations in high-density scenarios. *Ideal ballooning modes* instead do not require the inclusion of resistivity in the model and are inherently electromagnetic in nature, with the electron adiabaticity being broken by temporal fluctuations in the background magnetic field.

DRIFT WAVES

Another feature of the dynamics within the relevant temporal and spatial scales here under analysis for the tokamak boundary region is the existence of *drift waves*. They originate from the radial $\mathbf{E}\times\mathbf{B}$ advection of the background density/pressure profile gradient, without the requirement for any external force (gravitational, centrifugal, etc.). A simple scheme of how drift waves propagate in a plasma is given in figure 2.7, where the right-handed (x, y, z) orthogonal coordinate system has been used, with x and y respectively parallel and perpendicular to the background density gradient in the poloidal plane, while z is almost aligned with the magnetic field. If one assumes electron adiabaticity, the regions of high density are associated to peaks in the electrostatic potential, and viceversa for the regions of low density. Consequently, an electric field is established in between the density perturbation extrema, giving rise to an $\mathbf{E}\times\mathbf{B}$ drift aligned with the background density

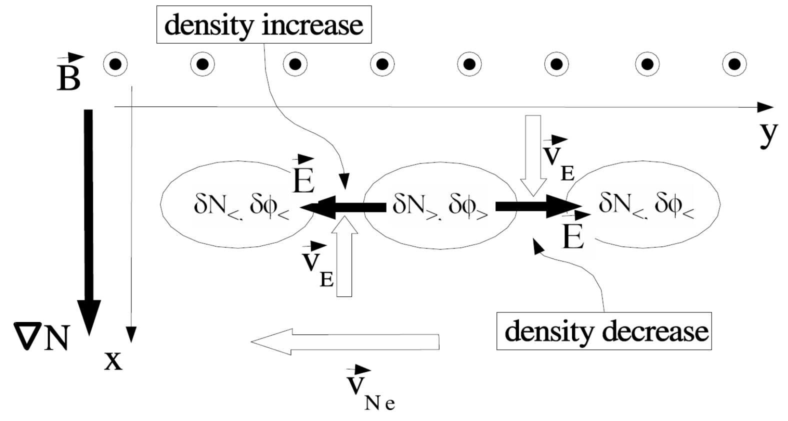

Figure 2.7: Simple physical picture of drift wave propagation. Reproduced from [87].

gradient. High density plasma is convected to the left of the density peak and low density plasma to its right, determining an overall shift of the density perturbation in the same direction as the electron diamagnetic drift.

In the first place, it must be said that in most applications where electrons are adiabatic the equality in equation 2.49 is not limited to density fluctuations, but it also applies to pressure, so that $\tilde{n}/n = \tilde{p}_e/p_e$. This is a consequence of the fact that the parallel dynamics tends to smooth out temperature disturbances, so that relative pressure and density perturbations become the same [86]. Then, a pressure fluctuation quasi-perpendicular to $\mathbf{B}$, with finite parallel wavelength (i.e. $k_\parallel \neq 0$, $k_\parallel \ll k_\perp$), is advected according to the linearized pressure equation

$$\frac{\partial \tilde{p}_e}{\partial t} = -\mathbf{v}_E \cdot \nabla p_e = -\frac{1}{B}\frac{\partial p_e}{\partial x}\frac{\partial \varphi}{\partial y}. \tag{2.50}$$

Exploiting equation 2.49 for electron adiabaticity and the first relation in equation 2.44 one gets

$$\frac{\partial \tilde{p}_e}{\partial t} = -\frac{T_e}{eB\lambda_{pe}}\frac{\partial \tilde{p}_e}{\partial y} \tag{2.51}$$

which, in the limit of isothermal electrons along x, corresponds to the equation for the propagation of a wave along y with velocity equal to the electron diamagnetic drift velocity $v_{*e} = T_e/\left(eB\lambda_{pe}\right)$, perpendicular to both the magnetic field and the pressure gradient. Fourier-decomposing the density fluctuation with wavenumber $\mathbf{k} \simeq k_y \mathbf{e}_y$ yields the dispersion relation for drift waves, containing the so-called *diamagnetic frequency*

$$\omega_* = k_y v_{*e} = \frac{T_e k_y}{eB\lambda_{pe}}. \tag{2.52}$$

Reproducing the treatment in the case of ions, accounting for inertial terms and assuming quasi-neutrality both for the background pressure and for its fluctuations within the drift ordering scalings, the dispersion relation undergoes slight modifications due to the finite perpendicular extension of the perturbation (see e.g. [86]). Finally, once again finite resistivity introduces a phase shift between density and potential fluctuations, thus an unbalance in the parallel flow. This potentially leads to the destabilization and growth of the drift wave, much like in the case of ballooning modes. On the contrary with respect to the latter, electromagnetic effects actually lead to a stabilization of drift wave turbulence [88].

2.4.3 PERPENDICULAR FILAMENTARY CONVECTIVE TRANSPORT

Both ballooning and drift wave turbulence are the result of the $\mathbf{E} \times \mathbf{B}$ convection of the background profile, arising from the interplay between small scale density/pressure and electrostatic potential fluctuations. The radial particle flux, which in section 2.4.1 has been modelled for simplicity by a purely diffusive approach, can be written as $\Gamma_r = n v_{E,r}$, assuming that the dominating radial convection contribution is given by the radial component of the $\mathbf{E} \times \mathbf{B}$ term. One can expand this expression further under the assumption that both the density and the electric field can be decomposed into a background and a fluctuating part, with the latter averaging to zero over its own period. The time-averaged radial particle flux is

$$\Gamma_r \simeq \frac{n E_\theta}{B} + \frac{\langle \tilde{n} \tilde{E}_\theta \rangle}{B}. \tag{2.53}$$

Equivalently, the radial heat flux is obtained by replacing density with pressure. The first contribution is a so-called *pinch term* linked to the radial convection of the background profiles by means of the equilibrium poloidal electric field distribution. It is often negligible with respect to the second part, which is instead linked to turbulent transport phenomena.

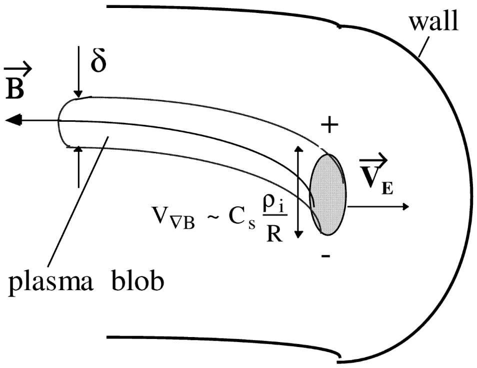

Figure 2.8: Scheme of the charge polarization mechanism driving outward blob propagation, resulting from ∇B and curvature drifts. Reproduced from [89].

As already remarked at the end of section 2.4.1, a strong increase in the particle diffusivity profile D_n takes place across the SOL plasma radius, first seen in Alcator C-Mod experiments [90, 49]. The second term in equation 2.53 is directly linked to this, since both measurements (e.g. [91, 92]) and first-principle turbulent simulations (e.g. [93, 59]) indicate that in the far SOL the fluctuation level is of order unity with respect to the local equilibrium profiles. Specifically, it is seen that far SOL turbulence is dominated by large amplitude coherently propagating structures, having an intermittent character [94]. These structures are seen to be highly localized on the poloidal plane, all the while being strongly elongated along a magnetic field line, so that they are often referred to as *blobs* or *filaments*. From a quantitative point of view, they have seen to be responsible for at least half of the total radial particle flux towards the first wall in the far SOL [94, 95]. As such, they represent a concern for the preservation of non-divertor plasma-facing components, which can possibly undergo significant sputtering or even be severely damaged.

The first physical picture of intermittent filamentary transport, and the currently most widely accepted one, was proposed in [89] and is represented in figure 2.8. On a theoretical ground, filaments are interpreted as the product of the non-linear growth and saturation of an interchange instability, being localized only on the bad curvature side of the machine. These high density structures are generated in the vicinity of the separatrix and detach from the main plasma, travelling radially outwards towards the first wall. Once a blob is born, curvature and ∇B particle drifts act in opposite directions for electrons and ions and induce a charge separation inside of it. The resulting poloidal electric field drives the outward blob propagation by means of its associated radial $\mathbf{E} \times \mathbf{B}$ drift. Since several filaments are expelled per unit time from the confined plasma with a given frequency, they effectively provide a further convective transport contribution to the radial particle flux towards the first wall, in the form of the second term of equation 2.53.

2.4.4 DENSITY SHOULDER AND MAIN CHAMBER RECYCLING

Since filamentary transport is inherently intermittent and non-local (i.e. it does not depend on the local density or pressure gradients), the assumption of purely diffusive transport introduced in section 2.4.1 is not completely correct. Nevertheless, blobs propagate within sub-ms temporal scales, whereas one is often interested in the overall effect of filaments over timescales of the order of (at least) several confinement times. The time-averaged effect of filamentary transport is ultimately translated into the observed anomalous increase of the particle diffusivity in the far SOL, and the consequent far SOL flattening of the density profile which is often referred to as *density shoulder*. This prominent feature of the background density

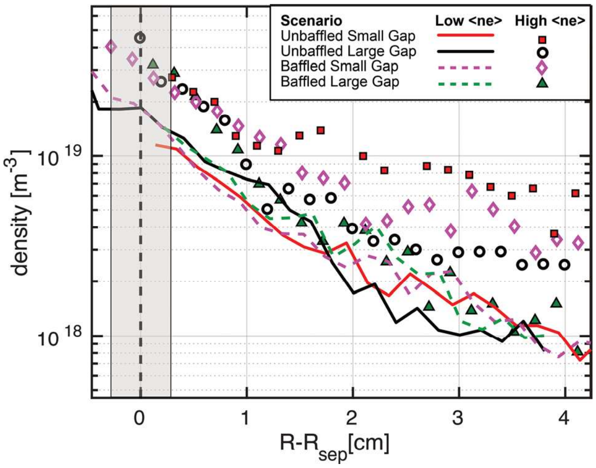

Figure 2.9: Radial SOL density profiles at the outer midplane of TCV discharges, in different core density and main chamber recycling conditions. Reproduced from [55].

profile, already introduced in section 1.4.3, is often observed in high density, high recycling regimes after some distance from the separatrix.

While the enhancement of cross-field transport via filament propagation is commonly identified as a necessary condition for density shoulder formation, the interaction between plasma and neutral particles in non-divertor regions has also been found crucial in its development. More in detail, as a consequence of radial filamentary transport a large part of the total particle flux can travel towards the first wall. Firstly, the parallel particle balance along the SOL field lines is altered in the presence of enhanced perpendicular fluxes, since this effectively removes particles, momentum and heat from a flux tube. As a result, the particle and heat load into the divertor targets are significantly lower than in total absence of perpendicular transport phenomena. Secondly, a large part of the ions is recycled at the first wall instead of the divertor targets, hence an additional particle balance must be established at non-divertor plasma-facing components. A situation in which the cross-field particle flux exhausted at the first wall dominates over the parallel flow towards the target in providing a balance for the incoming recycled neutrals is referred to as *main chamber recycling regime* [96].

In such a regime, the density shoulder feature develops by means of two main effects. The first one is the modification of the source/sink particle flux balance, where a higher far SOL density can be registered simply due to less particles being exhausted towards the target with respect to those travelling radially across the scrape-off layer. Secondly, the additional neutrals introduced in the main chamber by cross-field ion flux recycling at the first wall produce a local increase of the upstream neutral pressure, which can corresponds to higher far SOL local ionization sources if enough energy is provided by, for instance, enhanced perpendicular heat transport. The role of main chamber recycling sources has been well highlighted in recent experimental work on TCV [55]. As shown in figure 2.9, an enhancement of the density shoulder feature is clearly visible in situations of high main chamber neutral pressure, achieved either via low divertor closure or large plasma distance from the outer first wall.

2.5 Three-dimensional drift-Alfvén turbulence

While the description of ballooning modes and drift waves can be in principle made separately, in a typical tokamak plasma the approach to edge turbulence phenomena must necessarily take both of them into account at the same time, since they are ultimately driven by the same $\mathbf{E} \times \mathbf{B}$ transport in presence of a radial density or pressure gradient. The only difference between the two is the energy transfer mechanism from the background equilibrium profiles to the fluctuations, being this ∇B and magnetic curvature without the adiabatic coupling for the case of interchange turbulence, whereas parallel dynamics neglecting the typical ballooning effect on the bad curvature side for drift waves. Since the effect of curvature and magnetic gradient must be retained in any case in a toroidal geometry, which of the two turbulence-inducing mechanism prevails over the other ultimately depends on the validity of the adiabatic response assumption.

The most basic description of tokamak edge turbulence is a two-fluid model in flux tube geometry, called *three-dimensional drift-Alfvén turbulence* or DALF model, evolving the main fluctuation state variables and their respective fluxes. This model reproduces most of the main wave dynamics in a plasma, like sound waves and shear Alfvén waves, but it also includes drift wave and interchange turbulence. First derived in full form in [97], a simpler four-field version has been presented in [98, 99] retaining only the essential dynamics which involves the electrostatic potential $\tilde{\varphi}$, the electron pressure $\tilde{p}_e$, the parallel current $\tilde{j}_\parallel$ and the ion parallel velocity $\tilde{u}_\parallel$, neglecting the effects linked to temperature fluctuations and related heat fluxes. The first two fields act as forcing potentials for the latter two, which are instead regarded in the model as flux variables. The equations comprise the charge conservation law $\nabla \cdot \mathbf{j} = 0$ in the assumption of local charge quasi-neutrality, the electron thermal energy, the generalized Ohm's law and its counterpart for the ion parallel momentum balance. All the equations are formulated within the drift ordering assumption, meaning that at lowest order in $\rho_s/\lambda_\perp \ll 1$ all the fields are advected in the laboratory frame with the $\mathbf{E} \times \mathbf{B}$ velocity. Moreover, only the parallel electromagnetic Alfvén dynamics is retained in this model, with the parallel gradient operator modified accordingly. The full set of DALF equations, of which the derivation is presented in appendix C, is summarized below:

$$\frac{d\tilde{W}_i}{dt} = B\nabla_\parallel \frac{\tilde{j}_\parallel}{B} - \mathcal{K}\left(\tilde{p}_e + \tilde{p}_i\right) \tag{2.54}$$

$$\frac{d}{dt}\left(p_e + \tilde{p}_e\right) = B\nabla_\parallel \frac{\tilde{j}_\parallel - \tilde{u}_\parallel}{B} - \mathcal{K}\left(\tilde{p}_e - \tilde{\varphi}\right) \tag{2.55}$$

$$\hat{\beta}\frac{\partial \tilde{A}_\parallel}{\partial t} + \hat{\mu}\frac{d\tilde{j}_\parallel}{dt} = \nabla_\parallel\left(p_e + \tilde{p}_e - \tilde{\varphi}\right) - C\tilde{j}_\parallel \tag{2.56}$$

$$\hat{\varepsilon}\frac{d\tilde{u}_\parallel}{dt} = -\nabla_\parallel\left(p_e + \tilde{p}_e + p_i + \tilde{p}_i\right) + \eta_\parallel \nabla_\parallel^2 \tilde{u}_\parallel \tag{2.57}$$

The first one is called *vorticity equation* and is closed by a definition for the *vorticity*

$$\tilde{W}_i = \frac{1}{B^2}\nabla_\perp^2\left(\tilde{\varphi} + \tilde{p}_i\right). \tag{2.58}$$

The generalized Ohm's law for the electron parallel dynamics is instead closed by Ampère's law for the parallel magnetic vector potential

$$\tilde{j}_\parallel = -\nabla_\perp^2 \tilde{A}_\parallel. \tag{2.59}$$

The temporal and perpendicular spatial dimensions are normalized to the typical drift scales represented by $\lambda_\perp/c_s$ and ρ_s respectively, where $c_s^2 = T_e/m_i$ and $\rho_s^2 = m_i T_e/(e^2B^2)$. The reference perpendicular scale length is chosen to be the background pressure decay length, $\lambda_\perp = -p_e/\partial_x p_e$, so that at first order $p_e = -\Lambda_{pe}x$ with $\Lambda_{pe} = \lambda_\perp/\lambda_{pe} = 1$. Parallel scales are instead normalized to $L_\| /2\pi \simeq qR$. The dependent variables are scaled in terms of e/T_{e0} for the electric potential $\tilde{\varphi}$ with T_{e0} a reference background temperature, $n_{e0}T_{e0}$ for the pressure $\tilde{p}_e$ with n_{e0} a reference background density, $n_{e0}ec_s$ for the parallel current $\tilde{j}_\|$, c_s for the ion parallel velocity $\tilde{u}_\|$, $\hat{\beta}B\rho_s$ for the parallel magnetic potential $\tilde{A}_\|$ with $\hat{\beta}$ discussed below. All evolved fields are further normalized to a smallness parameter $\rho_s/\lambda_\perp$, so that e.g. $\tilde{\varphi} = 1$ in DALF space is equal to $e\tilde{\varphi}/T_e = \rho_s/\lambda_\perp$ in physical space. Although the ion pressure $\tilde{p}_i$ enters the model equations, it is not directly evolved via an ion energy balance but rather its contribution is considered via an ion-to-electron background temperature ratio $\tau_i = T_i/(\bar{Z}T_e)$, with the average charge number $\bar{Z} = n_e/\sum_j n_j$, so that $\tilde{p}_i = \tau_i\tilde{p}_e$. Furthermore, similarly to the equilibrium p_e profile, for the background ion pressure one has $p_i = -\Lambda_{pi}x$, where $\Lambda_{pi} = \lambda_{pi}/\lambda_{pe}$.

The coefficients appearing in the DALF model equations embody the competition between some characteristic parallel temporal scale of interest and the perpendicular drift time. In detail, the coefficient $\hat{\varepsilon}$ in equation 2.57 represents the square of the ratio between parallel and perpendicular scales, i.e. the contribution of ion sound waves with respect to drift waves

$$\hat{\varepsilon} = \frac{(qR/c_s)^2}{(\lambda_\perp/c_s)^2} = \left(\frac{qR}{\lambda_\perp}\right)^2. \tag{2.60}$$

Similarly, the normalized plasma beta $\hat{\beta}$, mass ratio $\hat{\mu}$ and collisionality C embody the relative parallel Alfvèn, electron thermal motion and electron-ion collisional times, respectively

$$\hat{\beta} = \frac{\mu_0 p_e}{B^2}\hat{\varepsilon}, \quad \hat{\mu} = \frac{m_e}{m_i}\hat{\varepsilon}, \quad C = \frac{0.51\nu_{ei}}{c_s/\lambda_\perp}\hat{\mu}. \tag{2.61}$$

with ν_{ei} the electron-ion Coulomb collision frequency. All these parameters appear in the generalized Ohm's law and set the level of departure from the adiabatic response, hence determining whether a phase shift arises between the pressure perturbation and the electric potential fluctuations because of, respectively, electromagnetic induction, electron inertia or parallel resistivity. The model also includes a viscosity coefficient $\eta_\|$, already introduced in section 2.2.1.

The operator $\mathcal{K}$ is the divergence of diamagnetic fluxes and as such it is called *curvature operator*, being linked to curvature and ∇B effects as explained in section 2.4.2. The functional form of the curvature operator, resulting from the diamagnetic convection of a given quantity f in a generic coordinate system, is $\mathcal{K}(f) = -(\nabla \times \mathbf{b}/B) \cdot \nabla f$. In a simple (x, y, s) field-aligned coordinate system, with s an unperturbed field line coordinate and x, y respectively the radial and binormal directions, the curvature operator can be expressed at first order in the inverse aspect ratio as [86]

$$\mathcal{K}(f) = \omega_B \left(\sin s \frac{\partial f}{\partial x} + \cos s \frac{\partial f}{\partial y} \right) \tag{2.62}$$

with $\omega_B = 2\lambda_\perp / R$ the curvature parameter, i.e. the ratio of the perpendicular profile gradient scale to the background magnetic field gradient scale. Since ballooning modes are essentially controlled by curvature, parametrized by the action of $\mathcal{K}$ on the field perturbations, ω_B takes on the role of a quantifier for the interchange drive.

The turbulent behaviour of the edge plasma stems from the non-linearity associated to the other two differentials operators, which oppositely to $\mathcal{K}$ can be written at zeroth order in the inverse aspect ratio. The first one is the total time derivative $d/dt = \partial/\partial t + \mathbf{v}_E \cdot \nabla$, embodying the $\mathbf{E} \times \mathbf{B}$ advection of the perturbations. It is expressed in the form

$$\frac{d}{dt} = \frac{\partial}{\partial t} + \left(\frac{\partial \tilde{\varphi}}{\partial x} \frac{\partial}{\partial y} - \frac{\partial \tilde{\varphi}}{\partial y} \frac{\partial}{\partial x} \right). \tag{2.63}$$

The second operator is the parallel gradient, which instead is a bit less straightforward. Since the parallel electromagnetic dynamics is an integral part of the model, the operator must be defined in terms of the total magnetic field including both the background part and the shear Alfvén waves disturbances, in the form $\nabla_\parallel = \mathbf{b} \cdot \nabla + \tilde{\mathbf{b}} \cdot \nabla$. The fluctuating component of the magnetic field, albeit small, couples only with the perpendicular component of the gradient, which because of the characteristics of edge turbulence is much larger than the parallel one. The result is that both background and fluctuating terms of $\nabla_\parallel$ are of the same order of magnitude. With this observation, neglecting perpendicular variations of $\mathbf{b}$, the operator can be written as

$$\nabla_\parallel = \frac{\partial}{\partial s} - \hat{\beta} \left(\frac{\partial \tilde{A}_\parallel}{\partial x} \frac{\partial}{\partial y} - \frac{\partial \tilde{A}_\parallel}{\partial y} \frac{\partial}{\partial x} \right) \tag{2.64}$$

reducing to the usual $\nabla_\parallel = \partial/\partial s$ in the fully electrostatic limit.

2.5.1 RESISTIVE BALLOONING - DRIFT WAVE COMPETITION

Among all the interchange instability branches, the resistive ballooning mode (RBM) plays a crucial role in the description of edge turbulent transport in high density regimes. As an example, in the model proposed by [100] diamagnetic RBM stabilization is believed to be key to the L-H transition and the appearance of electromagnetic flutter at increasing transport leads to the L-mode Greenwald density limit. Furthermore, a number of numerical studies made with first-principle turbulence codes indicate that RBM turbulent activity is responsible for the turbulent fluxes observed on the bad curvature side of a tokamak plasma in L-mode-like conditions [101, 29]. A brief linear stability analysis of the RBM, reporting on its maximum growth rate and characteristic spatial scales, is presented in appendix D.

As already noted in section 2.4.2, the turbulent transport drive associated to RBMs is controlled by the cross-phase between density and potential fluctuations. Drift waves are instead intrinsically linked to the adiabatic response of the electrons and their propagation requires pressure and potential perturbations to be in phase. Much like the treatment of the drift wave instability reported in appendix E, the procedure for finding the dominant mode relies on the estimation of the phase shift between density and potential perturbations. Again, the latter is controlled by the mechanism of parallel current closure.

In the treatment considered here, reproduced from [99, 102], all terms are retained in the vorticity equation, including the parallel current gradient and the curvature term. In order to consider only the drive for resistive ballooning modes, in the generalized Ohm's law both inductive and inertial terms are neglected. The following two linearized equations are considered

$$(1+\tau_i)\frac{\partial \nabla_\perp^2 \tilde{\varphi}}{\partial t} = \nabla_\| \tilde{j}_\| - (1+\tau_i)\,\omega_B \frac{\partial \tilde{p}_e}{\partial y} \tag{2.65}$$

$$\nabla_\| \left(\tilde{p}_e - \tilde{\varphi}\right) = C\tilde{j}_\| \tag{2.66}$$

Transformation into the Fourier domain is carried out by applying the substitutions $\partial/\partial t \to -i\omega$, $\nabla \to i\mathbf{k}$. Replacing the parallel current in the vorticity equation yields

$$i\,(1+\tau_i)\,\omega k_\perp^2 \tilde{\varphi} = -\frac{k_\|^2}{C}\left(\tilde{p}_e - \tilde{\varphi}\right) - i\,(1+\tau_i)\,\omega_B k_y \tilde{p}_e \tag{2.67}$$

from which a pressure-potential fluctuation correlation can be readily derived

$$\tilde{p}_e = \frac{k_\|^2 - iC\omega k_\perp^2\,(1+\tau_i)}{k_\|^2 + iC\omega_B k_y\,(1+\tau_i)}\tilde{\varphi}. \tag{2.68}$$

In the limit of finite $k_\|$ and large modes (low $k_\perp$), at which the interchange growth rate approaches the maximum (see appendix D), equation 2.68 can be simplified to

$$\tilde{p}_e \approx \left[1 - i\left(1+\tau_i\right) C\omega_B \frac{k_y}{k_\parallel^2}\right] \tilde{\varphi} \tag{2.69}$$

that is, the quantity

$$\alpha_t = \left(1+\tau_i\right) C\omega_B \tag{2.70}$$

regulates the phase shift between the pressure and potential fluctuations. Furthermore, the turbulent heat flux, given by equation 2.53 but replacing the density perturbation with the pressure one, is given in DALF units by

$$q_r = \left\langle \tilde{p}_e \frac{\partial \tilde{\varphi}}{\partial y} \right\rangle = ik_y \left\langle \tilde{p}_e \tilde{\varphi} \right\rangle = \alpha_t \frac{k_y^2}{k_\parallel^2} \left\langle \tilde{\varphi}^2 \right\rangle \tag{2.71}$$

with turbulent heat transport being low and drift-wave dominated at $\alpha_t \ll 1$, whereas high and interchange-dominated at $\alpha_t \gtrsim 1$. Ultimately, from this analysis α_t emerges as the natural parameter setting both the transition from drift wave turbulence to resistive ballooning transport, and regulating the level of electrostatic plasma edge turbulence, hence it is called *turbulence control parameter*. In particular, at an order-of-magnitude level the transition between different transport regimes is encountered at $\alpha_t \sim 1$ for the typical drift wave scales, i.e. $k_y \sim 1$, $k_\parallel \sim 1$.

The physical units expression for the α_t parameter in the limit of isothermal electrons and ions is [103]

$$\alpha_t = \sqrt{\frac{m_e}{m_i}} \left(1 + \frac{1}{\bar{Z}}\right) \frac{1.02\sqrt{2}e^4 \log \Lambda}{12\pi^{3/2}\varepsilon_0^2} \cdot Rq^2 \frac{n_e}{T_e^2} Z_{eff} f_{Z_{eff}}. \tag{2.72}$$

In equation 2.72, $\log \Lambda$ is the Coulomb logarithm and Z_{eff} is the effective ion charge, already introduced in section 1.1.2. The quantity $f_{Z_{eff}}$ is a function accounting for a $Z_{eff} > 1$ correction to the Spitzer resistivity numerical factor for singly-charged ion species [103].

Notably, α_t is closely related to the electron-ion collisionality (equation 2.11), where the former presents an extra safety factor dependence with respect to the former:

$$\alpha_t \propto q\nu^* \tag{2.73}$$

Despite the closeness in the two definitions, however, it must be beared in mind that the two quantities describe substantially different phenomena.

2.5.2 RELATION WITH THE ROGERS-DRAKE-ZEILER PHASE SPACE

The results obtained in the previous section by means of the DALF model pave the way for a more general description of the edge plasma properties in terms of a well-defined set of dimensionless operational parameters, whose values quantify the overall level of turbulent transport and hint at the dominant underlying instability process responsible for it. In addition, such an approach can yield the main tokamak boundaries separating safe operational conditions from potentially disruptive ones. As a matter of fact, such an approach, employing the α_t parameter among others, has been revisited in recent years in [102, 103] with the purpose of quantifying the power exhaust capabilities of a given plasma scenario, as well as determining the placement of various operational limits, such as the Greenwald L-mode density limit or the L-H (and H-L) transition. In this framework, the key dimensionless quantities are determined based on the main physical plasma properties at the separatrix, usually the electron density $n_{e,sep}$ and temperature $T_{e,sep}$, hence its name of *separatrix operational space theory*.

The concept of a separatrix operational space is actually not completely new. Indeed, an attempt at quantifying anomalous transport based on this approach had already been made in the work by B. Rogers, J. Drake and A. Zeiler [100], henceforth dubbed RDZ, in which a set of turbulence control parameters had been identified which potentially affect the plasma properties at the separatrix, including the profile gradient widths. In their work, RDZ proposed a set of two parameters controlling the edge turbulence level, namely the *ideal ballooning parameter* and the *diamagnetic parameter*, in physical units

$$\alpha_{MHD} = Rq^2 \frac{\beta}{\lambda_p}, \quad \alpha_d = \frac{1}{2\pi q R} \sqrt{\frac{m_i}{m_e} \frac{c_s R}{0.51 \nu_{ei}}} \left(\frac{R}{\lambda_p} \right)^{1/4} \tag{2.74}$$

or in DALF units

$$\alpha_{MHD} = (1 + \tau_i) \hat{\beta} \omega_B \Lambda_{pe}, \quad \alpha_d = \frac{k_\parallel}{\sqrt{(1 + \tau_i)\, C \left(\omega_B \Lambda_{pe} \right)^{3/2}}}. \tag{2.75}$$

These are, respectively, the normalized pressure gradient and the ratio between the characteristic drift wave to resistive ballooning mode scale. From a physical standpoint, ideal MHD ballooning modes become unstable when α_{MHD} reaches a critical value, or equivalently the pressure profile achieves a critical pressure gradient, depending on the plasma magnetic topology [102]. Instead, α_d compares the drift wave velocity to the resistive ballooning mode velocity, so that when $\alpha_d > 1$ the former exceeds the latter and the ballooning structures get entrained in the diamagnetic flow before they can grow and lead to fully developed turbulent transport. This leads to diamagnetic stabilization of RBM turbulence, hence the name of this parameter. In practical terms, α_d explores a physical picture opposite to that described by α_t, having the two opposite effects on the pressure and potential perturbations cross-phase.

The previous discussion does not mean, however, that the $\alpha_t > 1$ and $\alpha_d < 1$ criteria are completely equivalent in establishing which instability mechanism prevails over the other. As a matter of fact, α_t establishes when the characteristic drift wave scales $k_\perp \sim 1$ are destabilized against resistive ballooning, on the contrary α_d sets the boundary at which the typical RBM perpendicular wavelengths $k_\perp \sim k_{RBM}$ are stabilized by diamagnetic effects. This means that there can exist an intermediate range of wavelengths at which both resistive ballooning and drift waves are unstable at the same time and dominate the turbulence at their respective scales, in which case both parameters are lower than unity. On this regard, one can expect pure resistive ballooning (respectively, drift wave) turbulence when $\alpha_t \gg 1$ and $\alpha_d \ll 1$ (respectively, $\alpha_t \ll 1$ and $\alpha_t \gg 1$).

3

THE TCV TOKAMAK

In this chapter the TCV device is introduced. Section 3.1 lists the most relevant characteristics and parameters of the machine. The description of the main plasma scenario actuators is demanded to section 3.2. Lastly, in section 3.3 the extensive set of diagnostic systems for the proper characterization of the TCV scrape-off layer plasma is discussed.

3.1 MACHINE DESCRIPTION

The *Tomakak à Configuration Variable* (TCV) is an experimental fusion research device situated at the Swiss Plasma Center (SPC), École Polytechnique Fédérale de Lausanne (EPFL) in Lausanne, Switzerland [104]. It is a medium-sized tokamak experiment with major radius $R_0 = 0.88$ m, minor radius $a = 0.25$ m, vacuum central toroidal field up to $B_{\phi,0} = 1.54$ T and plasma current up to $I_p = 1$ MA. The machine main components and operational parameters are shown, respectively, in figure 3.1(a) and in table 3.1. The machine features a highly elongated vacuum vessel and is equipped with a set of in-vessel coils, providing stability against certain fast-growing MHD modes. Moreover, on top of the central ohmic solenoid, sixteen independently powered poloidal field coils are placed in between the vacuum vessel and the toroidal field coils. Furthermore, in 2019 removable baffle tiles were installed for the first time, visible in figure 3.1(b). Their purpose is to reduce the neutral penetration from the divertor to the main chamber, allowing easier access to dissipative divertor regimes while being compatible with a wide range of divertor configurations [105, 106].

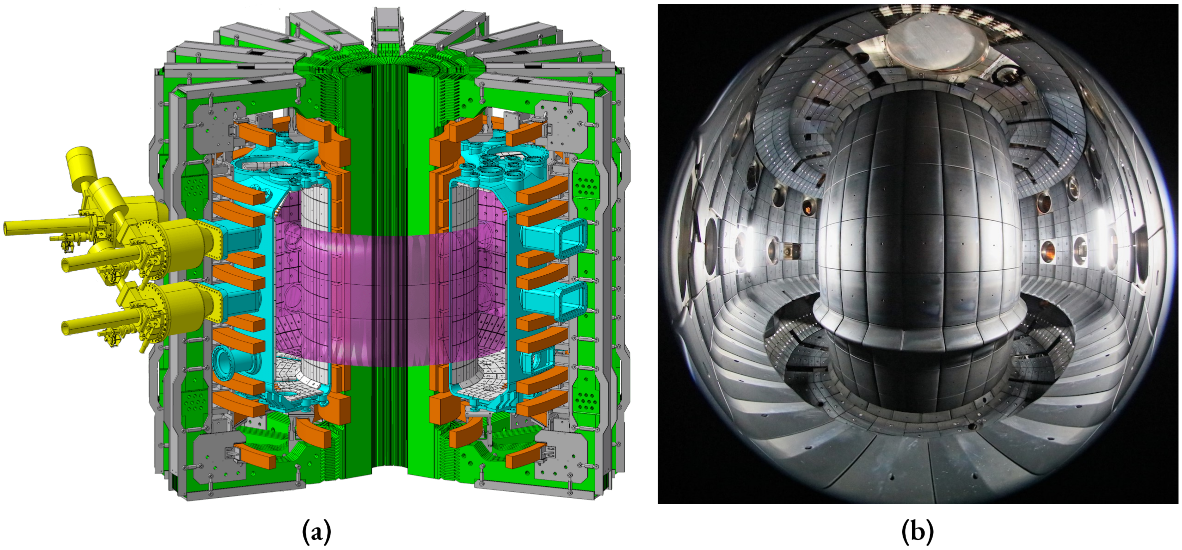

Figure 3.1: Panel (a): CAD model of the TCV tokamak and its main components: toroidal field coils (green), poloidal field coils and central solenoid (orange), vacuum vessel and access ports (cyan), graphite tiles (light gray), mechanical support structures (dark gray), gyrotron ports (yellow), plasma column (purple). Panel (b): Fish-eye photograph of the inside of a baffled TCV vessel, showing some of the machine ports, the graphite protection tiles making up most of the first wall and the baffle tiles protruding from the central column and outer first wall. Both figures: reproduced from *SPC, EPFL*.

Technical parameters of the TCV tokamak	
Major and minor radii	0.88/0.25 m
First wall material	graphite
Maximum toroidal field	1.54 T
Maximum plasma current	1.0 MA
Maximum elongation	2.8
Triangularity range	$-0.6/+0.9$
Core electron density	$1 - 20 \cdot 10^{19}$ m^{-3}
Maximum electron temperature	15 keV
Maximum ion temperature	2.5 keV
Maximum heating power	7 MW
Pulse duration	2 s typical, 4 s maximum
Main plasma ion species	D/H/He

Table 3.1: TCV main operational parameters. Data source: *SPC, EPFL*.

Around 95% of the first wall is covered by graphite tiles. On the one hand, the main advantages of choosing this material come from its very high thermal conductivity and high phase transition temperature of 3750 °C. Moreover, at this temperature graphite sublimes instead of melting, providing a safe high radiation zone in the close proximity of the wall in case of unwanted direct plasma-wall contact. Additionally, carbon is a low-Z impurity and leads to relatively low radiation levels, therefore a high concentration of it is required inside the confined plasma to cause significant loss of energy and confinement by excessive bremsstrahlung emission. These attractive properties made carbon as the material of choice for the design and operation of tokamak devices for many years. On the other hand, the most evident downside of a graphite wall is its large retention capability of hydrogen isotopes, leading to kilograms of tritium being potentially retained in the walls of a reactor-sized device. On top of this, carbon tiles are subject to high physical and chemical sputtering rates in high fluence reactor-relevant scenarios. All these reasons, together with the more favourable thermal and physical properties of tungsten, led to the adoption of the latter in bigger devices.

3.2 MAIN MACHINE ACTUATORS

Knowing how to achieve any given plasma *scenario*, i.e. a state in which some target operational quantities are defined and well-maintained during the whole duration of the plasma discharge, is not at all a trivial task and is necessary for both current and future tokamak devices and power stations. The specification of a scenario includes, for instance, the full behaviour of the plasma itself from its initialization to a stationary operating point up to plasma current ramp-down. The confinement level of the discharge (i.e. whether the plasma must be in L-mode or H-mode) and the state of the plasma in front of the divertor strike points represent other target quantities that must be taken into consideration when preparing a discharge. The desired scenario is used before the experiment to compute a series of feed-forward inputs that the plasma may receive. These include the (signed) currents in the poloidal field coils for the plasma shaping, as well as the the neutral gas flow of the main species and/or seeded impurities and the amount of external heating and current drive. The systems providing all these inputs, named *actuators*, are described in the following for TCV.

3.2.1 PLASMA SHAPING AND EQUILIBRIUM RECONSTRUCTION

The target magnetic configuration of a TCV pulse must be specified before the experiment by means of several geometrical parameters, like the position of the magnetic axis, the plasma shaping, the inner and outer gaps, the divertor configuration and the position of the strike points, the

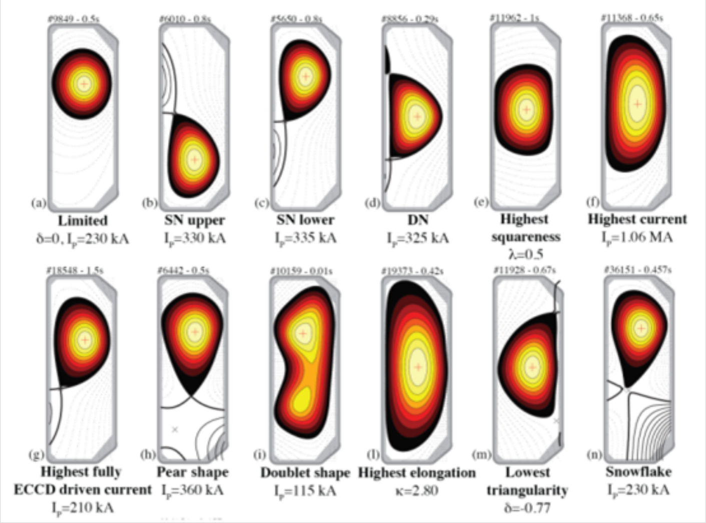

Figure 3.2: A selection of TCV magnetic configurations, including different separatrix shaping and divertor geometries. Reproduced from *SPC, EPFL*.

X-point position. Thanks to its sixteen independently powered poloidal field coils, TCV is allowed to explore a wide range of plasma shapes and magnetic configurations, with even different shaping parameters between the bottom and top halves of the plasma. Accurate definition and control of the currents in some poloidal field coils allows access also to certain divertor geometries different from the standard lower single null. A selection of discharges achieving both conventional and uncommon magnetic configurations is shown in figure 3.2.

Based on the given poloidal flux map, the FBTE code [107] yields the required feed-forward poloidal field coil current waveforms. Another code computes the inputs for the plasma control system, taking into account that the plasma, the central solenoid, the external poloidal field coils and the vacuum vessel (acting as a passive conductive shell) behave as a system of mutually and self coupled inductors. After the discharge has terminated, the actual time-dependent magnetic equilibrium is reconstructed by solving the Grad-Shafranov equation with the LIUQE code [108], where the boundary condition is given by discrete magnetic field measurements from an array of flux loops and a set of pick-up coils distributed around the vessel poloidal contour. LIUQE solves the Grad-Shafranov equation on the right-handed (R, ϕ, Z) orthogonal coordinate system. Following well-established TCV sign conventions [109], the radial coordinate R is directed towards the outside of the torus and zero on the machine central solenoid axis, the vertical coordinate Z is instead directed upwards with $Z = 0$ at the equatorial midplane. The toroidal angle direction ϕ increases when running counter-clockwise as seen from the top, so that the toroidal field and the plasma current have a positive sign when they are oriented accordingly. By TCV standard magnetics nomenclature, the positive and negative toroidal angle directions are named, respectively, *forward* and *reverse*, so that for instance a plasma discharge with $B_\phi > 0$ is said to be run in forward field configuration.

3.2.2 HEATING SYSTEMS

In order to reach ignition, the plasma in a reactor must be first heated to the desired central temperature value of $\sim$ 14 keV. The most trivial method of plasma heating in a tokamak is represented by *ohmic heating* and is actually intrinsic to the device operation, consisting in the dissipation, in the form of heat, of the particle momentum and energy associated to the plasma current by means of Coulomb collisions. The corresponding power density is given by the expression $S_{ohm} = j^2/\sigma$, with j the current density profile and σ the plasma electrical conductivity defined by L. Spitzer et al in the 1950's [110, 73] by the expression

$$\sigma = \frac{3}{4\sqrt{2\pi}} \frac{\left(4\pi\varepsilon_0\right)^2 T_e^{3/2}}{Ze^2 m_e^{1/2} \ln\Lambda} \tag{3.1}$$

where Z is the ion charge number and $\ln\Lambda$ is the Coulomb logarithm. A first problem with ohmic heating becomes immediately apparent when analyzing equation 3.1: given the $T_e^{-3/2}$ dependence, this mechanism is less and less efficient at heating the plasma as the temperature rises, hence external heating methods are required in a reactor to bring the plasma into burning conditions before alpha heating takes over. The most commonly used additional power sources for a magnetic confinement device are neutral beam injection and wave resonance heating, which can be used also to drive additional non-inductive plasma current components. The implementation of both methods on TCV is discussed in the following.

NEUTRAL BEAM INJECTION (NBI)

The *neutral beam injection* heating technique consists in launching a beam of fast neutral particles into the plasma, usually the same isotopes as the main ion species. The injected neutrals are then ionized through charge-exchange and electron impact processes with the plasma, getting trapped inside the device by the magnetic field as fast ions and ultimately transferring their energy to thermal electrons and ions by means of Coulomb collisions. The neutral beam itself is made starting from positive or negative ions extracted from a low temperature plasma source and accelerated through a series of grids biased with respect to one another. The extracted ions are then neutralized via charge-exchange processes by passing through a neutral gas cloud. The residual electrically charged component of the resulting beam is deflected away by a system of magnetic fields, so that only the neutralized component enters the tokamak vessel.

On TCV, two NBI heating systems are installed, shown in figure 3.3(a), which use a positive ion

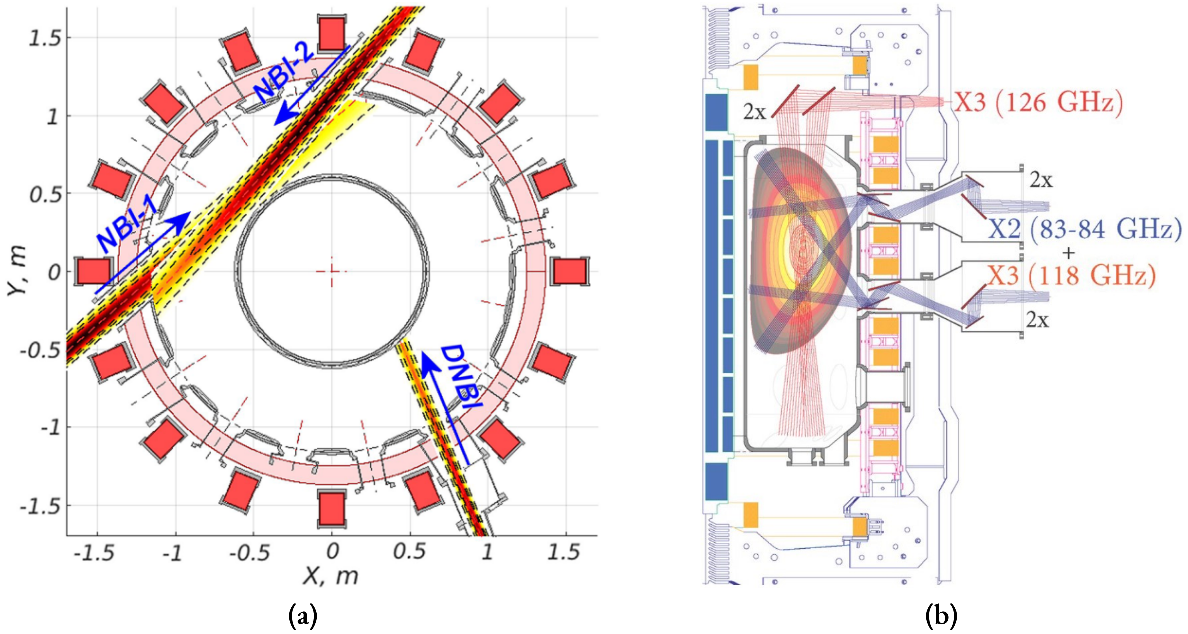

(a) (b)

Figure 3.3: Toroidal view of the TCV neutral beam injection position and geometry, including also the diagnostic beam. Reproduced from [111]. Panel (b): overview of the different ECRH launchers and injection directions on a TCV poloidal cut. Adapted from *SPC, EPFL*.

source with an average nominal current density of $\sim 230-250$ mA/cm^2 [111]. They both have a tangential injection direction, in order to maximize the absorption of the beam energy along their path. The first system (NBI-1), injecting in reverse direction, is able to provide a beam energy of up to 28 keV for a maximum injected power of 1.3 MW or maximum energy of 1.3 MJ per shot. The second system (NBI-2) injects neutrals in forward direction with an energy up to 52 keV and a maximum power of 1.1 MW. Both beams can be used in principle at the same time, however their power does not really add up because of the large first orbit losses on the counter-current directed system. A third system (DNBI) is installed with radial injection direction, a neutral energy of 50 keV and a power of 80 kW, and is used only for diagnostic purposes. For the discharges considered in this work, only the NBI-1 system has been used for heating.

ELECTRON CYCLOTRON RESONANCE HEATING (ECRH)

When an electromagnetic wave interacts with charged particles in a hot magnetized plasma, a resonant interaction between the two can take place if the frequency of the wave matches the gyrofrequency of the particles themselves or one of its harmonics. Depending on the wave frequency different resonant interactions can be promoted with either electrons or ions, giving rise to either *electron cyclotron resonance heating* (ECRH) or *ion cyclotron resonance heating* (ICRH). At a given injection frequency, the absorption position of the wave depends on the radial profile of the toroidal magnetic field and, in some cases, on the density profile. More importantly, the wave must have the possibility of propagating up to the absorption position without encountering reflection layers first, according to the dispersion relation of the plasma. Specifically for ECRH, the fundamental harmonic can be rarely used because of a cutoff layer preventing propagation up to the absorption radius, thus the second or third harmonics are much more often used in tokamak devices.

In TCV, only the ECRH scheme is implemented, with the injection geometry visualized in figure 3.3(*b*). The system is composed of two 83 GHz X2 gyrotrons providing up to 680 kW of power each at the second harmonic, with launchers located on one equatorial and one upper access ports. Three 118 GHz X3 gyrotrons operate at nominal power of 480 kW at the third harmonic, launching also from one equatorial and one upper ports. Finally, the machine is equipped with two dual frequency gyrotrons at either the second (X2, 84 GHz) or third (X3, 126 GHz) harmonics, launching respectively through equatorial/upper or top ports. In order to maximize the absorption, the top launcher injects in almost tangential direction to the resonant surface. The toroidal injection angle of the equatorial and upper launchers can be varied between discharges, whereas the poloidal angle can be changed even during a single pulse, making it possible to locally deposit power at different normalized plasma radii. In principle the injected wave can have two different polarizations, with the electric field either parallel to the magnetic field (O-mode) or perpendicular to it (X-mode). However, the latter is used for heating purposes most of the time, since it is much better absorbed.

3.2.3 GAS INJECTION SYSTEM

The TCV gas injection system, used mostly for fuelling or impurity seeding, is composed of several *piezoelectric gas valves* [112]. A voltage of up to 250 V is applied to a piezoelectric crystal to regulate the viscous gas flow through a capillary tubing, where the line pressure is measured in real-time by a pressure transducer. Since the actual gas flow is in a direct one-to-one relation with the pressure sensor voltage reading, the latter is converted to a measurement of the instantaneous gas flow rate after proper calibration. The fast control electronics acting on the opening voltage allows for sub-ms flow rate control that can match almost any arbitrary programmed waveform shape.

The whole system comprises a total of ten gas valves, distributed around different toroidal and poloidal locations. The currently most used injection locations are displayed in figure 3.4 and include a system at the top of the machine as well as two other valves, one located in the common

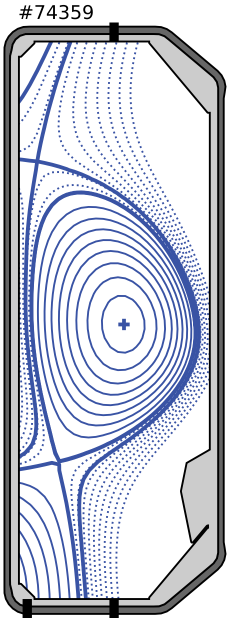

Figure 3.4: TCV poloidal cut with the three main gas injectors (black).

flux region and one in the private flux region, with reference to a conventional divertor configuration. The top and outer bottom valves are used routinely for main species fuelling, whereas the inner bottom one and the other systems are exploited mostly for impurity seeding. A further valve is used as flow gate for glow discharge cleaning and boronization. Finally, an additional valve at the midplane and two more at the inner and outer baffle tips inject trace amounts of hydrogen or helium for the GPI diagnostic [113].

3.3 OVERVIEW OF THE TCV EDGE DIAGNOSTICS

Achieving reliable measurements of the relevant plasma quantities is key in order to extrapolate physics considerations from an experiment. TCV is equipped with a large range of diagnostics yielding various kinds of measurements in different regions of the plasma, with the edge, scrape-off layer and divertor chamber being among the best diagnosed ones. This section contains the description of the main diagnostic systems used in this work.

3.3.1 BOLOMETRY

Bolometers measure the total radiative emission of the plasma integrated along several lines of sight. By covering the vessel poloidal cross section with a proper arrangement of mutually crossing lines of sight, the two-dimensional plasma emissivity profile can be tomographically reconstructed assuming toroidal symmetry. The TCV legacy bolometer system, installed until 2020, is composed of eight pinhole cameras with one looking top-down, one bottom up and two for each lateral ports, for a total of 64 lines of sight [114]. Each one of them features a gold foil sensitive to all photons emitted by the plasma in the spectral range between 1 eV and 10 keV, with a 4 μm thickness for minimization of their thermal inertia and therefore their effective response time τ_{eff}. The gold foil is in thermal contact with a temperature-dependent electrical resistor (thermistor). A change in foil temperature translates directly into a change of the thermistor electrical resistance and thus of the voltage drop across it, measured via the imbalance in a Wheatstone bridge. By means of the bolometer imbalance ΔV one can compute the line-integrated emissivity as

$$\int_{LOS} \frac{dP}{dV} dl = C_{eff} \left(\frac{d\Delta V}{dt} + \frac{\Delta V}{\tau_{eff}} \right) \tag{3.2}$$

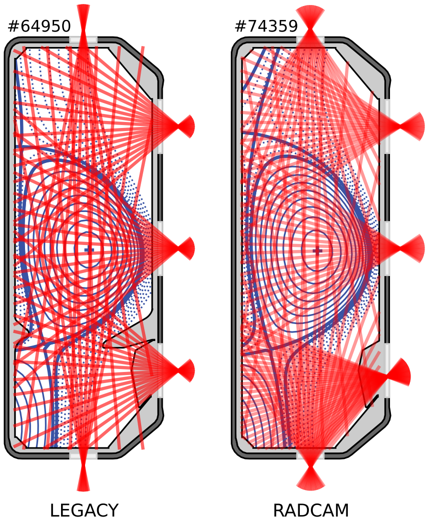

Figure 3.5: TCV bolometer system before (left) and after the 2020 RADCAM installation (right).

with C_{eff} taking into account the geometry and the electronics of the camera, the gold foil heat capacity and its temperature coefficient of resistance. The legacy bolometer lines of sight can be seen in the left panel of figure 3.5. The resulting tomographic inversion yields emissivity maps with a 4 cm spatial and 10 ms temporal resolutions.

The TCV bolometer system has been upgraded in 2020 in the context of the RADCAM diagnostic installation [115], which increased the number of lines of sight to 120 (20 top-down, 20 upper-lateral, 20 equatorial, 40 bottom-lateral for the divertor chamber, 20 bottom-up). The new lines of sight are visible in the right panel of figure 3.5. With respect to the legacy system, the RADCAM bolometers feature a reduced 3 μm gold foil thickness to decrease the heat capacity and thus the response time. A 200 nm platinum layer placed below the gold absorber increases the thermal conductivity, allowing greater sensitivity and smaller working voltage ranges. The new foils are able to absorb the full energy of the photons below 4 keV, albeit with photon energies below 10 eV suffering from a reflection of at least 20 %. To compensate for this issue, a further 50 nm carbon coating has been included in the design, allowing to fully extend the sensitivity to photons in the energy range $1 - 100$ eV.

3.3.2 BARATRON GAUGES

In highly dissipative divertor regimes like those considered in this work, having a reliable measurement of the neutral pressure in the divertor chamber and at the midplane is of crucial importance. *Baratron gauges* are a standard diagnostic to measure the neutral pressure in a high-vacuum device like a tokamak. The working principle of a baratron is based on the measurement of the capacitance between a fixed rigid electrode and a conductive diaphragm that deflects under a change in absolute pressure on the vessel side, independently of the type or the chemical/isotopical composition of the measured gas. This deflection causes an imbalance on the sensor capacitance, which can be converted to a voltage signal that is in a linear relation with the absolute pressure value.

On TCV, the neutral pressure measurements are provided by four magnetically shielded and vibrationally isolated JET-like baratron gauges [116]. They are installed outside the toroidal field coils and connected to the vacuum vessel by dedicated extension ducts, whose poloidal position is represented in figure 3.6 by means of green patches. The two baratrons relevant for this study are the divertor gauge, placed at the lower left cor-

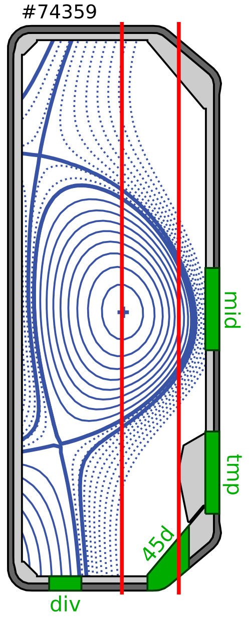

Figure 3.6: Ducts leading to the TCV baratrons (green), main and edge FIR vertical channels (red).

ner of the machine and the midplane gauge placed at the outer midplane wall. Two other gauges yield measurements at the lower 45-degree tiles on the low-field side and in the turbomolecular pump duct. The reference side of each baratron is permanently evacuated at a pressure of 10^{-5} Pa, where the vacuum is maintained by a chemical getter system. The instrument yields neutral pressure measurements between 10^{-3} and 1 Pa, with the former value being the reference level for the noise floor.

3.3.3 INTERFEROMETRY

One of the most essential quantities for the characterization of a plasma, both in general and in particular for this work, is the electron density at different radial and poloidal locations in the vessel. By using the *interferometry* technique one can obtain line-integrated measurements of the electron density along several lines of sight. Since the plasma is a dispersive medium with its own refraction index, by shooting a laser beam through it with a given wavelength λ_0, chosen so as to be far both from cutoff and resonance phenomena, a phase shift is introduced along the laser path given by

$$\Delta\varphi = \frac{e^2\lambda_0}{4\pi\varepsilon_0 m_e c^2}\int n_e\, dl. \tag{3.3}$$

In this way the line-integrated electron density can be obtained, which can be divided by the chord length to get the line-averaged estimate $\langle n_e \rangle$. The TCV Far-InfraRed (FIR) interferometry system features a Mach-Zehnder type interferometer measuring the line-averaged electron density along fourteen parallel chords, spanning the vessel in the vertical direction. In figure 3.6 two of them are shown, namely the main central chord normally used for feedback control of the core electron density, and the edge chord yielding the line-integrated density in the edge region on the outer midplane. The system uses a far-infrared CH_2F_2 laser pumped by a CO_2 laser, operating in continuous wave regime, and a detector unit sampling the line-integrated density at 20 kHz. Before crossing the vessel, the laser is split into a reference beam, whose phase is shifted by a rotating grating, and the fourteen channels spanning the vessel radially. The phase shift between the reference and plasma beams is estimated from the number of fringes arising from the interference pattern. At the operating wavelength of 184.3 μm, one fringe corresponds to a line-integrated density of $1.2078 \cdot 10^{19}$ m^{-2}.

3.3.4 INFRARED THERMOGRAPHY

Infrared thermography is a crucial diagnostic to estimate the heat load impinging on the tokamak first wall, in particular around the divertor strike points. This system is based on the measurement of the electromagnetic radiation emitted by any object having a temperature above absolute zero.

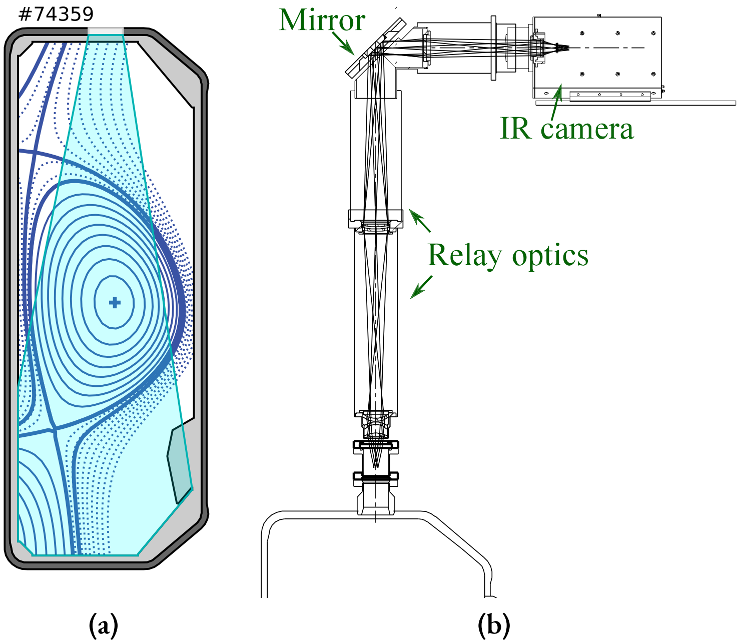

Figure 3.7: Panel (a): Field of view of the Vertical InfraRed (VIR) system. Panel (b): schematic view of the VIR system, with the position of the IR camera and the optical system. Reproduced from [67].

The spectral radiance for a perfect absorber and emitter, called black body, at thermal equilibrium is given at any wavelength λ and temperature T by the well-known Planck's law

$$I_{BB}\left(\lambda, T\right) = \frac{2hc^2}{\lambda^5} \frac{1}{\exp\left(\frac{hc}{\lambda T}\right) - 1} \tag{3.4}$$

where $I_{BB}\left(\lambda, T\right)$ is expressed in $\mathrm{W}/\left(\mathrm{m}^3 \cdot \mathrm{sr}\right)$ and represents the power emitted by a black body per unit surface area, solid angle and wavelength. By choosing appropriately a given narrow range of wavelengths, the number of counts detected by a single pixel of an infrared camera is given by

$$C_\lambda\left(T\right) = c_0 \varepsilon_\lambda I_{BB}\left(\lambda, T\right) \Delta t_{int} + C_{bg} \Delta t_{int}. \tag{3.5}$$

The quantity ε_λ is the surface emissivity, while Δt_{int} is the integration time during which the acquisition takes place and is directly related to the measurement time resolution. The proportionality coefficient c_0 takes care of the selected spectral bandwidth, the transmittance of the optical system, the geometry of the camera and its calibration relating the number of counts per second of a pixel to the output voltage. The additional term C_{bg} accounts for any other sources of counts per second not related to thermal radiation, like the electronic noise of the sensor. For the purposes of infrared thermography, equation 3.5 can be used as a calibration relation for counts to temperature conversion, provided the active component of the signal is much larger than the background part.

The TCV infrared thermography system comprises three cameras in total [117]. A vertical camera (VIR), whose field of view is shown in figure 3.7(*a*), acquires measurements of the tiles temperature at the machine floor where the outer strike point is typically located. A horizontal system (HIR) allows to probe the temperature distribution around the inner divertor leg on the central column and can be mounted either at the equatorial or at the bottom-lateral ports. A third system (TIR) yields measurements at the lower bottom port protection tiles with a tangential field of view and is useful for divertor configurations with large outer strike point radius. The latter two cameras are not shown in the figure, since for the purposes of this work only data from the VIR system is employed. Its setup, represented in figure 3.7(*b*), consists of a camera working in the medium-wave infrared (MWIR) spectral range, sensitive to wavelengths between 3.7 and 4.8 μm with no filter installed. The maximum frame rate and minimum spatial resolution are $\sim$ 200 Hz and $\sim$ 2 mm, respectively, in full frame mode. The camera can also operate in subframe mode, with a maximum temporal resolution of $\sim$ 30 kHz, useful for H-mode studies for which the short inter-ELM time intervals must be resolved. It is worth stressing out that the usage of IR thermography yields meaningful results only in situations of attached divertor with no rollover, where there is a non-zero heat flux impinging on the target. This condition is however always satisfied in the discharges considered in this work, as will be shown in chapters 5 and 6.

3.3.5 THOMSON SCATTERING

Thomson scattering consists in the elastic scattering of a photon by a free charged particle. It represents the classical limit of Compton scattering in the case of photon energy being much smaller than the particle rest mass energy, since neither the charged particle kinetic energy nor the photon energy change after the interaction. When a free charged particle interacts with a sinusoidal electromagnetic wave with angular frequency ω_i, it starts oscillating under the influence of the Lorentz force associated to the wave electric and magnetic fields. The particle will then produce its own dipole electromagnetic field due to the induced oscillation, with the same polarization as the incident wave and the amplitude being maximum at 90° to it. The scattered wave angular frequency is given by

$$\omega_s = \omega_i + (\mathbf{k}_s - \mathbf{k}_i) \cdot \mathbf{v}. \tag{3.6}$$

The frequency of the scattered wave is Doppler-shifted with respect to that of the incident wave. This shift arises because of the particle motion with respect to both the incident wave and the observation directions. Finally, since the amplitude of the particle oscillation depends inversely on its mass, the scattering contribution by an ion is negligible compared to an electron.

In a plasma the amplitude of the scattered wave is given by the sum of the electric fields produced by all electrons inside the scattering volume, thus the total scattered intensity will also depend on spatial correlations between the electrons themselves. These arise mainly because of plasma self-screening effects over a Debye length $\lambda_D = \sqrt{(\varepsilon_0 T_e)/(n_e e^2)}$, being therefore negligible when the wavelength of the incident radiation is much smaller. This is the typical case of a Thomson scattering measurement system used in a tokamak, exploiting high-energy pulsed laser beams in the near-IR or visible ranges. In this condition, being the velocity of electrons at thermal equilibrium distributed according to a Maxwell-Boltzmann function, the scattered power spectrum is a Gaussian function centered around the incident radiation wavelength. The spectrum full width at half maximum and integral are related to, respectively, the electron temperature and density inside the scattering volume, so that its measurement can yield direct estimates of both T_e and n_e. Some modifications to the spectrum shape must be taken into account at electron temperature higher than a few 100 eV, due to a significant part of the electrons travelling at non-negligible fractions of the speed of light.

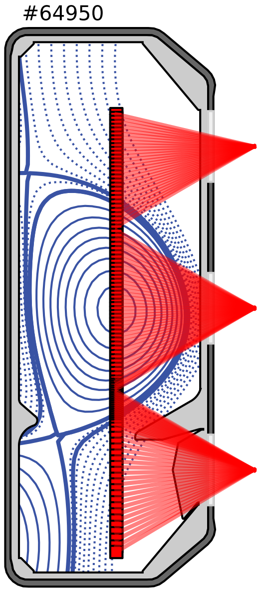

Figure 3.8: Setup of the TCV TS system, with the scattering volumes as red squares and the lines of sight as red lines.

The TCV Thomson scattering (TS) system [118], shown in figure 3.8, utilizes three Nd:YAG lasers at $\lambda_0 = 1.06\ \mu$m, injected in the vessel along the central vertical line at $R = 0.9$ m. Due to possible misalignment among the lasers, the measurements are benchmarked against the central FIR interferometer chord on a shot-to-shot basis. Each laser features a repetition rate of 20 Hz, nonetheless their relative timings can be adjusted to maximize either the acquisition frequency or the signal-to-noise ratio. The light scattered by the vertically distributed scattering volumes is gathered by three wide-angle camera lenses, placed one at each lateral port of a sector, and focused onto sets of optic fiber bundles directing the light towards detector units. The collected light is ultimately analyzed by filter polychromators with either four or five spectral channels, optimized to yield electron temperature measurements from 0.1 eV up to 20 keV. The present setup comprises 117 observation points covering vertical positions Z between -69 cm to $+67.9$ cm. The spatial resolution, given by the vertical extent of a single scattering volume, depends on the channel location and is 12 mm for most channels. Scattering volumes in the region $Z \in [-33.5, -22]$ cm have a resolution of 6 mm for pedestal, edge and scrape-off layer measurements, whereas the divertor channels with $Z < -36.9$ cm and the uppermost ones with $Z > 56$ cm have a lower spatial resolution of $17 - 19$ mm gaining instead on a higher sensitivity in a region where the plasma is typically much colder than in the confined and edge regions.

3.3.6 LANGMUIR PROBES

Langmuir probes yield measurements of plasma density and temperature at the first wall of a tokamak. They consist of an electrode inserted into the plasma that collects a certain current I when biased to a voltage V with respect to the vacuum vessel potential. The collected current depends on the geometry of the electrode itself, but also on the physics of the interaction between a plasma and a solid interface, governed by the Debye sheath theory (see section 2.2.2).

On TCV, the most recent Langmuir probe (LP) configuration [119, 120] consists of 194 probes distributed all around the machine poloidal contour, like shown in figure 3.9(*a*). The probe tips, all with a diameter of 4 mm, are made of graphite and have different shape according to their poloidal position, with domed probes covering the majority of the wall whereas flush probes are used around the midplane part of the inner column, see figure 3.9(*b*). For older discharges, rooftop probes were positioned on smaller portions of the TCV tiles either on the lower central column above the inner baffle, or well above the midplane at the outer wall.

All probes typically operate with a triangular wave bias voltage sweep between -100 V and $+80$ V at a frequency of 330 Hz. The acquired time-varying current signal is correlated to the applied voltage by means of the model function

$$I(V) = I_{sat}\left[1 + \alpha_{sheath}\left(V - V_{fl}\right) - \exp\left(\frac{V - V_{fl}}{T_e}\right)\right] \tag{3.7}$$

derived directly from Debye sheath theory. In equation 3.7, V is the probe bias voltage with respect to the vacuum vessel, I_{sat} is the ion saturation current, α_{sheath} is the Debye sheath expansion factor and V_{fl} the floating potential. Physically, I_{sat} quantifies the maximum ion current that can be gathered by the probe tip at very large negative bias. It is given by the parallel ion current at the sheath entrance

$$I_{sat} \approx \frac{1}{2} e n_e c_s A_s \tag{3.8}$$

with A_s the probe collection area. While the latter is a geometrical quantity and therefore fixed once the magnetic field topology is given in the proximity of the probe, at very large negative bias some non-linearities come into play causing the equivalent sheath surface area to increase, leading to imperfect saturation of the ion flux. This effect is modelled in equation 3.7 via a linear relation between the current and the voltage, with the slope given by the α_{sheath} coefficient. By fitting the experimental $I - V$ measurements over many sweeping cycles by means of equation 3.7, one can

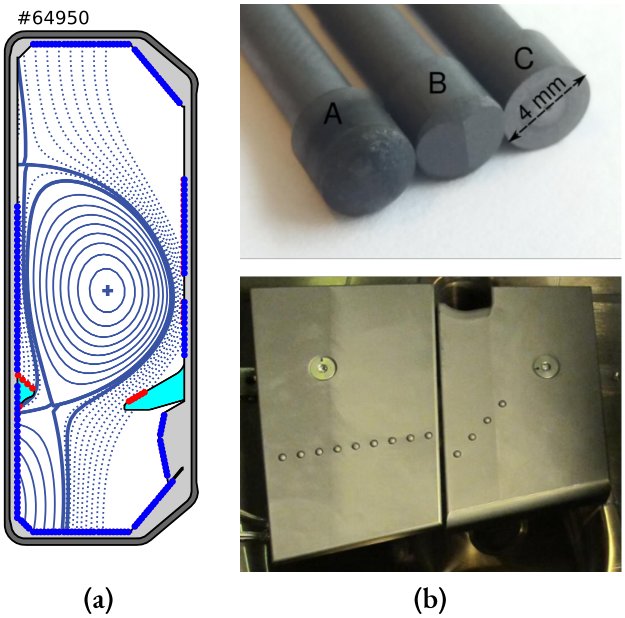

(a) (b)

Figure 3.9: Panel (a): spatial distribution of LPs along the TCV poloidal contour as blue dots. The probes in red are present in the vessel only when the baffle tiles (cyan) are installed. Panel (b), top: picture of the probe tips installed at TCV (A: domed, B: rooftop, C: flush). Reproduced from [119]. Panel (b), bottom: installation of some Langmuir probes on two TCV graphite tiles. Adapted from *SPC, EPFL*.

deduce an estimate for I_{sat}, V_{fl}, n_e and T_e at the same time. Notably, this equation is strictly valid only if the electron velocities are distributed according to a Maxwellian, which may not be the case at low temperatures when high-energy tails of the electron distribution function start to dominate and may lead to an overestimation of T_e. Typically, a lower bound on the reliability of the Langmuir probe measurement is posed when $T_e = 5$ eV.

Besides the swept mode, TCV LPs can operate also under large negative bias voltage to infer measurements of the ion saturation current with a sampling rate of $\sim$ 200 kHz (I_{sat} *mode*). In addition, the probes can be left electrically insulated and therefore biased to their respective floating potential (V_{fl} *mode*), giving information on the electric field distribution in the proximity of the wall. As a last mode of operation, the probes can be biased to the machine vessel potential (j_0 *mode*) in order to acquire the electric currents in the divertor (see e.g. [121]).

3.3.7 FAST RECIPROCATING PROBE

The extensive set of wall-mounted Langmuir probes has been extended on TCV in 2016 by the installation of a *fast reciprocating probe* [123, 124], mounted at the outer midplane as shown in figure 3.10(*a*), providing high spatial resolution measurements of the electron density and temperature in the edge and scrape-off layer regions. The probe head features ten graphite electrodes, embedded into a boron nitride body for electrical insulation and surrounded by a graphite shroud for protection against high heat fluxes. The diameter of the probe head is $\sim$ 2.5 cm, with each electrode being exposed to the plasma for a length of 1.6 mm and a diameter of 1.5 mm. The full setup of the diagnostic (not shown here) includes a shaft over which the head is mounted and a rear feedthrough transmitting the electrical signals. The system is mounted on a drive mechanism featuring a motor capable of providing a fast reciprocating motion over 20 cm within 90 ms, with a peak radial velocity of 2.2 m/s.

The probe tips are rotated by $\sim \pm 9^\circ$ from the nominal position so as to be aligned with the direction of the magnetic field without mutual shadowing, as shown in figure 3.10(*b*), where each electrode is assigned a different colour according to the measured quantity. One electrode (yellow) is in ion saturation, as are the two tips in black while being also aligned with the magnetic field in order to act as Mach probes for parallel ion flow investigation. Five pins (red) arranged in a cross-like pattern collect the floating potential over different radial and poloidal positions of the probe head. The radial separation between the three central floating potential electrodes is 1.57 mm, whereas the poloidal separation among the three that are aligned with the magnetic field are 4 and 10 mm respectively. All the V_{fl} and the I_{sat} pins provide measurements at a very high time resolution with sampling rate 2.5 MHz, with a bandwith of approximately 5 MHz. Finally, the two electrodes

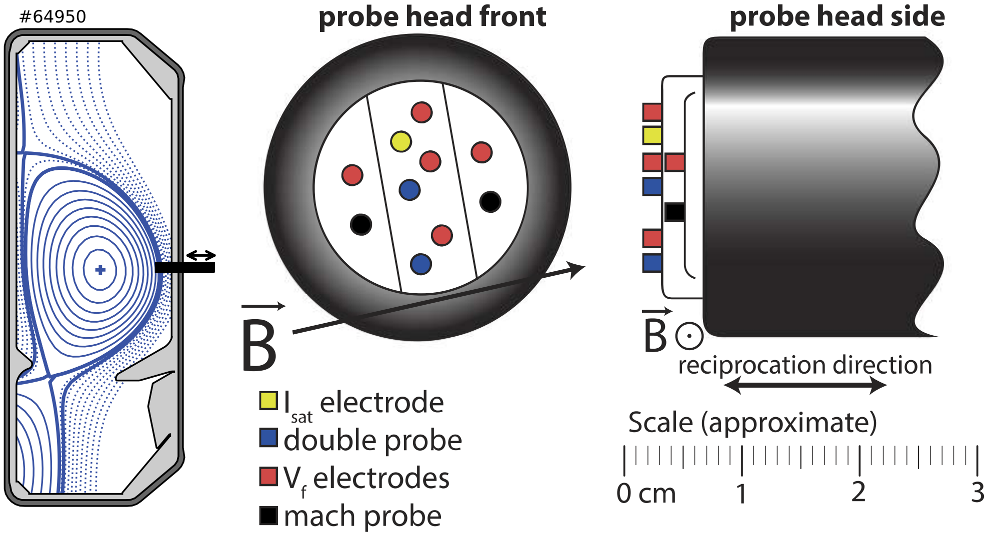

(a) (b)

Figure 3.10: Panel (a): position of the fast reciprocating probe at the TCV outer midplane. Panel (b): Front and lateral views of the probe head, together with a description of the installed electrodes. Reproduced from [122].

shown in blue operate in double probe setup with a 300 V peak-to-peak triangular voltage sweep at a frequency of 1 kHz, providing an I-V characteristic every 0.5 ms. The double probe setup consists in biasing one electrode with respect to the other with a voltage V without a common ground reference, so that the resulting current through both electrodes is given by the function

$$I(V) = I_{sat} \tanh\left[\frac{e\left(V - V_{off}\right)}{2T_e}\right] + I_{off}. \tag{3.9}$$

By fitting the experimental I-V characteristic with equation 3.9, one gets the ion saturation current I_{sat} and the electron temperature, as well as eventual offsets on the voltage and current signals V_{off} and I_{off}. The density at the sheat entrance in front of both probe tips follows from equation 3.8, where again the estimation of the probe collection area must account for non-linear expansion effects at large bias. A careful treatment of the sheath expansion can be found in reference [125].

3.3.8 THERMAL HELIUM BEAM

Most recently, a fast *Thermal Helium Beam* (THB) spectroscopic diagnostic has been installed at TCV, originally designed for the RFX-mod2 experiment [126, 127], with the aim of measuring the time evolution of the radial electron density and temperature profiles, along with fast turbulent fluctuations.

In its simplest setup, a THB system measures the intensity of three visible HeI lines at $\lambda_1 = 667.8$ nm, $\lambda_2 = 728.1$ nm and $\lambda_3 = 706.5$ nm originating from the spontaneous decay of neutral helium locally puffed into the plasma. By means of collisional-radiative model calculations like those in [128, 129] it can be shown that, at a first approximation, the ratio between the λ_1 and λ_2 intensities depends mainly on the electron density, whereas the ratio between λ_2 and λ_3 depends mainly on the electron temperature. As a consequence, both n_e and T_e can be experimentally obtained by measuring the I_{667}/I_{728} and I_{728}/I_{706} line ratios.

While this evaluation yields good results at low density, at medium-high n_e the plasma becomes optically thick with respect to certain resonance lines in the ultraviolet range. As a consequence of the radiation re-absorption some excited states of neutral helium present a higher population than expected, leading to inaccurate collisional-radiative estimates of the electron profiles. The re-absorption can be estimated by monitoring the I_{501}/I_{728} line ratio, where I_{501} is the intensity of a fourth HeI line at $\lambda_4 = 501.6$ nm. For the typical density values of $n_e \gtrsim 10^{17} - 10^{18}$ m^{-3} encountered in the edge and scrape-off layer regions of a tokamak, it has been shown that neglecting the radiation re-absorption by the neutral helium cloud leads to significant errors in the estimates of n_e and T_e.

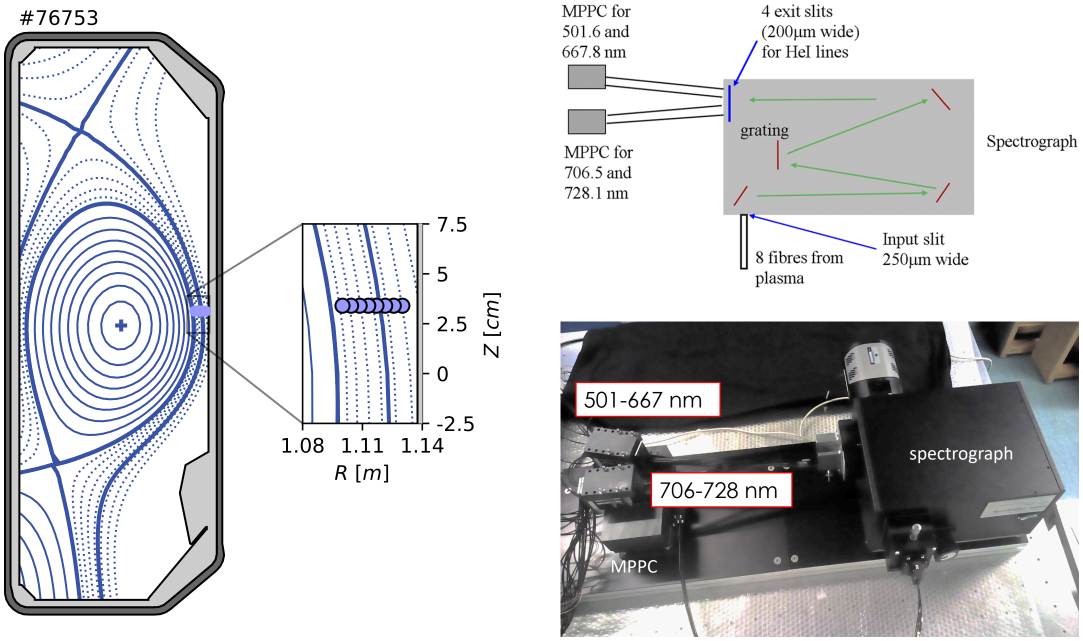

(a)

(b)

Figure 3.11: Panel (a): radial position of the THB observation volumes, with a zoom on the edge region for better visibility. Panel (b): schematic view and photo of the THB diagnostic, showing the spectrograph for separation of the four HeI lines and the two MPPCs for signal analysis. Top: reproduced from [127]. Bottom: courtesy of *M. Agostini*.

The THB system installed on TCV measures the electron density and temperature profiles at eight radially spaced locations at the outboard midplane, as seen in figure 3.11(*a*), with a spatial resolution of 4.3 mm. Given that the implemented line ratio analysis technique relies on the stationary solution of the collisional-radiative model, a reliable estimate of the electron density and temperature can be obtained only if the measurement sampling rate is lower than the decay rates associated to all the considered atomic transitions. The 706.5 μm line has the longest relaxation time at 1 μs for $n_e \sim 10^{19}$ m^{-3}, and larger for lower density, setting the maximum time resolution of the diagnostic at $\sim$ 1 MHz, which is nevertheless sufficient in order to resolve the fast time scales associated to turbulent structures in the scrape-off layer. The slower dynamics of the electron profiles at $\sim 1-10$ kHz can be also obtained by averaging light samples within a $\sim 0.1-1$ ms long time window.

The optical and acquisition systems of the THB are shown in figure 3.11(*b*). The HeI light emitted from each observed volume is gathered by optic fibers and delivered to the 250 μm-wide entrance slit of a spectrograph. The light is then bounced onto a small dispersion grating with 600 grooves/mm and a dispersion of 5 nm/mm. The separated light spectrum is then directed towards a 200 μm-wide exit slits, appropriately placed with respect to the rest of the optical system of the spectrograph so as to select only the four HeI lines of interest. The intensity of each line is measured by means of solid-state Multi-Pixel Photon Counter (MPPC) detectors, consisting in a large number of avalanche photodiode photomultiplier pixels operating in Geiger mode, arranged in two dimensions. The calibration of the MPPC output signals is operated by using a helium lamp at known intensity. The MPPC has the main advantage of being fairly insensitive to magnetic fields, therefore being preferable over ordinary photomultiplier tubes (PMTs) which must instead be magnetically shielded. In particular, this choice allows to place the whole system inside the torus hall, resulting in short optic fiber lengths and therefore low active signal loss between the experiment and the diagnostic.

4

ANALYSIS METHODOLOGY

In this chapter the main tools and methodologies used for the analysis of the experimental data acquired in the context of the present research project is described. In section 4.1 the fitting procedure used to regularize the upstream experimental profile data is introduced. A similar procedure, used for the characterization of the downstream outer target heat load profiles, is described in section 4.2. Section 4.3 gives an excursus on the scheme used for a physically robust evaluation of the separatrix position. Lastly, the conditional average procedure, employed in this manuscript to evaluate the properties of filamentary structures as measured by the midplane fast reciprocating probe, is summarized in section 4.4.

4.1 SELECTION AND FITTING OF UPSTREAM PROFILES

For the good pulses achieved in the experimental part of this work, electron temperature and density profile measurements have been obtained across the whole radial coordinate by means of the Thomson scattering system. In the case of the fuelling scan experiment, this data has been systematically complemented with RPTCV measurements, when available during the corresponding plunge time intervals. The latter diagnostic has not been available instead during the execution of the shaping scan programme, however for a reduced number of pulses the spectroscopic data from the THB diagnostic could be exploited.

In the first place, single profiles have been grouped within stationary time intervals, whose width has been varied according to the ELM regime under consideration, so as to obtain a good statistics

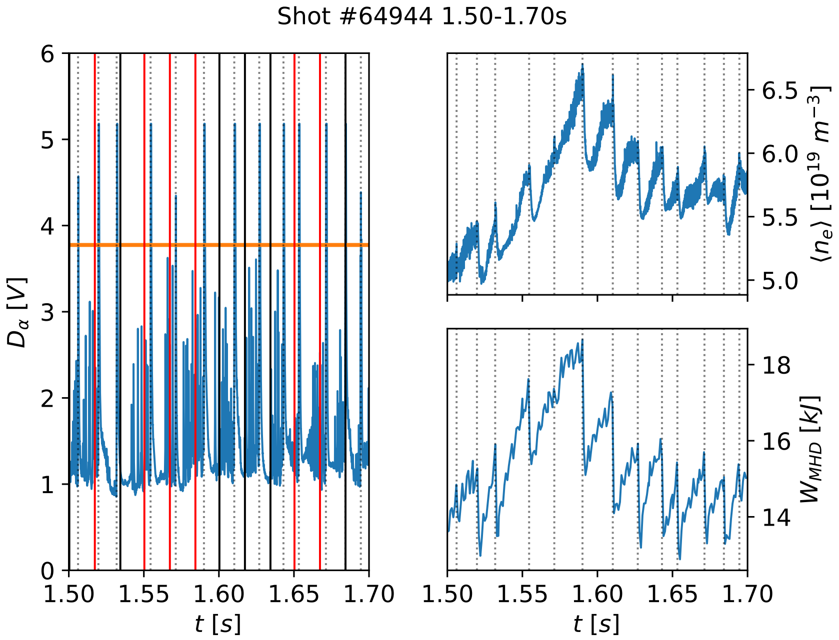

Figure 4.1: Example of ELM filtering procedure for a time interval with type-I ELMs during a fuelling scan plasma discharge. Left: top-down photodiode signal with a D_α line filter, serving as ELM monitor. The vertical continuous red and black lines represent TS measurement timings at which a profile has been, respectively, selected or discarded. Top right: line-averaged density from the central FIR chord. Bottom right: total plasma stored energy from the LIUQE reconstruction. In all panels, the vertical dotted lines indicate the type-I ELM timings as identified by the ELM filtering procedure.

at any given spatial coordinate. In detail, during type-I ELMy discharges a filtering procedure has been operated, depicted in figure 4.1, so that only pre-ELM profiles have been retained. The pre-ELM time intervals have been identified here as the 65%-95% phase of an ELM cycle, based on the top-down integral D_α line emission acting as a proxy for the ELM behaviour. This ensures that all selected data pertains only to plasma snapshots having recovered from the previous large ELM crash. The pre-ELM window width chosen here is slightly larger with respect to other works done e.g. at JET [130], with the aim of further improving the profile statistics without losing on the requirement of full profile recovery. Time slices at least 200 ms wide have been used in this case, so as to select the highest number of TS pulses. On the contrary, no proper ELM identification has been possible during QCE discharges, due to the inherently noisy behaviour of the D_α signal in such a regime. Consequently, in this case all profiles within a narrower time window of $100-150$ ms width have been selected with no filtering procedure being employed.

The selected profiles are then remapped onto a common normalized radial coordinate. In this work the ρ_ψ coordinate as defined in equation 2.1 is used in most cases, except for some situations (de-

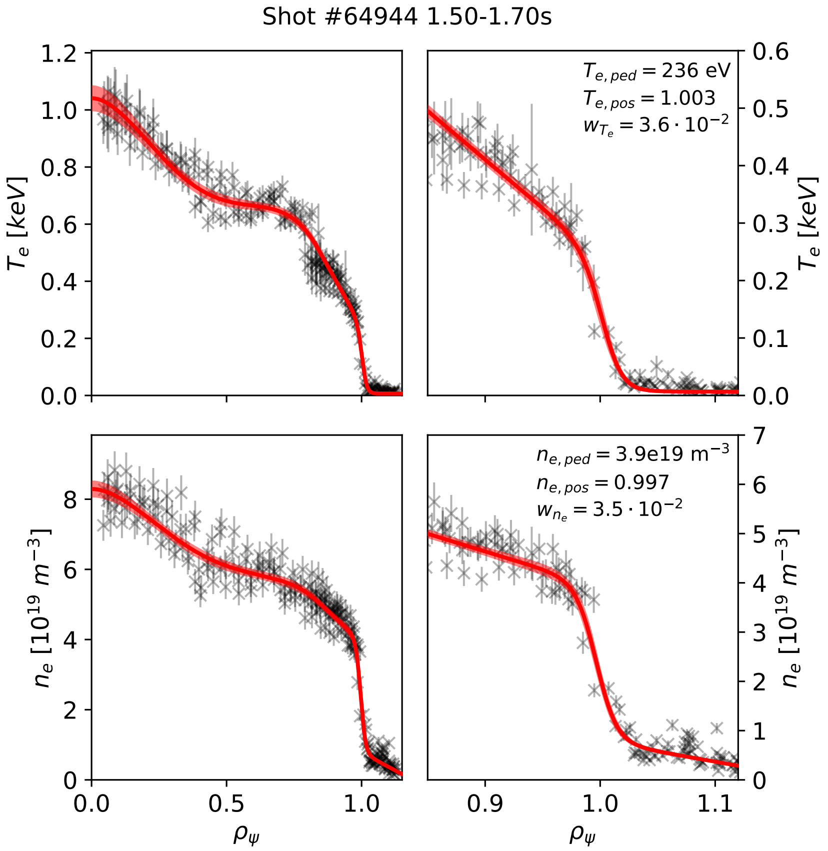

Figure 4.2: Temperature (top panels) and density (bottom panels) profiles for a type-I ELMy time slice. The black crosses and errorbars indicate the raw profile data, comprising TS and RPTCV measurements, and their experimental uncertainty. The continuous red lines represent the *mtanh* fit for each profile, shown over the whole normalized radial coordinate in the left panels, and zoomed in over the edge and SOL regions in the right panels. The most important parameters of the fitting function, as calculated from least squares optimization, are also reported. The red shaded regions indicate the 95% confidence interval of the fit.

scribed in detail later) in which the radial distance from the separatrix dr_u as in equation 2.2 must be necessarily used. The transition from the physical coordinates of the measurement location to either ρ_ψ or dr_u is carried out by means of suitable field line mapping numerical tools based on the LIUQE equilibrium reconstruction. The remapped profiles are regularized over the whole ρ_ψ coordinate, including the core region, by means of a composite piecewise function, following the approach exploited in [131]. The analytical form of the function is

$$F(\rho_\psi) = \mathcal{P}_4(\rho_\psi) \cdot \mathcal{H}(\rho_{\psi,c2e} - \rho_\psi) + \mathrm{mtanh}\,(\rho_\psi) \cdot \mathcal{H}(\rho_\psi - \rho_{\psi,c2e}). \tag{4.1}$$

In equation 4.1, $\mathcal{P}_4$ is a fourth-order polynomial fitting the confined region. The pedestal and scrape-off layer are fitted instead by means of a modified hyperbolic tangent (*mtanh*) function, defined in [132] as

$$\begin{aligned} \mathrm{mtanh}\,(z) &= \frac{F_{ped} - F_{off}}{2} \cdot \left[\frac{(1 + s_1 z)\exp(z) - (1 + s_2 z)\exp(-z)}{\exp(z) + \exp(-z)} + 1 \right] + F_{off} \\ z &= -\frac{\rho_\psi - F_{pos}}{(w_F/2)} \end{aligned} \tag{4.2}$$

where F_{ped} and F_{off} are the pedestal height and the SOL vertical offset, s_1 and s_2 are parameters correlated to the slope of the profile in the core and scrape-off layer respectively, F_{pos} is the position of the maximum gradient and w_F an estimate of the pedestal half-width.

With respect to the standard version of the *mtanh* function in [132], the slope parameter s_2 has been added for a proper first-order treatment of far SOL radial profile variations, where it may be necessary. The Heaviside step function $\mathcal{H}$ has been used in equation 4.1 in order to separate the core and the edge parts of the fit, joining at the radial coordinate $\rho_{\psi,c2e}$ which for this work has been fixed at $\sqrt{0.7} \approx 0.83$. In order to ensure $\mathcal{C}^1-$regularity, proper constraints are imposed on the free parameters in equation 4.1 so that the fitting function is at least continuous and differentiable at the core-edge boundary coordinate. In addition, a further zero-derivative constraint has been imposed at the magnetic axis coordinate. It is worth stressing out that the choice of a fourth-order polynomial for the functional shape of the core fit is completely arbitrary and it is relevant here only up to the extent of preventing an incorrect fitting of the pedestal, edge and SOL regions.

The fitting procedure is carried out numerically via Levenberg-Marquardt least-squares optimization of the free parameters in equation 4.1. The results are shown in figure 4.2 for a type-I ELMy time slice within the fuelling scan database, where the fitting curves in red, together with their 95% confidence intervals, are superimposed on the experimental data in black. A slope has been used only for density profile fitting only, addressing the overall decreasing trend of the far-SOL measurements. Instead, this is not necessary for the temperature profile, for which just a constant offset in the scrape-off layer is needed and implemented by adding the further constraint $s_2 = 0$.

4.2 DIVERTOR HEAT LOAD CHARACTERIZATION

Using the floor tile temperature distribution measured by the VIR thermography system, one can infer the outer target heat load by solving a heat conduction equation

$$\rho c_p \frac{\partial T}{\partial t} = \nabla \cdot (k \nabla T) \tag{4.3}$$

where ρ is the mass density of the tile material, c_p is its specific heat capacity and $k = k(T)$ its temperature-dependent thermal conductivity. Equation 4.3 is numerically solved by employing the THEODOR code [133, 134] in its explicit version (i.e. with forward finite time differences), assuming toroidal symmetry of the solution. The normally incident heat flux profile at the outer target is calculated by means of Fourier's law

$$q_{\perp t}(x) = -k\frac{\partial T}{\partial x} \tag{4.4}$$

on a staggered time base with respect to that over which the temperature distribution has been acquired, i.e. $t_q = t_T + \Delta t_T/2$, due to the finite differences numerical scheme exploited for discretization of the time derivative in the conduction equation. Each time instance of the perpendicular heat load profile is converted to a parallel one by means of the target field line grazing angle α introduced in section 2.1.3 through the relation $q_{\parallel t} = q_{\perp t}/\sin\alpha$.

The parallel heat load profile can be characterized by the simple exponential *ansatz* made in equation 2.7, where the relation between the upstream and target radial coordinate is $dr_u = dr_t/f_\chi$ accounting for target poloidal flux expansion. However, this does not take into account some diffusive leakage processes transporting part of the energy flowing downstream into the private flux region. This diffusion can be modelled via a convolution between the exponentially decaying model and a Gaussian function with given width S called *spreading factor*. The model used in this work to characterize the divertor target heat flux, first derived in [135], is

$$q_{\parallel t} = \frac{q_{\parallel t,0}}{2}\exp\left[\left(\frac{S}{2f_\chi\lambda_{q,u}}\right)^2 - \frac{dr_t}{f_\chi\lambda_{q,u}}\right] \times \operatorname{erfc}\left(\frac{S}{2f_\chi\lambda_{q,u}} - \frac{dr_t}{S}\right) + q_{BG} \tag{4.5}$$

with q_{BG} a constant background value. Given that most of the times f_χ presents a weak radial

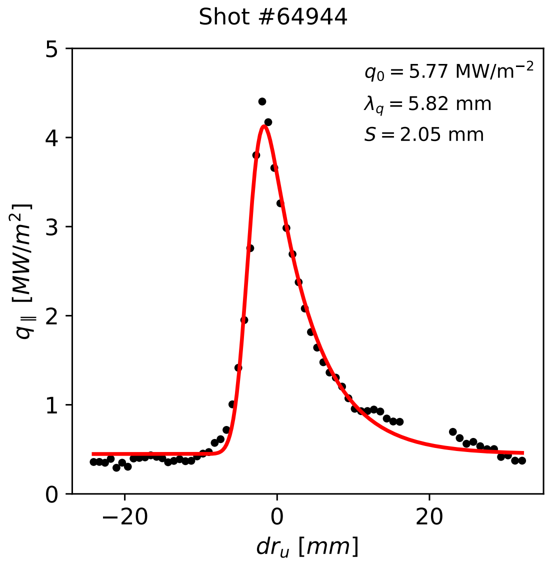

Figure 4.3: Example of an upstream-remapped heat load profile for a TCV discharge considered in this work. The parallel heat load profile estimated via VIR thermography measurements and the THEODOR code is represented as black dots. The red line indicates the best fitting Eich function, with its most important optimized parameters reported in the figure.

dependence itself, in this work equation 4.5 is re-parametrized at the upstream parallel coordinate to eliminate any dependence on the poloidal flux expansion. This implies that not only dr_t must be replaced with dr_u, but also that the magnitude of the profile at each radius must be rescaled according to the upstream-to-target total flux expansion.

An example of a measured and fitted $q_{\|u}$ profile is shown in figure 4.3. It must be stressed out that the subframe field of view of the VIR camera often comprises portions of the machine floor presenting tile edges, which notably constitute a difficulty in correctly estimating the temperature distribution and hence the heat load profile. To avoid the sistematic uncertainty sources associated to this issue, some parts of the experimental $q_{\|u}$ profiles have been discarded for fitting, right before and after a tile gap position. This explains, for instance, the missing measurements around $dr_u \sim$ 20 mm in figure 4.3.

4.3 SEPARATRIX POSITION ESTIMATION

The plasma parameters at the separatrix are needed for a proper characterization of the SOL properties by means of the α_t parameter. In turn, an equilibrium reconstruction-based experimental determination of the separatrix parameters in the presence of steep edge and H-mode pedestal gradients can be somewhat challenging, given that even a small (few mm-s) uncertainty on the LCFS position can lead to large errorbars on $n_{e,sep}$ and $T_{e,sep}$. For this reason, a power balance approach is often used in other machines [136, 137] and exploited in the analysis framework implemented in the present manuscript. The separatrix position is estimated via a slightly modified version of the two-point model, assuming that the great majority of the SOL input power is transported via parallel heat conduction. However, at a difference with respect to the treatment in section 2.2.3, it is further assumed that the power crossing the separatrix enters the scrape-off layer uniformly along a connection length, leading to the condition

$$\nabla_{\|} q_{\|} = \frac{P_{sep}}{A_{SOL} L_{\|}}. \tag{4.6}$$

Substituting equation 4.6 into 2.18 and integrating twice for the electron temperature results in

$$T_{e,sep} = \left(T_{e,t}^{7/2} + \frac{7}{4} \frac{P_{sep} L_{\|}}{A_{SOL} \kappa_{0e}} \right)^{2/7} \approx \left(\frac{7}{4} \frac{P_{sep} L_{\|}}{A_{SOL} \kappa_{0e}} \right)^{2/7} \tag{4.7}$$

where, as will be shown in chapter 5, the target temperature can be neglected because the condition $T_{e,sep} \gg T_{e,t}$ is often fulfilled in H-mode conditions. This expression differs from the one in equation 2.27 just for the $7/4$ numerical factor instead of the value $7/2$ obtained assuming that all the powers enters the scrape-off layer through a single point.

The power crossing the separatrix P_{sep} can be estimated from power balance as the total absorbed input power, minus the fraction that goes into plasma heating and the core radiative losses

$$P_{sep} = P_{ohmic} + P_{NBI} + P_{ECRH} - \frac{dW}{dt} - P_{rad,core}. \tag{4.8}$$

Here the ohmic heating power is determined as $P_{ohmic} = I_p V_{loop}$, where V_{loop} is the loop voltage induced by the central solenoid around the torus axis. P_{ECRH} is the total ECRH power coupled to the plasma calculated with the TORAY-GA ray tracing code [138]. The total absorbed NBI power $P_{NBI} = P_{NBI,net} - P_{SH} - P_{CX} - P_{FO}$ is given by the total NBI input power net of beam duct losses, minus the shine through, the charge-exchange and the first orbit losses. Since determining all the NBI loss contributions can be a quite difficult task, for the sake of simplicity they are neglected in this work and only the first term remains. This may actually represent a good approximation in high-density plasmas with co-current NBI injection like the majority of the discharges presented in later chapters, however a detailed analysis should take them into proper account, especially for low density scenarios in which at least the first two loss terms can be significant. $P_{rad,core}$ is estimated by means of tomographic reconstruction from either the legacy or the RADCAM bolometric system. Finally, the plasma heating term dW/dt is also neglected again for simplicity for the purposes of this analysis, since on average it vanishes within a stationary time interval. Nevertheless, it should be kept clear in mind that the actual relevant contribution comes from the inter-ELM behaviour of the total plasma stored energy, which as seen in figure 4.1 is not always stationary, and a proper analysis framework should take this term into account as well.

The determination of the geometrical and physical parameters in equation 4.7 is done according to reference [139]. The parallel electron heat conduction coefficient κ_{0e}, given in equation 2.18, assumes values of $\sim 2000\ \mathrm{W\,eV^{-7/2}\,m^{-1}}$ for typical $Z_{eff} \sim 2$ and is here corrected according to the regression in [43] based on Braginskii calculations of the numerical factors for discrete $Z \geq 1$ [72]

$$\kappa_{0e} \approx \frac{2600}{f(Z_{eff})}, \quad f(Z_{eff}) = 0.672 + 0.076 Z_{eff}^{0.5} + 0.252 Z_{eff}. \tag{4.9}$$

In all the following, Z_{eff} is derived from the determination of the neoclassical resistivity and bootstrap current , as described in [140, 141].

The connection length and the wetted area are defined as

$$L_{\parallel} \sim \pi q_{cyl} R, \quad A_{SOL} \sim 4\pi R \langle \lambda_q \rangle \frac{B_\phi}{B_\theta} \tag{4.10}$$

with $\langle\lambda_q\rangle$ the poloidally average SOL power decay length as defined in [135] and q_{cyl} the so-called *cylindrical safety factor*, calculated by assuming that the geometry of the separatrix flux surface can be traced back to a straight cylinder. Based on this, the latter is defined as

$$q_{cyl} = \frac{B_\phi}{B_\theta}\frac{a}{R}\hat{\kappa} \quad \text{with} \quad B_\theta = \frac{\mu_0 I_p}{2\pi a\hat{\kappa}} \quad \text{and} \quad \hat{\kappa} = \sqrt{\frac{1+\kappa_{geo}^2\left(1+2\delta^2-1.2\delta^3\right)}{2}}. \tag{4.11}$$

Finally, inserting equations 4.10 into 4.6 one gets

$$T_{e,sep} \approx \left(\frac{7}{16}\frac{P_{sep}q_{cyl}^2 R}{\kappa_{0e}\hat{\kappa}a\langle\lambda_q\rangle}\right)^{2/7}. \tag{4.12}$$

As a last step, the upstream temperature profile is rigidly shifted so that the value of the fit at $\rho_\psi = 1$ matches the power balance estimation in equation 4.12. The density profile is shifted as well by a like amount, being measured by the same diagnostics on a common spatial coordinate basis, for assessment of the separatrix density.

4.4 FILAMENT DETECTION AND CHARACTERIZATION

Fast electrostatic measurements are needed in order to characterize the intermittently fluctuating behaviour of the far SOL plasma. For this purpose, the fast midplane reciprocating probe (RPTCV) has been exploited during the fuelling scan experimental programme, whereas wall-mounted Langmuir probes biased at a constant negative voltage have been used for the shaping scan. In this section only the analysis methodology for the RPTCV diagnostic will be detailed.

The fast RPTCV I_{sat} and φ_{fl} measurements have been obtained at an acquisition frequency of approximately 5 MHz. The probe has been plunged once per each discharge, with each plunge having a duration of $\sim$ 90 ms and a depth from the first wall limiter tiles of $\sim 2.0-2.5$ cm, ensuring safe operation of the diagnostic and avoiding excessive carbon pollution of the confined and SOL plasmas. The fast I_{sat} measurement, properly ELM-filtered as described in section 4.1 when necessary, has been used as an indicator of filament appearance. Single filaments have been identified as the peaks having an amplitude satisfying the inequality

$$I_{sat} > \langle I_{sat}\rangle + 2.5\sigma_{I_{sat}} \tag{4.13}$$

where the background component $\langle I_{sat}\rangle$ and the standard deviation $\sigma_{I_{sat}}$ of the ion saturation current signal have been estimated by means of a moving window of 0.2 ms width. The calculation

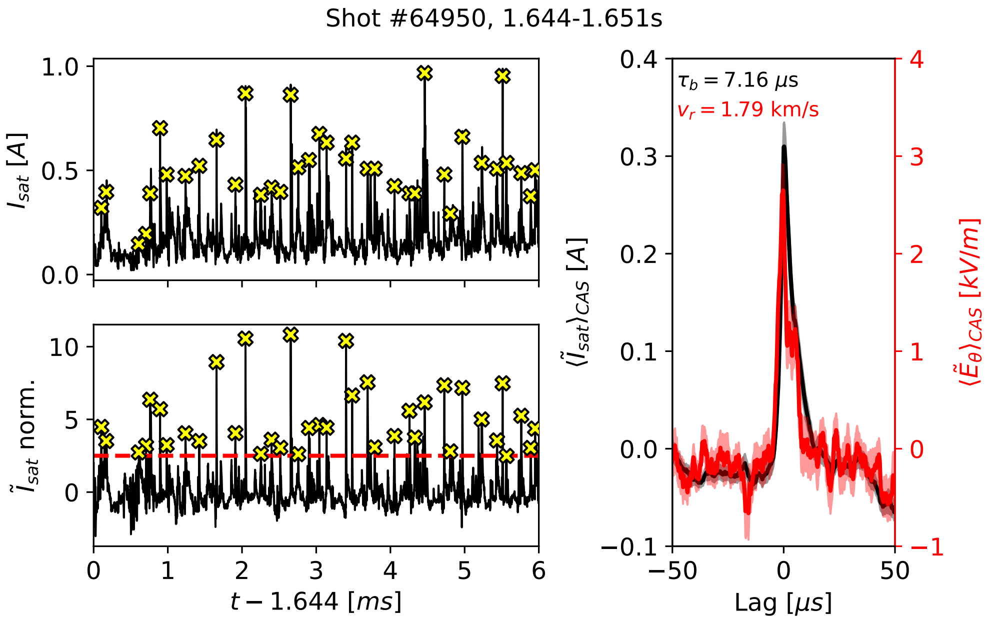

Figure 4.4: Top left: time trace of the fast I_{sat} RPTCV measurement. Bottom left: time trace of the fluctuating I_{sat} component, normalized to its moving standard deviation. Both the top and bottom left panels show single filaments as small yellow crosses. The detection threshold is shown in the bottom panel as a red line. Right: typical CAS filament I_{sat} waveform in black and its associated poloidal electric field E_θ perturbation in red, with their respective 95% confidence intervals indicated by the colored bands. Sample values of the filament FWHM duration and radial velocity as estimated by the CAS procedure are also reported in the figure.

of a moving average (and variance) is here necessary since, although the plasma state can be reasonably considered quasi-stationary during the short probe plunge, the probe itself moves and scans regions of the scrape-off layer at different background temperature and density, therefore different baseline I_{sat} value. On top of the threshold condition expressed by equation 4.13, the detected filaments are required to have a duration longer than 5 μs and a minimum temporal distance from the nearest neighbouring peaks of at least 50 μs. An example of the results of the detection procedure is shown in the two left panels of figure 4.4 for a TCV discharge in the present database. Single detected filaments are marked as yellow crosses, both in the top panel representing the absolute I_{sat} time trace, and in the bottom panel showing its normalized fluctuations, $\left(I_{sat} - \langle I_{sat} \rangle\right) / \sigma_{I_{sat}}$; the detection threshold appears in the bottom panel as a dashed red line.

Following up from the results of the detection procedure, filament properties have been estimated via the *conditional average sampling* (CAS) procedure as detailed in [94, 53, 142]. Each detected filament has been first shifted on a common timebase extending 50 μs before and after the identified peak, and subsequently linearly de-trended to remove the slow baseline time evolution due to the probe motion. The resulting waveform collection has been averaged into a single one representative of the sample average of the ion saturation current fluctuation $\langle \tilde{I}_{sat} \rangle$. An analogous procedure has been applied to all the fast φ_{fl} to obtain the corresponding CAS-averaged waveforms, using the previously detected I_{sat} peak timings. The fluctuating poloidal electric field has been calculated from the gradient of the floating potential between the two poloidally spaced top and middle φ_{fl} pins. An example of the CAS procedure results is shown in the right panel of figure 4.4, where the average I_{sat} and E_θ fluctuation waveforms are displayed.

From these waveforms a number of filament properties can be inferred. Firstly, the average blob radius is defined as

$$\delta_b = \frac{\tau_b}{2}\sqrt{v_{b,r}^2 + v_{b,p}^2} \tag{4.14}$$

where τ_b is the full-width at half maximum (FWHM) of the $\langle \tilde{I}_{sat} \rangle$ CAS waveform, which includes the possible effects of a trailing wake. The square root contains the total filament velocity, comprising both its radial and its poloidal component. The former is calculated as the radial component of the $\mathbf{E} \times \mathbf{B}$ velocity, therefore as

$$v_{b,r} = \frac{\langle \tilde{E}_\theta \rangle}{B} \tag{4.15}$$

While the poloidal velocity $v_{b,p}$ could in principle be derived in the same way, the available probe head setup prevents such an estimation, given the too small separation of the two radially spaced φ_{fl} pins and the lack of fast temperature gradient measurements. Therefore, following previous work [142, 143] the poloidal velocity estimation is made through a 2D cross-correlation technique, exploiting all five poloidally and radially separated pins measuring the floating potential.

5

OVERVIEW OF THE FUELLING SCAN EXPERIMENT

THE objective of this chapter is to report on the correlation between the divertor recycling state, the corresponding upstream separatrix density behaviour and the properties of the upstream SOL profiles and turbulent fluctuations. With this purpose in mind, a set of high density H-mode discharges, including both type-I ELMy and QCE scenarios, has been acquired on TCV. In this experiment the divertor neutral pressure, used as a measurement of the recycling state, has been evolved by changing the gas fuelling level and subsequently correlated with the α_t parameter via a change in $n_{e,sep}$. The impact on the upstream SOL plasma is measured through the experimental evaluation of the near SOL power and density e-folding lengths, far SOL density shoulder formation and filamentary transport behaviour. The experimental setup with the necessary engineering inputs is presented in section 5.1. Afterwards, in section 5.2 the correlation between $n_{e,sep}$, the divertor recycling state and α_t is addressed. Section 5.3 reports on the main results of the present analysis, linking the evolution of the separatrix properties with the divertor heat flux broadening and with changes in near SOL density decay length and far SOL density profile shape. Finally, the impact on filament properties is assessed in section 5.4.

5.1 Experimental setup of the fuelling scan database

The left side of figure 5.1 shows the setup of the fuelling scan experimental programme, while in the right one the considered magnetic geometry is represented. The database consists of several deuterium-fuelled, high density H-mode discharges run within a baffled TCV vessel. All discharges have a plasma current $I_p = 170$ kA and a central toroidal magnetic field $B_\phi = 1.4$ T, both in reverse configuration. The ion ∇B drift velocity is directed towards the active X-point for easier

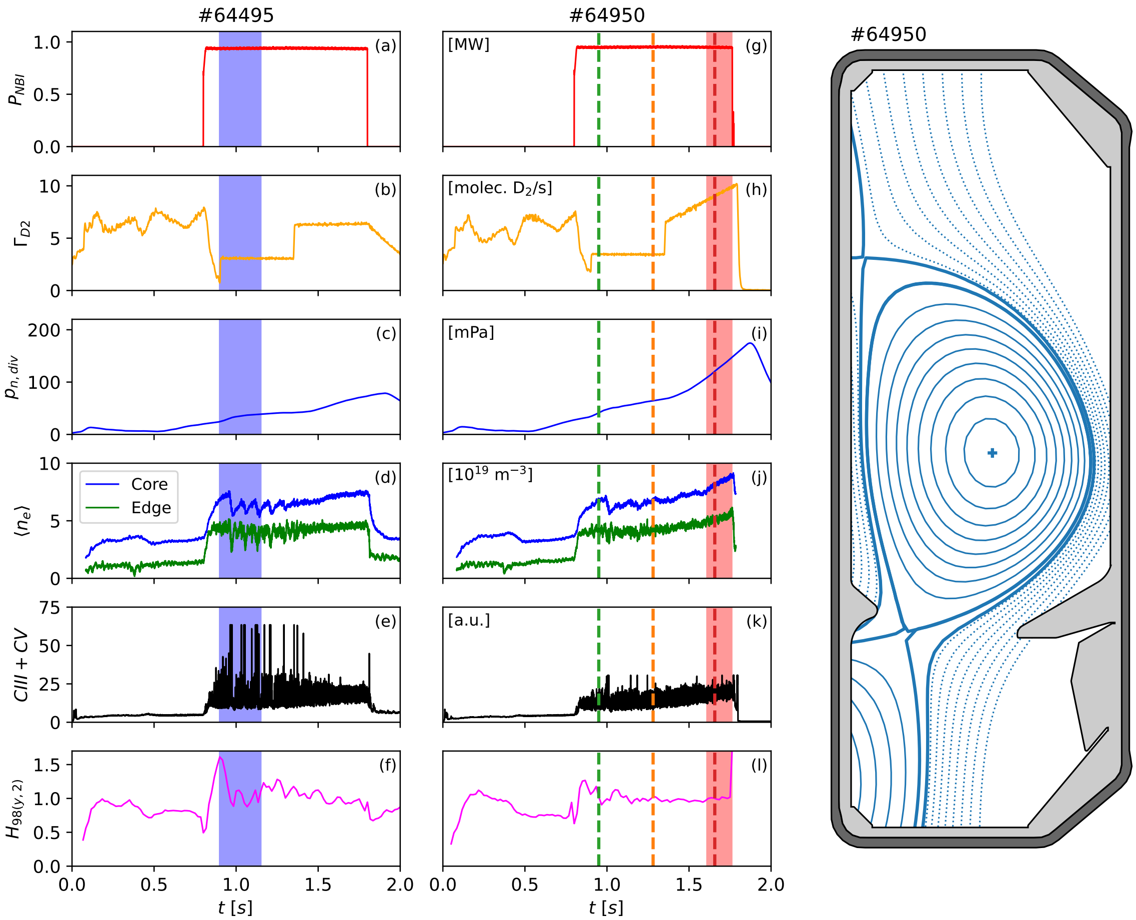

Figure 5.1: Left: time evolution of the (*a, g*) net NBI input power, (*b, h*) gas flow rate, (*c, i*) divertor neutral pressure, (*d, j*) core and edge line-averaged densities, (*e, k*) combined CIII-CV top-down line emission and (*f, l*) confinement factor. The blue bands in panels (*a*)-(*g*) and the red bands in panels (*h*)-(*l*) indicate two time intervals considered throughout this work for comparison of different plasma profiles at different recycling. The three vertical colored lines in panels (*h*)-(*l*) represent the VIR timings at which upstream parallel heat flux profiles are represented in section 5.3.1. Right: vessel configuration and typical plasma magnetic geometry considered for this dataset.

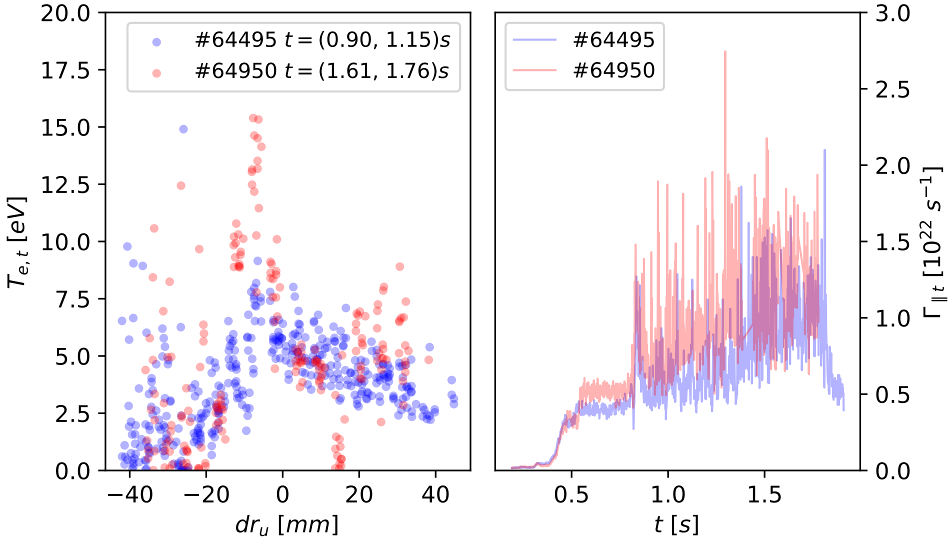

Figure 5.2: Langmuir probe measurements of the (left) outer target electron temperature, remapped upstream and (right) time evolution of the spatially integrated inter-ELM parallel particle flux at the outer target, for the TCV discharges #64495 and #64950. In the left panel, the two time intervals chose for representation correspond to the blue and red bands in figure 5.1. For both panels, ELM filtering has been carried out only for the blue case.

H-mode access. The magnetic configuration consists of a highly shaped conventional lower single null geometry with constant magnetic axis height and radius, strike point positions and shaping parameters for all discharges. In particular, the plasma elongation is $\kappa_{geo} \sim 1.5$, whereas the lower and upper triangularities are given by, respectively, $\delta_{low} \sim 0.6$ and $\delta_{up} \sim 0.4$.

Access to H-mode is provided via an additional heating power of 1 MW provided by central neutral beam injection, lasting between 0.8 s and 1.8 s for all discharges, as shown in panels (a) and (g) of figure 5.1(left). Gas fuelling has been provided by using either the top or the bottom piezoelectric valves, either as a simple two-step feed forward scheme as in panel (b), or via a step followed by a ramp as in (h). The wide range of gas rate levels, together with the different fuelling locations and the wall recycling capabilities providing different deuterium outgassing sources, allow to obtain a large scan in divertor neutral pressure $p_{n,div}$, between $\sim$ 20 mPa and $\sim$ 120 mPa, as indicated in panels (c) and (i). As a result of this variation, the edge line-averaged density changes between $\sim 3 \cdot 10^{19}$ m^{-3} and $\sim 7 \cdot 10^{19}$ m^{-3}, translating into an edge Greenwald density fraction between ~ 0.25 and ~ 0.63.

As a consequence of the modifications in divertor recycling conditions and associated increase in plasma density, the ELM behaviour undergoes significant changes, as registered by a top-down photodiode line of sight with a combined CIII-CV line emission filter. Specifically, as shown in panels (e) and (k) the plasma transitions from well defined type-I ELMs at low divertor neutral pressure to a small ELM/QCE regime at higher fuelling. The degree of confinement is in turn lower at higher recycling, with the $H_{98(y,2)}$ factor in panels (f) and (l) decreasing from ~ 1.2 to ~ 1. On the other hand, the fact that the confinement factor remains on relatively high levels even at the highest plasma densities can be actually considered as a beneficial feature of the QCE regime, given that H-mode-like properties are retained in the absence of type-I ELMs.

Swept Langmuir probes have been used in this work to infer the electron temperature and the integrated particle flux at the lower machine floor, around the outer strike point. Sample measurements are shown in figure 5.2, in particular the left panel indicates that the target temperature peaks around values of $T_{e,t} \sim 10$ eV. The typical threshold for the onset of detachment lies around ~ 5 eV, hence this observation is a clear indication that the divertor target remains attached at all times during a discharge, even at the highest density, albeit in high-recycling conditions. This is further confirmed by the behaviour of the target particle flux time evolution, which keeps increasing until the end of the NBI-heated phase. Furthermore, considering that the power balance evaluation of equation 4.12 typically leads to $T_{e,sep} \sim 50$ eV for a 1 MW NBI-heated plasma [144], the assumption made therein of neglecting the target temperature in the calculation is fully justified.

5.2 EVALUATION OF SEPARATRIX PARAMETERS

Examples of edge density and temperature profiles are shown in figure 5.3, respectively in the left and right panels, including both raw data points and the edge *mtanh* fitting curves with their associated uncertainties. The blue points and curves refer to a time interval with type-I ELMs, whereas the red one represents a profile during a fully established QCE regime. The first aspect to be noted is that a larger scatter in the Thomson scattering data is present in the case of the QCE time interval with respect to the type-I ELMy case. This is owed to the absence of an ELM filtering procedure during QCE, which leads to retaining all kinds of temperature and density fluctuations induced by small ELMs of any amplitude. Nonetheless, the quality of the fitting procedure is still good and a robust determination of the separatrix parameters and profile properties is still possible also in the QCE case.

At increasing divertor recycling the temperature profiles are affected only within the confined region, in terms of a decreasing pedestal height, and in the vicinity of the separatrix as the gradient of the profile becomes shallower. On the other hand, the separatrix temperature remains more or less constant across the whole database at $T_{e,sep} = (46.5 \pm 3.3) eV$, which is due to the $2/7$ exponent in equation 4.12 strongly attenuating the sensitivity of the separatrix temperature to any of its defin-

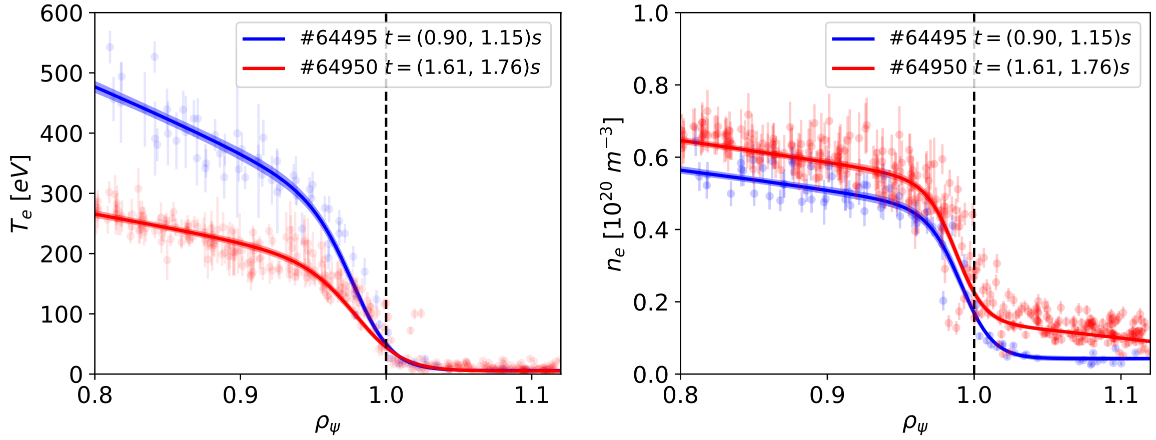

Figure 5.3: Upstream edge-SOL temperature (left) and density (right) profiles for the comsidered sample discharges during the two time intervals highlighted with matching colors in figure 5.1. The Thomson scattering and (only for the red case) RPTCV data are shown with semi-transparent points with their associated error bars. The solid curves represent the *mtanh* part of the fitting model, whereas the shaded regions indicate the 95% confidence interval of the fit. Both data and fits have been shifted along the radial coordinate in order to match their respective $T_{e,sep}$ estimation in equation 4.12. The separatrix position has been represented by means of a vertical line.

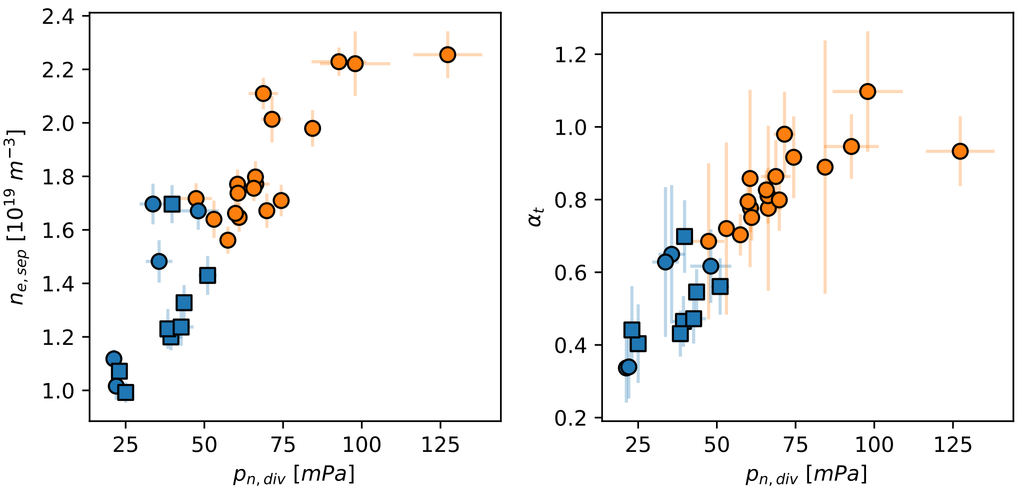

Figure 5.4: Correlation between the divertor neutral pressure and (left) the two-point model $n_{e,sep}$ estimate, (right) the turbulence control parameter α_t for the baffled divertor database analyzed in this manuscript. Type-I ELMy and QCE time intervals are distinguished by means of different colors, with blue indicating the former and orange the latter. The circles represent plasma discharges during which gas was puffed from the bottom valve, whereas the squares indicate fuelling from the top valve.

ing quantities. This reflects also on the amount of radial profile shifting required for the profiles to match the power balance model at the separatrix: throughout the whole database the average radial separatrix shift with respect to the equilibrium reconstruction is $\Delta\rho_{\psi} = (-5.6 \pm 3.8) \cdot 10^{-3}$, or equivalently $\Delta dr_u = (-1.5 \pm 1.1)$ mm in physical units. As for the density profile, a global upwards vertical shift is visible at higher divertor neutral pressure, with a higher pedestal top and separatrix densities achieved.

Figure 5.4 extends the last observation to the whole database, correlating $n_{e,sep}$ and α_t with the divertor neutral pressure. Each time interval has been marked here with a different color, according to whether the time slice is dominated by type-I ELMs (blue) or by QCE-like perturbations (orange). The location of the main species gas puffing has been highlighted as well, with circles and squares representing, respectively, the bottom or the top gas valve being used. Notably, some points have not been included in this and later figures due to being associated to a low VIR integration time, therefore a large noise level on the thermography signal and a highly fluctuating estimate of the SOL power width. As a general criterion throughout this work, points with an uncertainty bigger than their absolute value were discarded from the database. For the evaluation of α_t, an effective ion mass $m_i = 2m_p$ and an average ion charge $\bar{Z} \sim 1$ have been considered, while instead retaining the dependence on the effective charge Z_{eff}. The separatrix density follows the expected trend with the divertor neutral pressure, at least up until $p_{n,div} \sim 100$ mPa where saturation seemingly occurs at $n_{e,sep} \sim 2.3 \cdot 10^{19}$ m^{-3}. While some degree of saturation should be expected at some neutral pressure level at which the pedestal, edge and separatrix become opaque to additional gas puffing, the scarcity of points above ~ 100 mPa prevents any conclusive statements to be made here.

The α_t parameter follows the separatrix density accordingly, indicating a more dissipative divertor leads to an increase of the upstream collisionality and therefore to a more interchange-unstable plasma around the separatrix, leading to an enhancement of turbulent transport in the scrape-off layer. A clear regime separation can be seen around $n_{e,sep} \sim 1.6 \cdot 10^{19}$ m^{-3}, strengthening once again the role of the separatrix density in achieving the QCE regime. The corresponding α_t value at the QCE access threshold is ~ 0.65, which is a bit higher than that registered in some AUG-related works (e.g. [145]). On the other hand, for both $n_{e,sep}$ and α_t the gas puffing location does not have any more of an effect than producing an overall lower divertor neutral pressure for the discharges exploiting the top valve. It is worth saying also that the cases with top fuelling are associated to a slightly lower gas rate than those with bottom fuelling, therefore in the end this could explain the differences in $p_{n,div}$ and the puffing location may, indeed, have a negligible effect.

5.3 Evolution of the upstream SOL profiles

Once having established the extent of the separatrix parameter space explored via the variation in gas fuelling rate and the corresponding divertor neutral pressure scan, here the response of the upstream-remapped SOL plasma profiles is analysed and discussed.

5.3.1 Divertor heat load broadening

For the analysis of the divertor heat load, every single $q_{\|u}$ profile within the selected stationary time window is first fitted by means of the upstream-remapped version of equation 4.5, after operating the ELM filtering procedure as described in section 4.1. This results in a time-resolved measurement of $\lambda_{q,u}$, from which an average value for the whole time slice is estimated, weighted over the inverse of the single uncertainty values from each fit. Finally, for usage in equation 4.12 the local average value at the outer midplane is remapped to a *poloidal average* $\langle\lambda_q\rangle$ by accounting for an average-to-OMP poloidal flux expansion, as in [135].

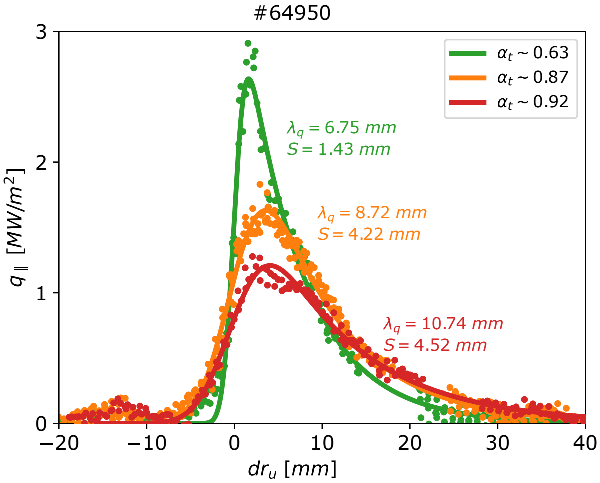

Figure 5.5: Inter-ELM, upstream-remapped outer target heat flux profiles at the three different times marked by dashed vertical lines with corresponding colors in figure 5.1. The respective λ_q and S values are also reported next to each fitted profile, together with their reference α_t values. Both the background heat load and the fitted strike point position have been subtracted from the vertical and horizontal axes, respectively.

In figure 5.5 three upstream-remapped heat load profiles are displayed from the discharge #64950, each corresponding to a different measurement timing as shown in figure 5.1 through vertical lines with corresponding colors. Each profile, and related fitting curve, are associated to a different value of α_t, as well as their respective Eich fit estimates of the power fall-off length λ_q and spreading factor S. For the purpose of comparing the profiles on common coordinate scales, both the background

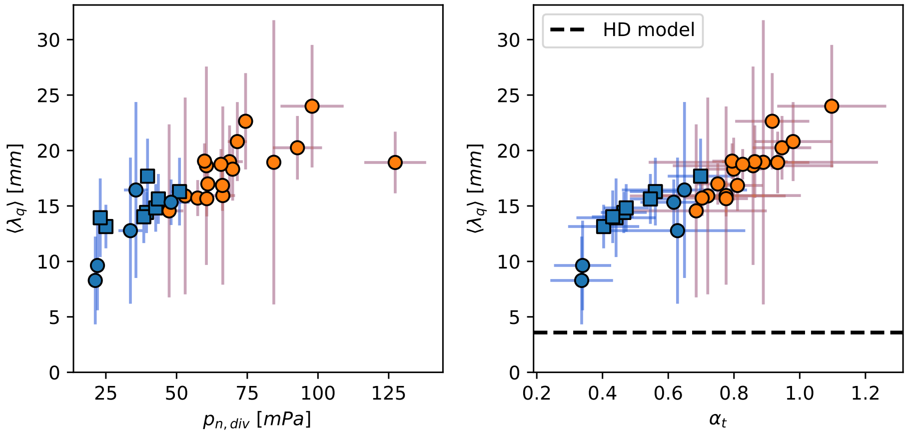

Figure 5.6: Dependence of the poloidally averaged SOL power decay length on (left) the divertor neutral pressure and (right) the turbulence control parameter α_t. The blue and orange colors are used, as in figure 5.4, to distinguish type-I ELMy time intervals from QCE regimes. Analogously, circles and squares are used to indicate bottom and top fuelling, respectively. The dashed horizontal line indicates the $\langle\lambda_q\rangle$ value predicted by a heuristic-drift (HD) model for the specific case of this database.

heat load and the fitted strike point position have been subtracted, respectively along the vertical and horizontal axes. The green profile corresponds to an early type-I ELM phase of the discharge, whereas the orange and red cases are referred to a fully established QCE phase without large ELMs. Coherently with previous AUG experimental results [145, 146], an increase of the α_t parameter is correlated with a clear broadening of the divertor heat flux profile, with a significant associated decrease of the peat heat flux. This confirms that high density regimes like QCE with a more dissipative divertor are indeed beneficial for a proper handling of the divertor heat load.

Quantitatively, λ_q increases by a factor ~ 1.5 along the discharge #64950, with S increasing as well by a factor ~ 3 and the peak heat flux reducing by a factor ~ 2 from ~ 2.5 MW/m^2 to ~ 1.2 MW/m^2. The overall broadening of the divertor heat flux footprint is even more pronounced globally across the whole database as shown in figure 5.6, where an increase of α_t from ~ 0.35 to ~ 1.1 from low to high gas fuelling is followed by a steady increase of the poloidally averaged SOL power width by a factor ~ 3.

RELATION TO A HEURISTIC DRIFT MODEL OF λ_q AND EXTENSION TO LOWER DENSITY

In recent years, the attempts at extrapolating a prediction for λ_q have been numerous, both on the experimental and on the modelling side. In section 2.10 the results of one of such attempts is reported, here repeated for convenience

$$\lambda_{q,u}\,[\text{mm}] = (0.63 \pm 0.08) \cdot (B_{\theta,u}\,[\text{T}])^{-1.19\pm0.08} \tag{5.1}$$

based on an empirical multi-machine database relying on λ_q estimates from infrared thermography systems [30]. The sole dependence on the poloidal field at the midplane and the lack of any whatsoever dependence on machine size stand out in this scaling. However, it finds support in a theoretical work based on neoclassical ion drifts only, called heuristic-drift (HD) model [64], predicting a poloidally-averaged estimate of

$$\langle \lambda_q \rangle = 1.6 \frac{a}{R} \rho_{s,pol}, \quad \rho_{s,pol} = \frac{\sqrt{m_i T_e}}{e B_\theta} \tag{5.2}$$

with $\rho_{s,pol}$ the poloidal ion sound Larmor radius and B_θ as in equation 4.11. The inverse poloidal field power law emerges as a natural conclusion of the HD model, albeit with some additional parameter dependencies.

Most importantly, both the empirical and the theoretical scaling laws have been derived under the condition of low gas puffing, and more in general of low separatrix collisionality, which are far

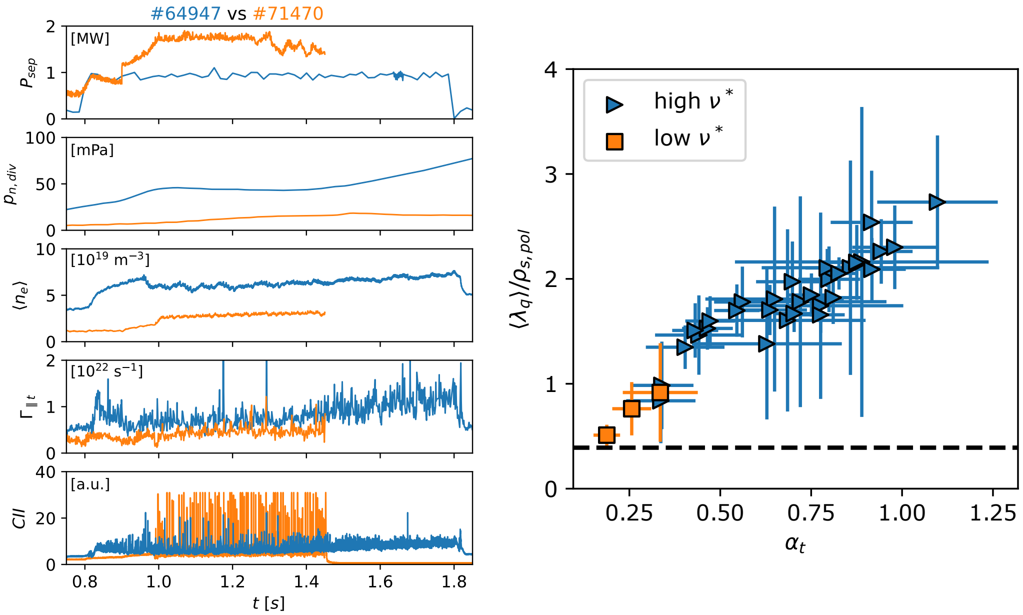

Figure 5.7: Left: time traces of a low collisionality type-I ELMy discharge (#71470) and comparison with a discharge within the fuelling scan database (#64947). From top to bottom, the shown quantities are the power crossing the separatrix, the divertor neutral pressure, the core line-averaged density, the spatially integrated outer target particle flux, the CII top-down integrated line emission. Right: correlation between α_t and the poloidally veraged λ_q, normalized to the poloidal ion sound Larmor radius. The horizontal dashed black line indicates the heuristic-drift model prediction. The low ν^* points in orange are distinguished from the fuelling scan dataset at high ν^* in blue.

from those encountered in the present work. In addition, while on one side these scalings manage to well reproduce the experimental data of low gas puffing datasets [30, 65], more recent work has shown that they tend to overestimate TCV data [147]. In this sense, however, equation 5.2 can be regarded at least as a reference lower boundary for low collisionality, i.e. low α_t data. Indeed, as shown in figure 5.6, the entirety of the $\langle\lambda_q\rangle$ values sits above the HD model prediction dashed line at $\langle\lambda_q\rangle \sim 3.6$ mm, for the present experimental conditions yielding$\rho_{s,pol} \sim 9$ mm.

The lowest achieved SOL power width value is $\langle\lambda_q\rangle \sim 8.3$ mm, or equivalently ~ 4.4 mm at the outer midplane, which is in any case larger than the highest value obtained in the low collisionality dataset of [147], considering plasmas with similar other input parameters (in particular, plasma current). Overall, the SOL broadening achieved here is well correlated with the increase in α_t, suggesting that an increase of the separatrix density, following from a higher gas puffing rate, indeed makes the region arond the separatrix more unstable towards resistive ballooning modes, coherently with previous AUG experimental results [103, 44].

Further support to this interpretation can be drawn by integrating the fuelling database with a subset of type-I ELMy discharges at low gas puffing and high input power, whose experimental setup is shown in the left panel of figure 5.7. Low core, edge and separatrix densities are achieved by both running the plasma at a lower current and by using a lower gas rate, which results in a low divertor recycling and therefore a smaller particle heat flux to the outer target. Higher core, pedestal and separatrix temperatures are obtained by injecting a further ~ 1.1 MW of ECRH heating, equally shared between on-axis and off-axis launchers. The corresponding plasma conditions allow to explore a different region of the separatrix parameter space in which $\alpha_t < 0.3$. As shown in the right panel of figure 5.7, the new data in orange line up well with the fuelling scan dataset in blue. Furthermore, the point at the lowest α_t is in good agreement with the HD model prediction, made here in terms of the normalized poloidally averaged SOL width $\langle\lambda_q\rangle/\rho_{s,pol}$. While these results are promising towards a full extension of the dataset at low α_t, it must be remembered that they are still preliminary due to the very small size of the low collisionality dataset. In addition, the two-point model power balance approach requires the parallel transport to be conduction-limited and recent experiments [147] have shown that low density type-I ELMy H-mode TCV plasmas may be in the flux-limited regime instead. Finally, at such low gas puffing rates the assumptions made on the power balance itself must be double checked, since NBI loss terms could be significant.

5.3.2 DENSITY SHOULDER FORMATION AND QUALIFIER

The formation of a density shoulder has been commonly observed in L-mode once target flux rollover is achieved at high density, further developing after divertor detachment [52, 53, 54]. In

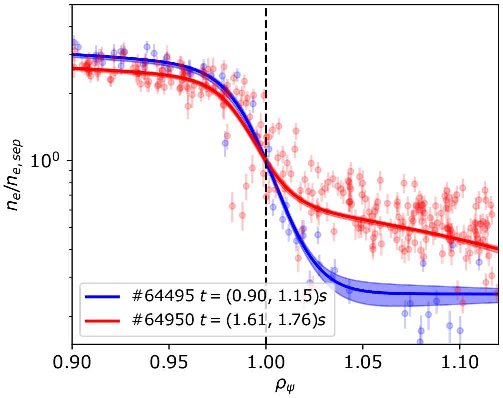

Figure 5.8: Upstream edge-SOL electron density profiles shown in figure 5.3, normalized to their respective density at the separatrix. For better visualization of the different shape features, the plot is shown in semi-logarithmic scale. The separatrix position is marked by a dashed black vertical line.

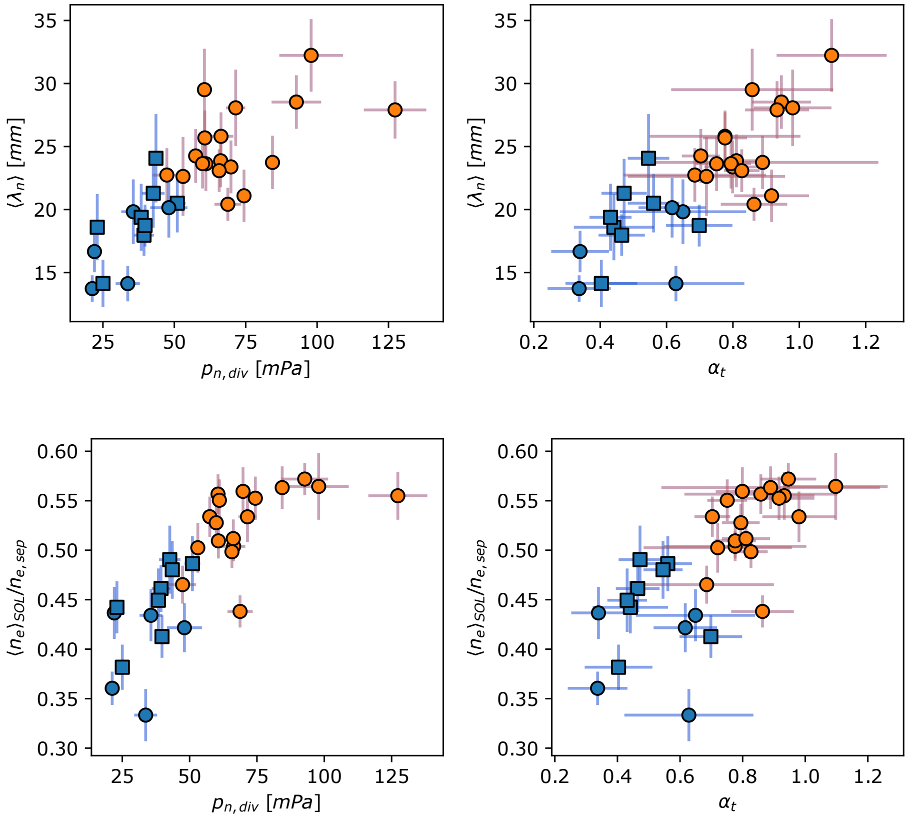

Figure 5.9: Modification of the (top) poloidally averaged near-SOL density decay length $\langle\lambda_n\rangle$ and (bottom) density shoulder amplitude parameter at increasing divertor neutral pressure and α_t parameter. The colormap distinguishes type-I ELMy time intervals from QCE regimes. Circles and squares indicate, respectively, bottom and top fuelling. λ_n has been estimated here in the radial interval $-6\text{ mm} \leq dr_u \leq 13\text{ mm}$, while the shoulder integral has been calculated over $0 \leq dr_u \leq 35\text{ mm}$.

H-mode conditions this requirement is less severe and previous experiments have shown that high recycling conditions are sufficient for shoulder formation [58].

Here the upstream density profiles introduced in figure 5.3 are shown once again in figure 5.8, however in this instance they have been normalized to their respective separatrix density and shown in semi-logarithmic scale, in order to highlight any differences in shape features. Some data points in the blue medium-low density case fall noticeably off of the fitting curve, owing however to the choice of the vertical scale which makes even small discrepancies stand out. One can see that, as the separatrix density increases at higher divertor neutral pressure, the upstream profiles undergo a significant modification both in terms of a flattening near the last-closed flux surface and a formation of a prominent density shoulder feature.

These two behaviours are once again extended to the whole fuelling scan database, where the global trends are visible in figure 5.9. The near SOL density *e*-folding length has not been estimated here directly from the fit: while the *mtanh* function can manage to well catch some features of an H-mode profile, like the pedestal height, the maximum gradient position and the gross SOL trends, it often fails at catching correctly the local near SOL slopes in situations where, like in QCE conditions, the radial gradients may be strongly asymmetric about the pedestal central position (see e.g. [145]). Consequently, λ_n at the midplane has been estimated via an exponential fitting of the raw profile data near the separatrix. The radial fitting range has been chosen here as an interval of ~ 19 mm width (i.e. $\sim 2\rho_{s,pol}$), partially comprising the confined region. The result has then been remapped to its poloidally averaged counterpart, which is shown in the top panels of figure 5.9 to increase at higher α_t.

In order to quantify the evolution of the density shoulder, a qualifier parameter can be defined based on the one introduced in [54], characterizing the global behaviour of the profile across the scrape-off layer rather than the far SOL region alone. The definition used here is

$$\frac{\langle n_e \rangle_{SOL}}{n_{e,sep}} = \frac{1}{n_{e,sep} \Delta dr_u} \int_0^{\Delta dr_u} n_e(dr_u) \partial dr_u \tag{5.3}$$

where the integral is carried out over a relative radius coordinate interval $0 \leq dr_u \leq 35$ mm. Equation 5.3 physically represents the ratio of the integrally averaged SOL density, divided by the separatrix density and as such it effectively measures the overall closeness of the SOL density profile to its LCFS value. As seen in the bottom panels of figure 5.9, the density shoulder amplitude steadily increases as the plasma becomes more interchange-unstable at higher α_t due to an increasing separatrix density. Again, like the latter a hint of saturation may be visible at the highest divertor neutral pressure levels, or similarly at α_t values higher than ~ 0.8.

5.4 Cross-field filamentary transport

In numerous experimental activities the role of convective filamentary transport has been suggested as key in achieving both the SOL power load broadening, and the formation of a far SOL density shoulder. As a matter of fact, an increase in the level of convective filamentary transport ensures that enough energy flows across the scrape-off layer to enhance the local ionization rates. This, combined with the increased recycled neutrals from the first wall, likely leads to a local increase in density and the formation of a SOL shoulder. This mechaism acquires particular relevance for high density H-mode scenarios, in which the inter-ELM transport is predominantly composed of filamentary structures, up to the extreme case of QCE in which filaments make up the largest part of the ELMy behaviour. In the following an assessment of the properties of turbulent blob-filaments has been made across the fuelling scan, and framed within the α_t parameter approach.

5.4.1 Filament parameters

For the purpose of estimating the properties of filamentary structures, the CAS procedure and characterization as described in section 4.4 has been exploited. The latter has been carried out over 3 to 8 ms long sub-intervals of the fast midplane reciprocating probe plunges, where the duration has been chosen based on the requirement of having a sufficiently robust statistics for a proper evaluation of the average and the filament properties. This choice has resulted in around $30 - 60$ filaments per interval, which are then averaged to yield the CAS results. Like with plasma profiles, longer sub-intervals are associated to type-I ELMy regimes and shorter ones to QCE H-modes. The blob size estimate resulting from the CAS averages have been here normalized to the ion sound Larmor radius. The dataset has been restricted to points with uncertainty smaller than their absolute value only, as in the previous sections. Moreover, some further points have been eliminated due to their respective plunge sub-interval corresponding to an average midplane-remapped probe position greater than the outer first wall major radius coordinate $R_{wall,out} = 1.1376$ m. This choice allows to compare only data with similar connection lengths and exclude the effects of field line shadowing at the first wall limiter tiles.

The results of the present analysis is shown in figure 5.10. The variation of each and every filament property has been assessed both as a function of α_t and, by means of the colormap, of the probe average normalized radial position. The α_t values shown here are the average ones pertaining to the corresponding time interval for profile analysis (section 5.3) within which the fast midplane probe has been plunged. This produces a narrower variation of the turbulence control parameter, nevertheless a significant variation in some of the main filamentary characteristics can still be seen. As a matter of fact, a significant rise of the radial velocity is visible in the top left panel as α_t increases,

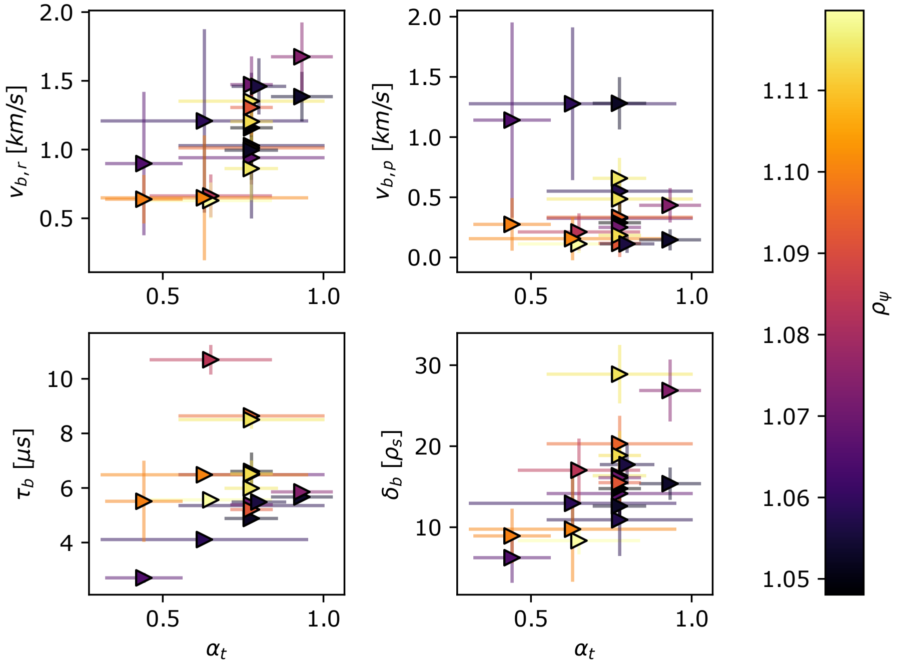

Figure 5.10: Filament properties correlation with the α_t parameter: radial velocity (top left), poloidal velocity (top right), FWHM blob time (bottom left), filament size (bottom right). The colormap and the associated colorbar indicate the average normalized radial position of the fast reciprocating probe during the corresponding plunge sub-interval over which the CAS procedure has been performed.

although the overall trend is affected by a large vertical scatter mainly due to a clustering of points around $\alpha_t \sim 0.75$. Typical filament velocity values are around $\sim$ 0.6 km/s for type-I ELMy measurements at the lowest α_t, up to $\sim$ 1.8 km/s at the largest values in QCE conditions. Similar values and trends have been achieved in other experimental efforts exploiting the THB diagnostic at AUG [45, 58] and the same probe used here at TCV in L-mode conditions [142], further supporting the observations shown in this manuscript. As a consequence of the rising radial velocity the blob size also increasing significantly, from $\sim$ 8 to $\sim$ 30 times the ion sound Larmor radius. The reported correlations constitute an indication of the fact that, as the edge plasma becomes more unstable towards resistive ballooning modes, faster and larger filaments start being expelled and travel radially outwards towards the first wall. On the other hand, no noticeable correlation is registered neither between α_t, the poloidal velocity $v_{b,p}$ and the FWHM blob duration τ_b, nor with the radial insertion position of the probe.

5.4.2 PROPAGATION REGIMES

The filament propagation mechanism is best described by the so-called *two-region model*, first introduced in [148] and later extended in [149] to allow for some blob non-idealities. In the following the two-region model is first briefly introduced, and later exploited to characterize the progagation regimes of the blobs measured here.

THE TWO-REGION MODEL

In [148], blob-filaments are modelled through an equivalent electrical circuit, with a voltage source located upstream and provided by the charge separation stemming from magnetic (i.e. ∇B and curvature) drifts at the outboard midplane. This, in turn, results in an $\mathbf{E} \times \mathbf{B}$ drift velocity propagating the filament radially outwards, whose magnitude depends on the parallel current return path of least resistance. The model reports on a functional dependence of the radial velocity on the filament size, parametrized in terms of a normalized blob size $\hat{a}$ and velocity $\hat{v}$

$$\hat{a} = \frac{\delta_b R^{1/5}}{L_{\|}^{2/5} \rho_s^{4/5}}, \quad \hat{v} = \frac{v_{b,r}}{c_s \left(\frac{2 L_{\|} \rho_s^2}{R^3} \right)^{1/5}}. \tag{5.4}$$

The functional relation $\hat{v} = \hat{v}\left(\hat{a}\right)$ depends, in turn, on the parallel current closure mechanism, giving rise to different propagation regimes. The closure scheme can be parametrized in terms of the three parameters

$$\Lambda = \frac{\nu_{ei}}{\Omega_{ce} \rho_s} L_{\|}, \quad \Theta = \hat{a}^{5/2}, \quad \varepsilon_\chi = \frac{1}{f_\chi} \tag{5.5}$$

where Λ is called *normalized collisionality* and ε_χ is the *flux flaring parameter*, quantifying how much the shape of a flux tube, and therefore of filaments, get distorted by the effect of flux expansion around the X-point. Based on these parameters, the filament regimes can be defined as follows:

- *Sheath-connected regime* (C_s): for $\Lambda < 1$ and $\Theta > 1/\varepsilon_\chi$ (small collisionality and large filament size) the return path is provided by parallel currents extending all the way to the divertor target, limited only by the resistivity of the plasma sheath. At increasing size the parallel damping is more effective, leading to a decrease of the radial velocity according to the dispersion relation $\hat{v} \sim \hat{a}^{-2}$.

- *Connected ideal-interchange regime* (C_i): for $\Lambda < \varepsilon_\chi \Theta$ and small filaments ($\Theta < 1/\varepsilon_1 \chi$), the cross-field ion polarization current in the divertor region dominates the return path for the current. Its effect is enhanced by X-point magnetic shear and weakened at larger filament size, so that the resulting size-velocity scaling is $\hat{v} \sim \varepsilon_\chi \hat{a}^{1/2}$.

- *Resistive X-point regime* (*RX*): at high collisionality and large blob size ($\Lambda < \Theta$), the upstream charge polarization is balanced by parallel flows up to the X-point, and by ion polarization currents from there on. This restricts the blob parallel extent so that they reach only partially into the divertor region. A higher upstream collisionality translates into a weaker return current, while parallel damping is enhanced at larger size, yielding $\hat{v} \sim \Lambda\hat{a}^{-2}$.
- *Resistive ballooning regime* (*RB*): at even higher collisionality with $\Lambda > \Theta$, parallel current becomes ineffective and the closure can be provided solely by the upstream cross-field ion polarization current. In turn, the parallel blob extension remains limited to above the X-point. Since larger blobs can sustain a higher charge separation, the dispersion relation is $\hat{v} \sim \hat{a}^{1/2}$.

The Λ parameter deserves particular attention here, since it has been recognized by several experimental efforts to play a key role in the enhancement of filamentary transport in high-density L-mode scenarios, the establishment of a density shoulder and the achievement of a detached divertor state. For each of these the condition $\Lambda > 1$ is often deemed necessary [150, 151], even if sometimes not sufficient [53]. Notably, a multi-machine study exploiting AUG, JET and COMPASS data has shown that most of the blob disconnection from the target happens when the effective divertor collisionality Λ_{div} is larger than 1 [151], where Λ_{div} is calculated from equation 5.5 using divertor plasma conditions as well as the X-point to target connection length. On JET alone, the condition $\Lambda_{div} > 1$ has been first seen to be linked to the achievement of a density shoulder both in L- and H-mode plasmas, however restricted only to cases in which high divertor collisionality is obtained by increasing the main species gas puffing rate [152]. Instead, in seeded scenarios with low gas puffing and high seeding rate a high Λ_{div} value is correlated to a detached divertor state but does not automatically imply the formation of a shoulder.

FILAMENT CLASSIFICATION

The $\Lambda_{div} - \Theta_{div}$ map for the fuelling scan analysis is shown in figure 5.10. The propagation regimes of the identified filament CAS waveforms are classified according to Λ_{div} and, by consistency, Θ_{div}. Data from swept floor Langmuir probes have been taken as representatives of the plasma conditions in the whole divertor region. In analogy with [142], the flux flaring parameter for a lower single null configuration has been set at $\varepsilon_\chi \sim 0.3$. Coherently with the observations made in L-mode conditions on AUG and TCV [153, 53], the detected blobs pertain mainly to the *RB* and *RX* regimes of propagation, signifying that they are either only partially connected to the divertor region or, in the highest collisionality cases, they are completely disconnected. Again, the colormap reveals no significant dependence on the radial measurement position. In support of the present observations, an experimental work on TCV [58] exploiting wall-mounted Langmuir probes at constant

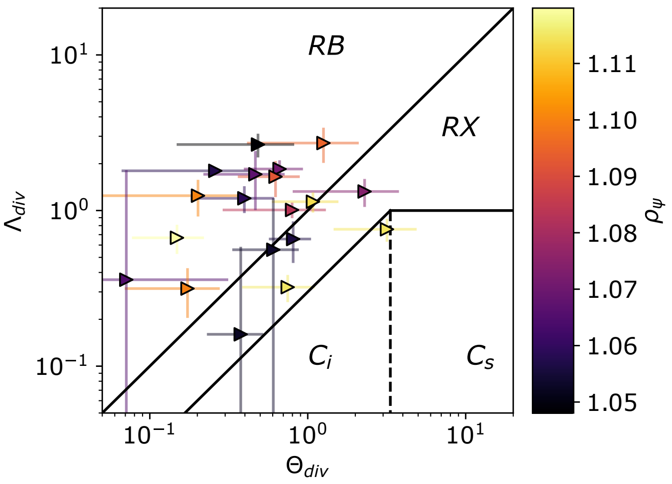

Figure 5.11: $\Lambda_{div} - \Theta_{div}$ map of the detected CAS blob waveforms. For visualization purposes, a double-logarithmic plot has been used. The colormap and associated colorbar represents the normalized radial position of the measurements during the corresponding plunge sub-interval. The boundaries among different propagation regimes are indicated as black lines, with the $C_i - C_s$ boundary sitting at $\Theta_{div} = 1/0.3$.

negative bias has found a continuous increase of the filament detection frequency at higher divertor dissipation both at the midplane and at the outer baffle tip. On the other hand, no significant variation has been registered by Langmuir probes at the machine floor, indeed suggesting that in the considered operating regimes the upstream filamentary dynamics is substantially decorrelated from that taking place downstream near the target.

6

THE ROLE OF PLASMA SHAPING

IN chapter 5 it was shown that an increase of the α_t parameter obtained via a higher separatrix density is correlated with a significant SOL heat load and density profile broadening, with formation of a far SOL shoulder and an enhancement of the filamentary activity. On the other hand, the approach used therein did not allow to explore other dependencies among those defining α_t and thus possibly influencing the SOL turbulent dynamics, for instance those linked to the magnetic equilibrium. Therefore, the purpose of the analysis presented in this chapter is to extend the fuelling scan database by probing the role of plasma shaping in setting the SOL properties during high density H-mode plasma discharges. At constant fuelling rate, the shaping variation has been achieved by a scan in upper triangularity, which directly influences the edge safety factor and consequently the α_t parameter. As in the previous chapter, firstly the response of the upstream plasma profiles to the shaping scan will be assessed, again with particular consideration of the SOL power width λ_q and the shape of the density profile in the near and far SOl regions. The second part of the chapter deals with plasma-wall interaction issues, in terms of both wall turbulent fluctuations and first wall recycling variations with shaping. In section 6.1 the experimental setup of the shaping scan database is presented. The impact of the upper triangularity on the separatrix plasma parameters, divertor heat load characteristics and density profile properties is assessed in section 6.2. In section 6.3 the variations of first wall density fluctuations are considered. Lastly, section 6.4 focuses on a change in plasma shaping may affect the plasma-wall interaction, in terms of first wall recycling and impurity sources.

6.1 Experimental setup of the shaping scan database

The left side of figure 6.1 shows the setup of the plasma shaping scan database, whereas the right side contains a visual representation of the δ_{up} variation throughout the experimental programme. All pulses have been carried out in an unbaffled TCV vessel and, like in the fuelling scan, are characterized by a plasma current $I_p = 170$ kA and toroidal field $B_\phi = 1.4$ T, both in reverse direction, as in panel (*a*). Any changes in plasma shaping are attributed to the upper triangularity alone: the

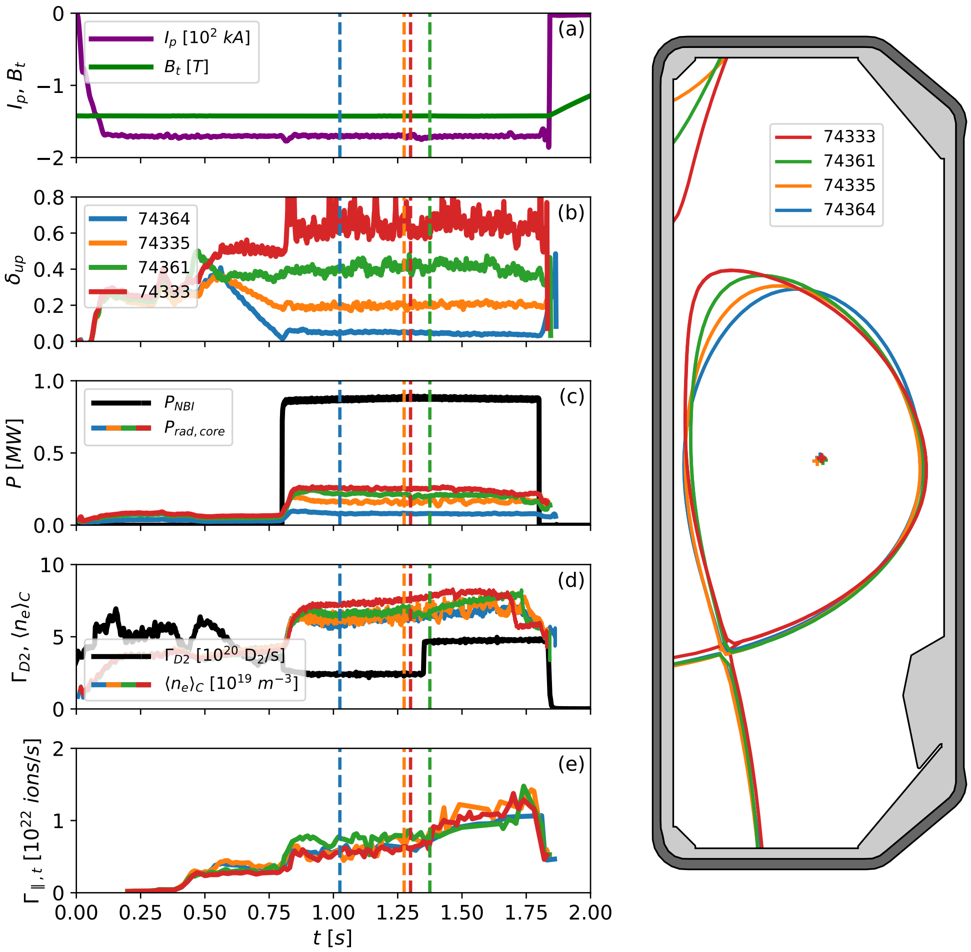

Figure 6.1: Left: time traces of the (*a*) plasma current and magnetic field, (*b*) upper triangularity, (*c*) NBI input power and core radiative losses, (*d*) input gas flow rate and core line-averaged density, (*e*) outer target particle flux. The four vertical colored lines indicate the center of the time intervals chosen for analysis of the shaping scan profiles in the chapter text. Right: vessel configuration and visualization of the extent of the upper triangularity variation through the typical four different equilibria used in this experimental programme.

elongation and the lower triangularity are, respectively, $\kappa \sim 1.5$ and $\delta_{low} \sim 0.6$, whereas δ_{up} has been varied uniformly among four equally spaced values between ~ 0.0 and 0.6, never probing negative triangularity scenarios, as seen in panel (*b*). The resulting variation in the cylindrical safety factor, using the expression in equation 4.11, is between ~ 4.4 and ~ 5.6, with a $\sim 27\%$ increase throughout the database from low to high shaping. At larger δ_{up} a higher feed-forward current is requested by the pre-shot equilibrium preparation modelling on the poloidal field coil controlling the radial position of the separatrix upper cusp. This puts more strain on the plasma control system, which has a harder time compensating deviations from the reference geometry, explaining the higher level of fluctuations in the δ_{up} reconstructed signal.

Like in the fuelling scan case, a further ~ 1 MW of NBI heating has been provided for H-mode access between 0.8 s and 1.8 s. The NBI trace is shown in panel (*c*), together with the bolometric value of the core radiation from RADCAM. The same flat-top gas fuelling scheme is applied throughout the database and shown in panel (*d*), consisting in two feed-forward steps at $\sim 2.5 \cdot 10^{20}$ D_2 molecules/s and $\sim 5.0 \cdot 10^{20}$ D_2 molecules/s puffed from the innermost floor piezoelectric valve. The temporal evolution of the spatially integrated outer target particle flux is represented in panel (*e*), indicating that, like in the previous experiment, no rollover occurs and the outer target is in attached, high-recycling divertor conditions at all times.

The core line-averaged density, shown in panel (*d*) together with the gas flow rate, varies between $\sim 6.5 \cdot 10^{19}$ m^{-3} and $\sim 8.0 \cdot 10^{19}$ m^{-3}. Moreover, the core radiated power increases at larger shaping from ~ 100 kW to ~ 200 kW. This indicates that, along with the shaping, a small variation in some of the other parameters inevitably takes place across the database. Notably, the first wall tiles are made of graphite, which may introduce to some degree a source of uncertainty in the control

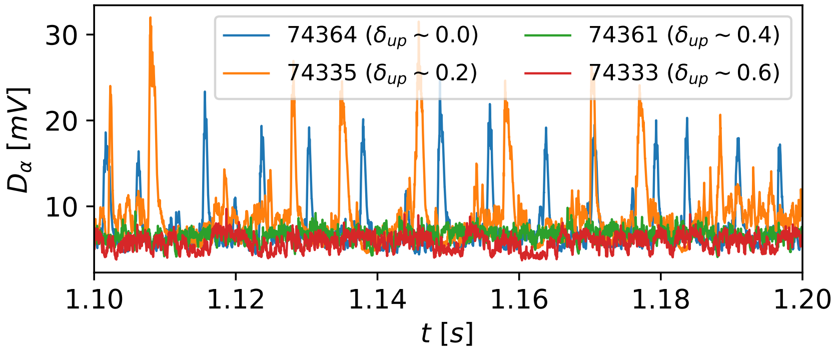

Figure 6.2: ELM behaviour at varying plasma shaping, as registered by a bottom-lateral line integrated D_α photodiode measurement looking at the divertor region. The color coding matches the different shapes in figure 6.1.

of neutral particle sources. Furthermore, the plasma approaches a close-to-double-null magnetic configuration at high δ_{up}, so that the machine roof becomes more and more involved in the parallel dynamics. Together with a smaller outer gap at high shaping, these may be responsible for an enhancement of both the first wall recycling and the impurity sources. In order to improve the reproducibility of the density traces across the experiment, long glow discharge cleaning phases have taken place in between the shots. In this work, the question of possible shaping-induced variations in the neutral and impurity sources is addressed more in detail in section 6.4.

The first consequence of a change in plasma shaping can be visualized in figure 6.2, where the time traces of the D_α line integrated light emission within a 100 ms long temporal window is displayed, as seen by a photodiode with a bottom-lateral line of sight looking into the divertor chamber. The two sample discharges at low shaping, namely $\delta_{up} \lesssim 0.2$, are characterized by a markedly type-I ELMy behaviour, with well-defined peaks distinctly visible in the signal. Conversely, at high shaping ($\delta \gtrsim 0.4$), a clear transition to the QCE regime takes place, with large bursts giving way to a much less coherent, low amplitude light emission.

6.2 CHARACTERIZATION OF THE UPSTREAM PROFILES

Like in the fuelling scan case, the separatrix parameters have been evaluated by the power balance approach in section 4.3 exploiting the two-point model. The overall database reports an estimate $T_{e,sep} \sim 45$ eV for the separatrix temperature on average, with a ~ 1.5 mm mean inwards radial profile displacement with respect to the equilibrium reconstruction. For the fitting procedure, differently from chapter 5 only the measurement volumes below the magnetic axis have been used instead of the entire Thomson scattering line of sight, due to a non-negligible radial shift between the upper and lower parts in the edge and pedestal regions. This displacement, which may be due to either finite poloidal gradients or uncertainties in the equilibrium reconstruction in the upper half of the machine, is a known issue of the diagnostic and has been already reported e.g. in [147]. Examples of edge-SOL temperature and density profiles are shown in figure 6.3, where only the *mtanh* fitting curves are displayed in order to avoid clustering and making visualization difficult. Each single profile has been chosen so as to be characterized by a similar separatrix density value $n_{e,sep} \sim 1.8 \cdot 10^{19}$ m^{-3}, within experimental error. Table 6.1 reports the shot numbers, the values of upper triangularity, the power balance estimation of the separatrix density and the α_t evaluation of the selected sample profiles.

A first analysis of the profiles in figure 6.3 suggests that the two QCE temperature fits display a lower pedestal height than the two type-I ELMy cases, coherently with the expected drop in energy confinement in the QCE regime. On the other hand there is no great variation taking place in the

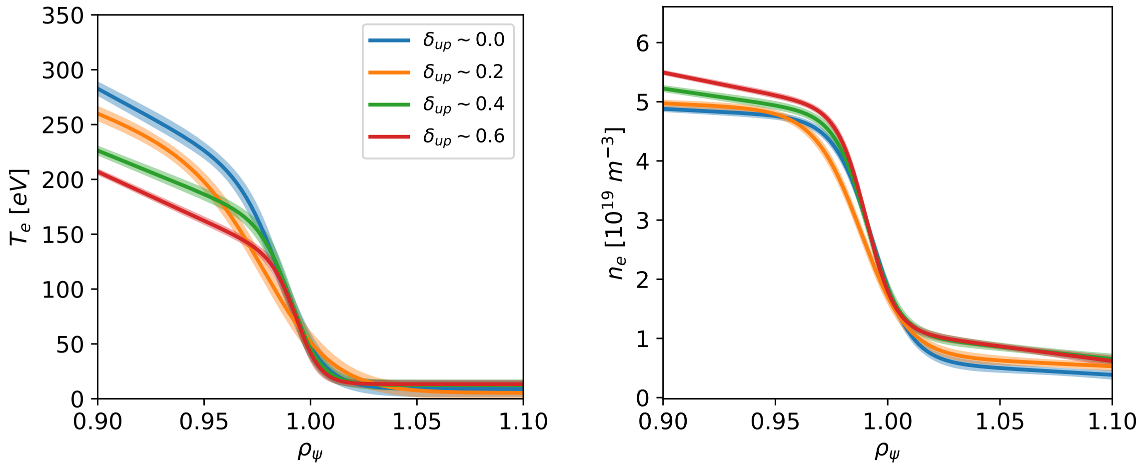

Figure 6.3: Temperature (a) and density (b) profiles for the four sample discharges shown in figure 6.1, one for each shape. The shown profiles have been obtained by fitting TS data only, due to the lack of THB data for this subset of the database. In order to highlight the effect on the profiles due to plasma shaping alone, the shown profiles have been selected in such a way as to have similar separatrix density. For the purpose of easier visualization and avoidance of clustering, only the profile fits are displayed as solid lines, with their respective uncertainty represented by the shaded areas.

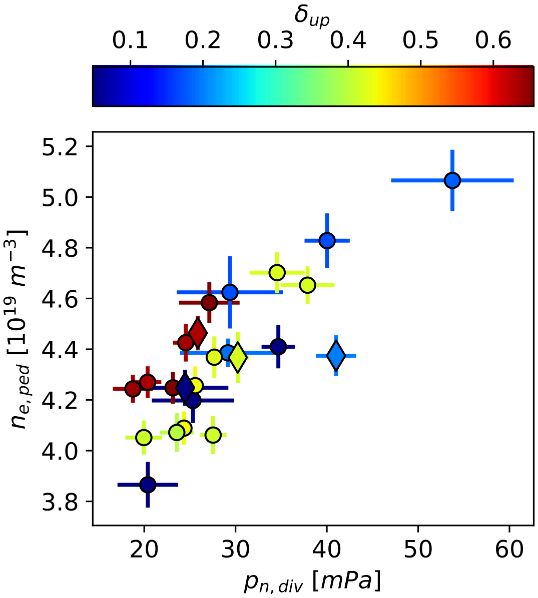

Figure 6.4: Pedestal top density dependence on the divertor neutral pressure and upper triangularity, respectively along the abscissa and as colormap. The large diamonds correspond to the profile fits shown in figures 6.3 and 6.8.

Shot #	δ_{up}	q_{cyl}	$n_{e,sep}$ $[m^{-3}]$	$T_{e,sep}$ [eV]	Z_{eff}	α_t
74364	0.05	4.43	$1.86 \cdot 10^{19}$	48.1	1.60	0.61
74335	0.17	4.80	$1.85 \cdot 10^{19}$	47.0	1.65	0.71
74361	0.42	5.25	$1.84 \cdot 10^{19}$	45.8	1.86	1.05
74333	0.63	5.60	$1.80 \cdot 10^{19}$	41.9	1.80	1.34

Table 6.1: Shot numbers, upper triangularity and basic separatrix properties of the selected subset of time slices within the available database, for which density and temperature profiles are shown in figures 6.3 and 6.8. For all the snapshots in the database, the major radius used for calculation of α_t is $R = 0.9$ m.

pedestal density, apparently in contrast with some previous results [154, 155] according to which high-δ plasmas are characterized by better confinement due to a higher $n_{e,ped}$. As a matter of fact, at high plasma shaping the pedestal stability boundary gets modified so as to include an operational region at larger edge bootstrap current and normalized pressure gradient. Despite this, in [130] it is noted that a low pedestal collisionality (i.e. low pedestal density, high pedestal temperature) is needed to be able to access these operational conditions, so that the density confinement starts to branch according to the δ_{up} value only when $\nu^*_{ped} \lesssim 1$. The fitted pedestal parameters can be used to infer values of pedestal collisionality of the order of $\sim 3-5$ for the low shaping cases, and $\sim 10-15$ at high δ_{up}, well above the mentioned threshold, so that a significant difference in pedestal particle confinement should not be seen. Indeed, as demonstrated in figure 6.4, the pedestal density obtained from the fits displays a similar value for all profiles at $n_{e,ped} \sim 4.3 \cdot 10^{19}$ m^{-3}, supporting the interpretation proposed in [130].

6.2.1 SEPARATRIX PARAMETERS OPERATIONAL RANGE

Figure 6.5 shows the separatrix parameter space achieved by varying the plasma shaping and, to a less extent, by the change in divertor neutral pressure deriving from the chosen feed-forward gas puffing scheme as well as the effect of plasma particles recycling at the first wall. As expected and shown in the left panel, the separatrix density keeps growing with the divertor neutral pressure, at least when considering each plasma shape separately. With respect to the fuelling scan, the absence of divertor baffles is translated into a higher slope for the $n_{e,sep} - p_{n,div}$ correlation and overall higher density values. This becomes particularly apparent when comparing the subset of discharges at $\delta_{up} \sim 0.4$, having an equilibrium geometry similar to that considered in chapter 5, at least when considering the $20 - 40$ mPa range in $p_{n,div}$ and using figure 5.4 for reference.

However, when considering the overall dataset, a clear dependence of the separatrix density on plasma shaping emerges via the branching of the $n_{e,sep} - p_{n,div}$ relation at different values of up-

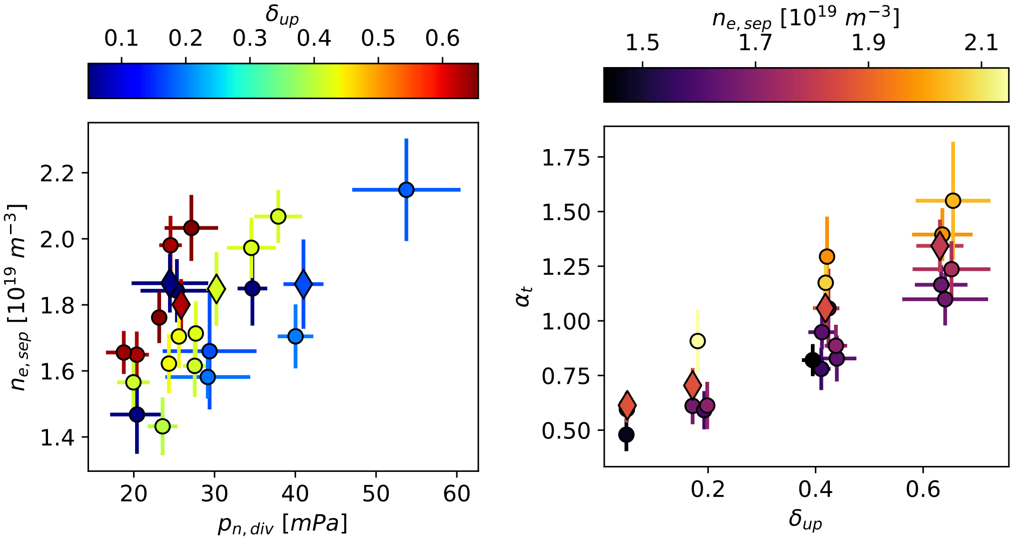

Figure 6.5: Left: upstream separatrix density dependence on the divertor neutral pressure, with the colorpam indicating the upper triangularity. Right: full α_t experimental range as a function of the shaping along the abscissa, and the separatrix density on the colormap. In both panels, the large diamonds correspond to the profile fits shown in figures 6.3 and 6.8.

per triangularity. An increase of $n_{e,sep}$ is observed at similar divertor neutral pressure when moving from low to high shaping plasmas, at least for $\delta_{up} \gtrsim 0.2$. One can also reason the other way around: choosing a fixed separatrix density value at different δ_{up} requires a variation in $p_{n,div}$. This observation serves as an indication that the features of the SOL profiles analyzed later in detail may be sensitive to the plasma shaping not only in a direct way, but also through its indirect effects on other separatrix parameters. Indeed, the predicted shaping-induced α_t increase is of the order of $\sim 60\%$ through the effect of the q_{cyl}^2 factor alone, whereas the achieved experimental variation between $\sim$ 0.48 and $\sim$ 1.56, shown in the right panel of figure 6.5, takes place in a larger interval. More specifically, the separatrix density ranges between $\sim 1.5 \cdot 10^{19}\ \mathrm{m}^{-3}$ and $\sim 2.1 \cdot 10^{19}\ \mathrm{m}^{-3}$, inducing a $\sim 40\%$ increase on α_t. A change in $T_{e,sep}$ takes place between $\sim$ 48 eV and $\sim$ 42 eV, linked to both a broadening of the scrape-off layer (see section 6.2.2) and the reduction of the SOL input power via an enhancement of core radiation (see figure 6.1. While this variaion may appear not so significant per se, the temperature appears in equation 2.70 with a squared exponent and a further $\sim 30\%$ α_t increase must be accounted for. Finally, the effectiove ion charge plays a role as well, since it undergoes a $\sim 20\%$ change between $\sim$ 1.6 and $\sim$ 1.9 across the database. Under the assumptions that these changes take place almost independently from one another, one can combine all these factors to yield a total $\sim 3.5-$fold increase in α_t, not so different from the ~ 3.25 factor between the maximum and minimum values.

6.2.2 EVOLUTION OF THE DIVERTOR HEAT FLUX PROFILES

The outcome of the SOL heat load width analysis through the VIR infrared thermography system is reported in figure 6.6. Notably, the average and local outer midplane poloidal field change as a consequence of the modifications in shaping. Therefore, all the measured poloidally averaged heat flux profile widths have been normalized to $\rho_{s,pol}$ for proper comparison with the heuristic-drift model. To maintain generality in evaluating the results of this analysis, also the near SOL density e-folding lengths calculated in section 6.2.3 have undergone the same normalization.

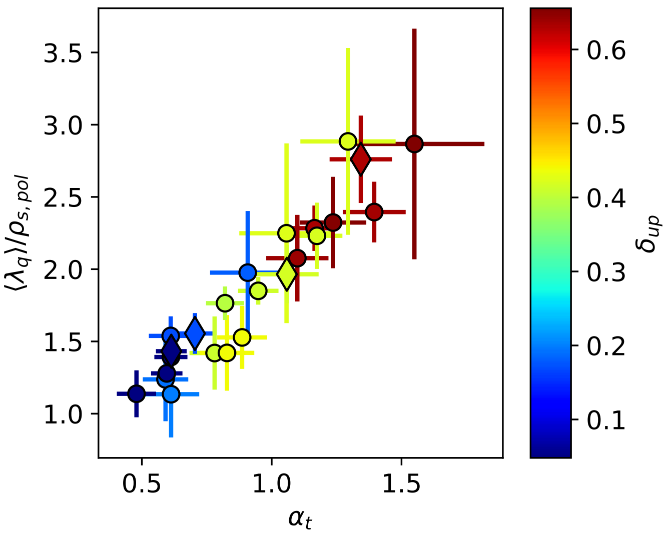

Figure 6.6: Normalized poloidally averaged SOL power fall-off length $\langle\lambda_q\rangle/\rho_{s,pol}$ dependence against the α_t parameter. The colormap serves as an indication of the upper triangularity value associated to each point. The large diamonds correspond to the profile fits shown in figures 6.3 and 6.8.

The analysis shows evidence of a significant broadening of the SOL power channel when increasing α_t by moving from low to high shaping. In particular, the increase of the normalized $\langle\lambda_q\rangle$ can be quantified by a factor ~ 2.5, corresponding to a variation in physical units between ~ 10.6 mm and ~ 27.2 mm. This variation is, once again, coherent with the expected divertor heat load broadening when moving from type-I ELMy regimes to QCE conditions. Moreover, it does not take place abruptly across the two scenarios but rather being gradual and already present at low δ_{up}, hinting at a progressive destabilization of resistive ballooning modes near the pedestal bottom for larger α_t. Coherently with previous AUG results [103, 44] and the fulling scan analysis in the previous

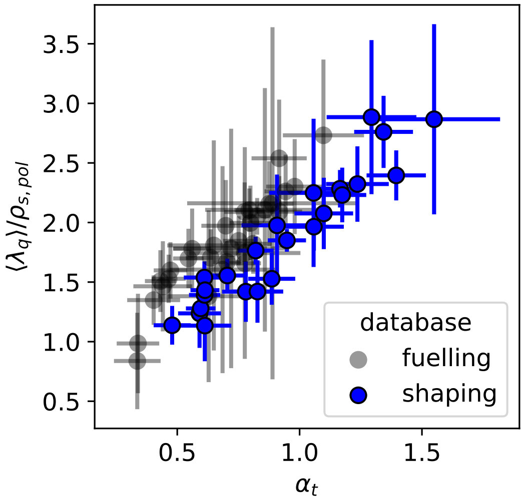

Figure 6.7: Comparison of the normalized $\langle\lambda_q\rangle$ trends obtained in the fuelling and shaping scan analysis, respectively as transparent gray and full blue circles.

chapter, all the normalized measured heat load widths are larger than the ~ 0.4 value predicted by the heuristic-drift model for low collisionality type-I ELMy H-mode conditions.

Comparing these results with those of the fuelling scan experiment reveals a remarkable closeness in trends, as shown in figure 6.7. In detail, a modification of α_t within similar operational ranges results in a qualitatively comparable variation of the normalized SOL power width. A slight discrepancy is nevertheless present, with the two trends seemingly shifted with respect to each other, which could be potentially attributed to the slight differences in analysis methodology for the two databases, with particular regard on the Thomson scattering diagnostic. Moreover, the shaping scan experiment has been carried out several months after the acquisition of the gas scan data, hence some drifts in the calibration of other key diagnostics like the VIR thermography system may have appeared in the meantime. Despite this slight mismatch, however, the similarity of the two trends can help point towards a unified description of the two datasets by means of the sole turbulence control parameter α_t.

6.2.3 DENSITY PROFILE MODIFICATION

The variation of the upstream density profiles is assessed here through figure 6.8, displaying the sample fitting curves from figure 6.3 zoomed in on the scrape-off layer region. Normalization to their respective separatrix density has been carried out and a semi-lograithmic scale has been chosen for representation, better emphasizing the differences in the gradients in the near and far SOL. Being characterized in any case by similar $n_{e,sep}$, any difference in the normalzied profiles can be reliably

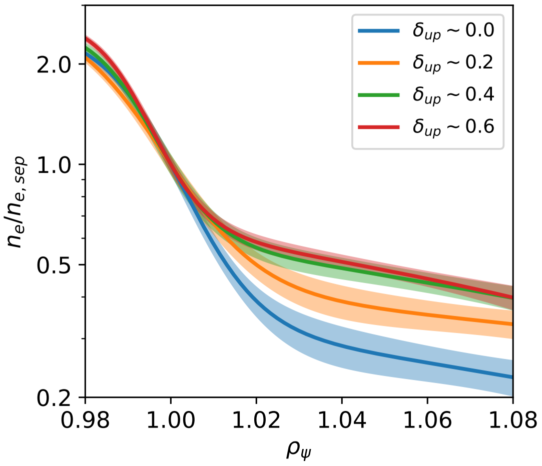

Figure 6.8: Upstream SOL density profiles for the four sample discharges in figure 6.1, normalized to their respective separatrix density. The semi-logarithmic scale helps putting into evidence the development of a shoulder feature in the far SOL. Raw data points have been excluded from the plot to avoid clustering.

attributed to the effect (direct or indirect) of plasma shaping. As a matter of fact, a visible modification in the profiles takes place when moving from low to high plasma shaping, with the near SOL gradient becoming progressively flatter and the distinct change in slope approaching the separatrix, which results in a more prononuced far SOL density shoulder.

Over the entire database, the near SOL density *e*-folding length has been calculated over the radial interval $0 \leq dr_u \leq 10$ mm and the shoulder amplitude qualifier as defined by equation 5.3 is here redefined on the ρ_ψ coordinate instead

$$\frac{\langle n_e \rangle_{SOL}}{n_{e,sep}} = \frac{1}{n_{e,sep}\Delta\rho_\psi} \int_{1.0}^{1.1} n_e(\rho_\psi) d\rho_\psi. \tag{6.1}$$

with the integration carried out over $1.0 \leq \rho_\psi \leq 1.1$. While the choice of a different fitting interval for λ_n and coordinate for the shoulder parameter is certainly inconvenient for comparison with the result of section 5.3.2, it is nevertheless necessary due to the changing field line distribution, flux expansion and wall gap around the outer midplane, imposing a common method of analysis across all geometries.

The overall density profile behaviour is shown in figure 6.9, with the normalized $\langle \lambda_n \rangle$ exhibiting a continuous growth at increasing α_t, with greater values generally corresponding to higher shaping. The broadening amounts to a similar factor as for the heat load, with $\langle \lambda_n \rangle$ changing from $\sim$ 16.0 mm to $\sim$ 39.2 mm in physical units. Moreover, the shoulder feature is more pronounced at higher

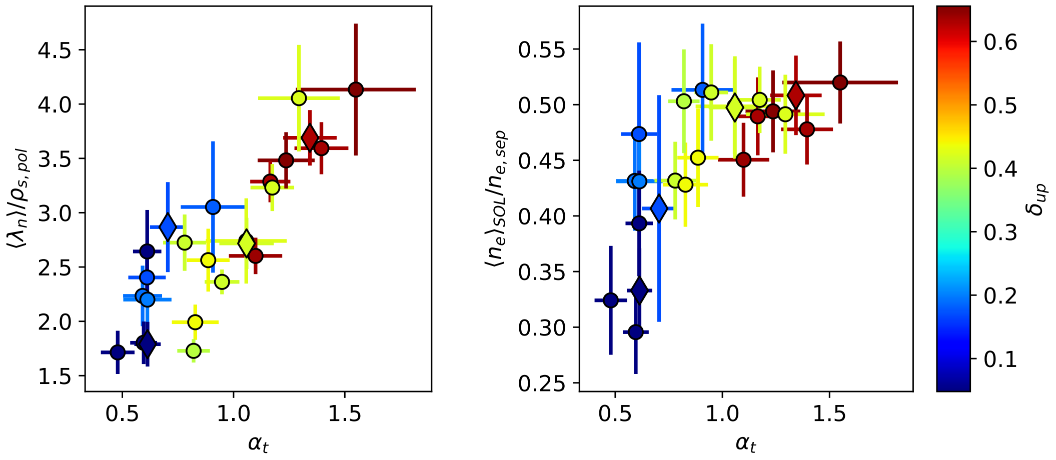

Figure 6.9: Variation of (left) the normalized near SOL density e-folding length and (right) density shoulder amplitude qualifier across the α_t variation within the shaping scan database. The colormap highlights the upper triangularity associated to each point. The normalized $\langle\lambda_n\rangle$ is calculated within the radial interval $0 \leq dr_u \leq 10$ mm. The shoulder amplitude is estimated on the normalized radius interval $1.0 \leq \rho_\psi \leq 1.1$. In both panels, the large diamonds correspond to the profile fits shown in figures 6.3 and 6.8.

shaping, increasing up until saturation takes place at $\alpha_t \gtrsim 0.8$, coinciding with the onset of the QCE regime at high δ_{up}. The two results show in the figure suggest that as the region in the proximity of the separatrix becomes more unstable towards resistive ballooning modes through a reduction of local magnetic shear stabilization, a greater level of radial particle transport ensues and this is accompanied by a broadening of the SOL density profile. The saturation in the shoulder amplitude, however, seems to indicate that this mechanism is efficient in flattening the density gradients only up until QCE is fully established, after which the average SOL density increases proportionally to $n_{e,sep}$.

6.3 ASSESSMENT OF FIRST WALL DENSITY FLUCTUATIONS

The enhancement of radial turbulent filamentary transport towards the first wall is believed to be one of the main causes underlying the formation of a density shoulder in high density H-mode regimes, and in particular during the transition from type-I ELMs to QCE. While in chapter 5 evidence for such an enhancement has been reported using the fast reciprocating probe at the midplane, such diagnostic was not available during the shaping scan programme and therefore neither the filament properties could be inferred along the SOL radius, nor information about the radial

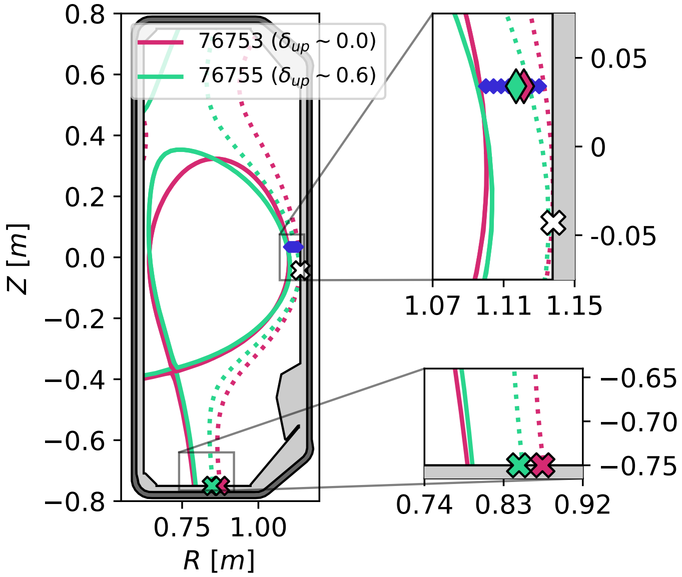

Figure 6.10: Edge-SOL diagnostics layout used for the study of first wall fluctuations, with the relevant midplane and divertor systems zoomed in. The solid and dotted lines represent, respectively, the separatrix geometry of the two shapes and the first magnetic flux surfaces intercepting the first wall. The white cross at the outer midplane and the two colored ones at the machine floor indicate the midplane LP used for fluctuation analysis and the two probes magnetically connected to it. The measurement volumes of the THB diagnostic are given by the blue diamonds at the midplane, with the selected channels being marked by a bigger symbol at different colors.

particle load on the first wall could be deduced. On the other hand, the response of first wall fluctuations with respect to changes in shaping could be studied at various poloidal wall positions by means of the full set of wall-mounted Langmuir probes operated at constant negative bias. These measurements have been complemented here with the high frequency signals acquired by the THB diagnostic.

No time-resolved fluctuation measurements are available for the profile database presented in section 6.2, since the Langmuir probes have been therein operated in swept mode and a change in operational settings could be possible only in between the shots. For this reason, a small dedicated subset of discharges have been run at the extreme δ_{up} values, with the two considered geometries and the diagnostic setup as in figure 6.10. The full set of wall-mounted Langmuir probes has been operated at constant negative bias for fast measurements of the ion saturation current signal. The engineering inputs are otherwise the same as in section 5.1, although for the discharge #76755 the duration of the NBI heating waveform had to be halved due to operational restrictions. A 300 ms long steady state time interval has been analyzed for both discharges, being characterized again by a similar separatrix density $n_{e,sep} \sim 1.7 \cdot 10^{19}$ m^{-3}. Given that the VIR thermography system was not available at the time of the experiment, a 45 eV estimate has been used as a representation of the separatrix temperature, in line with the average value obtained within the profile analysis in section 6.2.

Firstly, the fast temporal measurements of the ion saturation current density at the first wall and the light emission detected by the THB diagnostic have been analyzed. In figure 6.11 the normalized probability distribution functions (PDFs) of the two signals have been plotted. The top one reports the distribution of the inter-ELM j_{sat} measurement on the Langmuir probe #63, which is located just below the midplane and is marked in figure 6.10 by a white cross. Cross-validation of this signal has been made against the HeI line emission at a wavelength of 667 nm, which is the most intense one recorded by the THB spectrometer and whose PDF is shown in the bottom panel. For a proper comparison of the two systems taking into account the change in magnetic field topology around the outer midplane induced by the modification in δ_{up}, the displayed THB distribution refers to the radial channel with the highest temporal cross-correlation with respect to the midplane probe. The chosen channels are shown in the upper right zoom in figure 6.10 as large diamonds, with their colors matching the different geometries. The normalized PDF are seen to undergo a significant change when moving from low to high shaping, with the average value increasing and the overall distribution exhibiting larger variance and skewness. On the one hand, the observation of a higher first wall j_{sat} average at high upper triangularity is a possible indication of a larger plasma density in contact with the solid surface, coherently with the formation of a density shoulder in QCE. On the other hand, the increasing standard deviation points towards a higher level of fluctuations at large δ_{up}. On top of this, the marked positive skewness of the two distributions, both for the midplane LP and for the chosen THB channels, is a strong indicator of the intermittent filamentary nature of far-SOL transport [95, 156, 94, 81].

In figure 6.12 the previous observations are extended to the full set of Langmuir probes located on the low field side first wall tiles. Following TCV geometric conventions [109], the poloidal distribution of the j_{sat} signal average and standard deviation at each probe has been mapped to a curvilinear abscissa running clockwise around the TCV unbaffled vessel contour, originating at the high field side midplane. The portions of the wall taken under consideration are the upper and lower parts of the vertical tiles, together with the port protection just above the 45-degree tiles in the lowermost outer machine corner. The increase of both the j_{sat} average and standard deviation is localized on the lower vertical tiles below the outer midplane, with negligible changes in the other regions. This indicates that an enhancement in radial particle transport may be localized only around and/or just below the midplane when moving from low to high plasma shaping.

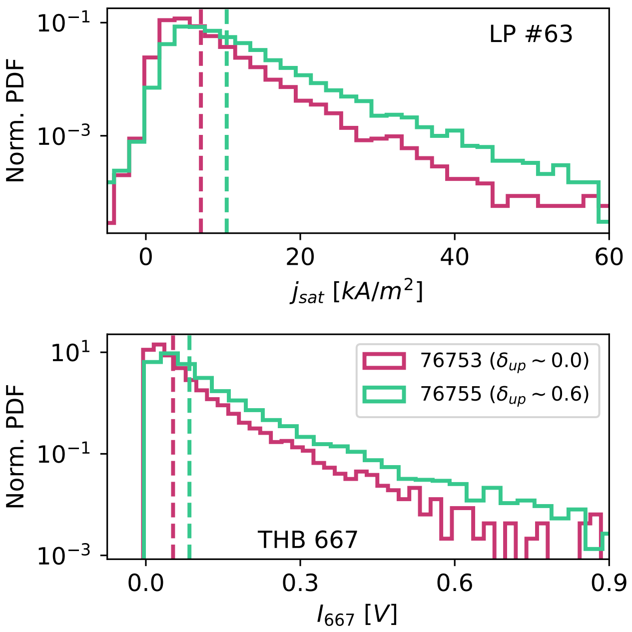

Figure 6.11: Top: normalized probability distribution function of the inter-ELM j_{sat} signal from the Langmuir probe at the midplane. Bottom: normalized probability distribution function of the 667 nm HeI line emission registered by the THB. For each shape, the chosen THB channel is the one correlating best in time with the midplane probe. The colors indicate the shaping, with magenta and green used respectively for low and high δ_{up}. The vertical dashed lines indicate the PDF averages.

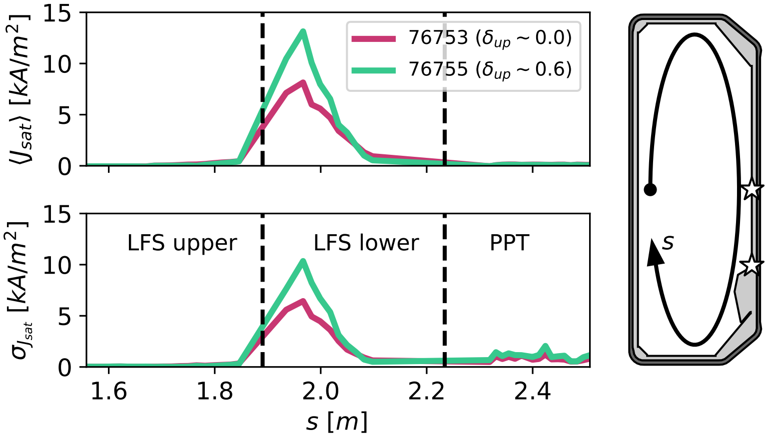

Figure 6.12: Poloidal distribution of the (top left) average and (bottom left) standard deviation of the full set of Langmuir probes located at the low field side portion of the first wall. The horizontal axis s is a curvilinear abscissa running clockwise around the vessel perimeter, starting at the high field side with the direction marked by the elliptical arrow in the right panel. The boundaries between different sections of the LFS wall are marked by vertical dashed lines in the two left plots, and by stars in the TCV cross-section on the right.

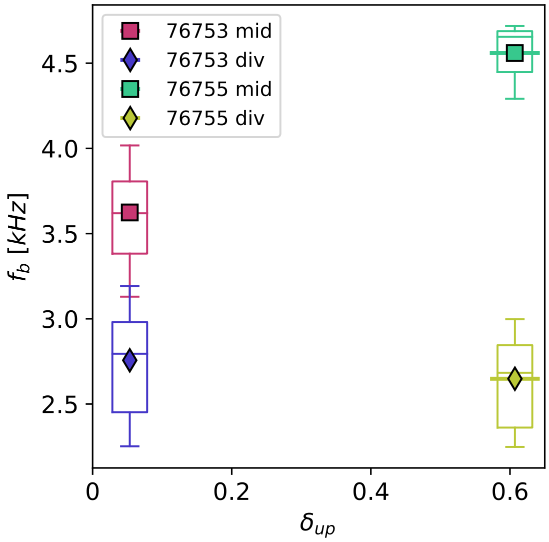

Figure 6.13: Right: filament frequency dependence on upper triangularity, measured by the midplane and divertor Langmuir probes. The mean values are represented as either squares (midplane) or diamonds (target). The boxplots hint at the frequency data dispersion, with the middle bar being the median and the whiskers indicating the inter-quartile range.

Finally, one can estimate the filament frequency at the midplane probe and the two other divertor ones poloidally connected to it at the vessel floor. Single peaks can be identified in the j_{sat} signal by operating the threshold detection procedure as in section 4.4, resulting in a time-resolved collection of fluctuation frequency values. The characterization of the latter is displayed in figure 6.13, where the solid markers indicate the frequency average while the boxplots hint at the dispersion of the data. In detail, the midplane probe registers a significant increase in the filament frequency at higher plasma shaping, supporting the interpretation according to which a more resistive-ballooning unstable plasma, which is subject to an enhanced turbulent activity around the edge and separatrix, ejects a greater number of coherent structures reaching the wall per unit time. On the contrary, the divertor probes do not register a significant change as the shape evolves towards high δ_{up}, with the overall signal statistics seemingly unaffected. This may indicate that the filamentary dynamics at the divertor target be substantially uncorrelated from that taking place upstream, which nevertheless does not exclude that filaments actually reach at least partially into the divertor chamber, as demonstrated for instance in L-mode TCV experiments [157]. Another possible interpretation could be partly provided by the generation and propagation of divertor-localized filaments, originating below the X-point by means of plasma turbulence localized along the divertor leg [158].

6.4 Plasma-wall interaction issues

The outcomes of the analysis presented in sections 6.2 and 6.3 reveal the prominent role of plasma shaping in setting the characteristic lengths of the SOL plasma profiles and the behaviour of turbulent fluctuations propagating across the scrape-off layer. Nevertheless, some observations made throughout this chapter, for instance those in section 6.2.1, indicate that the influence of the upper triangularity could extend beyond its direct effects, indirectly affecting other operational parameters which enter into play when setting the SOL dynamics. Some TCV works already showed something in this sense, particularly on the correlation among the plasma geometry relative to the vessel physical boundaries, the degree of divertor closure and the neutral particle concentration in the main chamber [55]. This is particularly important for this work, since the outer gap beween the separatrix and the first wall tiles has not been kept constant during the execution of the shaping scan experimental programme, potentially leading to a change in the particle balance around the midplane via modified neutral sources. On top of this, the variation of the core radiative losses observed in section 6.1 when moving from low to high δ_{up} calls for a proper evaluation of the impurity sources.

6.4.1 Midplane neutral pressure measurements

In order to carry out this evaluation, the time evolution of the midplane neutral pressure can be considered, as measured by the midplane baratron gauge for two sample discharges within the profile database analyzed in section 5.3. High frequency noise in the raw pressure time trace has been pre-treated by means of a digital finite impulse response filter, passing a bandwidth between 12 Hz and 24 Hz. The result, displayed in figure 6.14, nonetheless still shows some large variation for the low shaping signal with respecto to high δ_{up} case. This however may be due to both the finite time

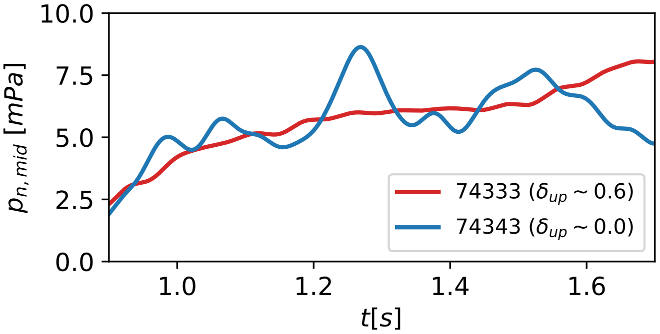

Figure 6.14: Time evolution of the midplane neutral pressure time trace, with the low δ_{up} discharge represented in red and the high δ_{up} discharge in blue.

response of the baratron gauge and to its inherent time delay, which causes big excursions in the signal, possibly induced by ELMy activity, to be smoothed out and appear as large oscillations.

Despite these, though, the two time evolutions remain relatively close to each other throughout the whole duration of the H-mode phase shown in the figure, suggesting that the upstream neutral density around the outer midplane is not greatly affected by the change in shaping. Then, a variation in the local ionization sources near the first wall, contributing to the far SOL density level, would be affected by the enhanced turbulent behaviour of the SOL plasma leading to the formation of a density shoulder.

It is worth stressing out that the measurements reported by the midplane baratron gauge is taken several tens of centimeters away from the vessel and as such it may be not completely representative of the actual neutral pressure in the main chamber, at least on a quantitative side. The reason for this resides on the fact that the hot SOL neutral atoms and molecules, upon entering the baratron duct, collide with its walls and transfer to it a significant part of their momentum and kinetic energy, until they thermalize at the baratron ambient temperature (approximately $\sim$ 293 K, or $\sim$ 0.025 meV). Hence, a significant pressure drop takes place within the duct volume itself between the vessel and the measurement location, further enhanced by the recombination processes turning atoms into molecules and therefore subtracting particles from the overall momentum balance along the duct. Simple 0D models could be potentially used, like the ones proposed by Niemczewski [159] or its extension by Wensing [121], relating the neutral pressure at the first wall and that measured by a distant baratron gauge, assuming full atomic recombination along the way. Unfortunately, the physics information necessary to make this evaluation, like the actual atomic and molecular deuterium temperatures at the first wall, is lacking in the present manuscript and these models cannot be applied properly, however in common situations they tend to predict in-vessel neutral pressure values differing from the gauge measurement by even an order of magnitude.

Regardless of the experimental observations reported here, it must be stressed out that a more concentrated neutral population, ensuing from an increase of the main chamber recycling phenomena in the vicinity of the outer midplane due to a smaller outer gap at high shaping, is not enough to ensure the formation of a density shoulder feature in the scrape-off layer. As a matter of fact, as also well outlined in [160] through numerical simulations of plasma-neutral interaction in AUG, the additional neutrals must necessarily be provided sufficient energy to become ionized, so as to effectively observe an increase in the local ionization sources and produce a higher far SOL electron density. Even in the presence of more neutrals, anyway not observed in this work as far as the diagnostic capabilities can suggest, the additional energy input to the scrape-off layer can only come from an enhancement in turbulent transport such as that observed in section 6.3.

6.4.2 CORE RADIATIVE LOSSES

Despite the conclusions made on the relation between the upper triangularity and the first wall recycling, changes in magnetic topology have still measurable, non-negligible consequences on the level of carbon impurity intake from the plasma-facing components, hence on the core radiative losses. An example of this is given in figure 6.15, illustrating two emissivity maps obtained by tomographic inversion of RADCAM bolometry data, obtained with field-aligned smoothing with a reconstruc-

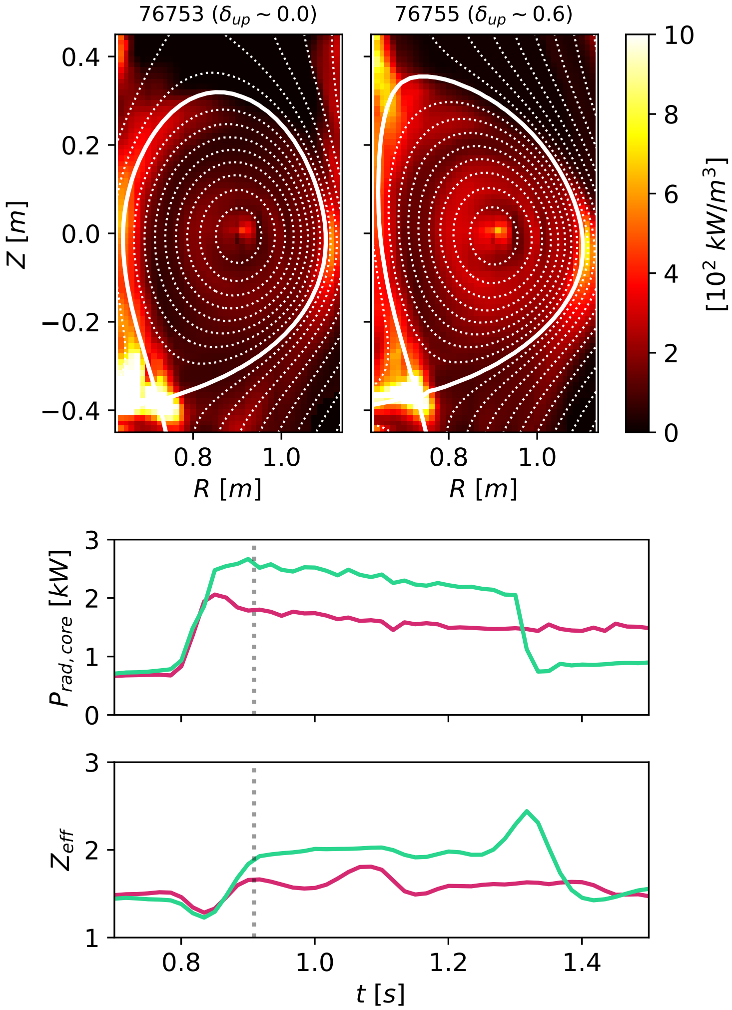

Figure 6.15: Top: emissivity maps tomographically reconstructed from RADCAM bolometry at a time frame around 0.91 s for the two discharges #76753 (low δ_{up}) and #76755 (high δ_{up}), with the colorbar saturated at 1 MW/m^3. Middle and bottom: time evolution of, respectively, the total core radiated power and the effective ion charge for the two discharges. The vertical dotted lines represent the timing of the emissivity maps in the top panels.

tion error of $\sim 5\%$. The time evolution of the total core radiation is shown in the middle panel, whereas the bottom panel contains the time trace of the effective ion charge. The two emissivity maps indicate that the highly shaped magnetic geometry is correlated with a larger radiative power loss from the confined region.

The cause of this increase may be researched for in a greater carbon impurity intake from the first wall, since Z_{eff} is quite higher in the high upper triangularity case than in the low δ_{up} one. Specifically, within the H-mode period common to the two discharges, the effective ion charge is ~ 1.9 for the former and ~ 1.6 for the latter. This variation may take place owing to a series of aspects, first and foremost the already reported enhancement in radial convective turbulent transport which, coupled with the smaller outer gap at high shaping, yields a greater carbom erosion at the outer midplane first wall. In addition to this, the plasma geometry itself most likely plays a role in that, most importantly, the machine roof tiles are magnetically connected to the outer midplane through the SOL field lines on the low field side, thus they do act as an effective impurity source for the main plasma. As observed in the time evolution of the core radiation, this behaviour lasts for the entirety of the H-mode phase of the discharge, with a moderate increase in $P_{rad,core}$ of $\sim 80 - 120$ kW overall throughout the discharge when passing from the low to the high shaping case. Inevitably, this has repercussions on the SOL power balance and on the two-point model estimate of the separatrix temperature since P_{sep} decreases by an equal and opposite amount as $P_{rad,core}$. Nonetheless, the dominant contribution to the power balance is still the NBI heating power, moreover the 2/7 exponent in equation 4.12 makes the $T_{e,sep}$ evaluation fairly robust and insensitive to small variations in its inputs. As a result, the reduction in separatrix temperature due to the increased core radiative losses has a much lower importance than the SOL power width broadening, where instead $\langle \lambda_q \rangle$ increases by a much larger factor than the decrease in P_{sep}.

7

Summary and outlook

This thesis summarizes the results of an experimental and analysis work carried out at the TCV tokamak, with the purpose of characterizing the properties of the upstream SOL profiles and the features of the underlying transport mechanisms in reactor-relevant operating scenarios such as high density H-modes. This work is motivated by the need within the fusion research community of propelling forward the current knowledge on the mechanisms regulating the particle and heat fluxes towards the divertor and plasma-facing components. A commonly accepted solution for the exhaust challenge must inevitably reconcile a good core plasma performance maximizing the fusion reaction rate, with the requirement of controlling the peak heat loads below the technically acceptable values. The latter, of the order of $\sim$ 10 MW/m^2 for actively cooled tungsten plasma-facing components, is unfortunately extrapolated to be far exceeded in next generation devices like ITER and DEMO, if unmitigated during both steady state H-mode phases and fast magnetohydrodynamic type-I ELM transients. On this regard, high density H-mode regimes represent a promising scenario for proper power handling in reactor-sized devices since they naturally allow to work closer to at least partial divertor target detachment. In addition, coupling high density with a highly shaped, close to double null magnetic configuration leads to an operational scenario, called Quasi-continuous exhaust (QCE) regime, in which large, coherent type-I ELM events are completely suppressed and replaced by much more frequent, small amplitude, noise-like bursts of particles and energy.

An extensive analysis of the SOL properties in high density H-mode regimes is here presented, comprising both type-I ELMy and QCE conditions, with particular focus on the role played by the upstream separatrix density as well as the geometry of the last closed flux surface. In order to parametrize these variations in terms of operational plasma boundary parameters, the full three-dimensional turbulence four-field Drift-Alfvén (DALF) model has been exploited. Leveraging on previous works based on the definition of a separatrix operational space, one of the main insights of the DALF model is the possibility of describing the SOL dynamics and different transport regimes by means of a single quantity α_t, called turbulence control parameter. This quantity has been shown to regulate the relative phase between the pressure and potential disturbances in the vicinity of the separatrix, regulating the competition between drift wave turbulence and resistive ballooning modes, ultimately setting the level of cross-field turbulent particle and heat fluxes reaching radially towards the first wall.

The physical models and aspects necessary for a sound description of the SOL dynamics, including the DALF model and the α_t parameter, have been firstly introduced. The extensive diagnostic capabilities of the TCV tokamak device and the main analysis methodologies used in this work followed right after. In particular, the upstream electron kinetic profiles have been characterized mainly by means of the Thomson scattering diagnostic, coupled (when possible) to other systems like a fast reciprocating probe at the midplane and the Thermal Helium Beam diagnostic. The separatrix has been evaluated in a physically robust methodology by means of a power balance approach under the assumption of conduction-limited parallel transport, which allowed to use the two-point model for a straightforward explicit evaluation of the separatrix temperature in terms of the main operational and physical parameters.

These models and methods have then been applied for the characterization of a gas fuelling scan experimental programme at TCV, with the objective of studying the variations induced by a change in divertor recycling conditions and upstream separatrix density on the properties of the SOL profiles and fluctuations. The experiment has been carried out at constant toroidal field, plasma current, magnetic geometry and NBI heating scheme, while changing the gas rate from either the top or the bottom valves, without sensible variation induced by gas fuelling injection location. A transition from a type-I ELMy to a QCE regime has been seen, even during a single plasma discharge, with the increase in divertor neutral pressure inducing a strong change of the separatrix density and a higher resistive ballooning turbulence level as measured by the α_t parameter. Accordingly, the upstream SOL profiles undergo significant modifications, with a broadening of the divertor heat load footprint, a flattening of the upstream near SOL density profile and the formation of a density shoulder feature in the far SOL, following from an increase in divertor neutral pressure. It is important to highlight that a change in the latter affects primarily the upstream separatrix density, while every other engineering input has been kept constant, so that every correlation reported with α_t was actually with $n_{e,sep}$. However, even so and coupled with other experimental results previously obtained in a similar way at the ASDEX-Upgrade device, this database successfully serves as a first test bed of the α_t parameter framework on TCV.

At higher divertor dissipation also the filamentary activity has been seen to undergo significant variations as registered by the fast midplane reciprocating probe high time resoultion signals, with bigger blobs travelling radially faster across the scrape-off layer. A mapping of the detected filament waveforms within the two-region model $\Lambda - \Theta$ plane indicates that their propagation is mostly consistent with the resistive ballooning or resistive X-point regimes, suggesting that they manage to extend at most partially into the divertor chamber, while being mostly disconnected from the outer target. It must be further noticed that, within the available experimental limitations, no filamentary regime transitions have been observed within the scanned parameter space. It is important to stress out how the present filamentary analysis is affected by some limitations due to the point-like nature of the reciprocating probe measurements and the lack of an independent evaluation scheme for the blob velocities and size. Furthermore, filaments are inherently structures out of local thermodynamic equilibrium and any deviations from a Maxwell-Boltzmann electron velocity distribution function could affect the floating potential measurement, presumably limiting the validity of the scheme used for evaluation of the filament velocity. Nevertheless, the observed correlations allow for a preliminary interpretation of the link between the upstream separatrix density, the α_t parameter, the upstream profiles and the resistive ballooning turbulent transport.

The plasma shaping scan database helped in extending the previous observations and the scanned operating space beyond the upstream separatrix density only. In this experiment, the magnetic geometry has been varied from shot to shot by changing the upper triangularity at constant plasma current, toroidal field, NBI heating scheme and gas puffing feed-forward waveform. Once again, a clear transition from a type-I-ELM dominated regime to a pure QCE scenario is observed as α_t increases, this time by the increase of the edge safety factor induced by the upper triangularity alone. This observation supports previous results according to which high shaping is associated to a more turbulent ballooning plasma behaviour in the scrape-off layer via a reduction of the stabilizing effect of local magnetic shear around the separatrix and the outer midplane. A large part of the α_t variation has been obtained via the sole change in plasma shaping, nevertheless the co-variance between δ_{up} and other operational parameters like the separatrix density plays a prominent role in the α_t determination. Regardless, the near SOL heat load and density profiles have been observed once again to undergo significant modifications, closely similar to those observed in the fuelling scan case, with the e-folding lengths increasing by a factor ~ 2.5 across the spanned δ_{up} and α_t intervals. Notably, the two λ_q trends obtained separately within the gas rate and shaping scan datasets are quite resemblant to each other, with small quantitative discrepancies being potentially explained by the slight differences in analysis methods as well as deviations in the calibration of some diagnostic systems. In the far SOL, a shoulder develops when moving to high α_t into the QCE boundaries, similar to other H-mode experiments.

The geometry of the last closed flux surface also affects the level of turbulent fluctuations reaching the first wall, as demonstrated by measurements from the full set of wall-mounted Langmuir probes operated at constant negative bias, coupled with the fast THB line emission signals. The probability distributions of the ion saturation current density and the 667 nm HeI line intensity are characterized by a larger average value and a higher variance at high triangularity. This behaviour is not limited to the narrow region just around the outer midplane, but rather it extends to the full first wall portion below it. The markedly positive skewness of the probability distribution functions is a strong indicator of the filamentary character of the fluctuations reaching the first wall. The frequency of the aforementioned filaments strongly increases at the midplane, while no change is registered at the divertor target. These measurements can serve as a possible indication that the turbulent particle and heat fluxes travelling radially towards the first wall are enhanced at high plasma shaping, even if direct measurements of the radial loads have not been possible in this manuscript and are indeed auspicable for future work.

Finally, lacking direct measurements, the possible modification of plasma wall-interaction as caused by LCFS plasma shaping modification has been inferred by means of both neutral pressure measurements and bolometry data. Readings from a midplane neutral pressure gauge reveal negligible variation in the neutral population density around the outer first wall, indicating that the upper triangularity indeed plays a negligible role on setting the first wall recycling sources as far as the diagnostic capabilites can reach. Then, the observed changes in turbulent filamentary behaviour at the first wall can be most likely ascribed at leading order to a direct effect of the magnetic geometry on the SOL transport mechanisms. Regardless of this, even if an increase in neutral particles population were to be registered, a sufficiently high power crossing radially towards the first wall would be requested in order for these extra neutrals to be ionized and contribute locally to the formation of a density shoulder. This condition can be met only under the hypothesis of an enhanced power originating from the separatrix and convected in the far SOL, which coincides with the observations reported here when moving from low to high shaping. The upper triangularity has instead a significant effect on the volume-integrated core radiation, which increases as a consequence of a higher carbon impurity input from the first wall. The higher turbulent level may be partly responsible for this, in that it can potentially cause a more pronounced level of sputtering from the first wall tiles material. However, the magnetic topology also likely plays a large role, since at high shaping the plasma is closer to the outer wall by means of a smaller outer gap, and the overall configuration is much closer to a double null which gets the machine roof tiles involved in providing a further impurity source.

The evolution of the upstream and downstream SOL profiles reported here, as well as the changes in filamentary transport behaviour, show robust correlations with the α_t parameter, changed either via a separatrix density scan or via a plasma shaping scan. The reported results therefore support the interpretation of the α_t parameter as being key in regulating the level of turbulent transport originatig near the separatrix, around the outer midplane. As a consequence, with this work the turbulence control parameter framework has been successfully established on the TCV device, representing a welcome extension to a machine with different size and wall material than ASDEX-Upgrade, on which the framework was first established. However, this work is still far from completion and an extension to reactor-sized machines must be operated in the coming years. On this line, data validation at JET is currently underway and an extension to this machine should be available soon, allowing to explore even different machine sizes and plasma-facing component materials. Finally, other unexplored parametric dependencies include the direct proportionality of α_t to the total impurity content quantified by the effective ion charge, especially considering that a dissipative divertor obtained via impurity seeding is not always a necessary condition for density shoulder formation and turbulent transport enhancement. Future work will therefore also focus on the assessment of the upstream SOL profiles and fast fluctuations in impurity-seeded plasmas, like the Ne-seeded ITER baseline scenario or novel power dissipation concepts like the X-point radiator.

APPENDIX

A PARTICLE MOTION IN AN EXTERNAL MAGNETIC FIELD

Knowing the single particle motion in an external magnetic field is crucial for the assessment of the confinement level in a MCF plasma. The equation of motion for a charged particle in an external electromagnetic field is

$$m\frac{d\mathbf{v}}{dt} = q\left(\mathbf{E} + \mathbf{v} \times \mathbf{B}\right). \tag{A.1}$$

This equation is highly non-linear, since in principle both **E** and **B** are themselves not uniform in space and not constant in time, thus some simplifying assumptions must be made beforehand. Firstly, one can use a field-aligned Cartesian coordinate system (x, y, z), with z along and (x, y) across the magnetic field lines. For the solution in the case of a static, uniform magnetic field with no electric field, dot multiplication with **v** and **B** reveals the conservation of, respectively, the total and parallel particle kinetic energy. On the other hand, cross multiplication with **v** leads instead to the solution for the cross-field motion

$$\mathbf{v}'_\perp(t) = v_{\perp 0}\left[\cos\left(\Omega_c t + \zeta_0\right)\mathbf{e}_x - \sin\left(\Omega_c t + \zeta_0\right)\mathbf{e}_y\right] \tag{A.2}$$

describing a uniform circular motion on the (x, y) plane whith Ω_c the cyclotron frequency, whereas $v_{\perp 0}$ and ζ_0 are the magnitude and initial phase of the trajectory. Integration of equation A.2 leads to the evolution of the particles' physical coordinates

$$\mathbf{x}(t) = \mathbf{x}_c(t) + \mathbf{x}'(t) = \mathbf{x}_c(t) + \rho_L\left[\sin(\Omega_c t + \zeta_0)\mathbf{e}_x + \cos(\Omega_c t + \zeta_0)\mathbf{e}_y\right]. \tag{A.3}$$

The vector $\mathbf{x}'(t)$ describes the circular particle motion along the magnetic field line, at a distance from it given by the Larmor radius ρ_L (both Ω_c and ρ_L have been defined already in equation 1.12). The $\mathbf{x}_c(t)$ part represents the motion of the center of the helical orbit, also called *guiding centre*: in absence of external forces, this motion is uniform and purely parallel to the magnetic field lines.

The addition of a static, uniform external electric field has two main consequences. Firstly, the parallel guiding centre motion is uniformly accelerated under the influence of the parallel electric force, i.e. $v_{\parallel c} = v_{\parallel 0} + q(E_\parallel/m)t$. Secondly, the basic equation for the perpendicular motion

$$m\frac{d\mathbf{v}_\perp}{dt} = q\left(\mathbf{E}_\perp + \mathbf{v}_\perp \times \mathbf{B}\right). \tag{A.4}$$

can be solved analytically as $\mathbf{v}_\perp = \mathbf{v}'_\perp + \mathbf{v}_E$, where $\mathbf{v}'_\perp$ is again the gyromotion, whereas the second term $\mathbf{v}_E$ is the $\mathbf{E} \times \mathbf{B}$ drift velocity introduced in equation 1.13.

In the case of $\mathbf{E} = \mathbf{E}(\mathbf{x}, t)$ and $\mathbf{B} = \mathbf{B}(\mathbf{x}, t)$, an approximate solution to the equation of motion can be found if one assumes that any variation in the external electromagnetic field takes place over much larger characteristic temporal and spatial scales than those associated to the gyromotion

$$L_\perp = \left|\frac{\nabla_\perp B}{B}\right|^{-1} \gg \rho_L, \quad L_\parallel = \left|\frac{\nabla_\parallel B}{B}\right|^{-1} \gg L_\parallel, \quad T = \left|\frac{1}{B}\frac{dB}{dt}\right| \gg \frac{1}{\Omega_c} \tag{A.5}$$

and similar for the electric field. This allows to exploit a perturbative approach, by means of a Taylor expansion of the $\mathbf{E}$ and $\mathbf{B}$ fields about the guiding centre position up to the desired order, where the maximum displacement is given by $\mathbf{x}'(t)$. The zero-order solution corresponds to the case of a static, uniform external electromagnetic field and results in the superposition of a gyromotion and an $\mathbf{E} \times \mathbf{B}$ drift, i.e. $\mathbf{v}_{\perp c}^{(0)} = \mathbf{v}_E$ as previously described. At first order in the Taylor expansion and time-averaging over one gyration period ($\langle \mathbf{v}'_\perp \rangle_{1/\Omega_c} = 0$) one gets

$$\frac{d\mathbf{v}_c}{dt} - \Omega_c \mathbf{v}_c \times \mathbf{b} = -\frac{v'_\perp}{2B}\nabla B\left(\mathbf{x}_c\right) + \frac{q}{m}\mathbf{E}\left(\mathbf{x}_c\right) \tag{A.6}$$

having used $\mathbf{b} = \mathbf{B}/B$. Cross-multiplying this equation by $\mathbf{b}$ yields the first-order perpendicular guiding centre motion, comprising both the $\mathbf{E} \times \mathbf{B}$ drift and some additional terms

$$\mathbf{v}_{\perp c} = \mathbf{v}_{\perp c}^{(0)} + \mathbf{v}_{\perp c}^{(1)} = \mathbf{v}_E \pm \frac{\left(v'_\perp\right)^2}{2\Omega_c}\frac{\mathbf{b} \times \nabla B}{B} \pm \frac{1}{\Omega_c}\mathbf{b} \times \frac{d\mathbf{v}_c^{(0)}}{dt} \tag{A.7}$$

with the top and bottom sign referred, respectively, to electrons and ions. The first term after the zero-order motion, called *∇B drift*, is correlated to the spatial inhomogeneity of the magnetic field magnitude. The second part stems instead from the inertial term and leads to two contributions, each related to a different part of the zero-order motion. Indeed, it can be shown that [3]

$$\pm\frac{1}{\Omega_c}\mathbf{b} \times \frac{d\mathbf{v}_c^{(0)}}{dt} = \pm\frac{v_\parallel^2}{\Omega_c}\frac{\mathbf{b} \times \nabla B}{B} \pm \frac{1}{\Omega_c B}\frac{d\mathbf{E}_\perp}{dt} \tag{A.8}$$

The combination of the first term, called *curvature drift*, with the ∇B drift leads to the full magnetic drift expression introduced in equation 1.14. The second term is called *polarization drift* and is related to a time variation of the perpendicular electric field as seen in the frame of reference moving with the charged particle's velocity. Even if the polarization drift is a factor $T\Omega_c \gg 1$ smaller than all the other terms, it is still the only non-zero perpendicular drift in the direction of $\mathbf{E}_\perp$ and it cannot be discarded at first order. In fact, as it will be shown later (see appendix C), such a drift component can be derived also at the level of macroscopic fluid motion and plays a major role in establishing the turbulent phenomena in the edge-SOL tokamak region.

All the relevant drift velocity contributions for the purposes of this work are all and only those discussed in this appendix. The first-order effects of an external electric field were not discussed here, but they can be shown to be smaller than all other terms [3] and as such, along with other higher-order expansions of the electromagnetic field, will not be taken into further consideration.

B FLUID DYNAMICS IN THE EDGE AND SCRAPE-OFF LAYER

The most detailed description of a plasma can be obtained through the kinetic model and the Boltzmann equation for the $a-$th plasma species accounting for particle collisions

$$\frac{\partial f_a}{\partial t} + \mathbf{v} \cdot \nabla_{\mathbf{x}} f_a + \frac{eZ_a}{m_a} \left(\mathbf{E} + \mathbf{v} \times \mathbf{B} \right) \cdot \nabla_{\mathbf{v}} f_a = \left(\frac{\partial f_a}{\partial t} \right)_c \tag{B.1}$$

which is however not only difficult to deal with but also unnecessarily detailed when treating most collective behaviours, like waves and instabilities, taking place in the edge and scrape-off layer regions.

A simpler description can be made through the fluid model, obtained from the kinetic one by taking the velocity moments of the distribution function. At the lowest orders in the moments hierarchy and including only elastic collisions, this results in the evolution equations for the particle density, fluid velocity and temperature

$$\frac{\partial n_a}{\partial t} + \nabla \cdot \left(n_a \mathbf{v}_a \right) = 0 \tag{B.2}$$

$$m_a n_a \left(\frac{\partial}{\partial t} + \mathbf{v}_a \cdot \nabla \right) \mathbf{v}_a = -\nabla p_a - \nabla \cdot \underline{\mathbf{\Pi}}_a + eZ_a n_a \left(\mathbf{E} + \mathbf{v}_a \times \mathbf{B} \right) + \mathbf{R}_a \tag{B.3}$$

$$\frac{3}{2} n_a \left(\frac{\partial}{\partial t} + \mathbf{v}_a \cdot \nabla \right) T_a + p_a \nabla \cdot \mathbf{v}_a = -\nabla \cdot \mathbf{q}_a - \underline{\mathbf{\Pi}}_a : \nabla \mathbf{v}_a + Q_a \tag{B.4}$$

stating the conservation of particles, momentum and energy for the $a-$th plasma species.

All the evolved fluid quantities are defined starting from the distribution function as

$$n_a = \int f_a d\mathbf{v}, \quad \mathbf{v}_a = \frac{1}{n_a}\int \mathbf{v} f_a d\mathbf{v}, \quad T_a = \frac{m_a}{3n_a}\int \|\mathbf{v}-\mathbf{v}_a\|^2 f_a d\mathbf{v}. \tag{B.5}$$

In the momentum equation, any variation of the $a-$th species fluid velocity is due to the Lorentz force density, as well as frictional, pressure and viscosity forces, where

$$p_a = n_a T_a, \quad \underline{\mathbf{\Pi}}_a = m_a n_a \int (\mathbf{v}-\mathbf{v}_a)(\mathbf{v}-\mathbf{v}_a) f_a d\mathbf{v} - p_a \underline{\mathbf{I}}, \quad \mathbf{R}_a = \int m_a \mathbf{v}\left(\frac{\partial f_e}{\partial t}\right)_c d\mathbf{v}. \tag{B.6}$$

The terms in the temperature equation account instead for pressure work, heat conduction, viscous and frictional energy dissipation, as well as collisional inter-species energy transfer

$$\mathbf{q}_a = \frac{m_a n_a}{2}\int \|\mathbf{v}-\mathbf{v}_a\|^2 (\mathbf{v}-\mathbf{v}_a) f_a d\mathbf{v}, \quad Q_a = \int \frac{1}{2} m_a v^2 \left(\frac{\partial f_a}{\partial t}\right)_c d\mathbf{v}. \tag{B.7}$$

The electromagnetic field closure is provided via the Maxwell's equations, with charge and current sources respectively $\rho = \rho_{ext} + e\sum_a n_a Z_a$ and $\mathbf{j} = \mathbf{j}_{ext} + e\sum_a n_a Z_a \mathbf{v}_a$.

A closure for the higher order moments and collisional terms can be provided in the limit of high collisionality (see section 2.2) as done in the work by Braginskii [72] for a simple plasma made of electrons and singly charged ions, yielding the 3D two-fluid description of the edge-SOL plasma by means of the so-called *Braginskii equations*. In this limit, following the reasoning provided e.g. in [76] for the kinetic treatment of neutral gases, the velocity distribution function can be decomposed into a Maxwellian part accounting for local thermodynamic equilibrium, and a first-order small correction. This procedure yields expressions for $\mathbf{R}$, $\underline{\mathbf{\Pi}}$, $\mathbf{q}$ and Q proportional to fluid moments and their gradients by means of a given set of transport coefficients. This approach allows also to distinguish the different collisional dynamics between the parallel and perpendicular directions. Leaving the complete derivation and physical explanation of each term to the review by Braginskii [72], one can write

$$\mathbf{R}_e = -\mathbf{R}_i = en_e\left(\frac{j_\parallel}{\sigma_\parallel}\mathbf{b} + \frac{\mathbf{j}_\perp}{\sigma_\perp}\right) - 0.71 n_e \nabla_\parallel T_e - \frac{3}{2}\frac{n_e}{\Omega_{ce}\tau_e}\mathbf{b}\times\nabla T_e \tag{B.8}$$

$$\mathbf{q}_e = -\chi_{\parallel e}\nabla_\parallel T_e - \chi_{\perp e}\nabla_\perp T_e - \frac{5}{2}\frac{n_e T_e}{eB}\mathbf{b}\times\nabla T_e + 0.71 n_e T_e w_\parallel \mathbf{b} + \frac{3}{2}\frac{n_e T_e}{\Omega_{ce}\tau_e}\mathbf{b}\times\mathbf{w} \tag{B.9}$$

$$\mathbf{q}_i = -\chi_{\parallel i}\nabla_\parallel T_i - \chi_{\perp i}\nabla_\perp T_i + \frac{5}{2}\frac{n_i T_i}{eB}\mathbf{b}\times\nabla T_i \tag{B.10}$$

$$\begin{pmatrix}\Pi_{xx}\\ \Pi_{yy}\\ \Pi_{zz}\\ \Pi_{yz}\\ \Pi_{xz}\\ \Pi_{xy}\end{pmatrix} = \begin{pmatrix} -\left(\eta_0+\eta_1\right)/2 & -\left(\eta_0-\eta_1\right)/2 & 0 & 0 & 0 & -\eta_3\\ -\left(\eta_0+\eta_1\right)/2 & -\left(\eta_0-\eta_1\right)/2 & 0 & 0 & 0 & \eta_3\\ 0 & 0 & -\eta_0 & 0 & 0 & 0\\ 0 & 0 & 0 & -\eta_2 & -\eta_4 & 0\\ 0 & 0 & 0 & -\eta_4 & -\eta_2 & 0\\ \eta_3/2 & -\eta_3/2 & 0 & 0 & 0 & -\eta_1 \end{pmatrix} \cdot \begin{pmatrix}W_{xx}\\ W_{yy}\\ W_{zz}\\ W_{yz}\\ W_{xz}\\ W_{xy}\end{pmatrix} \tag{B.11}$$

$$Q_i = 3\frac{m_e n_e}{m_i \tau_e}\left(T_e - T_i\right), \quad Q_e = -\mathbf{w}\cdot\mathbf{R}_e - Q_i \tag{B.12}$$

where $\mathbf{w} = \mathbf{v}_e - \mathbf{v}_i$ is the electron-ion relative fluid velocity, while $\underline{\mathbf{\Pi}}$ and $\underline{\mathbf{W}} = \nabla\mathbf{v} + \left(\nabla\mathbf{v}\right)^T - 2/3\left(\nabla\cdot\mathbf{v}\right)\underline{\mathbf{I}}$ are traceless symetric tensors. In all the equations and in the following ones, τ_e and τ_i are the electron and ion mean collision times. The transport coefficients are

$$\sigma_\perp = \frac{e^2 n_e \tau_e}{m_e}, \quad \sigma_\parallel = 1.96\sigma_\perp \tag{B.13}$$

$$\chi_{\parallel e} = 3.16\frac{n_e T_e \tau_e}{m_e}, \quad \chi_{\perp e} = 4.66\frac{n_e T_e}{m_e \Omega_{ce}^2 \tau_e}, \quad \chi_{\parallel i} = 3.9\frac{n_i T_i \tau_i}{m_i}, \quad \chi_{\perp i} = 2\frac{n_i T_i}{m_i \Omega_{ci}^2 \tau_i} \tag{B.14}$$

$$\eta_{0e} = 0.73 n_e T_e \tau_e, \quad \eta_{1e} = 0.51\frac{n_e T_e}{\Omega_{ce}^2 \tau_e}, \quad \eta_{2e} = 4\eta_{1e}, \quad \eta_{3e} = -\frac{n_e T_e}{2\Omega_{ce}}, \quad \eta_{4e} = 2\eta_{3e} \tag{B.15}$$

$$\eta_{0i} = 0.96 n_i T_i \tau_i, \quad \eta_{1i} = 0.3\frac{n_i T_i}{\Omega_{ci}^2 \tau_i}, \quad \eta_{2i} = 4\eta_{1i}, \quad \eta_{3i} = \frac{n_i T_i}{2\Omega_{ci}}, \quad \eta_{4i} = 2\eta_{3i} \tag{B.16}$$

C DERIVATION OF THE DALF EQUATIONS

The fluid equations B.2-B.4, either in the ideal collisionless limit or with the Braginskii closure, admit a plasma dynamics over a vast range of spatial and temporal scales. One of the most common textbook examples of this variety is the treatment of compressional and shear Alfvén waves (see e.g. [86]), both resulting from a cross-field plasma motion $\mathbf{u} \perp \mathbf{B}$ but associated to orthogonal orientations of the velocity oscillation direction with respect to the wave vector, respectively $\mathbf{k} \parallel \mathbf{u}$ and $\mathbf{k} \perp \mathbf{u}$. In the situation of tokamak edge turbulence, which has been seen to be associated to very different scales along and across the equilibrium magnetic field lines, the frequency of the corresponding oscillations are also quite different. One can then reduce the complexity of the fluid description by implementing the drift ordering assumption, retaining only the parts of the dynamics happening on scales larger than the ion Larmor radius and slower than the ion cyclotron frequency, with perpendicular gradients being much larger than parallel ones

$$\delta \equiv \frac{\rho_s}{\lambda_\perp} \gg 1, \quad \omega \ll \Omega_i, \quad k_\perp \gg k_\parallel. \tag{C.1}$$

PERPENDICULAR ION FORCE BALANCE

The first step into the treatment of fluid drift dynamics is to assess the relevant contributions to the perpendicular velocity. At zeroth-order in δ, as done in section 2.4.2, this has led to writing the electron and ion fluid velocities as $\mathbf{v}_{\perp a}^{(0)} = \mathbf{v}_E + \mathbf{v}_{*a}$, with $\mathbf{v}_E$ the $\mathbf{E} \times \mathbf{B}$ drift drift and $\mathbf{v}_{*a}$ the $a-$th species diamagnetic drift. The first-order treatment implies retaining all terms in equation B.3, including inertial and viscous effects. For the electrons this is unnecessary, given their small perpendicular inertia and $m_e \ll m_i$. For the ions, using the notation $\mathbf{u}$ for the ion fluid velocity one has

$$m_i n_i \frac{d\mathbf{u}}{dt} = -\nabla p_i - \nabla \cdot \underline{\underline{\mathbf{\Pi}}}_i + e n_i \left(\mathbf{E} + \mathbf{u} \times \mathbf{B}\right) \tag{C.2}$$

with $d/dt = \partial/\partial t + \mathbf{u} \cdot \nabla$. As already done in appendix A, the first-order expansion of the ion velocity is found by cross-multiplying the whole equation by $\mathbf{b}$ and keeping only the leading velocity terms on the left-hand side

$$\mathbf{u}_\perp = \mathbf{u}_\perp^{(0)} + \mathbf{u}_\perp^{(1)} = \frac{\mathbf{E} \times \mathbf{b}}{B} + \frac{1}{e n_i} \frac{\mathbf{b} \times \nabla p_i}{B} + \frac{1}{\Omega_{ci}} \mathbf{b} \times \frac{d\mathbf{u}_\perp^{(0)}}{dt} + \frac{1}{e n_i} \frac{\mathbf{b} \times \left(\nabla \cdot \underline{\underline{\mathbf{\Pi}}}_i\right)}{B} \tag{C.3}$$

A proper treatment of the last term, related to the perpendicular component of the divergence of viscous stresses, can be found in [85]. Following the derivation of the fluid drift equations in [86], it is taken into consideration here only up to the point that, as properly demonstrated in the mentioned reference, part of it cancels out the diamagnetic advection of $\mathbf{u}_\perp$ in the third term. Furthermore, parallel advection can be neglected due to the applied ordering, $\partial/\partial t \sim \mathbf{v}_E \cdot \nabla \gg u_\parallel \nabla_\parallel$. The remaining first-order term is the polarization drift velocity

$$\mathbf{u}_p = \frac{1}{\Omega_{ci}} \mathbf{b} \times \frac{d_E \mathbf{u}_\perp^{(0)}}{dt} \tag{C.4}$$

with the zero-order perpendicular velocity being advected solely by the $\mathbf{E} \times \mathbf{B}$ velocity, $d_E/dt = \partial/\partial_t + \mathbf{v}_E \cdot \nabla$. Although much smaller than $\mathbf{u}_\perp^{(0)}$, retaining the polarization drift in the ion dynamics is necessary at least in situations where it appears under the divergence operator, scaling with δ in the same way as the divergence of the leading order drifts [86].

CHARGE CONSERVATION - THE VORTICITY EQUATION

One of the main well-known defining properties of a plasma is its capability of restoring local charge neutrality by means of large electric fields that arise following small local charge separations. The timescales over which the plasma can be considered quasi-neutral are of the order of the ion and electron plasma frequencies, which are much larger than the maximum frequency Ω_{ci} allowed by the drift ordering and must thus be eliminated from the dynamics. With this purpose in mind, another fundamental reason to retain the polarization drift is to recover quasineutrality in the system. Indeed, by employing Ampère-Maxwell's law the divergence of the total current in the system (material plus displacement) vanishes, yielding the charge conservation equation

$$\nabla \cdot \left[j_{\|}\mathbf{b} + \frac{\mathbf{b} \times \nabla (p_e + p_i)}{B} + \frac{\rho}{B}\mathbf{b} \times \frac{d\mathbf{u}_{\perp}^{(0)}}{dt} \right] + \nabla \cdot [\varepsilon_0 (\nabla \cdot \mathbf{E}) \mathbf{v}_E] + \varepsilon_0 \frac{\partial}{\partial t} (\nabla \cdot \mathbf{E}) = 0 \quad \text{(C.5)}$$

where the Gauss' law for the electric field $e(n_i - n_e) = \varepsilon_0 \nabla \cdot \mathbf{E}$ and the definition of mass density $\rho \approx n_i m_i$ have been used. All the terms inside the square brackets are related to a material current, while the last two terms are related to the charge continuity equation in violation of local neutrality. Approximating $\mathbf{u}_{\perp}^{(0)} \sim \mathbf{v}_E$ at leading order and knowing that $\mathbf{b} \times \mathbf{v}_E = \mathbf{E}_{\perp}/B$, one can see that the two last terms vanish to first order in δ if $\varepsilon_0 \ll \rho/B^2$. This condition automatically follows from the natural ordering of the local neutrality scales with respect to the drift scales

$$\lambda_D \ll \rho_s, \quad \Omega_{ci} \ll \omega_{pi} \quad \text{(C.6)}$$

with λ_D and ω_{pi} the Debye length and ion plasma frequency, respectively. This allows to consider the drift dynamics quasi-neutral for all purposes, and thus to use a common density for electrons and ions $n_e = n_i \equiv n$ with only one continuity equation (here $\mathbf{v} \equiv \mathbf{v}_e$ is used for electron fluid velocities)

$$\frac{\partial n}{\partial t} + \nabla \cdot n \left(\mathbf{v}_E + \mathbf{v}_* + v_{\|}\mathbf{b} \right) = 0 \quad \text{(C.7)}$$

The charge conservation equation is also modified in the sense that, on top of using a single density, the terms associated to a violation of local charge neutrality vanish, leaving only the material current terms in absence of a charge density. The equation reduces down to $\nabla \cdot \mathbf{j} = 0$, which can be then rewritten as

$$\nabla \cdot \frac{n}{B\Omega_{ci}} \frac{d_E}{dt} \left(\mathbf{E}_{\perp} - \frac{\nabla_{\perp} p_i}{ne} \right) + \nabla \cdot j_{\|}\mathbf{b} + \nabla \cdot \frac{\mathbf{b} \times \nabla (p_e + p_i)}{B} = 0 \quad \text{(C.8)}$$

This equation effectively replaces the need for a charge continuity law, since it yields directly the evolution of $\nabla \cdot \mathbf{E}_\perp$. This quantity is proportional to $\mathbf{b} \cdot \nabla \times \mathbf{v}_E$ and therefore, in analogy with neutral fluid dynamics, it represents the vorticity of the $\mathbf{E} \times \mathbf{B}$ drift velocity. For this reason, equation C.8 is called *vorticity equation*.

THE SEMI-ELECTROSTATIC LIMIT

The compressional branch of Alfvén waves propagates much faster than the shear branch, so that along a field line the motion can be assumed almost incompressible on the typical low-frequency drift turbulence timescales. Retaining the shear Alfvén wave is then of crucial importance, since the characteristic timescale associated to its disturbances is sufficiently slow to interact with and affect the turbulent edge phenomena at the long parallel wavelengths under consideration. A proper treatment of Alfvén waves within the MHD framework [86] shows that the compressional and shear components propagate with dispersion relations

$$\omega_{compr} \approx k_\perp c_A \gg k_\parallel c_A \sim \omega_{shear} \tag{C.9}$$

where $c_A = B/\sqrt{\mu_0 m_i n}$ is the Alfvén velocity and the inequality holds because of the ordering $k_\parallel \ll k_\perp$.

The electromagnetic field can, in turn, be written as a function of the scalar and vector electrodynamic potentials by solving the homogeneous Maxwell's equations

$$\mathbf{E} = -\nabla\varphi - \frac{\partial \mathbf{A}}{\partial t}, \quad \mathbf{B} = \nabla \times \mathbf{A}, \quad \nabla^2 \mathbf{A} = -\mu_0 \mathbf{j} \tag{C.10}$$

with the vector potential obeying a Poisson's equation under the Coulomb gauge $\nabla \cdot \mathbf{A} = 0$.

Due to the elimination of the fast compressional Alfvén timescale, along the perpendicular direction the electric field can be considered electrostatic. Instead, since parallel wavelengths are much larger than perpendicular ones, electromagnetic effects still play a role in the direction parallel to the magnetic field. The same ordering, coupled with the Coulomb gauge, leads to neglecting the perpendicular components of **A** and retain only the parallel one. The electric field then reduces to

$$\mathbf{E}_\perp = -\nabla_\perp\varphi, \quad E_\parallel = -\nabla_\parallel\varphi - \frac{\partial A_\parallel}{\partial t}, \quad \nabla^2_\perp A_\parallel = -\mu_0 j_\parallel \tag{C.11}$$

so that φ and $A_\parallel$ effectively replace the electromagnetic field as dynamical variables. Finally, in the limit of small plasma beta the parallel magnetic field disturbances induced by diamagnetic currents are small and can be neglected, so that only the perpendicular part of the magnetic field perturbation is retained. The parallel gradient operator is modified accordingly as described in section 2.5.

Parallel dynamics

The equations of parallel fluid motion are derived by dot-multiplying equation B.3 by **b**

$$m_e n \frac{d_E v_\parallel}{dt} = -\nabla_\parallel p_e - enE_\parallel + R_{\parallel ei}, \tag{C.12}$$

$$m_i n \frac{d_E u_\parallel}{dt} = -\nabla_\parallel p_i - \nabla \cdot \Pi_{\parallel\parallel i}\mathbf{b} + enE_\parallel - R_{\parallel ei} \tag{C.13}$$

where the parallel viscous stresses have been retained only for the ions while neglected for the electrons, due to the small inertia of the latter.

Adding the two equations and neglecting the electron inertia yields a simpler evolution equation for the ion parallel velocity

$$m_i n \frac{d_E u_\parallel}{dt} = -\nabla_\parallel \left(p_e + p_i\right) - \nabla \cdot \Pi_{\parallel\parallel i}\mathbf{b} \tag{C.14}$$

while subtracting them, while dropping first-order terms in the electron-to-ion mass ratio and using Faraday's law for the parallel electric field yields the generalized Ohm's law

$$en \frac{\partial A_\parallel}{\partial t} + m_e \frac{d_E j_\parallel}{dt} = \nabla_\parallel p_e - en\nabla_\parallel \varphi - R_{\parallel ei} \tag{C.15}$$

Temperature equations

The temperature evolution is obtained starting from equation B.4, neglecting viscous dissipation and collisional inter-species energy transfer. For the electrons, neglecting the parallel temperature advection and separating the remaining part of the zero-order velocity field leads to

$$\frac{3}{2} n \frac{d_E T_e}{dt} + \frac{3}{2} n_e \mathbf{v}_* \cdot \nabla T_e + p_e \nabla \cdot \left(\mathbf{v}_E + \mathbf{v}_* + v_\parallel \mathbf{b}\right) = -\nabla \cdot \mathbf{q}_{\perp e} - \nabla \cdot q_{\parallel e}\mathbf{b} \tag{C.16}$$

where the cross-field thermal conduction and the transverse relative velocity part of $\mathbf{q}_{\perp e}$ can be neglected due to being of order $\Omega_{ce}\tau_e \ll 1$ with respect to the rest. The two terms containing the diamagnetic velocity combine with the divergence of the transverse heat flux. In addition, the parallel velocity is eliminated in favour of the parallel current. A simple calculation results in

$$\frac{3}{2} n \frac{d_E T_e}{dt} = -p_e \nabla \cdot \mathbf{v}_E + \frac{T_e}{e} \nabla \cdot j_\parallel \mathbf{b} - p_e \nabla \cdot u_\parallel \mathbf{b} - T_e \nabla \cdot n \mathbf{v}_* - p_e \nabla \frac{\mathbf{q}_{\perp e}}{p_e} - \nabla \cdot q_{\parallel e}\mathbf{b} \tag{C.17}$$

The ion temperature equation is obtained via a similar calculation, keeping in mind that in this case the divergence of the polarization drift does not vanish in the pressure work term. However, it can be easily eliminated by using either the ion continuity or the vorticity equations, leaving

$$\frac{3}{2}n\frac{d_E T_i}{dt} = -p_i\nabla\cdot\mathbf{v}_E + \frac{T_i}{e}\nabla\cdot j_\|\mathbf{b} - p_i\nabla\cdot u_\|\mathbf{b} - T_i\nabla\cdot n\mathbf{v}_* - p_i\nabla\frac{\mathbf{q}_{\perp i}}{p_i} - \nabla\cdot q_{\|i}\mathbf{b} \tag{C.18}$$

where the appearance of $j_\|$ and $\mathbf{v}_*$ is a consequence of the elimination of the polarization drift divergence.

SUMMARY OF THE DALF EQUATIONS

The equations derived here allow for a self-consistent description of the plasma dynamics under the drift ordering assumption. Here below they are summarized and rewritten, in physical units, in terms of the operators introduced in section 2.5 and using $\nabla\cdot f\mathbf{b} = B\nabla_\|\left(f/B\right)$

$$\frac{d_E n}{dt} = \frac{1}{e}B\nabla_\|\frac{j_\|}{B} - nB\nabla_\|\frac{u_\|}{B} + n\mathcal{K}\left(\varphi\right) - \frac{1}{e}\mathcal{K}\left(p_e\right) \tag{C.19}$$

$$\nabla\cdot\frac{m_i n}{B^2}\frac{d_E W_i}{dt} = B\nabla_\|\frac{j_\|}{B} - \mathcal{K}\left(p_e + p_i\right) \tag{C.20}$$

$$en\frac{\partial A_\|}{\partial t} + \frac{m_e}{e}\frac{d_E j_\|}{dt} = \nabla_\| p_e - en\nabla_\|\varphi - R_{\|ei} \tag{C.21}$$

$$m_i n\frac{d_E u_\|}{dt} = -\nabla_\|\left(p_e + p_i\right) - B\nabla_\|\frac{\Pi_{\|\|\|}}{B} \tag{C.22}$$

$$\frac{3}{2}n\frac{d_E T_e}{dt} = \frac{T_e}{e}B\nabla_\|\frac{j_\|}{B} - p_e B\nabla_\|\frac{u_\|}{B} - B\nabla_\|\frac{q_{\|e}}{B} + p_e\mathcal{K}\left(\varphi\right) - \frac{T_e}{e}\mathcal{K}\left(p_e\right) - \frac{5}{2}\frac{p_e}{e}\mathcal{K}\left(T_e\right) \tag{C.23}$$

$$\frac{3}{2}n\frac{d_E T_i}{dt} = \frac{T_i}{e}B\nabla_\|\frac{j_\|}{B} - p_i B\nabla_\|\frac{u_\|}{B} - B\nabla_\|\frac{q_{\|i}}{B} + p_i\mathcal{K}\left(\varphi\right) + \frac{T_i}{e}\mathcal{K}\left(p_e\right) + \frac{5}{2}\frac{p_i}{e}\mathcal{K}\left(T_i\right) \tag{C.24}$$

where a closure for the vorticity and the magnetic potential is given by, respectively

$$W_i = \varphi + \frac{p_i}{en}, \quad \nabla_\perp^2 A_\| = -\mu_0 j_\|. \tag{C.25}$$

The four-field DALF model introduced in section 2.5 is derived from this set of equations. The pressure evolution is obtained by multiplying the density equation by the background T_e and neglecting the temperature disturbances, which also allows to eliminate the temperature equations. Finally, linearization and normalization yields equations 2.54-2.57.

D Linear analysis of resistive ballooning modes

Following the simple picture of this instability presented in section 2.4.2, a minimum derivation of the ballooning mode within the equations 2.54-2.57 can be carried out by considering just the linearized vorticity and pressure equations at the bad curvature side of the tokamak (i.e. $\cos s = 1$), eliminating all terms containing a product of fluctuations. Dropping the ion dynamics is equivalent to neglecting the coupling between sound waves and ballooning modes, whereas drift waves are eliminated from the system by neglecting the parallel gradients in both equations. One can also exclude the compressibility terms associated to the action of magnetic curvature in the pressure equation. Applying the substitions $\partial/\partial t \rightarrow \gamma$, $\nabla_\perp \rightarrow ik_\perp$, $\partial/\partial y \rightarrow ik_y$ for a pure instability, with γ a growth rate and k_y, $k_\perp$ wavenumbers, the minimum RBM model results as

$$\gamma\tilde{p}_e = ik_y\Lambda_{pe}\tilde{\varphi} \tag{D.1}$$

$$-\gamma k_\perp^2\tilde{\varphi} = -ik_y\omega_B\tilde{p}_e \tag{D.2}$$

where a $\pi/2$ phase shift between potential and pressure fluctuations emerges naturally. Substituting one into the other, and assuming that $k_\perp \sim k_y$ (see e.g. [161]), one gets the ideal ballooning growth rate in DALF units

$$\gamma_{int} = \sqrt{\omega_B\Lambda_{pe}} \tag{D.3}$$

which reduces to the well-known expression $\gamma_{int} = c_s\sqrt{2/\left(R\lambda_{pe}\right)}$ in physical units. This is actually the maximum achievable interchange growth rate, since the parallel current term in the vorticity equation (so far neglected) tends to limit it below this value. The limiting mechanism, and therefore the prevailing branch, is set by which term in the Ohm's law is dominant in causing the breaking of the adiabatic electron response. For the description of resistive ballooning modes one can retain just the potential gradient together with the collisional term in the generalized Ohm's law

$$\nabla_\parallel\tilde{\varphi} = -C\tilde{j}_\parallel \tag{D.4}$$

which closes the parallel current in equation 2.54. Applying the substitution $\nabla_\parallel \rightarrow ik_\parallel$ and solving for the potential perturbation yields the dispersion relation of the resistive ballooning mode growth rate

$$\gamma^2 + \frac{k_\parallel^2}{\left(1+\tau_i\right)Ck_y^2}\gamma - \gamma_{int}^2 = 0. \tag{D.5}$$

At a difference with the minimum RBM model, the growth rate in presence of a parallel current is actually a function of both parallel and perpendicular wavenumbers. The maximum value γ_{int}

is recovered when the first order term in equation D.5 vanishes at $k_\parallel = 0$, coherently with the preliminary ballooning mode analysis in section 2.4.2 which showed that ballooning turbulence is intrinsically 2D. Nevertheless the parallel wavenumber cannot be arbitrarily small, being bounded by at least the minimum value $k_\parallel = 1$ (in DALF units) allowed by the domain geometry, since the mode must be localized in the bad curvature region around the outer midplane. When the first-order parallel gradient term is no more negligible, equation D.5 yields a characteristic RBM perpendicular scale

$$k_{RBM} = \frac{k_\parallel}{\sqrt{(1+\tau_i)\,C\gamma_{int}}}. \tag{D.6}$$

For perpendicular wavenumbers larger than k_{RBM} the mode grows at a rate similar to γ_{int}. Below this value the mode is no more localized at the outer midplane and the growth rate is considerably smaller.

E LINEAR BEHAVIOUR OF THE DRIFT WAVE INSTABILITY

Like in the case of resistive ballooning modes, the simplest drift wave behaviour can be derived by linearizing equations 2.54-2.57, again dropping the sound wave coupling and magnetic curvature in the pressure equation. The treatment reproduced here corresponds to the one proposed in [86], albeit including the effects of ion temperature. RBMs are eliminated by getting rid of the curvature term in the vorticity equation, equivalent to the case of e.g. a homogeneous magnetic field, whereas all parallel current gradient terms must be now considered. At a difference with the case of RBMs, the substitution on time derivatives is now $\partial/\partial t \to -i\omega$, where ω is a complex number whose real part accounts for wave propagation and the imaginary part for growth/damping. By subtracting equation 2.55 from equation 2.54 one gets the dispersion relation

$$\left[1 + (1+\tau_i)\,k_\perp^2\right]\omega - \omega_* = -\frac{\tilde{p}_e - \tilde{\varphi}}{\tilde{\varphi}}\omega \tag{E.1}$$

where $\omega_* = k_y \Lambda_{pe}$ in DALF units. First and foremost, in absence of a phase shift between pressure and potential fluctuations the right-hand side of equation E.1 yields the dispersion relation for drift waves at arbitrary perpendicular wavelength

$$\omega = \frac{\omega_*}{1 + (1+\tau_i)\,k_\perp^2} \equiv \omega_L. \tag{E.2}$$

or $\omega = \omega_* / \left[1 + (1+\tau_i)\,k_\perp^2 \rho_s^2\right]$ in physical units. Here the frequency reduces to a real number, meaning that the drift wave undergoes pure propagation without growth or damping, approaching the result $\omega = \omega_*$ already known from section 2.4.2 at large perpendicular wavelength.

Equation E.2 also demonstrates that a phase shift is strictly required for the drift wave to turn into an instability. Assuming that the source of such phase shift is already known, one can write $\tilde{p}_e = \tilde{\varphi} \exp\left(-i\zeta\right) \approx \tilde{\varphi}\left(1 - i\zeta\right)$, with the latter expression valid for $\zeta \ll 1$. In the same limit, equation E.1 yields the new dispersion relation

$$\omega \approx \omega_L + i\zeta \frac{\omega_L}{1 + \left(1 + \tau_i\right) k_\perp^2} \tag{E.3}$$

revealing growth, hence instability, of the drift wave for a positive phase shift ζ.

Once again, the source of non-adiabaticity must be looked for in the generalized Ohm's law, equation 2.56. Combining it with the Fourier-decomposed vorticity equation $\omega k_\perp^2 \tilde{\varphi} = k_\parallel \tilde{j}_\parallel$ and Ampère's law $\tilde{j}_\parallel = k_\perp^2 \tilde{A}_\parallel$ one gets

$$\frac{\tilde{p}_e - \tilde{\varphi}}{\tilde{\varphi}} = \frac{\omega}{k_\parallel^2}\left(1 + \tau_i\right)\left[\hat{\beta}\left(\omega_* - \omega\right) - \left(\hat{\mu}\omega + iC\right) k_\perp^2\right] \tag{E.4}$$

For a phase shift to be established, it is crucial that $k_\parallel$ does not vanish, since if it did there would be no possible parallel current closure to respond to imbalances between pressure and potential perturbations, hence an instability could not be found in this way. On the other hand, for large enough parallel wavenumber the right-hand side of equation E.4 is very small, making the parallel current response fast enough to reduce the dispersion relation back to $\omega = \omega_L$. For growth or damping to take place, intermediate $k_\parallel$ of order unity are hence needed.

In the $k_\parallel$ ranges relevant for an instability, in the case of a *resistive drift wave*, where C is much larger than both $\hat{\beta}$ and $\hat{\mu}$, the correction approaches a purely imaginary value and one can extrapolate the phase shift in a straightforward way as

$$\frac{\tilde{p}_e - \tilde{\varphi}}{\tilde{\varphi}} \approx -iC\omega \frac{k_\perp^2}{k_\parallel^2} \Rightarrow \zeta = C\omega \frac{k_\perp^2}{k_\parallel^2}. \tag{E.5}$$

Collisional dissipation leads therefore to an instability, with the perturbation amplitude growing proportionally to C. In the limit $C \ll 1$, by inserting equation E.5 into equation E.3 the growth rate γ can be easily calculated as

$$\gamma \approx C \frac{k_\perp^2}{k_\parallel^2} \frac{\omega_*^2}{\left[1 + \left(1 + \tau_i\right) k_\perp^2\right]^3} \tag{E.6}$$

being maximum at the typical drift normalization scales, i.e. $k_\perp \sim 1$ and $k_\parallel \sim 1$.

When instead inertial effects overtake the collisional dissipation term, still at low $\hat{\beta}$, another unstable branch arises called *inertial drift wave*. While not discussed in detail here, a first glance at how the inertial term leads to a collisionless instability can be inferred at first order in equation E.4, by replacing ω with its real part except for outside of the square brackets, where its full complex number form must be used. In the same way, one can see that the overall effect of the $\hat{\beta}$ term is stabilizing instead.

BIBLIOGRAPHY

[1] U.S. Energy Information Administration. *International Energy Outlook 2021*. 2021. URL: `https://www.eia.gov/outlooks/ieo/pdf/IEO2021_Narrative.pdf`.

[2] National Nuclear Data Center, Brookhaven National Laboratory. *NuDat3 database of evaluated nuclear structure data*. URL: `https://www.nndc.bnl.gov/nudat3/`.

[3] J. P. Freidberg. *Plasma Physics and Fusion Energy*. Cambridge University Press, 2007. ISBN: 9780521851077.

[4] D.A. Brown, M.B. Chadwick, R. Capote, A.C. Kahler, A. Trkov, M.W. Herman, A.A. Sonzogni, Y. Danon, A.D. Carlson, M. Dunn, D.L. Smith, G.M. Hale, G. Arbanas, R. Arcilla, C.R. Bates, B. Beck, B. Becker, F. Brown, R.J. Casperson, J. Conlin, D.E. Cullen, M.-A. Descalle, R. Firestone, T. Gaines, K.H. Guber, A.I. Hawari, J. Holmes, T.D. Johnson, T. Kawano, B.C. Kiedrowski, A.J. Koning, S. Kopecky, L. Leal, J.P. Lestone, C. Lubitz, J.I. Márquez Damián, C.M. Mattoon, E.A. McCutchan, S. Mughabghab, P. Navratil, D. Neudecker, G.P.A. Nobre, G. Noguere, M. Paris, M.T. Pigni, A.J. Plompen, B. Pritychenko, V.G. Pronyaev, D. Roubtsov, D. Rochman, P. Romano, P. Schillebeeckx, S. Simakov, M. Sin, I. Sirakov, B. Sleaford, V. Sobes, E.S. Soukhovitskii, I. Stetcu, P. Talou, I. Thompson, S. van der Marck, L. Welser-Sherrill, D. Wiarda, M. White, J.L. Wormald, R.Q. Wright, M. Zerkle, G. Žerovnik, and Y. Zhu. "ENDF/B-VIII.0: The 8th Major Release of the Nuclear Reaction Data Library with CIELO-project Cross Sections, New Standards and Thermal Scattering Data". In: *Nuclear Data Sheets* 148 (2018). Special Issue on Nuclear Reaction Data, pp. 1–142. DOI: `10.1016/j.nds.2018.02.001`.

[5] Cross Section Evaluation Working Group, National Nuclear Data Center, Brookhaven National Laboratory. *ENDF/B-VIII.0 Evaluated Nuclear Data Library*. 2018. URL: `https://www.nndc.bnl.gov/endf-b8.0/`.

[6] J D Lawson. "Some Criteria for a Power Producing Thermonuclear Reactor". In: *Proceedings of the Physical Society. Section B* 70.1 (1957), pp. 6–10. DOI: `10.1088/0370-1301/70/1/303`.

[7] E. Gibney. "Nuclear-fusion reactor smashes energy record". In: *Nature* 602 (2022), p. 371. DOI: `10.1038/d41586-022-00391-1`.

[8] J. Tollefson and E. Gibney. “Nuclear-fusion lab achieves ’ignition’: what does it mean?” In: *Nature* 612 (2022), pp. 597–598. DOI: `10.1038/d41586-022-04440-7`.

[9] S. Atzeni and J. Meyer-ten Vehn. *The Physics of Inertial Fusion: Beam-Plasma Interaction, Hydrodynamics, Hot Dense Matter*. New York: Oxford University Press Inc., 2004. ISBN: 9780199568017.

[10] R. Betti and O. A. Hurricane. “Inertial-Confinement Fusion with Lasers”. In: *Nature Phys.* 12 (2016), pp. 435–448. DOI: `10.1038/nphys3736`.

[11] T. Klinger et al. “Overview of first Wendelstein 7-X high-performance operation”. In: *Nuclear Fusion* 59.11 (2019), p. 112004. DOI: `10.1088/1741-4326/ab03a7`.

[12] J. Wesson. *Tokamaks (The International Series of Monographs in Physics)*. New York: Oxford University Press Inc., 2004. ISBN: 9780198509226.

[13] *ITER website*. URL: `https://www.iter.org`.

[14] *The DEMO power plant*. URL: `https://www.euro-fusion.org/programme/demo`.

[15] Harold Grad and Hanan Rubin. “Hydromagnetic equilibria and force-free fields”. In: *Journal of Nuclear Energy (1954)* 7.3 (1958), pp. 284–285. DOI: `10.1016/0891-3919(58)90139-6`.

[16] V.D. Shafranov. “Plasma Equilibrium in a Magnetic Field”. In: *Reviews of Plasma Physics* 2 (1966), p. 103.

[17] Justin E. Barton, William P. Wehner, Eugenio Schuster, Federico Felici, and Olivier Sauter. “Simultaneous closed-loop control of the current profile and the electron temperature profile in the TCV tokamak”. In: *2015 American Control Conference (ACC)*. 2015, pp. 3316–3321. DOI: `10.1109/ACC.2015.7171844`.

[18] M. Kruskal, J. L. Tuck, and Subrahmanyan Chandrasekhar. “The instability of a pinched fluid with a longitudinal magnetic field”. In: *Proceedings of the Royal Society of London. Series A. Mathematical and Physical Sciences* 245.1241 (1958), pp. 222–237. DOI: `10.1098/rspa.1958.0079`.

[19] V.D. Shafranov. “The stability of a cylindrical gaseous conductor in a magnetic field”. In: *The Soviet Journal of Atomic Energy* 1 (1956), pp. 709–713. DOI: `10.1007/BF01480907`.

[20] F Troyon, R Gruber, H Saurenmann, S Semenzato, and S Succi. “MHD-Limits to Plasma Confinement”. In: *Plasma Physics and Controlled Fusion* 26.1A (Jan. 1984), pp. 209–215. DOI: `10.1088/0741-3335/26/1a/319`.

[21] M. Greenwald, J.L. Terry, S.M. Wolfe, S. Ejima, M.G. Bell, S.M. Kaye, and G.H. Neilson. "A new look at density limits in tokamaks". In: *Nuclear Fusion* 28.12 (Dec. 1988), pp. 2199–2207. DOI: `10.1088/0029-5515/28/12/009`. URL: `https://doi.org/10.1088%2F0029-5515%2F28%2F12%2F009`.

[22] P. Manz, T. Eich, O. Grover, and the ASDEX Upgrade Team. "The power dependence of the maximum achievable H-mode and (disruptive) L-mode separatrix density in ASDEX Upgrade". In: *Nuclear Fusion* 63.7 (2023), p. 076026. DOI: `10.1088/1741-4326/acd9db`.

[23] R.A. Pitts, X. Bonnin, F. Escourbiac, H. Frerichs, J.P. Gunn, T. Hirai, A.S. Kukushkin, E. Kaveeva, M.A. Miller, D. Moulton, V. Rozhansky, I. Senichenkov, E. Sytova, O. Schmitz, P.C. Stangeby, G. De Temmerman, I. Veselova, and S. Wiesen. "Physics basis for the first ITER tungsten divertor". In: *Nuclear Materials and Energy* 20 (2019), p. 100696. DOI: `doi.org/10.1016/j.nme.2019.100696`.

[24] P. Stangeby. *The Plasma Boundary of Magnetic Fusion Devices*. CRC Press, LLC., 2000. ISBN: 9780367801489.

[25] F. Wagner, G. Fussmann, T. Grave, M. Keilhacker, M. Kornherr, K. Lackner, K. McCormick, E. R. Müller, A. Stäbler, G. Becker, K. Bernhardi, U. Ditte, A. Eberhagen, O. Gehre, J. Gernhardt, G. v. Gierke, E. Glock, O. Gruber, G. Haas, M. Hesse, G. Janeschitz, F. Karger, S. Kissel, O. Klüber, G. Lisitano, H. M. Mayer, D. Meisel, V. Mertens, H. Murmann, W. Poschenrieder, H. Rapp, H. Röhr, F. Ryter, F. Schneider, G. Siller, P. Smeulders, F. Söldner, E. Speth, K. -H. Steuer, Z. Szymanski, and O. Vollmer. "Development of an Edge Transport Barrier at the H-Mode Transition of ASDEX". In: *Phys. Rev. Lett.* 53 (15 1984), pp. 1453–1456. DOI: `10.1103/PhysRevLett.53.1453`.

[26] P.T. Lang, A. Loarte, G. Saibene, L.R. Baylor, M. Becoulet, M. Cavinato, S. Clement-Lorenzo, E. Daly, T.E. Evans, M.E. Fenstermacher, Y. Gribov, L.D. Horton, C. Lowry, Y. Martin, O. Neubauer, N. Oyama, M.J. Schaffer, D. Stork, W. Suttrop, P. Thomas, M. Tran, H.R. Wilson, A. Kavin, and O. Schmitz. "ELM control strategies and tools: status and potential for ITER". In: *Nuclear Fusion* 53.4 (2013), p. 043004. DOI: `10.1088/0029-5515/53/4/043004`.

[27] ITER Physics Expert Group on Confinement, Transport, ITER Physics Expert Group on Confinement Modelling, Database, and ITER Physics Basis Editors. "Chapter 2: Plasma confinement and transport". In: *Nuclear Fusion* 39.12 (1999), p. 2175. DOI: `10.1088/0029-5515/39/12/302`.

[28] Y R Martin, T Takizuka, and the ITPA CDBM H-mode Threshold Database Working Group. “Power requirement for accessing the H-mode in ITER”. In: *Journal of Physics: Conference Series* 123.1 (2008), p. 012033. DOI: `10.1088/1742-6596/123/1/012033`.

[29] M. Giacomin and P. Ricci. “Turbulent transport regimes in the tokamak boundary and operational limits”. In: *Physics of Plasmas* 29.6 (2022), p. 062303. DOI: `10.1063/5.0090541`.

[30] T. Eich, A.W. Leonard, R.A. Pitts, W. Fundamenski, R.J. Goldston, T.K. Gray, A. Herrmann, A. Kirk, A. Kallenbach, O. Kardaun, A.S. Kukushkin, B. LaBombard, R. Maingi, M.A. Makowski, A. Scarabosio, B. Sieglin, J. Terry, A. Thornton, and and. “Scaling of the tokamak near the scrape-off layer H-mode power width and implications for ITER”. In: *Nuclear Fusion* 53.9 (Aug. 2013), p. 093031. DOI: `10.1088/0029-5515/53/9/093031`.

[31] A. Loarte, B. Lipschultz, A.S. Kukushkin, G.F. Matthews, P.C. Stangeby, N. Asakura, G.F. Counsell, G. Federici, A. Kallenbach, K. Krieger, A. Mahdavi, V. Philipps, D. Reiter, J. Roth, J. Strachan, D. Whyte, R. Doerner, T. Eich, W. Fundamenski, A. Herrmann, M. Fenstermacher, P. Ghendrih, M. Groth, A. Kirschner, S. Konoshima, B. LaBombard, P. Lang, A.W. Leonard, P. Monier-Garbet, R. Neu, H. Pacher, B. Pegourie, R.A. Pitts, S. Takamura, J. Terry, E. Tsitrone, the ITPA Scrape-off Layer, and Divertor Physics Topical Group. “Chapter 4: Power and particle control”. In: *Nuclear Fusion* 47.6 (2007), S203. DOI: `10.1088/0029-5515/47/6/S04`.

[32] G. Federici, R. Kemp, D. Ward, C. Bachmann, T. Franke, S. Gonzalez, C. Lowry, M. Gadomska, J. Harman, B. Meszaros, C. Morlock, F. Romanelli, and R. Wenninger. “Overview of EU DEMO design and R&D activities”. In: *Fusion Engineering and Design* 89.7 (2014), pp. 882–889. DOI: `10.1016/j.fusengdes.2014.01.070`.

[33] Hartmut Zohm. “The physics of edge localized modes (ELMs) and their role in power and particle exhaust”. In: *Plasma Physics and Controlled Fusion* 38.8 (1996), p. 1213. DOI: `10.1088/0741-3335/38/8/012`.

[34] J.E. Boom. “Characterization of edge localized modes in tokamak plasmas”. PhD thesis. Applied physics and science education, Technische Universiteit Eindhoven, 2012. DOI: `10.6100/IR737554`.

[35] E. Viezzer. “Access and sustainment of naturally ELM-free and small-ELM regimes”. In: *Nuclear Fusion* 58.11 (2018), p. 115002. DOI: `10.1088/1741-4326/aac222`.

[36] P. B. Snyder, H. R. Wilson, J. R. Ferron, L. L. Lao, A. W. Leonard, T. H. Osborne, A. D. Turnbull, D. Mossessian, M. Murakami, and X. Q. Xu. “Edge localized modes and the pedestal: A model based on coupled peeling–ballooning modes”. In: *Physics of Plasmas* 9.5 (2002), pp. 2037–2043. DOI: `10.1063/1.1449463`.

[37] H. R. Wilson, P. B. Snyder, G. T. A. Huysmans, and R. L. Miller. “Numerical studies of edge localized instabilities in tokamaks”. In: *Physics of Plasmas* 9.4 (2002), pp. 1277–1286. DOI: `10.1063/1.1459058`.

[38] R.A. Pitts, S. Carpentier, F. Escourbiac, T. Hirai, V. Komarov, S. Lisgo, A.S. Kukushkin, A. Loarte, M. Merola, A. Sashala Naik, R. Mitteau, M. Sugihara, B. Bazylev, and P.C. Stangeby. “A full tungsten divertor for ITER: Physics issues and design status”. In: *Journal of Nuclear Materials* 438 (2013), S48–S56. DOI: `10.1016/j.jnucmat.2013.01.008`.

[39] J. Stober, M. Maraschek, G.D. Conway, O. Gruber, A. Herrmann, A.C.C. Sips, W. Treutterer, H. Zohm, and ASDEX Upgrade Team. “Type II ELMy H modes on ASDEX Upgrade with good confinement at high density”. In: *Nuclear Fusion* 41.9 (2001), p. 1123. DOI: `10.1088/0029-5515/41/9/301`.

[40] G. Saibene, P.J. Lomas, R. Sartori, A. Loarte, J. Stober, Y. Andrew, S.A. Arshad, G.D. Conway, E. de la Luna, K. Günther, L.C. Ingesson, M.A.H. Kempenaars, A. Korotkov, H.R. Koslowski, J.S. Lönnroth, D.C. McDonald, A. Meigs, P. Monier-Garbet, V. Parail, C.P. Perez, F.G. Rimini, S. Sharapov, and P.R. Thomas. “Characterization of small ELM experiments in highly shaped single null and quasi-double-null plasmas in JET”. In: *Nuclear Fusion* 45.5 (2005), p. 297. DOI: `10.1088/0029-5515/45/5/001`.

[41] G.F. Harrer, E. Wolfrum, M.G. Dunne, P. Manz, M. Cavedon, P.T. Lang, B. Kurzan, T. Eich, B. Labit, J. Stober, H. Meyer, M. Bernert, F.M. Laggner, F. Aumayr, the EUROfusion MST1 Team, and the ASDEX Upgrade Team. “Parameter dependences of small edge localized modes (ELMs)”. In: *Nuclear Fusion* 58.11 (2018), p. 112001. DOI: `10.1088/1741-4326/aad757`.

[42] B. Labit et al. “Dependence on plasma shape and plasma fueling for small edge-localized mode regimes in TCV and ASDEX Upgrade*”. In: *Nuclear Fusion* 59.8 (2019), p. 086020. DOI: `10.1088/1741-4326/ab2211`.

[43] R J Goldston, M L Reinke, and J A Schwartz. “A new scaling for divertor detachment”. In: *Plasma Physics and Controlled Fusion* 59.5 (2017), p. 055015. DOI: `10.1088/1361-6587/aa5e6e`.

[44] M. Faitsch, T. Eich, G.F. Harrer, E. Wolfrum, D. Brida, P. David, M. Griener, and U. Stroth. “Broadening of the power fall-off length in a high density, high confinement H-mode regime in ASDEX Upgrade”. In: *Nuclear Materials and Energy* 26 (2021), p. 100890. DOI: `10.1016/j.nme.2020.100890`.

[45] M. Griener, E. Wolfrum, G. Birkenmeier, M. Faitsch, R. Fischer, G. Fuchert, L. Gil, G.F. Harrer, P. Manz, D. Wendler, and U. Stroth. "Continuous observation of filaments from the confined region to the far scrape-off layer". In: *Nuclear Materials and Energy* 25 (2020), p. 100854. doi: `10.1016/j.nme.2020.100854`.

[46] A. Stagni, N. Vianello, C.K. Tsui, C. Colandrea, S. Gorno, M. Bernert, J.A. Boedo, D. Brida, G. Falchetto, A. Hakola, G. Harrer, H. Reimerdes, C. Theiler, E. Tsitrone, N. Walkden, the TCV Team, and the EUROfusion MST1 Team. "Dependence of scrape-off layer profiles and turbulence on gas fuelling in high density H-mode regimes in TCV". In: *Nuclear Fusion* 62.9 (2022), p. 096031. doi: `10.1088/1741-4326/ac8234`.

[47] A. Redl, T. Eich, N. Vianello, and P. David. "Energy load on first wall components in high density, small ELM regimes in ASDEX Upgrade". In: *Nuclear Materials and Energy* 34 (2023), p. 101319. doi: `10.1016/j.nme.2022.101319`.

[48] A. Stagni, N. Vianello, M. Agostini, C. Colandrea, S. Gorno, B. Labit, U. Sheikh, L. Simons, G. Sun, C.K. Tsui, M. Ugoletti, Y Wang, C. Wütrich, J.A. Boedo, H. Reimerdes, and C. Theiler. "The effect of plasma shaping on high density H-mode SOL profiles and fluctuations in TCV". Submitted to *Nuclear Fusion*.

[49] B. LaBombard, R. L. Boivin, M. Greenwald, J. Hughes, B. Lipschultz, D. Mossessian, C. S. Pitcher, J. L. Terry, S. J. Zweben, and Alcator Group. "Particle transport in the scrape-off layer and its relationship to discharge density limit in Alcator C-Mod". In: *Physics of Plasmas* 8.5 (2001), pp. 2107–2117. doi: `10.1063/1.1352596`.

[50] D.L. Rudakov, J.A. Boedo, R.A. Moyer, P.C. Stangeby, J.G. Watkins, D.G. Whyte, L. Zeng, N.H. Brooks, R.P. Doerner, T.E. Evans, M.E. Fenstermacher, M. Groth, E.M. Hollmann, S.I. Krasheninnikov, C.J. Lasnier, A.W. Leonard, M.A. Mahdavi, G.R. McKee, A.G. McLean, A.Yu. Pigarov, W.R. Wampler, G. Wang, W.P. West, and C.P.C. Wong. "Far SOL transport and main wall plasma interaction in DIII-D". In: *Nuclear Fusion* 45.12 (2005), p. 1589. doi: `10.1088/0029-5515/45/12/014`.

[51] O. E. Garcia, J Horacek, R.A Pitts, A.H Nielsen, W Fundamenski, V aulin, and J. Juul Rasmussen. "Fluctuations and transport in the TCV scrape-off layer". In: *Nuclear Fusion* 47.7 (June 2007), pp. 667–676. doi: `10.1088/0029-5515/47/7/017`.

[52] D. Carralero, S. Artene, M. Bernert, G. Birkenmeier, M. Faitsch, P. Manz, P. de Marne, U. Stroth, M. Wischmeier, E. Wolfrum, and and. "On the role of filaments in perpendicular heat transport at the scrape-off layer". In: *Nuclear Fusion* 58.9 (July 2018), p. 096015. doi: `10.1088/1741-4326/aacb04`.

[53] N. Vianello, D. Carralero, C.K. Tsui, V. Naulin, M. Agostini, I. Cziegler, B. Labit, C. Theiler, E. Wolfrum, D. Aguiam, S. Allan, M. Bernert, J. Boedo, S. Costea, H. De Oliveira, O. Fevrier, J. Galdon-Quiroga, G. Grenfell, A. Hakola, C. Ionita, H. Isliker, A. Karpushov, J. Kovacic, B. Lipschultz, R. Maurizio, K. McClements, F. Militello, A.H. Nielsen, J. Olsen, J.J. Rasmussen, T. Ravensbergen, H. Reimerdes, B. Schneider, R. Schrittwieser, E. Seliunin, M. Spolaore, K. Verhaegh, J. Vicente, N. Walkden, W. Zhang, the ASDEX Upgrade Team, the TCV Team, and the EUROfusion MST1 Team. "Scrape-off layer transport and filament characteristics in high-density tokamak regimes". In: *Nuclear Fusion* 60.1 (2019), p. 016001. DOI: `10.1088/1741-4326/ab423e`.

[54] O Février, C Theiler, J R Harrison, C K Tsui, K Verhaegh, C Wüthrich, J A Boedo, H De Oliveira, B P Duval, B Labit, B Lipschultz, R Maurizio, H Reimerdes, the TCV Team, and the EUROfusion MST1 Team. "Nitrogen-seeded divertor detachment in TCV L-mode plasmas". In: *Plasma Physics and Controlled Fusion* 62.3 (2020), p. 035017. DOI: `10.1088/1361-6587/ab6b00`.

[55] C. K. Tsui, J. A. Boedo, D. Brida, O. Février, G. F. Harrer, A. Perek, H. Reimerdes, B. P. Duval, S. Gorno, U. A. Sheikh, C. Theiler, N. Vianello, N. Walkden, M. Wensing, M. Baquero-Ruiz, TCV Team, and MST1 Team. "Evidence on the effects of main-chamber neutrals on density shoulder broadening". In: *Physics of Plasmas* 29.6 (2022), p. 062507. DOI: `10.1063/5.0090260`.

[56] H.W. Müller, M. Bernert, D. Carralero, A. Kallenbach, B. Kurzan, A. Scarabosio, B. Sieglin, L. Tophøj, N. Vianello, and E. Wolfrum. "Far scrape-off layer particle and heat fluxes in high density – High power scenarios". In: *Journal of Nuclear Materials* 463 (2015), pp. 739–743. DOI: `10.1016/j.jnucmat.2015.01.012`.

[57] D. Carralero, J. Madsen, S.A. Artene, M. Bernert, G. Birkenmeier, T. Eich, G. Fuchert, F. Laggner, V. Naulin, P. Manz, N. Vianello, and E. Wolfrum. "A study on the density shoulder formation in the SOL of H-mode plasmas". In: *Nuclear Materials and Energy* 12 (2017), pp. 1189–1193. DOI: `10.1016/j.nme.2016.11.016`.

[58] N. Vianello, N. Walkden, M. Dunne, B. Lomanowski, E. Wolfrum, C.K. Tsui, A. Stagni, M. Griener, B. Tal, T. Eich, D. Refy, D. Brida, O. Février, M. Agostini, H. De Oliveira, S. Aleiferis, M. Bernert, J.A. Boedo, M. Brix, D. Carralero, I. Carvalho, G. Falchetto, L. Frassinetti, C. Giroud, A. Hakola, A. Huber, J. Karhunen, A. Karpushov, B. Labit, A. Meigs, V. Naulin, T. Pereira, C. Perez Von Thun, H. Reimerdes, S. Gorno, C. Theiler, the ASDEX Upgrade team, the TCV team, the EUROfusion MST1 team, and the JET Contributors. "SOL profile and fluctuations in different divertor recycling conditions in

H-mode plasmas". In: *Preprint: 2020 IAEA Fusion Energy Conference, Nice*. [EX/P3-14]. 2021. URL: `https://nucleus.iaea.org/sites/fusionportal/Shared%20Documents/FEC%202020/fec2020-preprints/preprint1051.pdf`.

[59] M. Giacomin, A. Stagni, P. Ricci, J.A. Boedo, J. Horacek, H. Reimerdes, and C.K. Tsui. "Theory-based scaling laws of near and far scrape-off layer widths in single-null L-mode discharges". In: *Nuclear Fusion* 61.7 (2021), p. 076002. DOI: `10.1088/1741-4326/abf8f6`.

[60] D. Mancini, P. Ricci, N. Vianello, M. Giacomin, and A. Coroado. "Investigation of the density shoulder formation by using self-consistent simulations of plasma turbulence and neutral kinetic dynamics". In: *Nuclear Fusion* 61.12 (2021), p. 126029. DOI: `10.1088/1741-4326/ac30c9`.

[61] D. Mancini, P. Ricci, N. Vianello, G. Van Parys, and D.S. Oliveira. "Self-consistent multicomponent simulation of plasma turbulence and neutrals in detached conditions". In: *Nuclear Fusion* 64.1 (2023), p. 016012. DOI: `10.1088/1741-4326/ad0a0b`.

[62] G. F. Harrer, M. Faitsch, L. Radovanovic, E. Wolfrum, C. Albert, A. Cathey, M. Cavedon, M. Dunne, T. Eich, R. Fischer, M. Griener, M. Hoelzl, B. Labit, H. Meyer, F. Aumayr, The ASDEX Upgrade Team, and The EUROfusion MST1 Team. "Quasicontinuous Exhaust Scenario for a Fusion Reactor: The Renaissance of Small Edge Localized Modes". In: *Phys. Rev. Lett.* 129 (16 2022), p. 165001. DOI: `10.1103/PhysRevLett.129.165001`.

[63] L. Radovanovic, M. Dunne, E. Wolfrum, G. Harrer, M. Faitsch, R. Fischer, F. Aumayr, the ASDEX Upgrade Team, and the EUROfusion MST1 Team. "Developing a physics understanding of the quasi-continuous exhaust regime: pedestal profile and ballooning stability analysis". In: *Nuclear Fusion* 62.8 (2022), p. 086004. DOI: `10.1088/1741-4326/ac6d6a`.

[64] R.J. Goldston. "Heuristic drift-based model of the power scrape-off width in low-gas-puff H-mode tokamaks". In: *Nuclear Fusion* 52.1 (2011), p. 013009. DOI: `10.1088/0029-5515/52/1/013009`.

[65] R.J. Goldston. "Theoretical aspects and practical implications of the heuristic drift SOL model". In: *Journal of Nuclear Materials* 463 (2015), pp. 397–400. DOI: `doi.org/10.1016/j.jnucmat.2014.10.080`.

[66] T. C. Luce. "An analytic functional form for characterization and generation of axisymmetric plasma boundaries". In: *Plasma Physics and Controlled Fusion* 55.9 (July 2013), p. 095009. DOI: `10.1088/0741-3335/55/9/095009`.

[67] R. Maurizio. "Investigating Scrape-Off Layer transport in alternative divertor geometries on the TCV tokamak". PhD thesis. Lausanne, 2020, p. 206. doi: 10.5075/epfl-thesis-9893.

[68] R. Maurizio, B.P. Duval, B. Labit, H. Reimerdes, C. Theiler, C.K. Tsui, J. Boedo, H. De Oliveira, O. Février, U. Sheikh, M. Spolaore, K. Verhaegh, N. Vianello, and M. Wensing. "Conduction-based model of the Scrape-Off Layer power sharing between inner and outer divertor in diverted low-density tokamak plasmas". In: *Nuclear Materials and Energy* 19 (2019), pp. 372–377. doi: 10.1016/j.nme.2019.03.020.

[69] H. Reimerdes, R. Ambrosino, P. Innocente, A. Castaldo, P. Chmielewski, G. Di Gironimo, S. Merriman, V. Pericoli-Ridolfini, L. Aho-Mantilla, R. Albanese, H. Bufferand, G. Calabro, G. Ciraolo, D. Coster, N. Fedorczak, S. Ha, R. Kembleton, K. Lackner, V.P. Loschiavo, T. Lunt, D. Marzullo, R. Maurizio, F. Militello, G. Ramogida, F. Subba, S. Varoutis, R. Zagórski, and H. Zohm. "Assessment of alternative divertor configurations as an exhaust solution for DEMO". In: *Nuclear Fusion* 60.6 (2020), p. 066030. doi: 10.1088/1741-4326/ab8a6a.

[70] R.A. Pitts, S. Bardin, B. Bazylev, M.A. van den Berg, P. Bunting, S. Carpentier-Chouchana, J.W. Coenen, Y. Corre, R. Dejarnac, F. Escourbiac, J. Gaspar, J.P. Gunn, T. Hirai, S-H. Hong, J. Horacek, D. Iglesias, M. Komm, K. Krieger, C. Lasnier, G.F. Matthews, T.W. Morgan, S. Panayotis, S. Pestchanyi, A. Podolnik, R.E. Nygren, D.L. Rudakov, G. De Temmerman, P. Vondracek, and J.G. Watkins. "Physics conclusions in support of ITER W divertor monoblock shaping". In: *Nuclear Materials and Energy* 12 (2017), pp. 60–74. doi: 10.1016/j.nme.2017.03.005.

[71] A.C.C. Sips, J. Schweinzer, T.C. Luce, S. Wolfe, H. Urano, J. Hobirk, S. Ide, E. Joffrin, C. Kessel, S.H. Kim, P. Lomas, I. Nunes, T. Pütterich, F. Rimini, W.M. Solomon, J. Stober, F. Turco, P.C. de Vries, JET Contributors, The ASDEX Upgrade team, The DIII-D team, The C-Mod team, The JT-60U team, ITPA-IOS TG members, and experts. "Assessment of the baseline scenario at q95 3 for ITER". In: *Nuclear Fusion* 58.12 (2018), p. 126010. doi: 10.1088/1741-4326/aade57.

[72] S. I. Braginskii. "Transport processes in a plasma". In: *Reviews of plasma physics* 1 (1965), pp. 205–311.

[73] Lyman Spitzer and Richard Härm. "Transport Phenomena in a Completely Ionized Gas". In: *Phys. Rev.* 89 (5 1953), pp. 977–981. doi: 10.1103/PhysRev.89.977.

[74] A. Piel. “Plasma Boundaries”. In: *Plasma Physics: An Introduction to Laboratory, Space, and Fusion Plasmas*. Cham: Springer International Publishing, 2017, pp. 175–209. ISBN: 978-3-319-63427-2. DOI: `10.1007/978-3-319-63427-2_7`.

[75] Roland Chodura. “Plasma Flow in the Sheath and the Presheath of a Scrape-Off Layer”. In: *Physics of Plasma-Wall Interactions in Controlled Fusion*. Boston, MA: Springer US, 1986, pp. 99–134. ISBN: 978-1-4757-0067-1. DOI: `10.1007/978-1-4757-0067-1_4`.

[76] S. Chapman and T. G. Cowling. *The Mathematical Theory of Non-Uniform Gases*. Cambridge University Press, 1991. ISBN: 9780521408448.

[77] R. Balescu. *Transport Processes in Plasmas. Vol. 1: Classical Transport Theory*. Amsterdam: North Holland, 1988.

[78] R. Balescu. *Transport Processes in Plasmas. Vol. 2: Neoclassical Transport Theory*. Amsterdam: North Holland, 1988. ISBN: 9780444870926.

[79] R. Balescu. *Aspects of Anomalous Transport in Plasmas (Series in Plasma Physics)*. Bristol, UK: IOP Publishing, 2005. ISBN: 9780750310307.

[80] D. Carralero, M. Siccinio, M. Komm, S.A. Artene, F.A. D’Isa, J. Adamek, L. Aho-Mantila, G. Birkenmeier, M. Brix, G. Fuchert, M. Groth, T. Lunt, P. Manz, J. Madsen, S. Marsen, H.W. Müller, U. Stroth, H.J. Sun, N. Vianello, M. Wischmeier, and E. Wolfrum. “Recent progress towards a quantitative description of filamentary SOL transport”. In: *Nuclear Fusion* 57.5 (Apr. 2017), p. 056044. DOI: `10.1088/1741-4326/aa64b3`. URL: `https://doi.org/10.1088%2F1741-4326%2Faa64b3`.

[81] A. Q. Kuang, B. LaBombard, D. Brunner, O.E. Garcia, R. Kube, and A. Theodorsen. “Plasma fluctuations in the scrape-off layer and at the divertor target in Alcator C-Mod and their relationship to divertor collisionality and density shoulder formation”. In: *Nuclear Materials and Energy* 19 (2019), pp. 295–299. DOI: `10.1016/j.nme.2019.02.038`.

[82] M. Francisquez, B. Zhu, and B.N. Rogers. “Global 3D Braginskii simulations of the tokamak edge region of IWL discharges”. In: *Nuclear Fusion* 57.11 (Aug. 2017), p. 116049. DOI: `10.1088/1741-4326/aa7f23`.

[83] M. Giacomin and P. Ricci. “Investigation of turbulent transport regimes in the tokamak edge by using two-fluid simulations”. In: *Journal of Plasma Physics* 86.5 (2020), p. 905860502. DOI: `10.1017/S0022377820000914`.

[84] Bruce D Scott. “Tokamak edge turbulence: background theory and computation”. In: *Plasma Physics and Controlled Fusion* 49.7 (2007), S25. DOI: `10.1088/0741-3335/49/7/S02`.

[85] A. Zeiler. *Tokamak Edge Turbulence*. Garching-bei-München, Germany: Max Planck Institut für Plasmaphysik, 1999.

[86] Bruce Scott. *Turbulence and Instabilities in Magnetised Plasmas, Volume 1*. 2053-2563. IOP Publishing, 2021. ISBN: 978-0-7503-2504-2. DOI: `10.1088/978-0-7503-2504-2`.

[87] S. Brunner. *Waves and Instabilities in Inhomogeneous Plasmas*. PhD course notes. CRPP, EPFL, Lausanne.

[88] A. Mosetto, F. D. Halpern, S. Jolliet, J. Loizu, and P. Ricci. "Turbulent regimes in the tokamak scrape-off layer". In: *Physics of Plasmas* 20.9 (2013), p. 092308. DOI: `10.1063/1.4821597`.

[89] S.I. Krasheninnikov. "On scrape off layer plasma transport". In: *Physics Letters A* 283.5 (2001), pp. 368–370. DOI: `10.1016/S0375-9601(01)00252-3`.

[90] B LaBombard, M.V Umansky, R.L Boivin, J.A Goetz, J Hughes, B Lipschultz, D Mossessian, C.S Pitcher, J.L Terry, and Alcator Group. "Cross-field plasma transport and main-chamber recycling in diverted plasmas on Alcator C-Mod". In: *Nuclear Fusion* 40.12 (Dec. 2000), pp. 2041–2060. DOI: `10.1088/0029-5515/40/12/308`.

[91] J. Horacek, RA Pitts, and JP Graves. "Overview of edge electrostatic turbulence experiments on TCV". In: *Czechoslovak Journal of Physics* 55.3 (2005), pp. 271–283.

[92] J. A. Boedo. "Edge turbulence and SOL transport in tokamaks". In: *Journal of Nuclear Materials* 390-391 (2009), pp. 29–37. DOI: `10.1016/j.jnucmat.2009.01.040`.

[93] P. Paruta, P. Ricci, F. Riva, C. Wersal, C. Beadle, and B. Frei. "Simulation of plasma turbulence in the periphery of diverted tokamak by using the GBS code". In: *Physics of Plasmas* 25.11 (2018), p. 112301. DOI: `10.1063/1.5047741`.

[94] D. A. D'Ippolito, J. R. Myra, and S. J. Zweben. "Convective transport by intermittent blob-filaments: Comparison of theory and experiment". In: *Physics of Plasmas* 18.6 (2011), p. 060501. DOI: `10.1063/1.3594609`.

[95] J. A. Boedo, D. Rudakov, R. Moyer, S. Krasheninnikov, D. Whyte, G. McKee, G. Tynan, M. Schaffer, P. Stangeby, P. West, S. Allen, T. Evans, R. Fonck, E. Hollmann, A. Leonard, A. Mahdavi, G. Porter, M. Tillack, and G. Antar. "Transport by intermittent convection in the boundary of the DIII-D tokamak". In: *Physics of Plasmas* 8.11 (2001), pp. 4826–4833. DOI: `10.1063/1.1406940`.

[96] P. C. Stangeby. "Modeling plasma contact with the main vessel walls of a divertor tokamak". In: *Physics of Plasmas* 9.8 (2002), pp. 3489–3507. DOI: `10.1063/1.1493207`.

[97] B Scott. In: 40.5 (1998), p. 823. DOI: 10.1088/0741-3335/40/5/050.

[98] Bruce D Scott. "The nonlinear drift wave instability and its role in tokamak edge turbulence". In: *New Journal of Physics* 4.1 (2002), p. 52. DOI: 10.1088/1367-2630/4/1/352.

[99] B. D. Scott. "Drift wave versus interchange turbulence in tokamak geometry: Linear versus nonlinear mode structure". In: *Physics of Plasmas* 12.6 (2005), p. 062314. DOI: 10.1063/1.1917866.

[100] B. N. Rogers, J. F. Drake, and A. Zeiler. "Phase Space of Tokamak Edge Turbulence, the $L - H$ Transition, and the Formation of the Edge Pedestal". In: *Phys. Rev. Lett.* 81 (20 1998), pp. 4396–4399. DOI: 10.1103/PhysRevLett.81.4396.

[101] M. Giacomin, L. N. Stenger, and P. Ricci. "Turbulence and flows in the plasma boundary of snowflake magnetic configurations". In: *Nuclear Fusion* 60.2 (Jan. 2020), p. 024001. DOI: 10.1088/1741-4326/ab6435.

[102] T. Eich, P. Manz, and the ASDEX Upgrade team. "The separatrix operational space of ASDEX Upgrade due to interchange-drift-Alfvén turbulence". In: *Nuclear Fusion* 61.8 (2021), p. 086017. DOI: 10.1088/1741-4326/ac0412.

[103] T. Eich, P. Manz, R.J. Goldston, P. Hennequin, P. David, M. Faitsch, B. Kurzan, B. Sieglin, E. Wolfrum, the ASDEX Upgrade team, and the EUROfusion MST1 team b. "Turbulence driven widening of the near-SOL power width in ASDEX Upgrade H-Mode discharges". In: *Nuclear Fusion* 60.5 (2020), p. 056016. DOI: 10.1088/1741-4326/ab7a66.

[104] F Hofmann, J B Lister, W Anton, S Barry, R Behn, S Bernel, G Besson, F Buhlmann, R Chavan, M Corboz, M J Dutch, B P Duval, D Fasel, A Favre, S Franke, A Heym, A Hirt, C Hollenstein, P Isoz, B Joye, X Llobet, J C Magnin, B Marletaz, P Marmillod, Y Martin, J M Mayor, J M Moret, C Nieswand, P J Paris, A Perez, Z A Pietrzyk, R A Pitts, A Pochelon, R Rage, O Sauter, G Tonetti, M Q Tran, F Troyon, D J Ward, and H Weisen. "Creation and control of variably shaped plasmas in TCV". In: *Plasma Physics and Controlled Fusion* 36.12B (1994), B277. DOI: 10.1088/0741-3335/36/12B/023.

[105] H. Reimerdes, S. Alberti, P. Blanchard, P. Bruzzone, R. Chavan, S. Coda, B.P. Duval, A. Fasoli, B. Labit, B. Lipschultz, T. Lunt, Y. Martin, J.-M. Moret, U. Sheikh, B. Sudki, D. Testa, C. Theiler, M. Toussaint, D. Uglietti, N. Vianello, and M. Wischmeier. "TCV divertor upgrade for alternative magnetic configurations". In: *Nuclear Materials and Energy* 12 (2017), pp. 1106–1111. DOI: 10.1016/j.nme.2017.02.013.

[106] A. Fasoli, H. Reimerdes, S. Alberti, M. Baquero-Ruiz, B.P. Duval, E. Havlikova, A. Karpushov, J.-M. Moret, M. Toussaint, H. Elaian, M. Silva, C. Theiler, D. Vaccaro, and the TCV team. "TCV heating and divertor upgrades". In: *Nuclear Fusion* 60.1 (2020), p. 016019. DOI: `10.1088/1741-4326/ab4c56`.

[107] F. Hofmann. "FBT - a free-boundary tokamak equilibrium code for highly elongated and shaped plasmas". In: *Computer Physics Communications* 48.2 (1988), pp. 207–221. DOI: `10.1016/0010-4655(88)90041-0`.

[108] J.-M. Moret, B.P. Duval, H.B. Le, S. Coda, F. Felici, and H. Reimerdes. "Tokamak equilibrium reconstruction code LIUQE and its real time implementation". In: *Fusion Engineering and Design* 91 (2015), pp. 1–15. DOI: `10.1016/j.fusengdes.2014.09.019`.

[109] J.-M. Moret, F. Buhlmann, D. Fasel, F. Hofmann, and G. Tonetti. "Magnetic measurements on the TCV Tokamak". In: *Review of Scientific Instruments* 69.6 (June 1998), pp. 2333–2348. DOI: `10.1063/1.1148940`.

[110] Robert S. Cohen, Lyman Spitzer, and Paul McR. Routly. "The Electrical Conductivity of an Ionized Gas". In: *Phys. Rev.* 80 (2 1950), pp. 230–238. DOI: `10.1103/PhysRev.80.230`.

[111] Alexander N. Karpushov, Filippo Bagnato, Marcelo Baquero-Ruiz, Stefano Coda, Claudia Colandrea, Frédéric Dolizy, Jérémie Dubray, Basil P. Duval, Damien Fasel, Ambrogio Fasoli, Rémy Jacquier, Pierre Lavanchy, Blaise Marlétaz, Yves Martin, Lorenzo Martinelli, Dmytry Mykytchuk, Marta M. Pedrini, Jesús Poley, Holger Reimerdes, Umar Sheikh, Ugo Siravo, Matthieu Toussaint, and Matteo Vallar. "Upgrade of the neutral beam heating system on the TCV tokamak – second high energy neutral beam". In: *Fusion Engineering and Design* 187 (2023), p. 113384. DOI: `j.fusengdes.2022.113384`.

[112] S. C. Bates and K. H. Burrell. "Fast gas injection system for plasma physics experiments". In: *Review of Scientific Instruments* 55.6 (1984), pp. 934–939. DOI: `10.1063/1.1137845`.

[113] N. Offeddu, C. Wüthrich, W. Han, C. Theiler, T. Golfinopoulos, J. L. Terry, E. Marmar, C. Galperti, Y. Andrebe, B. P. Duval, R. Bertizzolo, A. Clement, O. Février, H. Elaian, D. Gönczy, J. D. Landis, and TCV Team. "Gas puff imaging on the TCV tokamak". In: *Review of Scientific Instruments* 93.12 (2022), p. 123504. DOI: `10.1063/5.0126398`.

[114] I. Furno, H. Weisen, J. Mlynar, R. A. Pitts, X. Llobet, Ph. Marmillod, and G. P. Pochon. "Fast bolometric measurements on the TCV tokamak". In: *Review of Scientific Instruments* 70.12 (1999), pp. 4552–4556. DOI: `10.1063/1.1150111`.

[115] U. A. Sheikh, L. Simons, B. P. Duval, O. Février, D. Moret, A. Allegrucci, M. Bernert, F. Crisinel, T. Tersztyánszky, and O. Villinger. "RADCAM—A radiation camera system combining foil bolometers, AXUV diodes, and filtered soft x-ray diodes". In: *Review of Scientific Instruments* 93.11 (2022), p. 113513. DOI: `10.1063/5.0095907`.

[116] Uron Kruezi, G. Sergienko, P. D. Morgan, G. F. Matthews, S. Brezinsek, S. Vartanian, and JET-EFDA Contributors. "JET divertor diagnostic upgrade for neutral gas analysisa)". In: *Review of Scientific Instruments* 83.10 (2012), p. 10D728. DOI: `10.1063/1.4732175`.

[117] R. Maurizio, S. Elmore, N. Fedorczak, A. Gallo, H. Reimerdes, B. Labit, C. Theiler, C.K. Tsui, W.A.J. Vijvers, The TCV Team, and The MST1 Team. "Divertor power load studies for attached L-mode single-null plasmas in TCV". In: *Nuclear Fusion* 58.1 (2017), p. 016052. DOI: `10.1088/1741-4326/aa986b`.

[118] J. Hawke, Y. Andrebe, R. Bertizzolo, P. Blanchard, R. Chavan, J. Decker, B. Duval, P. Lavanchy, X. Llobet, B. Marlétaz, P. Marmillod, G. Pochon, and M. Toussaint. "Improving spatial and spectral resolution of TCV Thomson scattering". In: *Journal of Instrumentation* 12.12 (2017), p. C12005. DOI: `10.1088/1748-0221/12/12/C12005`.

[119] O. Février, C. Theiler, H. De Oliveira, B. Labit, N. Fedorczak, and A. Baillod. "Analysis of wall-embedded Langmuir probe signals in different conditions on the Tokamak à Configuration Variable". In: *Review of Scientific Instruments* 89.5 (2018), p. 053502. DOI: `10.1063/1.5022459`.

[120] H. De Oliveira, P. Marmillod, C. Theiler, R. Chavan, O. Février, B. Labit, P. Lavanchy, B. Marlétaz, R. A. Pitts, and TCV team. "Langmuir probe electronics upgrade on the tokamak à configuration variable". In: *Review of Scientific Instruments* 90.8 (2019), p. 083502. DOI: `10.1063/1.5108876`.

[121] Mirko Wensing. "Drift-related transport and plasma-neutral interaction in the TCV divertor". In: (2021), p. 263. DOI: `10.5075/epfl-thesis-8447`.

[122] C.K. Tsui, J.A. Boedo, D. Galassi, J. Loizu, R. Maurizio, H. Reimerdes, B.P. Duval, O. Février, M. Spolaore, M. Wensing, the TCV Team, and the Eurofusion MST1 Team. "Parallel convection and E × B drifts in the TCV snowflake divertor and their effects on target heat-fluxes". In: *Nuclear Fusion* 61.4 (2021), p. 046004. DOI: `10.1088/1741-4326/abdb93`.

[123] J. A. Boedo, N. Crocker, L. Chousal, R. Hernandez, J. Chalfant, H. Kugel, P. Roney, J. Wertenbaker, and NSTX Team. "Fast scanning probe for the NSTX spherical tokamak". In: *Review of Scientific Instruments* 80.12 (2009), p. 123506. DOI: `10.1063/1.3266065`.

[124] C. K. Tsui, J. A. Boedo, F. D. Halpern, J. Loizu, F. Nespoli, J. Horacek, B. Labit, J. Morales, H. Reimerdes, P. Ricci, C. Theiler, S. Coda, B. P. Duval, I. Furno, TCV Team, and EUROfusion MST1 Team. "Poloidal asymmetry in the narrow heat flux feature in the TCV scrape-off layer". In: *Physics of Plasmas* 24.6 (2017), p. 062508. DOI: `10.1063/1.4985075`.

[125] C. K. Tsui, J. A. Boedo, P. C. Stangeby, and TCV Team. "Accounting for Debye sheath expansion for proud Langmuir probes in magnetic confinement fusion plasmas". In: *Review of Scientific Instruments* 89.1 (2018), p. 013505. DOI: `10.1063/1.4995353`.

[126] M. Agostini, P. Scarin, R. Cavazzana, L. Carraro, L. Grando, C. Taliercio, L. Franchin, and A. Tiso. "Fast Thermal Helium Beam diagnostic for measurements of edge electron profiles and fluctuations". In: *Review of Scientific Instruments* 86.12 (2015), p. 123513. DOI: `10.1063/1.4939003`.

[127] M. Agostini, P. Scarin, R. Milazzo, V. Cervaro, and R. Ghiraldelli. "Development and characterization of thermal helium beam diagnostic with four helium lines for RFX-mod2 experiment". In: *Review of Scientific Instruments* 91.11 (2020), p. 113503. DOI: `10.1063/5.0023310`.

[128] M Goto. "Collisional-radiative model for neutral helium in plasma revisited". In: *Journal of Quantitative Spectroscopy and Radiative Transfer* 76.3 (2003), pp. 331–344. DOI: `10.1016/S0022-4073(02)00060-2`.

[129] O Schmitz, I L Beigman, L A Vainshtein, B Schweer, M Kantor, A Pospieszczyk, Y Xu, M Krychowiak, M Lehnen, U Samm, B Unterberg, and the TEXTOR team. "Status of electron temperature and density measurement with beam emission spectroscopy on thermal helium at TEXTOR". In: *Plasma Physics and Controlled Fusion* 50.11 (2008), p. 115004. DOI: `10.1088/0741-3335/50/11/115004`.

[130] L. Frassinetti, S. Saarelma, G. Verdoolaege, M. Groth, J.C. Hillesheim, P. Bilkova, P. Bohm, M. Dunne, R. Fridström, E. Giovannozzi, F. Imbeaux, B. Labit, E. de la Luna, C. Maggi, M. Owsiak, R. Scannell, and JET contributors. "Pedestal structure, stability and scalings in JET-ILW: the EUROfusion JET-ILW pedestal database". In: *Nuclear Fusion* 61.1 (2020), p. 016001. DOI: `10.1088/1741-4326/abb79e`.

[131] Edoardo Rovere. "Development of the EUROfusion pedestal database for ELMy H-Mode for the TCV tokamak". MA thesis. Milano, Italy: Politecnico di Milano, 2019. URL: `http://hdl.handle.net/10589/145958`.

[132] R.J Groebner, D.R Baker, K.H Burrell, T.N Carlstrom, J.R Ferron, P Gohil, L.L Lao, T.H Osborne, D.M Thomas, W.P West, J.A Boedo, R.A Moyer, G.R McKee, R.D Deranian, E.J Doyle, C.L Rettig, T.L Rhodes, and J.C Rost. “Progress in quantifying the edge physics of the H mode regime in DIII-D”. In: *Nuclear Fusion* 41.12 (2001), pp. 1789–1802. DOI: `10.1088/0029-5515/41/12/306`.

[133] A Herrmann, W Junker, K Gunther, S Bosch, M Kaufmann, J Neuhauser, G Pautasso, Th Richter, and R Schneider. “Energy flux to the ASDEX-Upgrade diverter plates determined by thermography and calorimetry”. In: *Plasma Physics and Controlled Fusion* 37.1 (1995), p. 17. DOI: `10.1088/0741-3335/37/1/002`.

[134] B. Sieglin, M. Faitsch, A. Herrmann, B. Brucker, T. Eich, L. Kammerloher, and S. Martinov. “Real time capable infrared thermography for ASDEX Upgrade”. In: *Review of Scientific Instruments* 86.11 (2015), p. 113502. DOI: `10.1063/1.4935580`.

[135] T. Eich, B. Sieglin, A. Scarabosio, W. Fundamenski, R. J. Goldston, and A. Herrmann. “Inter-ELM Power Decay Length for JET and ASDEX Upgrade: Measurement and Comparison with Heuristic Drift-Based Model”. In: *Phys. Rev. Lett.* 107 (21 2011), p. 215001. DOI: `10.1103/PhysRevLett.107.215001`.

[136] A. Kallenbach, N. Asakura, A. Kirk, A. Korotkov, M.A. Mahdavi, D. Mossessian, and G.D. Porter. “Multi-machine comparisons of H-mode separatrix densities and edge profile behaviour in the ITPA SOL and Divertor Physics Topical Group”. In: *Journal of Nuclear Materials* 337-339 (2005), pp. 381–385. DOI: `doi.org/10.1016/j.jnucmat.2004.10.099`.

[137] H J Sun, E Wolfrum, T Eich, B Kurzan, S Potzel, U Stroth, and the ASDEX Upgrade Team. “Study of near scrape-off layer (SOL) temperature and density gradient lengths with Thomson scattering”. In: *Plasma Physics and Controlled Fusion* 57.12 (2015), p. 125011. DOI: `10.1088/0741-3335/57/12/125011`.

[138] J. Kinsey and Myunghee Choi. *The TORAY Electron Cyclotron Heating and Current Drive Code*. 2004. URL: `https://w3.pppl.gov/ntcc/TORAY/`.

[139] T. Eich, R.J. Goldston, A. Kallenbach, B. Sieglin, H.J. Sun, ASDEX Upgrade Team, and JET Contributors. “Correlation of the tokamak H-mode density limit with ballooning stability at the separatrix”. In: *Nuclear Fusion* 58.3 (2018), p. 034001. DOI: `10.1088/1741-4326/aaa340`.

[140] O. Sauter, C. Angioni, and Y. R. Lin-Liu. “Neoclassical conductivity and bootstrap current formulas for general axisymmetric equilibria and arbitrary collisionality regime”. In: *Physics of Plasmas* 6.7 (1999), pp. 2834–2839. DOI: `10.1063/1.873240`.

[141] O. Sauter, C. Angioni, and Y. R. Lin-Liu. "Erratum: "Neoclassical conductivity and bootstrap current formulas for general axisymmetric equilibria and arbitrary collisionality regime" [Phys. Plasmas 6, 2834 (1999)]". In: *Physics of Plasmas* 9.12 (2002), pp. 5140–5140. DOI: `10.1063/1.1517052`.

[142] C. K. Tsui, J. A. Boedo, J. R. Myra, B. Duval, B. Labit, C. Theiler, N. Vianello, W. A. J. Vijvers, H. Reimerdes, S. Coda, O. Février, J. R. Harrison, J. Horacek, B. Lipschultz, R. Maurizio, F. Nespoli, U. Sheikh, K. Verhaegh, and N. Walkden. "Filamentary velocity scaling validation in the TCV tokamak". In: *Physics of Plasmas* 25.7 (2018), p. 072506. DOI: `10.1063/1.5038019`.

[143] D. Carralero, G. Birkenmeier, H.W. Müller, P. Manz, P. deMarne, S.H. Müller, F. Reimold, U. Stroth, M. Wischmeier, E. Wolfrum, and The ASDEX Upgrade Team. "An experimental investigation of the high density transition of the scrape-off layer transport in ASDEX Upgrade". In: *Nuclear Fusion* 54.12 (2014), p. 123005. DOI: `10.1088/0029-5515/54/12/123005`.

[144] U A Sheikh, M Dunne, L Frassinetti, P Blanchard, B P Duval, B Labit, A Merle, O Sauter, C Theiler, C Tsui, the TCV Team, and the EUROfusion MST1 Team. "Pedestal structure and energy confinement studies on TCV". In: *Plasma Physics and Controlled Fusion* 61.1 (2018), p. 014002. DOI: `10.1088/1361-6587/aae7bd`.

[145] M. Faitsch, T. Eich, G.F. Harrer, E. Wolfrum, D. Brida, P. David, M. Dunne, L. Gil, B. Labit, U. Stroth, the ASDEX Upgrade Team, and the EUROfusion MST1 Team. "Analysis and expansion of the quasi-continuous exhaust (QCE) regime in ASDEX Upgrade". In: *Nuclear Fusion* 63.7 (2023), p. 076013. DOI: `10.1088/1741-4326/acd464`.

[146] A. Redl, T. Eich, N. Vianello, J. Adamek, M. Bernert, G. Birkenmeier, D. Brida, P. David, M. Dreval, M. Faitsch, R. Fischer, G. Grenfell, R. Ochoukov, V. Rohde, B. Tal, the ASDEX Upgrade team, and the EUROfusion MST1 team. ""An extensive analysis of SOL properties in high-δ plasmas in ASDEX Upgrade"". Submitted to *Nucl. Fusion*. 2023.

[147] R. Maurizio, B.P. Duval, B. Labit, H. Reimerdes, M. Faitsch, M. Komm, U. Sheikh, C. Theiler, the TCV team, and the EUROfusion MST1 team. "H-mode scrape-off layer power width in the TCV tokamak". In: *Nuclear Fusion* 61.2 (2021), p. 024003. DOI: `10.1088/1741-4326/abd147`.

[148] J. R. Myra, D. A. Russell, and D. A. D'Ippolito. "Collisionality and magnetic geometry effects on tokamak edge turbulent transport. I. A two-region model with application to blobs". In: *Physics of Plasmas* 13.11 (2006), p. 112502. DOI: `10.1063/1.2364858`.

[149] P. Paruta, C. Beadle, P. Ricci, and C. Theiler. "Blob velocity scaling in diverted tokamaks: A comparison between theory and simulation". In: *Physics of Plasmas* 26.3 (2019), p. 032302. DOI: `10.1063/1.5080675`. URL: `https://doi.org/10.1063/1.5080675`.

[150] D. Carralero, P. Manz, L. Aho-Mantila, G. Birkenmeier, M. Brix, M. Groth, H. W. Müller, U. Stroth, N. Vianello, and E. Wolfrum. "Experimental Validation of a Filament Transport Model in Turbulent Magnetized Plasmas". In: *Phys. Rev. Lett.* 115 (21 Nov. 2015), p. 215002. DOI: `10.1103/PhysRevLett.115.215002`.

[151] D. Carralero, H.W. Müller, M. Groth, M. Komm, J. Adamek, G. Birkenmeier, M. Brix, F. Janky, P. Hacek, S. Marsen, F. Reimold, C. Silva, U. Stroth, M. Wischmeier, and E. Wolfrum. "Implications of high density operation on SOL transport: A multimachine investigation". In: *Journal of Nuclear Materials* 463 (2015), pp. 123–127. DOI: `doi.org/10.1016/j.jnucmat.2014.10.019`.

[152] A. Wynn, B. Lipschultz, I. Cziegler, J. Harrison, A. Jaervinen, G. F. Matthews, J. Schmitz, B. Tal, M. Brix, C. Guillemaut, D. Frigione, A. Huber, E. Joffrin, U. Kruzei, F. Militello, A. Nielsen, N.R. Walkden, S. Wiesen, and JET Contributors. "Investigation into the formation of the scrape-off layer density shoulder in JET ITER-like wall L-mode and H-mode plasmas". In: *Nuclear Fusion* 58.5 (2018), p. 056001. DOI: `10.1088/1741-4326/aaad78`.

[153] N. Vianello, C. Tsui, C. Theiler, S. Allan, J. Boedo, B. Labit, H. Reimerdes, K. Verhaegh, W.A.J. Vijvers, N. Walkden, S. Costea, J. Kovacic, C. Ionita, V. Naulin, A.H. Nielsen, J. Juul Rasmussen, B. Schneider, R. Schrittwieser, M. Spolaore, D. Carralero, J. Madsen, B. Lipschultz, F. Militello, The TCV Team, and The EUROfusion MST1 Team. "Modification of SOL profiles and fluctuations with line-average density and divertor flux expansion in TCV". In: *Nuclear Fusion* 57.11 (2017), p. 116014. DOI: `10.1088/1741-4326/aa7db3`.

[154] G Saibene, R Sartori, A Loarte, D J Campbell, P J Lomas, V Parail, K D Zastrow, Y Andrew, S Sharapov, A Korotkov, M Becoulet, G T A Huysmans, H R Koslowski, R Budny, G D Conway, J Stober, W Suttrop, A Kallenbach, M von Hellermann, and M Beurskens. "Improved performance of ELMy H-modes at high density by plasma shaping in JET". In: *Plasma Physics and Controlled Fusion* 44.9 (2002), p. 1769. DOI: `10.1088/0741-3335/44/9/301`.

[155] J Stober, O Gruber, A Kallenbach, V Mertens, F Ryter, A Stäbler, W Suttrop, W Treutterer, and the ASDEX Upgrade Team. "Effects of triangularity on confinement, density limit and profile stiffness of H-modes on ASDEX upgrade". In: *Plasma Physics and Controlled Fusion* 42.5A (2000), A211. DOI: `10.1088/0741-3335/42/5A/324`.

[156] J. A. Boedo, D. L. Rudakov, R. A. Moyer, G. R. McKee, R. J. Colchin, M. J. Schaffer, P. G. Stangeby, W. P. West, S. L. Allen, T. E. Evans, R. J. Fonck, E. M. Hollmann, S. Krasheninnikov, A. W. Leonard, W. Nevins, M. A. Mahdavi, G. D. Porter, G. R. Tynan, D. G. Whyte, and X. Xu. "Transport by intermittency in the boundary of the DIII-D tokamak". In: *Physics of Plasmas* 10.5 (2003), pp. 1670–1677. doi: `10.1063/1.1563259`. url: `https://doi.org/10.1063/1.1563259`.

[157] N. Offeddu, W. Han, C. Theiler, T. Golfinopoulos, J.L. Terry, E. Marmar, C. Wüthrich, C.K. Tsui, H. de Oliveira, B.P. Duval, D. Galassi, D.S. Oliveira, D. Mancini, and the TCV Team. "Cross-field and parallel dynamics of SOL filaments in TCV". In: *Nuclear Fusion* 62.9 (2022), p. 096014. doi: `10.1088/1741-4326/ac7ed7`.

[158] C. Wüthrich, C. Theiler, N. Offeddu, D. Galassi, D.S. Oliveira, B.P. Duval, O. Février, T. Golfinopoulos, W. Han, E. Marmar, J.L. Terry, C.K. Tsui, and the TCV Team. "X-point and divertor filament dynamics from gas puff imaging on TCV". In: *Nuclear Fusion* 62.10 (2022), p. 106022. doi: `10.1088/1741-4326/ac8692`.

[159] A. Niemczewski. "Neutral particle dynamics in the Alcator C-mod tokamak". PhD thesis. Massachusetts Institute of Technology, Cambridge, MA, 1995, p. 144. url: `http://hdl.handle.net/1721.1/11284`.

[160] A Zito, M Wischmeier, D Carralero, P Manz, I Paradela Pérez, M Passoni, and the ASDEX Upgrade Team. "Numerical modelling of an enhanced perpendicular transport regime in the scrape-off layer of ASDEX Upgrade". In: *Plasma Physics and Controlled Fusion* 63.7 (2021), p. 075003. doi: `10.1088/1361-6587/abfcb6`.

[161] P. Ricci, B. N. Rogers, and S. Brunner. "High- and Low-Confinement Modes in Simple Magnetized Toroidal Plasmas". In: *Phys. Rev. Lett.* 100 (22 June 2008), p. 225002. doi: `10.1103/PhysRevLett.100.225002`.

Scientific production

Publications

M. Giacomin, **A. STAGNI**, P. Ricci, J.A. Boedo, J. Horacek, H. Reimerdes, C.K. Tsui. “Theory-based scaling laws of near and far scrape-off layer widths in single-null L-mode discharges”. In: *Nuclear Fusion* 61.7 (2021), p. 076002. doi: 10.1088/1741-4326/abf8f6.

H. Reimerdes, [...] T. Ravensbergen, D. Ricci, P. Ricci, N. Rispoli, F. Riva, J.F. Rivero-Rodriguez, M. Salewski, O. Sauter, B.S. Schmidt, R. Schrittweiser, S. Sharapov, U.A. Sheikh, B. Sieglin, M. Silva, A. Smolders, A. Snicker, C. Sozzi, M. Spolaore, **A. STAGNI** et al. “Overview of the TCV tokamak experimental programme”. In: *Nuclear Fusion* 62.4 (2022), p. 042018. doi: 10.1088/1741-4326/ac369b.

A. STAGNI, N. Vianello, C.K. Tsui, C. Colandrea, S. Gorno, M. Bernert, J. A. Boedo, D. Brida, G. Falchetto, A. Hakola, G. Harrer, H. Reimerdes, C. Theiler, E. Tsitrone, N. Walkden, the TCV team and the EUROfusion MST1 team. “Dependence of scrape-off layer profiles and turbulence on gas fuelling in high density H-mode regimes in TCV”. In: *Nuclear Fusion* 62.9 (2022), p. 096031. doi: 10.1088/1741-4326/ac8234.

L.Frassinetti, C. Perez von Thun, B. Chapman-Oplopoiou, H.Nyström, M. Poradzinski, J.C. Hillesheim, L. Horvath, C.F. Maggi, S. Saarelma, **A. STAGNI**, G. Szepesi, A. Bleasdale, R.B. Morales, M. Brix, P. Carvalho, D. Dunai, A.R. Field, J. M. Fontdecaba, H.J. Sun, D.B. King et al. “Effect of the isotope mass on pedestal structure, transport and stability in D, D/T and T plasmas at similar β_N and gas rate in JET-ILW type I ELMy H-modes”. In: *Nuclear Fusion* 63.11 (2023), p. 112009. doi: 10.1088/1741-4326/acf057

A. STAGNI, N. Vianello, M. Agostini, C. Colandrea, S. Gorno, B. Labit, U. Sheikh, L. Simons, G. Sun, C.K. Tsui, M. Ugoletti, Y. Wang, C. Wüthrich, J.A. Boedo, H. Reimerdes, C. Theiler and the TCV team. “The effect of plasma shaping on high density H-mode SOL profiles and fluctuations in TCV”. In: *Nuclear Fusion* (2024) in press. DOI: `https://doi.org/10.1088/1741-4326/ad1a56`10.1088/1741-4326/ad1a56.

CONFERENCES AND WORKSHOPS

N. Vianello, N. Walkden, M. Dunne, B. Lomanowski, E. Wolfrum, C.K. Tsui, **A. STAGNI**, M. Griener, B. Tal, T. Eich, D. Refy, D. Brida, O. Fèvrier, M. Agostini, H. De Oliveira, S. Aleiferis, M. Bernert, J.A. Boedo, M. Brix, D. Carralero et al. "SOL profile and fluctuations in different divertor recycling conditions in H-mode plasmas". *28th IAEA Fusion Energy Conference* (Nice, France), 10/05-15/05/2021, poster presentation [EX/P3-14].

N. Vianello, **A. STAGNI**, N. Walkden, G. Falchetto, A. Hakola, M. Bernert, E. Wolfrum, M. Griener, B. Tal, D. Brida, C.K. Tsui, C. Theiler, H. Reimerdes, O. Fèvrier, B. Labit, S. Gorno, B. Lomanowski, M. Dunne, I. Carvalho, D. Refy et al. "H-mode density shoulder and the role of separatrix conditions". *30th ITPA Scrape-off Layer and Divertor Topical Group Meeting* (Online), 28/06-08/07/2021, presentation [DSOL-34]

M. Giacomin, P. Ricci, J.A. Boedo, J. Horacek, D. Mancini, H. Reimerdes, **A. STAGNI**, C.K. Tsui, N. Vianello. "Theory-based scaling laws of the near and far scrape-off layer widths in L-mode discharges". *30th ITPA Scrape-off Layer and Divertor Topical Group Meeting* (Online), 28/06-08/07/2021, presentation [DSOL-34]

M. Giacomin, P. Ricci, J. Horacek, A. Pau, H. Reimerdes, O. Sauter, **A. STAGNI**. "Theory-based scaling laws of the near scrape-off layer width in L-mode discharges and density limit crossing, including comparison with experiments". *18th International Workshop on Plasma Edge Theory in Magnetic Fusion Devices* (Online), 13/09-15/09/2021, oral presentation [Abstract]

A. STAGNI, N. Vianello, C.K. Tsui, C. Colandrea, S. Gorno, N. Walkden, G. Falchetto, A. Hakola, M. Bernert, D. Brida, G. Harrer, E. Tsitrone, J.A. Boedo, H. Reimerdes, C. Theiler, the TCV team and the EUROfusion MST1 team. "Dependence of scrape-off layer profiles and transport on gas fuelling in high-density H-mode regimes in TCV". *31st ITPA Scrape-off Layer and Divertor Topical Group Meeting* (Online), 18/01-26/01/2022, presentation [DSOL-34]

A. STAGNI, N. Vianello, C.K. Tsui, C. Colandrea, S. Gorno, B. Labit, J.A. Boedo, D. Brida, M. Dunne, T. Eich, G. Falchetto, L. Frassinetti, R.J. Goldston, G. Harrer, H. Reimerdes, C. Theiler, N. Walkden, the TCV Team and the EUROfusion MST1 Team. "Effect of divertor fuelling and plasma shaping on scrape-off layer profiles and transport properties in TCV H-mode discharges". *25th International Conference on Plasma-Surface Interactions in Fusion Devices* (Jeju, South Korea), 13/06-17/06/2022, oral presentation [TO27].

A. STAGNI, N. Vianello, C.K. Tsui, C. Colandrea, S. Gorno, B. Labit, J.A. Boedo, H. Reimerdes, C. Theiler and the TCV team. "Effect of shaping on SOL profiles in high density TCV H-mode plasmas". *32nd ITPA Scrape-off Layer and Divertor Topical Group Meeting* (Cadarache, France), 24/10-28/10/2022, presentation [DSOL-34]

A. STAGNI, N. Vianello, M. Agostini, C. Colandrea, S. Gorno, B. Labit, G. Sun, C.K. Tsui, M. Ugoletti, Y. Wang, C. Wütrich, J.A. Boedo, H. Reimerdes, C. Theiler and the TCV team. "Investigating the role of plasma shaping in the evolution of high density H-mode SOL profiles and fluctuations in TCV". *49th European Conference on Plasma Physics* (Bordeaux, France), 03/07-07/07/2023, poster presentation [Mo_MCF11].

L.Frassinetti, C. Perez von Thun, B. Chapman-Oplopoiou, H.Nyström, M. Poradzinski, J.C. Hillesheim, L.Horvath, C.F. Maggi, S. Saarelma, **A. STAGNI**, G. Szepesi, A. Bleasdale, R.B. Morales, M. Brix, P. Carvalho, D. Dunai, A.R. Field, J.M. Fontdecaba, S. Hongjuan, D.B. King et al. "Understanding pedestal structure, pedestal stability and pedestal turbulent transport in D, DT and T plasmas in JET-ILW". *49th European Conference on Plasma Physics* (Bordeaux, France), 03/07-07/07/2023, invited talk [I4.106].

N. Vianello, **A. STAGNI**, A. Redl, T. Eich, C.K. Tsui, D. Brida, J.A. Boedo, C. Colandrea, P. David, M. Dreval, M. Faitsch, G. Grenfell, M. Griener, S. Gorno, G. Harrer, B.Labit, R. Ochoukov, H. Reimerdes, C. Theiler the ASDEX-Upgrade team and the TCV team. "H-Mode SOL Profiles and transport dependence on separatrix operational space". *29th IAEA Fusion Energy Conference* (London, UK), 16/10-21/10/2023, poster presentation [EXD/P1955].

Acknowledgments

Yet another long journey, yet another important milestone in my life and academic career has come to an end. These three and a half years spent carrying out my PhD research project have been some of the most demanding and consuming in terms of the mental effort I have had to put in, but at the same time and also for these reasons they have been some of the most satisfying. Once again, before embarking on a new path, the time has come for me to rethink what I have left behind. In doing so, I can only acknowledge the fundamental role that some people have played over the years.

Firstly, I would like to dedicate some special and immeasurable thanks to all the people who have accompanied me throughout my studies. Thank you to my parents, my brother Alessandro, my grandparents and my entire family for constantly placing their trust in me, for making me feel proud in the good times, as well as for supporting me and listening to me in the bad times. Thank you to my partner Carla for always standing by me and constantly being a reference, both during the first difficult pandemic period and during the last year and a half spent together in Padova. Thanks to all my friends in Barletta and in particular to Maurizio, Alessia, Giuseppe, Angela, Claudio, and Stefania for always making me feel at home during my now sporadic returns to my hometown. Thanks to all my Ugly Office® friends and colleagues Stefano, Francesco, Nicholas, Andrea, Luca^2, Rachele and Matteo, with whom I have had the pleasure of sharing time, space, conversations, lunches and several coffees since the beginning of my PhD. Thanks to all the people of the Jungle Office and especially Edoardo and Matteo, sooner or later you will explain to me how you manage to go to the park to train even in near-zero temperatures. I would like to thank Andreas for sharing with me part of my travels and visits to Europe at research facilities and conferences. Finally, I would like to thank all my fellow RFX researchers and PhD students with whom I have had the pleasure of sharing these three years.

I cannot refrain from thanking all those figures who have been an academic reference guide, without whom it would not have been possible to complete this journey. Thanks in the first place to Nicola Vianello, towards whom I have a sincere esteem and respect, for having welcomed me to Consorzio RFX and led me through the meanders of European research on plasma physics and thermonuclear fusion within the EUROfusion programmes. Thanks to Matteo Zuin, with whom

I had the pleasure of sharing some teaching and research activities. I would also like to thank the team of researchers who allowed this experimental work to see the light of day: Claudia Colandrea, Sophie Gorno, Cedric Tsui, Matteo Agostini, and Margherita Ugoletti, for devoting part of their time to carrying out the preliminary analyses required to obtain the results presented in this doctoral dissertation thesis. Thanks to Christian Theiler, Holger Reimerdes and Benoit Labit for their invaluable supervision and constant input so that the two research articles published so far could come to completion. Thanks to Thomas Eich, Michael Faitsch and all the people with whom I have had the pleasure of sharing discussions and opinions on plasma physics.

RINGRAZIAMENTI

Un altro lungo percorso, un'altra importante tappa della mia vita e della mia carriera accademica sono giunti al termine. Questi tre anni e mezzo di dottorato sono stati alcuni tra i più impegnativi e consumanti dal punto di vista degli sforzi mentali che ho dovuto sostenere, ma allo stesso tempo ed anche per queste ragioni sono stati alcuni tra i più soddisfacenti. Ancora una volta, prima di intraprendere un nuovo percorso è arrivato il momento per me di ripensare a ciò che ho lasciato alle spalle. In fare ciò, non posso che riconoscere il ruolo fondamentale che alcune persone hanno avuto in questi anni.

In primo luogo, voglio dedicare un ringraziamento speciale ed incommensurabile a tutte le persone che mi hanno accompagnato durante questo percorso di studi. Grazie ai miei genitori, a mio fratello Alessandro, ai miei nonni e a tutta la mia famiglia per aver costantemente riposto in me la loro fiducia, per avermi fatto sentire orgoglioso nei momenti positivi, così come per avermi supportato e saputo ascoltare in quelli negativi. Grazie alla mia compagna Carla per essermi rimasta sempre accanto ed aver costantemente rappresentato un punto di riferimento, tanto nel primo difficile periodo pandemico di distanza quanto durante l'ultimo anno e mezzo trascorso assieme a Padova. Grazie a tutti i miei amici di Barletta e in particolare a Maurizio, Alessia, Giuseppe, Angela, Claudio, Stefania per avermi sempre fatto sentire a casa durante i miei ormai pochi sporadici ritorni nella mia città. Grazie a tutti i miei amici e colleghi dell'Ufficio Brutto® Stefano, Francesco, Nicholas, Andrea, Luca^2, Rachele, Matteo, con cui ho avuto il piacere di condividere tempo, spazi, conversazioni, pranzi e svariati caffè sin dall'inizio del mio dottorato. Grazie a tutti gli inquilini dell'Ufficio Giungla e in particolar modo ad Edoardo e Matteo, prima o poi mi spiegherete come fate ad andare al parchetto ad allenarvi anche con temperature prossime allo zero. Ringrazio Andreas per aver condiviso con me parte dei miei viaggi e visite in Europa presso strutture di ricerca e conferenze. Infine, ringrazio tutti i miei colleghi ricercatori e dottorandi di RFX con cui ho avuto il piacere di condividere questi tre anni.

Non posso esimermi dal ringraziare tutte quelle figure che hanno rappresentato una guida accademica di riferimento, senza le quali non sarebbe stato possibile portare a compimento questo percorso. Grazie in primo luogo a Nicola Vianello, verso il quale nutro una sincera stima e rispetto, per

avermi accolto al Consorzio RFX e condotto attraverso i meandri della ricerca europea sulla fisica dei plasmi e la fusione termonucleare all'interno dei programmi EUROfusion. Grazie a Matteo Zuin, con il quale ho avuto il piacere di condividere alcune attività di didattica e di ricerca. Ringrazio anche il team di ricercatori che ha permesso a questo lavoro sperimentale di vedere la luce: Claudia Colandrea, Sophie Gorno, Cedric Tsui, Matteo Agostini, Margherita Ugoletti, per aver dedicato parte del loro tempo allo svolgimento delle analisi preliminari necessarie al fine di ottenere i risultati presentati in questa tesi di dottorato. Grazie a Christian Theiler, Holger Reimerdes e Benoit Labit per la loro preziosa supervisione e il costante apporto fornito affinché i due articoli finora pubblicati giungessero a compimento. Grazie a Thomas Eich, Michael Faitsch e a tutte le persone con cui ho avuto il piacere di condividere discussioni e opinioni sulla fisica dei plasmi.